

**Correlative ex-situ analysis and operando ellipsometric
investigation during oxygen evolution reaction of mesoporous
iridium oxide model catalysts**

vorgelegt von
Master of Science
René Sachse

ORCID: 0000-0002-3611-3352

von der Fakultät II - Mathematik und Naturwissenschaften
der Technischen Universität Berlin
zur Erlangung des akademischen Grades

Doktor der Naturwissenschaften
– Dr. rer. nat. –

genehmigte Dissertation

Promotionsausschuss:

Vorsitzender: Prof. Dr. Thomas Friedrich

Gutachter: Dr.-Ing. habil. Ralph Krähnert

Gutachter: Prof. Dr. Peter Strasser

Gutachter: Prof. Dr. Regine von Klitzing

Tag der wissenschaftlichen Aussprache: 09.06.2021

Berlin 2022

Danksagung

Während meiner Doktorarbeit haben mich viele Menschen in vielfältiger Weise fachlich und moralisch unterstützt, bei denen ich mich ganz herzlich bedanken möchte.

Ich möchte mich bei meinem Betreuer Dr.-Ing. habil. Ralph Krähnert dafür, dass er mich in seine Gruppe aufgenommen hat und mir die Möglichkeit gab, diese Arbeit anzufertigen, bedanken. Ohne seine strukturierte wissenschaftliche Betrachtung und der ergebnisorientierten Planung neuer Experimente wäre diese Arbeit nicht möglich gewesen.

Ebenso danke ich Dr. Andreas Hertwig für seine wissenschaftliche Betreuung und die ausführliche Anleitung zur spektroskopischen Ellipsometrie. Er ermöglichte mir, durch die Einwerbung des EU-Projekts HyMET (16ENG03), diese Dissertation anzufertigen. Auch für die Möglichkeit des wissenschaftlichen Austausches auf nationalen und internationalen Konferenzen möchte mich bei ihm bedanken.

Ein besonderer Dank gilt auch Prof. Dr. Peter Strasser und Prof. Dr. Regine von Klitzing für die Übernahme und Erstellung der Gutachten. Bei Herrn Prof. Dr. Thomas Friedrich bedanke ich mich für die bereitwillige Übernahme des Prüfungsvorsitzes.

Diese Arbeit ist durch eine Vielzahl an Kooperationen entstanden, weshalb ich mich bei Mario Sahre für XRD und XRR Messungen und bei Mika Pflüger für die ausführlichen XRR Auswertungen bedanken möchte. Ich möchte auch Dr. Juan J. Velasco-Vélez für die detaillierten XPS und XAS Messungen danken. Einen großen Dank möchte ich an Dr. Vasile-Dan Hodoroba richten, der mir bei wissenschaftlichen Fragestellungen zur Elektronenmikroskopie geholfen hat. Ich möchte auch Sigrid Benemann für ihre Unterstützung bei den REM-Messungen danken. Mein Dank gilt auch dem Team der ZELMI, insbesondere Sören Selve und Jan Simke, die mich bei zahlreichen TEM-Messungen fachlich und technisch unterstützt haben. Ebenso danke ich Dr. Roman Schmack für seine Anleitung zur TEM-Analyse. Dr. Michael Griepentrog und Thorid Lange danke ich für instrumentierte Eindringprüfungen. Bei Gundula Hidde, Olivia Netzbund und Michaela Lagleder bedanke ich mich für verschiedene analytische Messungen und Unterstützung bei präparativen Arbeiten.

Ich danke meinen Kollegen an der TU Berlin Dr. Denis Bernsmeier, Dr. Michael Bernicke, Dr. Katrin Krafft, Dr. Roman Schmack, Benjamin Paul, Aleks Arinchtein, Marvin Frisch und Kornelia Weh für das angenehme Arbeitsklima, die wissenschaftlichen Diskussionen und die gemeinsam verbrachten Abende abseits der Wissenschaft. Bedanken möchte ich mich auch bei Prof. Dr. Peter Strasser und den Kollegen seiner Arbeitsgruppe für den freundlichen Umgang und den einen oder anderen lustigen Kickerabend.

Ein großer Dank richtet sich auch an Dr. Uwe Beck, der mich im Fachbereich 6.7 aufgenommen hat und mir somit meine experimentellen Arbeiten ermöglichte. Ich möchte mich auch bei ihm für seine Hilfsbereitschaft und sein Engagement in allen Belangen und Fragen bedanken. Ebenso möchte ich mich bei allen Kollegen der Abteilung 6.7 und 6.1 für ihre freundliche Unterstützung und Geduld bei wissenschaftlichen Fragestellungen bedanken.

Bedanken möchte ich mich auch bei der Werkstatt der Bundesanstalt für Materialforschung und -prüfung, insbesondere bei Herrn Thomas Bernstein für die gemeinsame Planung und Anfertigung der entwickelten Durchflusszelle, ohne die ein großer Teil dieser Arbeit nicht möglich gewesen wäre.

Weiterhin möchte ich mich bei der EU und dem Projektträger EURAMET (HyMet, Projektnummer: 16ENG03) sowie der Bundesanstalt für Materialforschung und -prüfung für die finanzielle Unterstützung in den vergangenen Jahren bedanken.

Ein besonders großes Dankeschön geht schließlich an meine Familie, die mich bei all meinen Vorhaben immer unterstützt hat. Ein großes Dankeschön geht auch an Friederike Schmidt, für ihre Ermutigung und Motivation während der letzten Jahre und an meine Freunde für die schöne Zeit in all den Jahren.

Abstract

In the face of rising energy demand and the impending climate change, the development of sustainable, fossil-free fuel and chemical production is of global importance. One way to achieve these goals is the development of electrochemical conversion processes using catalysts. Key to the development of improved catalysts is a better understanding of the relations between their performance, stability, and physicochemical properties. However, the complex morphology of such catalysts constitutes a challenge even for modern analytical techniques. For example, standard rotating disc electrode experiments are performed to study the impact of the catalysts structure on electrochemical processes, but do not provide any information about changing material properties during the experiment.

Ellipsometry is a very versatile spectroscopic method, often used to study film thickness and refractive index, but also providing access to electrical and electronic properties. Spectroscopic ellipsometry (SE) further offers the possibility to study materials under different environments. However, since material properties cannot be taken directly from the measured spectra, suitable models have to be developed and validated.

In this thesis, a model for ellipsometric fit studies of a calcination series of mesoporous iridium oxide films (300 °C – 600 °C) was developed and validated in terms of film thickness and porosity as well as electrical and electronic properties using various ex-situ characterization methods such as scanning electron microscopy (SEM), X-ray reflectometry (XRR), conductivity measurements, and UV-VIS-NIR absorption spectroscopy. SE data also offer the possibility to derive valence electron energy loss spectra (VEELS), which provide further information about the electronic structure of the materials. Comparison of the data from the VEEL spectra with activity measurements of the oxygen evolution reaction (OER) suggests that the intrinsic activity (surface charge normalized activity) of IrO_x scales with interband transition energies between the Ir 5d t_{2g} sub-level and the O 2p orbital.

For SE studies under operando conditions, an environmental cell setup was developed that allows simultaneous spectroscopic characterization while measuring the catalytic activity of a reaction. Analyses on a platinum surface successfully demonstrate the oxidation and reduction of a platinum oxide layer as a function of the potential. Electrochemical SE studies (ECSE) on mesoporous IrO_x films show a dependence of the electrical and electronic properties on the applied potential. Furthermore, the degree of filling of the pores with the generated gas (oxygen) can be detected. The influence of the calcination temperature can also be related to the potential dependent changes of the electrical and electronic properties as well as the pore filling degree.

This work further discusses a possible band structure of the IrO_x materials as a function of calcination temperature as well as potential and calcination temperature dependent changes during OER catalysis. Furthermore, a time-resolved and potential-dependent quantification analysis of the gas accumulation in the pores of the catalyst systems is discussed.

Zusammenfassung

Angesichts des steigenden Energiebedarfs und des drohenden Klimawandels ist die Entwicklung einer nachhaltigen, fossilfreien Kraftstoff- und Chemieproduktion von globaler Bedeutung. Eine Möglichkeit, diese Ziele zu erreichen, ist die Entwicklung von elektrochemischen Umwandlungsprozessen unter Verwendung von Katalysatoren. Der Schlüssel zur Entwicklung verbesserter Katalysatoren ist ein besseres Verständnis der Zusammenhänge zwischen ihrer Leistung, Stabilität und ihren physikochemischen Eigenschaften. Die komplexe Morphologie solcher Katalysatoren stellt jedoch selbst für moderne analytische Techniken eine Herausforderung dar. So werden z. B. Standard-Experimente mit rotierenden Scheibenelektroden durchgeführt, um den Einfluss der Katalysatorstruktur auf elektrochemische Prozesse zu untersuchen, liefern aber keine Informationen über sich ändernde Materialeigenschaften während des Experiments.

Die Ellipsometrie ist eine sehr vielseitige spektroskopische Methode, die häufig zur Untersuchung von Schichtdicke und Brechungsindex eingesetzt wird, aber auch Zugang zu elektrischen und elektronischen Eigenschaften bietet. Die spektroskopische Ellipsometrie (SE) bietet außerdem die Möglichkeit, Materialien unter verschiedenen Umgebungsbedingungen zu untersuchen. Da die Materialeigenschaften jedoch nicht direkt aus den gemessenen Spektren entnommen werden können, müssen geeignete Modelle entwickelt und validiert werden.

In dieser Arbeit wurde ein Modell für ellipsometrische Fit-Studien einer Kalzinierungsserie mesoporöser Iridiumoxid-Filme (300 °C – 600 °C) entwickelt und hinsichtlich Filmdicke und Porosität sowie elektrischer und elektronischer Eigenschaften unter Verwendung verschiedener Ex-situ-Charakterisierungsmethoden wie Rasterelektronenmikroskopie (REM), Röntgenreflektometrie (XRR), Leitfähigkeitsmessungen und UV-VIS-NIR-Absorptionsspektroskopie validiert. SE-Daten bieten auch die Möglichkeit, Valenzelektronen-Energieverlustspektren (VEELS) abzuleiten, die weitere Informationen über die elektronische Struktur der Materialien liefern. Der Vergleich der Daten aus den VEEL-Spektren mit Aktivitätsmessungen der Sauerstoff-Evolutionsreaktion (OER) legt nahe, dass die intrinsische Aktivität (oberflächenladungsnormierte Aktivität) von IrO_x mit den Zwischenband-Übergangsenergien zwischen dem Ir 5d t_{2g} Niveau und dem O 2p Orbital skaliert.

Für SE-Untersuchungen unter operando-Bedingungen wurde ein Umgebungszellen-Setup entwickelt, das die gleichzeitige spektroskopische Charakterisierung bei gleichzeitiger Messung der katalytischen Aktivität einer Reaktion erlaubt. Analysen auf einer Platinoberfläche zeigen erfolgreich die Oxidation und Reduktion einer Platinoxidschicht als Funktion des Potentials. Elektrochemische SE-Studien (ECSE) an mesoporösen IrO_x -Filmen zeigen eine Abhängigkeit der elektrischen und elektronischen Eigenschaften vom angelegten Potential. Weiterhin kann der Füllungsgrad der Poren mit dem erzeugten Gas (Sauerstoff) nachgewiesen werden. Der Einfluss der Kalzinierungstemperatur kann ebenfalls mit den potenzialabhängigen Änderungen der elektrischen und elektronischen Eigenschaften sowie des Porenfüllungsgrades in Verbindung gebracht werden.

In dieser Arbeit wird weiterhin eine mögliche Bandstruktur der IrO_x-Materialien in Abhängigkeit von der Kalzinierungstemperatur diskutiert, sowie die potenzial- und kalzinierungstemperaturabhängigen Änderungen während der OER-Katalyse. Weiterhin wird eine zeitaufgelöste und potenzialabhängige Quantifizierungsanalyse der Gasanreicherung in den Poren der Katalysatorsysteme diskutiert.

Abbreviations

α	absorption coefficient	\vec{D}	electric displacement field vector
α_e	constant proportional to the probability of an electron transition between occupied and empty states	d	film thickness
a_0	Bohr radius	d_n	thickness of the specified layer
A	area of the measuring spot	$d_{crystalite}$	mean size of the crystallite
Amp	amplitude of the oscillator function	$d_{lattice}$	distance between the lattice planes
a-BEMA	anisotropic Bruggeman effective medium approximation	δ	phase shift
Ag/AgCl	silver/silver chloride reference electrode	Δ	ellipsometric angle, corresponds to the phase difference
ALD	atomic layer deposition	DFT	density functional theory
AOI	angle of incidence	DOS	density of states
\vec{B}	magnetic field vector	ε	complex dielectric function
β	phase factor	ε_0	dielectric function in vacuum
β_{EELS}	collection semi-angle	ε_1	real part of the dielectric function
BEMA	Bruggeman effective medium approximation	ε_2	imaginary part of the dielectric function
BET	Brunauer Emmett Teller model for physisorption	ε_{EMA}	dielectric function of the mixed phase
c_g	concentration of the produced gas during OER (oxygen)	ε_i	dielectric function of the i^{th} component (i.e., the guest dielectric function, $i = a, b, c$)
CA	chronoamperometry	ε_h	host dielectric function
CV	cyclovoltammetry / cyclic voltammetry	$\varepsilon_{eff,j}$	effective major dielectric function ($j = x, y, z$)
		ε_r	relative dielectric constant

ε_{∞}	real dielectric constant	EPMA	electron probe microanalysis
\vec{E}	electric field vector	EPMA-EDS	electron probe microanalysis using energy dispersive X- ray spectroscopy
E	photon energy		
E_0	standard electrode potential	EQCM	electrochemical quartz crystal microbalance
En_n	center energy of the oscillator function	EtOH	Ethanol
E_{EELS}	energy-loss	EXAFS	extended X-ray absorption near-edge structure
E_g	bandgap or transition energy		
E_F	Fermi level	f	filling factor, i.e. volume fraction of produced gas (air/void) within the pores
E_{pole}	position of a pole in the infrared as part of the Sellmeier dispersion layer	f_i	volume fraction of the i^{th} component
erf	deviation function	f_s	shape factor
ECSE	operando electrochemical spectroscopic ellipsometry	FFT	Fast Fourier Transformation
EDS	energy dispersive X-ray spectroscopy	FWHM	full width at half maximum
EEL	electron energy loss	h	Planck constant
EELS	electron energy loss spectroscopy	\hbar	reduced Planck constant
EEP	environmental ellipsometric porosimetry	\vec{H}	magnetic field strength
EISA	evaporation induced self- assembly	HER	hydrogen evolution reaction
ELF	energy loss function	γ	shape factor of the guest volume
EMA	effective medium approximation	γ_s	surface tension
EO	ethylene oxide	Γ	width of the oscillator function (full width at half maximum)
EP	ellipsometric porosimetry	$g(\sigma_0; \theta)$	Gaussian beam profile
		ΔG^0	free enthalpy change

I	intensity of the transmitted light	LN	liquid nitrogen
		LSV	linear sweep voltammetry
I_0	intensity of the incident light	m	nature of electron transition using the Tauc relation (i.e., direct or indirect allowed or forbidden transitions)
I_{EELS}	zero-loss intensity		
$I_{m,XRR}(\theta)$	measured XRR intensity	\dot{m}_A	mass flow
$I_{s,XRR}(\theta)$	simulated XRR intensity	m^*	electron effective mass
I_{X-ray}	incident X-ray intensity	m_0	electron rest mass
$-\text{Im}(\varepsilon^{-1})$	bulk valence electron energy loss spectra	m_d	diffraction order
$-\text{Im}((1 + \varepsilon)^{-1})$	surface valence electron energy loss spectra	μ	electron mobility
\vec{j}	electric current density	μ_0	magnetic permeability in vacuum
\vec{k}	wave vector	μ_r	relative magnetic permeability
k	extinction coefficient	$\mu_1\text{-OH}$	terminal/single-coordinated protonated oxygen species
k_A	kinetic constant	$\mu_3\text{-O}$	triple-coordinated oxygen species
$k_A V$	volume related kinetic constant	MSA	multi-sample-analysis
K_{EPMA}	ratio of the X-ray intensity of the element to be examined in the unknown sample to the X-ray intensity of the same element in a sample with known element concentration	n	refractive index
		N	electron concentration
K_{XRD}	dimensionless shape factor for crystallite size calculation	\tilde{N}	complex refractive index
		ω	angular frequency
λ	wavelength	φ_0	angle of incidence
l_{XRR}	length of the sample relative to the length of the X-ray beam in XRR measurements	φ_1	angle of refraction
		OCP	open circuit potential
L	depolarization factor	OER	oxygen evolution reaction
		p	pressure

(p/p_0)	partial pressure	r.H.	relative humidity
P	porosity	RDE	rotating disc electrode
P_{int}	principal value of the integral	RHE	reversible hydrogen electrode
\vec{P}	polarizability	RMSD	root mean squared deviation
Ψ	ellipsometric angle, $\tan \Psi$ corresponds to the amplitude ratio	rpm	revolutions per minute
PB	polybutadiene	σ	electrical conductivity
PDF	powder diffractometer file	σ_{dw}	Debye-Waller-like factor for roughness and interdiffusion
PEEK	polyether ether ketone	σ_θ	width of the Gaussian beam
PEO	polyethylene oxide	$S(E_n)$	single scattering distribution
PSD	pore size distribution	SAED	selected area electron diffraction
PO	propylene oxide	SAXS	small angle X-ray scattering
q	electron charge	SDD	silicon drift detector
q_t	momentum transfer	SE	spectroscopic ellipsometry
ρ	complex reflection ratio	SEM	scanning electron microscopy
ρ_n	specified density	SHE	standard hydrogen electrode
ρ_R	electrical resistivity	SOC	spin orbit coupling
r_K	Kelvin radius	θ	angle between the X-rays and the lattice plane
r_{Pore}	pore radius	θ_0	offset of the incidence angle
r_p	amplitude of reflection coefficient for parallel polarization	θ_{Bragg}	Bragg angle
r_s	amplitude of reflection coefficient for perpendicular polarization	θ_c	surface contact angle
R	molar gas constant	θ_E	characteristic scattering angle
R_{XRR}	XRR reflectivity	$\Theta_{XRR,i}$	angle of incidence
X			

t	time	XRD	X-ray diffraction
T	temperature in Kelvin [K]	XRR	X-ray reflectometry
$T_{calc.}$	calcination temperature in degrees Celsius [°C]	Y	number of wavelengths
τ	mean scattering time	Z	number of fit parameters.
TEM	transmission electron microscopy		
$u(\theta)$	uncertainty of XRR fitting		
U_j	shape parameters for the room directions x, y, z		
U_{RHE}	potential referred to the reversible hydrogen electrode		
UV-VIS-NIR	ultraviolet - visible - near infrared		
ν	frequency		
ν_e	electron beam velocity		
V	volume		
V_{pore}	pore volume		
V_{total}	volume of the entire layer		
VEELS	valence electron energy loss spectroscopy		
WDS	wavelength dispersive X-ray spectroscopy		
XANES	X-ray absorption near-edge structure		
XAS	X-ray absorption spectroscopy		
XPS	X-ray photoelectron spectroscopy		

Table of contents

Danksagung	I
Abstract	III
Zusammenfassung	V
Abbreviations	VII
1. Introduction	1
1.1 Motivation	1
1.2 Aims and structure of this thesis	2
2. State of the art	5
2.1 Electrochemical splitting of water	5
2.2 Characterization methods of thin (porous) films	12
2.3 Spectroscopic ellipsometry and modeling approaches	20
3 Experimental	35
3.1 Chemicals	35
3.2 Synthesis of mesoporous iridium oxide model catalysts	36
3.3 Ellipsometry and developed operando flow cell setup	37
3.4 Electrochemical testing (ECSE and RDE)	40
3.5 Complementary and additional analytical methods	42
4. Ex-situ characterization of mesoporous templated iridium oxide (IrO_x) films	44
4.1 Material analysis and physicochemical properties	45
4.2 Ellipsometric investigations and modeling	57
4.3 Electrochemical studies in the OER and lower potential regime	71
4.4 Validation of ellipsometric derived properties and correlation to electrochemical activity	76
5. Studies combining electrochemistry and spectroscopic ellipsometry using bulk Pt as an example	81
5.1 Ex-situ ellipsometric analysis and modeling	82
5.2 Operando investigations during cyclic voltammetry	84
6. Operando ECSE analysis of mesoporous IrO_x films under OER conditions	89
6.1 Study of the ellipsometric behavior using linear sweep voltammetry	90
6.2 Ellipsometric analysis and modeling during cyclic voltammetry	95
6.3 Influence of calcination temperature on material properties	102
7. General discussion	110
7.1 Impact of the calcination temperature on a proposed band structure of mesoporous IrO _x films	111
7.2 Influence of potential and calcination temperature on the intensity of VEEL spectra	114
7.3 Effect of T _{calc.} on potential-dependent changes of catalyst properties under OER conditions	117
7.4 Impact of calcination temperature, potential and time on gas transport	120
8. Conclusion and Outlook	124
Bibliography	127

A Appendix	137
A1 Dielectric function and optical constants of pure water / perchloric acid	137
A2 TEM / SAED analysis of a mesoporous IrO _x film	138
A3 XPS C1s spectra and summarization of the fitted photoelectron spectra	139
A4 Analysis of an uncoated Si substrate treated in a muffle furnace at 600 °C in flowing air for 2h	141
A5 Dielectric functions and optical constants of the a-BEMA (IrO _x 375 °C)	142
A6 SEM cross-section images of mesoporous IrO _x films (375 °C) at Si and Si/SiO ₂ substrates	143
A7 Instrumented indentation testing and XRR measurements at different humidity conditions	144
A8 SE analysis of titanium substrates	146
A9 Mean scattering time as a function of calcination temperature	147
A10 Ex-situ VEELS analysis of mesoporous IrO _x films on titanium substrates	148
A11 Physisorption via ellipsometric porosimetry	149
A12 Transmission spectra of mesoporous IrO _x films on quartz substrates	151
A13 Operando ECSE investigation of a non-conductive mesoporous titanium oxide film	152
A14 Operando ECSE investigations of mesoporous IrO _x (375 °C) in the lower potential range	156
A15 Operando ECSE investigations of the calcination series in the lower potential range	162
B List of publications and presentations	169

1. Introduction

1.1 Motivation

In view of the increasing energy demand, the limited availability of fossil fuels (coal, oil and gas) and the threat of climate change, efforts to develop sustainable and fossil-free energy sources are of great importance.¹ In this aspect, the producing of fuels and chemicals plays an important role in reducing carbon dioxide emissions, while at the same time providing the raw materials needed to manufacture the products used on a daily basis.^{2, 3} One way to create a sustainable energy system can be electrochemical conversion processes, in which molecules (e.g. water, carbon dioxide and nitrogen) are converted into higher-value products (e.g. hydrogen, hydrocarbons, oxygenated compounds and ammonia) using renewable energies.^{1, 2}

In the development of fossil-free fuels, molecular hydrogen is a very attractive candidate because of its high mass-specific energy density.⁴ Electricity can thus be converted from renewable energies (e.g. wind, solar and/or water) into storable molecular hydrogen. The stored energy can then be recovered as electrical energy in fuel cells, in which only water is a by-product.⁵

Industrial hydrogen production is based, for instance, on steam reforming or the partial oxidation of hydrocarbons (e.g. methane), in which the unwanted carbon dioxide is generated as a by-product.^{6, 7} A different approach follows the splitting of water by photocatalysis and/or water electrolysis.^{8, 9} Hydrogen can also be obtained as a co-product in chlor-alkali electrolysis.¹⁰

Catalysts play a key role in such electrolysis processes as they increase the rate, efficiency, and selectivity of the chemical conversions involved.¹ In water electrolysis, these factors are limited by a complex reaction mechanism in the oxygen evolution reaction. In recent years, however, considerable progress has been made in the understanding of electrocatalysts, especially in water splitting, i.e., both the oxygen evolution reaction (OER) and the hydrogen evolution reaction (HER). The combination of theoretical and experimental investigations has led to a new understanding of catalytic trends, which provides the opportunity for new approaches to develop more efficient electrocatalysts.

However, the experimental investigation of the developed catalysts also includes the further development of established analytical methods. For example, in-situ and/or operando methods have been developed that allow the catalytic activity to be analyzed under certain measurement parameters and/or directly during the reaction. In most cases, these analytical methods are based on X-rays or synchrotron radiation, which are carried out in an ultra-high vacuum and with specially developed measurement setups. For such investigations, the catalysts are applied to special sample carriers or substrates. The latter can react very sensitively to mechanical and thermal stress, which can lead to problems during catalyst preparation. A further property that the materials under investigation must possess is stability in ultra-high vacuum and insensitivity to high-energy radiation.

Therefore, the interest in the investigation of activity-defining parameters under ambient pressure (vacuum-free) and the use of non-destructive analysis is important and facilitates the elucidation of structure-activity relationships in realistic environments. Furthermore, a vacuum-free and non-destructive analysis offers the possibility to monitor certain parameters, such as gas detection or catalyst degradation, in real-time even under industrially relevant operating conditions.

1.2 Aims and structure of this thesis

The development of a vacuum-free and non-destructive analysis by means of spectroscopic ellipsometry (SE) of electrocatalysts for the OER under operando conditions is a central aim of this thesis. This requires well-studied, established and highly reproducible model catalysts that are used in the electrochemical splitting of water. Mesoporous metal oxide films such as iridium oxide are well suited because of their high internal surface area and the resulting increased intensity of the interfacial reactions compared to bulk materials. Iridium oxide also offers a high activity and stability under acidic conditions during the OER. Since ellipsometry is a model-based method, the development of a suitable model for the investigation of material-relevant properties, i.e. layer thickness, porosity, electrical and electronic parameters as well as the validation of the model are essential aims of this thesis.

Electrochemical (EC) studies under environmental conditions using SE on a platinum surface serve as a test measurement of the developed cell setup to support the understanding of operando studies of IrO_x films. Platinum is considered the best known of all electrode materials and is known for its high reproducibility in electrochemistry. The aim is the modeling of the changes in the measured SE spectra during EC testing and the correlation of the results with the potential dependent processes at the platinum surface.

A major aim of this thesis is to study the mesoporous iridium oxide model type catalyst films under operando conditions and to combine relevant material properties with the activity. The developed and validated SE model from the ex-situ measurements is used to investigate the potential dependent change of the material properties.

Structure of the thesis

To achieve these aims, a methodology has been developed which includes the synthesis of mesoporous iridium oxide films as model type catalysts, a detailed characterization by conventional analytical methods, the analysis by spectroscopic ellipsometry, electrochemical studies in the acidic OER and the validation and correlation of relevant obtained parameters. Furthermore, the methodology includes the operando electrochemical spectroscopic ellipsometry (ECSE) investigations on a platinum surface as well as the ECSE analyses of mesoporous iridium oxide films in the acidic OER. Scheme 1 illustrates the developed methodology.

For this purpose, Chapter 2 summarizes the relevant principles of electrochemical water splitting, characterization methods used, and the state of the art. Chapter 2.1 describes the acidic OER, activity relationships and examples of precious metal oxide catalysts. Chapter 2.2 gives an overview of methods for the characterization of (porous) materials with their strengths and limitations. Finally, Chapter 2.3 describes the principles of ellipsometry as a method for the characterization of (porous) materials and the state of the art.

Chapter 3 illustrates experimental data and gives information about the chemicals used (Chapter 3.1), the synthesis of mesoporous templated catalytic coatings on different substrates (Chapter 3.2), and an overview of the applied physicochemical techniques for the determination of structural properties (Chapter 3.3). In addition, Chapter 3.4 describes the electrocatalytic testing procedures for the quantification of mesoporous coatings and their experimental setups.

Chapter 4 describes the ex-situ characterization of the synthesized mesoporous iridium oxide calcination series (300 °C – 600 °C). Chapter 4.1 gives an overview of the morphology and physicochemical properties of the materials using electron-based and X-ray based methods as well as conductivity measurements and absorption spectroscopy. The investigation by SE, the development of a suitable model and derived results are described in Chapter 4.2. Chapter 4.3 presents the electrochemical investigations in the acidic OER using rotating disc electrodes and the developed flow cell setup. Finally, Chapter 4.4 discusses the validation of the derived results from the ex-situ spectroscopic ellipsometric investigations with results of electron-based and X-ray based methods as well as the correlation with the electrochemical investigations.

For operando ellipsometric investigations, the fundamentals on a platinum surface are described in Chapter 5. First, the ex-situ characterization (Chapter 5.1) of the platinum surface by means of SE serves as the basis for these investigations, and then the changes in properties during cyclic voltammetry are investigated (Chapter 5.2).

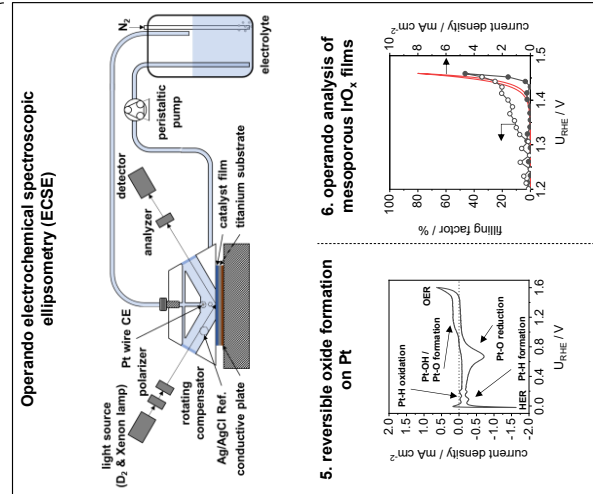
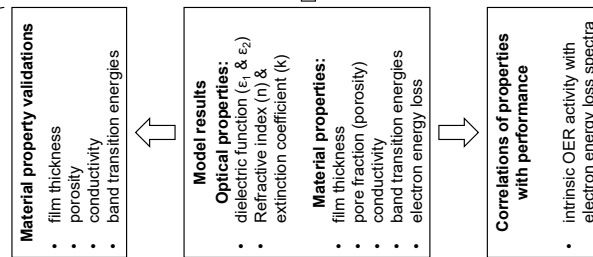
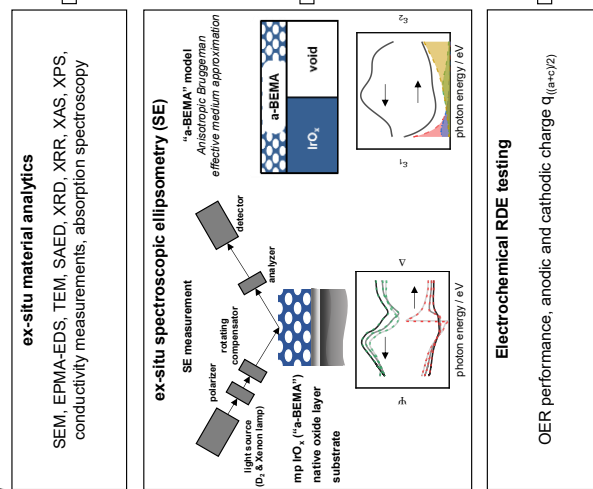
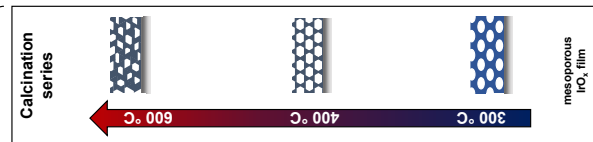
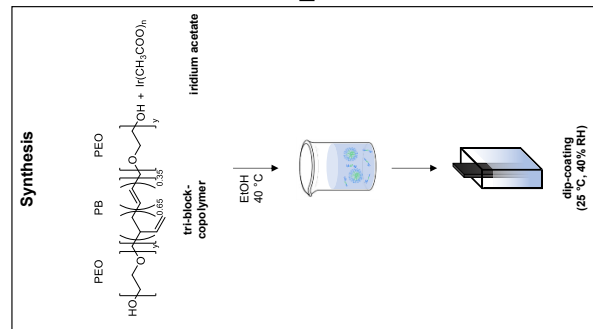
Chapter 6 presents the operando ECSE investigations of the synthesized mesoporous iridium oxide films. The investigation of the ellipsometric behavior is exemplarily presented on a mesoporous iridium oxide film calcined at 375 °C using linear sweep voltammetry in the OER region in Chapter 6.1. Ellipsometric analysis and modeling using cyclic voltammetry under OER conditions of the 375 °C calcined mesoporous iridium oxide film are discussed in Chapter 6.2. Finally, the influence of the calcination temperature on the material properties of the entire calcination series of the mesoporous iridium oxide films under operando OER conditions is presented in Section 6.3. An analysis in the lower potential range (0.40 V_{RHE}– 1.40 V_{RHE}) of the mesoporous iridium oxide films is presented in the Appendix.

In Chapter 7, a general discussion on the identification of structure-activity parameters resulting from the observations of the ex-situ and operando studies is discussed. Finally, Chapter 8 summarizes the results and gives an outlook on further investigation possibilities for the developed system consisting of the combination of the metrological ex-situ and operando measurements.

Chapter 3

Chapter 4

Chapter 5 & 6



Scheme 1: Illustration of the methodology for ex-situ characterization, validation and operando electrochemical investigations of mesoporous iridium oxide films using spectroscopic ellipsometry, and the correlation of derived parameters with electrochemical activities in the acidic oxygen evolution reaction. The first part of this methodology includes the synthesis and calcination of the mesoporous iridium oxide films, which is described in detail in the experimental chapter 3. The analysis of the synthesized films by conventional ex-situ characterization methods, i.e. by scanning electron microscopy (SEM), transmission electron microscopy (TEM), selected area electron diffraction (SAED), electron probe microanalysis using energy dispersive X-ray spectroscopy (EPMA-EDS), X-ray diffraction (XRD), X-ray absorption spectroscopy (XAS), photoelectron spectroscopy (XPS), conductivity measurements and UV-VIS-NIR absorption spectroscopy, is described in chapter 4. Furthermore, Chapter 4 presents the analysis by spectroscopic ellipsometry and the model development for the mesoporous iridium oxide films, as well as electrochemical investigations in the acidic oxygen evolution reaction (OER). Finally, within this chapter the derived parameters from ellipsometric investigations are validated with the conventional methods and correlated with activity trends in the OER. Chapter 5 describes operando investigations on a platinum surface to validate the measurement setup and finally, the operando investigations of the mesoporous iridium oxide films are described in chapter 6.

2. State of the art

2.1 Electrochemical splitting of water

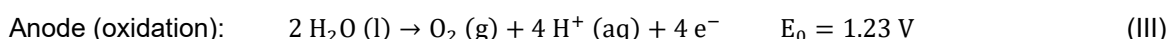
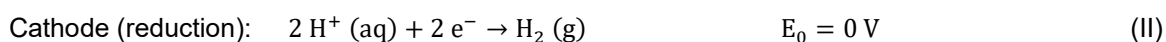
A central aspect of this work is the investigation of electrocatalysts for water splitting. In order to correlate relevant catalyst parameters with activities in electrolysis, a basic understanding of the reactions and mechanisms involved is required. For this reason, this Chapter describes the fundamentals of water splitting with the primary view on the acidic OER, its proposed activity relationships and examples of materials investigated so far.

Oxygen evolution reaction and activity relationships

In general, the splitting of water (equation (I)) is a thermodynamically unfavorable process that does not occur spontaneously. The free enthalpy change (ΔG^0) required to convert one molecule of water into hydrogen and oxygen under standard conditions ($T = 298.15 \text{ K}$, $p = 1.013 \cdot 10^5 \text{ Pa}$) is $237.2 \text{ kJ mol}^{-1}$ (or $474.4 \text{ kJ mol}^{-1}$ in case of 2 molecules of water), which corresponds to a thermodynamic potential of 1.23 V relative to the standard hydrogen electrode (SHE).¹¹



The overall reaction can be further separated into two half-cell reactions, the hydrogen evolution reaction (HER) at the cathode and the oxygen evolution reaction (OER) at the anode. Furthermore, a distinction can be made between acidic and alkaline conditions for the half-cell reactions, although the latter is not discussed any further in this thesis. The half-cell reactions under acidic conditions can be expressed as follows:



In the cathodic half-cell reaction, two protons and two electrons combine to form a molecule of hydrogen at a thermodynamic potential of 0 V. In the anodic half-cell reaction, two water molecules are split into molecular oxygen, four protons and electrons at a standard cell thermodynamic potential of 1.23 V. However, the anodic oxidation comprises several intermediates whose thermodynamic stability and conversion kinetics determine the overall catalytic activity. Additionally, the stability of intermediates on a catalytic surface determines the potential, which also requires voltages of more than 1.23 V.^{12, 13} Besides the thermodynamics of stable intermediates, factors such as the kinetics of chemical and electrochemical steps as well as mechanisms of O-O bond formation and O_2 release determine the efficiency of catalysts.^{13, 14} The OER catalysis process involves various intermediates with proton-coupled electron transfer steps, in which O-O bond formation plays a key role. In the last decades numerous reaction mechanisms have been proposed.¹⁵ According to the current state of knowledge, two qualitatively different mechanisms

have been proposed, the acid-base mechanism and the direct coupling mechanism (or radical coupling mechanism), which are shown in Figure 1.^{13, 14}

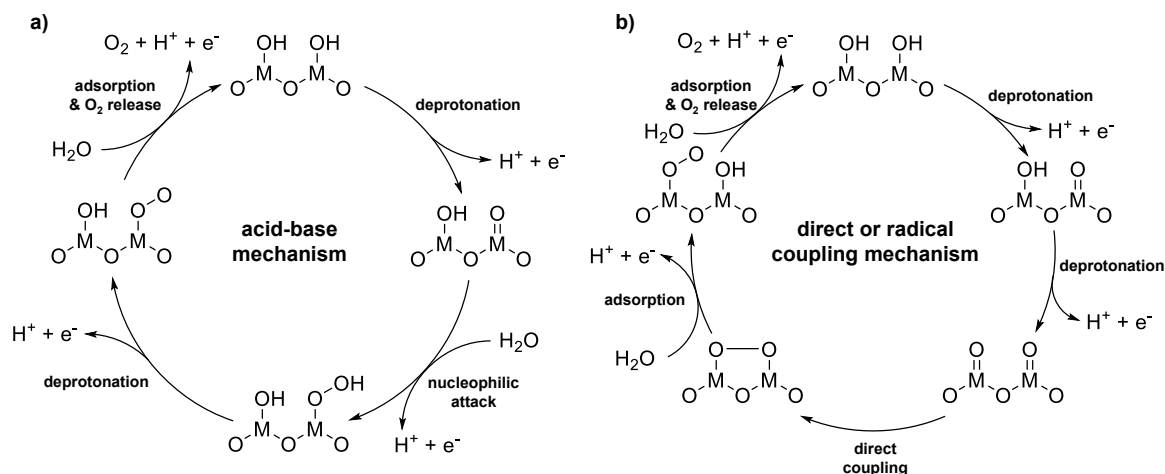


Figure 1: Illustrations of the qualitatively proposed mechanisms for the electrochemical oxygen evolution reaction. a) proposed acid-base mechanism in which a water molecule is adsorbed on an active metal site by the release of a proton and an electron. The second step is the deprotonation of the adsorbed hydroxide species with a release of another proton and electron, followed by a nucleophilic attack of a water molecule. The last step includes the deprotonation of the O-OH species and the release of molecular oxygen. b) proposed direct or radical coupling mechanism, in which an adsorbed water molecule is deprotonated in the first step, similar to the acid-base mechanism. In the next step, further deprotonation occurs, followed by a direct coupling of two adjacent oxygen species. Finally, the formation of the O-O species and the release of molecular oxygen is probably induced by the adsorption of a water molecule.

In the acid-base mechanism (Figure 1a), the first step involves the adsorption of a water molecule with the release of a proton and electron at an active metal center. In a further step, the hydroxide species ($\text{M}-\text{OH}$) is deprotonated, releasing another proton and electron, which now serves as an electrophilic oxygen species. The electrophilicity of this oxide species is determined by the metal oxidation state and the geometry of the metal.¹⁴ The electrophilic oxide species can be attacked by a nucleophilic oxygen species (e.g. water or hydroxide) in a further step, releasing another proton and electron, leading to the formation of an O-OH bond. Finally, the O-OH species is further deprotonated, followed by the release of molecular O_2 .

A proposed alternative mechanistic possibility to form O-O bonds is the coupling of two oxygen radicals (Figure 1b).^{13, 14} The first two steps (adsorption and deprotonation) are similar to the acid-base mechanism. For the coupling of two high valent metal oxo species ($\text{M}=\text{O}$) a further deprotonation occurs first with the release of a proton and an electron, followed by the direct coupling of the oxygen radicals. In the last step, the $\text{M}-\text{O}-\text{O}-\text{M}$ formation takes place, which can probably be initiated by a water molecule, followed by the release of molecular O_2 .¹⁴

In both cases, water molecules are first adsorbed on the catalyst surface, followed by a series of processes such as electron-proton transfer, chemical bond splitting/forming and adsorption/desorption of a surface oxygen intermediate. These processes are largely determined by the ligand field of the metal and its d-electron number.¹⁴ A high d-electron number makes a metal-oxo bond ($\text{M}-\text{O}$) difficult, while a too low d-electron number tends to form a strong metal-oxo bond, making the activation more difficult.¹⁴ Density functional theory (DFT) calculations show that

the adsorption of the metal-oxo intermediate species on a ruthenium oxide (RuO_2) surface is too strong, which hinders the formation of a metal-oxo-oxyl (M-OO) or metal-hydroperoxo species (M-OOH).¹² Therefore, it can be concluded that the OER activity is strongly dependent on the adsorption strength of different oxygen intermediate species at the active sites of the metal catalysts used.

From these findings a universal scaling relationship between the binding energies of metal oxide species (M-O, M-OH, M-OOH) for transition metal oxides has been derived and thus a descriptor describing the OER overpotential and the catalyst nature.^{12, 16-18} This behavior results in a volcano-like relationship, which describes that when oxygen is bound too strongly to the surface, the activity is limited by the formation of the M-OOH species. If oxygen is bound too weakly, the activity is limited by M-OH species. This volcano trend, which follows the Sabatier principle, generally serves as a guide for the development of highly active catalysts.¹⁹ It has been reported that coordinatively unsaturated (CUS) metal sites play a significant role in OER activity in octahedral structures such as rutile or perovskite.^{20, 21} This was confirmed by Rossmeisl *et al.* with simulations on an oxygen terminated RuO_2 (110) surface.¹² These CUS metal sites can be induced for instance by oxygen defect sites of the material or the break of M-O bonds when applying an anodic potential.²² From these observations, it is clear that a major aspect of the OER catalysts are the transition metal sites, which are considered to be active sites, although some controversy still remains. In the further part of this Chapter, relevant relationships between catalyst properties and OER activity, which have been described in recent years, will be described.

Catalyst crystallinity

Many studies report that crystallinity has a significant influence on the activity. For example, amorphous metal oxides show significantly higher OER activities than their well-crystalline counterparts.²³⁻²⁵ In a first approximation, it is assumed that the differences are due to the different number of catalytically active sites.²³ Investigations of the crystallinity of iridium oxide (IrO_2) catalysts by Bernicke *et al.* showed a relatively constant intrinsic OER activity (surface charged normalized activity) for low crystalline catalysts, while more crystalline catalysts exhibited a reduction in OER activity.²⁶ However, a closer look suggests that the reaction barrier of amorphous metal oxides is lowered by electrophilic $\text{O}^{\cdot-}$ species.²⁴ Pfeifer *et al.* demonstrated with X-ray photoelectron (XPS) and absorption spectroscopy (XAS) studies on amorphous iridium oxide (IrO_x) catalysts that electrophilic $\text{O}^{\cdot-}$ species are active in catalyzing the OER and that enhanced OER performance of iridium hydroperoxo (Ir-OOH) can be achieved by the accommodation of larger amounts of reactive oxygen species.²⁴ Furthermore, XAS observations by Gao *et al.* have shown that the Ir-O bond length in low crystalline materials is significantly reduced due to a more flexible structure compared to high crystalline materials, which increases the electrophilic character.²⁷

Covalent M-O bond

Another factor which determines the OER activity is the covalency of the M-O bond, i.e. the strength of the M-O bond, which is determined by the overlap of the metal d-band and the oxygen 2p band.²⁸⁻³⁰ It has been shown that the covalent nature of M-O bonds in metal oxides has a significant influence on catalytic activity and stability.^{28, 31-33} An increase in covalency thus leads to an increased electron density at the metal ion, which weakens the binding energy between the metal ion and the intermediate oxygen species.^{34, 35} In addition, the metal-oxygen bond is shortened by increasing the covalency, which promotes the formation of electrophilic oxygen intermediates and enables a better nucleophilic attack of water molecules.²⁷ Another effect described by Kuznetsov *et al.* is the nearing of the Fermi level (E_F) to the O 2p level induced by the increase in M-O binding covalency.³⁶ This can promote the activation of a redox active center of the O 2p orbital, which also has a positive effect on the OER activity.^{37, 38}

Defect structures and vacancies

Lattice defects and vacancies, which are closely related to the crystallinity, show a significant influence on the catalytic performance in the OER. Among these defect structures are mainly oxygen vacancies and cation defects. For instance, the valence state of the metal ion can be changed by introducing oxygen vacancies, which in turn affects the covalency of the M-O bond.^{39, 40} Cation defects, on the other hand, increase the content of the oxide species to ensure charge balance.⁴¹ The increased oxide content can thus promote the nucleophilic attack of water and the formation of M-OOH species.⁴¹ Furthermore, these cation defects cause unsaturated oxygen coordination, which leads to protonation of surface oxide species and thus weakens M-O bonds.⁴¹ Strasser and co-workers studied iridium nickel oxide nanoparticles and showed that nickel leaching leads to cation defects and thus increases the hole character of iridium ions adjacent to vacancies.³³ As a consequence, Ir-O bond lengths decrease and the degree of covalency increases, which may lead to increased OER activity.

Electronic structure and position of the metal d-band

In addition to the previously described parameters, a proposed occupancy or the electronic structure and the position of the metal d-band can also influence the catalytic activity.^{42, 43} Shao-Horn and co-workers showed that the transition energy between the metal d-band and the O 2p band is closely related to the OER activity, i.e. the binding strength of the metal oxo species (M-O) increases with decreasing transition energy.⁴⁴ As a consequence of the increased binding strength, the activation of the M-O bond is inhibited and thus the nucleophilic attack of a water molecule. Additionally, the position of the metal d-band affects the OER activity. A shift of the metal d-band to higher energies leads to an increased adsorption of oxide species, while a shift to lower energies weakens the adsorption.^{45, 46} Two main factors for the shift of the metal d-band are proposed. One is the metal oxidation state, where an increasing oxidation state leads to a decrease of the d-band filling. This results in a shift of the d-band to higher energies, which strengthens the metal-oxygen bond. In the opposite case, the d-band filling increases with decreasing oxidation state and the M-O bond energy is weakened.⁴²⁻⁴⁴ Nørskov and co-workers propose lattice stress as another factor for the d-band shift, where tensile stress is associated with the shift of the d-band to higher energies.⁴³ In the case of compressive strain, the d-band is shifted to lower energies.⁴³

Catalyst materials

Based on the catalyst properties listed above and the correlations with the identified and proposed OER activities, a variety of novel catalysts with high activity and stability have been developed in recent years. Due to their high activity under acidic conditions, iridium and ruthenium play a major role in the further development of their practical applicability for the OER. Thus, novel materials have been proposed by doping with heteroatoms, alloys or different structures (e.g., perovskites, pyrochlore or amorphous catalysts).^{25, 47-52}

In the case of perovskite materials, for instance, the ABO_3 structure can be used to adjust the number of atoms at the A and B sites in order to regulate the lattice oxygen content and the electronic structure, thus enabling the construction of oxygen defects that have a significant influence on the catalytic activity in the OER.⁴⁴ In general, the A sites are alkaline earth metals (Ca, Sr or Ba) or rare earth metals (e.g. La or Pr) and the B sites are transition metal ions which form a coordinate structure with the oxygen ions.⁵³ Jaramillo and co-workers demonstrated that SrIrO_3 films on SrTiO_3 substrate exhibit high activity and stability in the acidic OER, which is due to the Sr dissolution and the in-situ formation of IrO_x on the surface.⁵⁴ Similar to the cation defects described above, Sr leaching leads to a decrease in Ir-O bond lengths due to an increased hole character of iridium ions, resulting in higher activity during OER.³³

Even pyrochlore compounds with an ideal chemical $A_2B_2O_7$ formula show versatile and flexible structure, which allows to control their properties. The A sites can consist of Pb, Bi, Tl or a rare earth metal and the B sites of a noble metal such as Ir or Ru.⁵⁵ T. J. Schmidt and co-workers demonstrated that pyrochlore compounds with the composition $Y_2Ir_2O_7$ exhibit a similar activity to IrO_2 nanoparticles.⁵⁶ The leaching of Y^{3+} ions under acidic conditions leads to an increase in activity, which is correlated with a highly active IrO_x surface layer.⁵⁶

In addition to the above-mentioned materials, single atom catalytically active materials (e.g., Ir, Ru) are still of great interest. According to current knowledge, not all interrelationships of OER catalysis are understood in detail yet. Therefore, single atom catalysts offer the advantage of facilitated elucidation of thermodynamic and kinetic processes, as well as stability studies that can lead to a better understanding of the acidic OER. Mayrhofer and co-workers demonstrated the dissolution behavior of iridium and iridium oxide films under acidic conditions and thus insights into the stability of the catalysts.⁵⁷⁻⁵⁹ For instance, amorphous iridium oxides show a high activity, which is however associated with a high iridium dissolution.⁶⁰ It is assumed that both the activity and the dissolution rate are caused by the presence of activated lattice oxygen atoms due to the resulting oxygen vacancies.⁶⁰

Since OER is an interface reaction between catalyst and electrolyte, materials with a high active surface area are suitable for understanding the thermodynamic and kinetic processes due to an increased intensity of the interface reactions. Many approaches to increase the surface area were reported in the literature, such as the synthesis of nanoparticles.^{47, 61}

Another approach besides the preparation of nanoparticles follows the synthesis of porous materials to increase the surface area. According to the IUPAC three classes can be defined by the pore size, microporous (< 2 nm), mesoporous (2 – 50 nm) and macroporous (> 50 nm) materials.⁶² For the synthesis of such porous materials, principally two different template approaches can be used.⁶³ For hard-templating, compounds with holes are used, which are infiltrated with the material precursor. The template framework can then be removed, e.g., by etching. In contrast, soft-templating involves a structure-directing template being surrounded by the material precursor, whereas the template can be removed, e.g., by thermal treatment. In the latter, amphiphilic molecules (e.g., block copolymers) are typically used as structuring templates, that form micelles within the material precursor solution.

Porous metal oxides can thus be synthesized by soft-templating according to the evaporation-induced self-assembly (EISA) concept. An amphiphilic block copolymer forms micelle together with the metal oxide precursor in a highly volatile solvent. The evaporation of the solvent leads to self-assembly of the micelles surrounded by the metal oxide precursor. Subsequent thermal treatment removes the structure directing template and the precursor is converted into a metal oxide with an accessible pore system with a large surface area.

Based on this synthesis method, the use of mesoporous iridium oxide films as an efficient anode material for electrocatalytic water electrolysis has been reported in the past. Ortel *et al.* presented a synthesis approach for a locally ordered mesoporous IrO₂ structure using iridium acetate (Ir(CH₃COO)_n) as metal oxide precursor and a triblock copolymer (PEO₂₁₃PB₁₈₄PEO₂₁₃) as pore template with subsequent thermal treatment in air.⁶⁴ The films reveal a pore diameter of about 16 nm and possess a high surface area.⁶⁴ In a further work, Bernicke *et al.* demonstrated a high OER activity as well as chemical and mechanical stability under acidic conditions for such synthesized IrO₂ films.²⁶ In addition, a porous structure allows the formation of an effective electron conduction path through the entire catalyst layer and ensures an efficient transfer of gas and electrolyte.^{26, 65, 66}

In a similar approach, Chandra *et al.* used an [Ir(OH)₆]²⁻ precursor derived from alkaline hydrolysis of K₂IrCl₆ and a triblock copolymer (Pluronic F127, EO₁₀₆PO₇₀EO₁₀₆) to synthesize an ordered open mesoporous IrO₂ layer.⁶⁷ Physicochemical analyses exhibit a pore diameter of about 7 nm, a high surface area and up to 2 times higher O₂ evolution during the OER compared to a non-templated IrO₂ film.⁶⁷

In general, according to current knowledge, there is still a need to further investigate the OER due to the high overpotential required and the reaction mechanism which is not yet fully understood. Therefore, the development and synthesis of such mono metal oxide films with high surface area and a high number of active sites can improve the understanding of the catalytic process under acidic conditions. A scalable model system with adjustable pore size, controlled layer thickness and high accessibility can be used to study both structure-activity relationships and transport phenomena.²⁶

2.2 Characterization methods of thin (porous) films

An analytical characterization of the materials is essential to correlate the activity relationships mentioned in the previous Chapter with the structure of the materials used. As previously described, porous monometallic materials, such as mesoporous iridium oxide films, offer an increased intensity of interface reactions due to their high internal surface area. Thus, structure-activity relationships and transport phenomena can be studied more easily due to a better surface sensitivity. In general, electron-based methods, such as scanning electron microscopy (SEM) and transmission electron microscopy (TEM), or X-ray based methods, such as X-ray diffraction (XRD), X-ray photoelectron spectroscopy (XPS), X-ray reflectometry (XRR), and X-ray absorption spectroscopy (XAS) are used to characterize materials, including porous thin films. Optical methods like reflection spectroscopy, absorption spectroscopy and ellipsometry are also increasingly used to analyze such materials. This Chapter gives an overview of the strengths and limitations of electron-based, X-ray based and optical methods for the characterization of mesoporous materials, which are relevant for this thesis. A detailed description of the individual methods can be found in the literature references, which are given in 68, 69, 70, 71, 72, 73, 74, 75 and 76.

Electron-based characterization methods

Electron microscopy is suitable for the investigation and analysis of the surface and subsurface of nanostructured systems and provides insights into the morphology of the samples. By using electrons, higher resolutions can be achieved compared to light microscopy. Electrons are typically generated in a cathode (e.g., field emission cathode or lanthanum hexaboride (LaB_6) filament) and focused into a beam via a Wehnelt-cylinder. Excitation voltages of 1 - 30 kV (SEM) or 100 - 200 kV (TEM) are used. This primary electron beam interact with the specimen and different signals are obtained depending on the structure (SEM or TEM). An overview is shown in Figure 2.

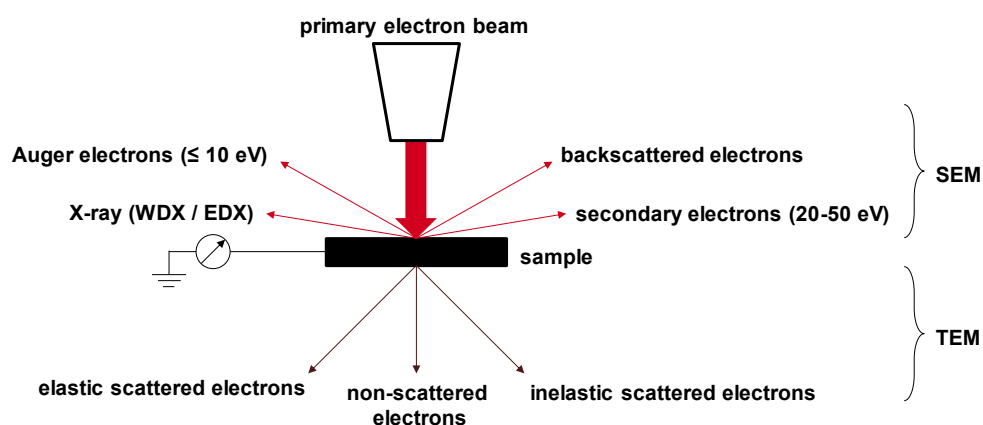


Figure 2: Illustration of the principle of electron-based characterization methods and the interaction of a primary electron beam with a sample surface as well as the different resulting signals.

Secondary electrons are electrons emitted by the sample with kinetic energies between 20 - 50 eV. The amount of secondary electrons is dependent on the excitation voltage, but they are abundant, and therefore used for topological imaging. The backscattered electrons are primary electrons emitted from the sample by atomic nucleus interactions with little change of their kinetic energy. They can also be used for imaging, where the mean atomic number of atoms can be used to image a material contrast. In addition, so-called Auger electrons can be generated, which can be used for elemental analysis. However, these are not relevant in the context of this thesis and will therefore not be discussed further. Figure 3a shows an example of a top-view SEM image of a mesoporous titanium dioxide film on a silicon substrate recorded with secondary electrons. The bright areas indicate the titanium dioxide wall material, while darker areas represent the mesopores. A detailed analysis of this kind of material with SEM is reported by Ortel *et al.* in ref. 77.

In the case of sufficiently thin samples (a few hundred nanometers) the imaging of the internal microstructure can be performed in a TEM. Due to the higher excitation voltage compared to the SEM, higher imaging resolutions can be achieved and thus structures down to lattice planes can be resolved in crystalline samples. Typically, samples can be recorded in brightfield and darkfield mode. In the brightfield mode, the intensity distribution of the non-scattered primary beam is displayed, where darker contrast means higher absorption of the primary beam and vice versa. In dark field mode, the intensity distribution of the diffracted beam by elastic scattered electrons is used for imaging. This allows a material contrast similar to the backscattered electrons in the SEM, i.e. elements that scatter the electron beam more strongly have a brighter contrast and vice versa. Figure 3b shows a film fragment of a titanium dioxide layer, which was recorded in a TEM in bright field mode. In this case, the areas of darker contrast show the titanium dioxide wall material and brighter contrast areas can be assigned to thinner sample fragments, due to the pore structure. A detailed analysis with TEM of such materials can also be found in ref. 77.

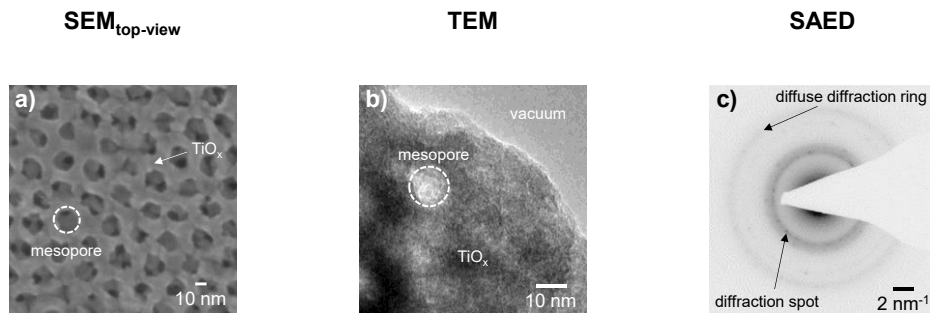


Figure 3: Electron-based characterization of porous samples. a) SEM top-view image of a mesoporous titanium oxide film on a silicon substrate. b) TEM image in bright field mode of a film fragment of a mesoporous titanium oxide film. c) SAED of a mesoporous carbon film with integrated nanoparticles.

The elastically scattered electrons at the individual atoms of the material can be used in the TEM setup to generate constructive interference (so-called diffraction patterns). These diffraction patterns depend on the nature of the materials. For example, amorphous materials have diffuse diffraction rings, which are due to the average interatomic distances between the atoms. In crystalline materials, the atoms are periodically arranged at regular intervals, resulting in a periodic distribution of elastically scattered electrons at precisely defined angles (given by Bragg's law).

Selected area electron diffraction (SAED) is shown as an example in Figure 3c on a mesoporous carbon film with integrated precious metal nanoparticles. Due to the amorphous structure of the carbon, diffuse rings are formed, while the precious metal nanoparticles show a mixture of diffuse rings and diffraction spots indicating polycrystalline particles.

Electron analysis can also be used to excite atoms in a sample by ejecting an electron close to the nucleus. When the inner shell hole is filled by an electron of higher energy (i.e., an electron from the outer shells), X-ray photons are emitted due to the energy difference. Due to the well-defined nature of the different atomic energy levels, these photons are characteristic of the respective atomic species. On this basis, energy dispersive or wavelength dispersive X-ray spectroscopy (EDS or WDS) can be used to provide information on the chemical composition and distribution of the elements. This X-ray analysis is used in the so-called electron beam microanalysis (EPMA) to quantify the chemical composition and to determine the mass distribution. In addition, this method can also be used to determine the density of a sample and thus to determine its porosity.⁷⁸ A general scheme for determining the porosity of a sample using EPMA is given in Figure 4.

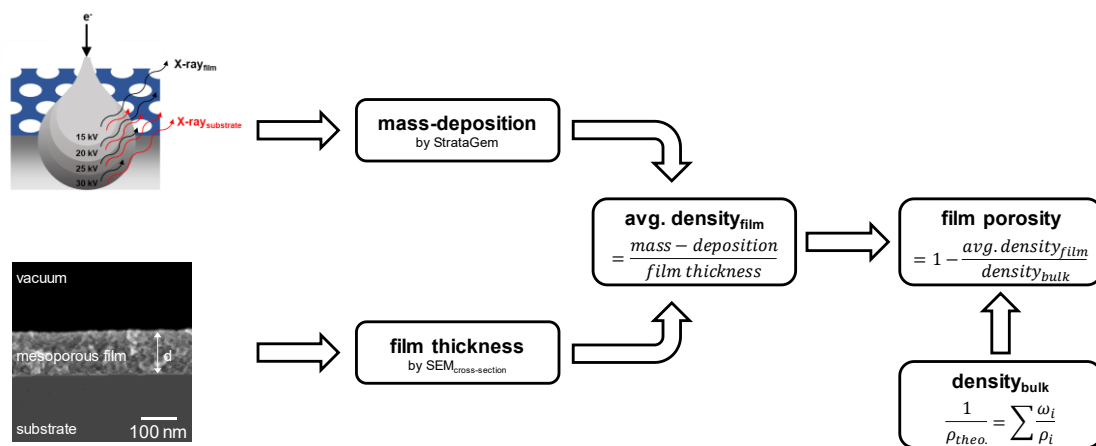


Figure 4: Illustration of the EPMA approach to determine film porosity using energy dispersive X-ray spectroscopy (EDS) in a scanning electron microscope (SEM). This approach involves the measurement of the X-ray intensities of the elements of interest with different acceleration voltages to determine the mass-deposition and the calculation of the average density using the layer thickness obtained from cross-sectional SEM imaging. The film porosity can then be calculated by dividing the average film thickness by the density of the bulk material.⁷⁸

In this method, the film mass-deposition is determined by EPMA (EDS or WDS) using several excitation voltages and the film thickness by cross-sectional imaging in the SEM. With the layer thickness and the mass-deposition the average density of the sample can be calculated. The film porosity can then be calculated using the density of a non-porous layer of the same material or a reference material and the average density determined. Using EPMA using EDS and the methodology described above, the porosity of mesoporous titanium oxide films could be determined accurately and shows good agreement with other techniques.⁷⁸ An advantage of this method over the normally used gas sorption measurements (e.g. BET physisorption), which are typically applied to powder materials, is the small amount of sample required and the possibility of determining the porosity of thin films.

Finally, electron energy loss spectroscopy (EELS) for the analysis of electronic structures will be described. This is typically performed in a TEM setup and includes the analysis of inelastically scattered electrons. A typically EELS spectrum is given in Figure 5.

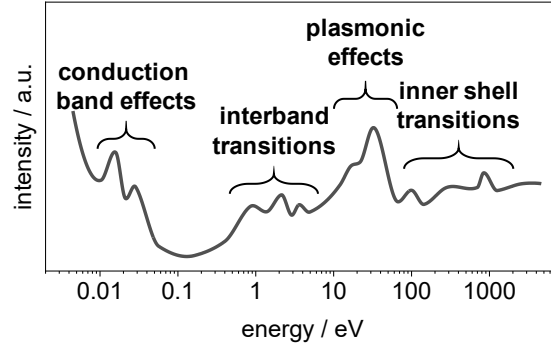


Figure 5: Electron energy loss spectra with indication of the obtained information from the different energy regions.

The spectra can generally be divided into two ranges, the low-loss and the high-loss range. The latter ranges from 50 eV to several 1000 eV and corresponds to the excitation of electrons from the inner orbitals of the atom. The analysis in the high-loss region is comparable to X-ray absorption analysis (XAS), which is described in more detail in the X-ray based methods section. The low-loss range extends from few eV to 50 eV and corresponds to the excitation of electrons in the valence band. This range provides information about interband transitions, dielectric properties and plasmon excitations. The very low-loss region (< 1 eV) provides information about conduction band effects. The access to dielectric properties can be related to the energy loss function (ELF) with the single scattering distribution as follows:

$$S(E_{EELS}) = \frac{I_{EELS}d}{\pi a_0 m_0 v_e^2} \text{Im}(-\varepsilon(q_t, E_{EELS})^{-1}) \ln \left(1 + \left(\frac{\beta_{EELS}}{\theta_E} \right)^2 \right) \quad (1)$$

where I_{EELS} is the zero-loss intensity, d the specimen thickness, a_0 the Bohr radius, m_0 the electron rest mass, v_e the electron beam velocity, β_{EELS} the collection semi-angle, θ_E the characteristic scattering angle and $\varepsilon(q_t, E_{EELS})$ the complex dielectric function at energy-loss E_{EELS} and momentum transfer q_t .^{76, 79-81} According to equation (1), the EEL spectra contain the complete characteristic of the complex dielectric function ε and the real (ε_1) and imaginary (ε_2) part of the dielectric function can be determined by Kramers-Kronig transformation for the bulk (equation (2)) and surface (equation (3)) energy loss function.⁸²

bulk energy loss function:
$$-\text{Im}(\varepsilon^{-1}) = \frac{\varepsilon_2(E)}{\varepsilon_1(E)^2 + \varepsilon_2(E)^2} \quad (2)$$

surface energy loss function:
$$-\text{Im}((1 + \varepsilon)^{-1}) = \frac{\varepsilon_2(E)}{(1 + \varepsilon_1(E))^2 + \varepsilon_2(E)^2} \quad (3)$$

Thus, EELS is not only suitable for identifying and determining the chemistry nature of the sample, but also offers the possibility to derive optical properties of the material.

In general, electron-based analyses provide access to the morphological evaluation of porous samples regarding an ordered and accessible pore structure. Furthermore, a characterization of the samples by electron-based methods allows the quantification of chemical composition and mass-loading, as well as the possibility to identify the porous volume of thin films. However, these methods are not always non-destructive analyses, which additionally require a high vacuum.

X-ray based analysis methods

In addition to the electron-based methods described above, X-ray based methods are often used for the analysis of (porous) film materials, providing elucidation of the structure of the materials. As mentioned in Chapter 2.1, the crystallinity of the catalysts plays an important role in electrochemical catalysis. The determination of crystalline phase compositions can typically be performed by X-ray diffraction analysis (XRD). Monochromatic X-rays are diffracted and detected over an angular range (typically 10-80°) onto a sample, e.g., in the Bragg-Brentano arrangement. The X-rays are diffracted by the structure of the sample, e.g., by ordered structures such as crystals. Bragg's equation can be used to calculate the lattice parameters of the investigated structure:

$$m_d \lambda = 2 d_{lattice} \sin \theta \quad (4)$$

where m_d is the diffraction order, λ is the wavelength of the X-rays, $d_{lattice}$ is the distance between the lattice planes and θ is the angle between the X-rays and the lattice plane.

The diffraction patterns obtained represent the so-called fingerprint of the crystal structure and phase compositions can be identified by comparison with a database such as the powder diffractometer file (PDF). The diffraction patterns are dependent on the crystallite grain size, i.e., small crystallites produce a broadening of the reflection due to their limited amount of diffraction planes, while large crystallites produce a sharp narrow reflection due to the higher amount of diffraction planes. Figure 6a displays a diffractogram of a highly crystalline sample with sharp reflections. The crystallite size can be estimated using the Scherrer equation:

$$d_{crystalite} = \frac{K_{XRD} \lambda}{\Delta(2\theta) \cos \theta_{Bragg}} \quad (5)$$

where $d_{crystalite}$ is the mean size of the crystallite, K_{XRD} is a dimensionless shape factor (typically 0.9), λ is the wavelength of the X-ray source used (e.g., Cu K $_{\alpha}$ = 0.15406 nm), $\Delta(2\theta)$ is the full width at half maximum intensity (FWHM) and θ_{Bragg} is the Bragg angle of the reflection.

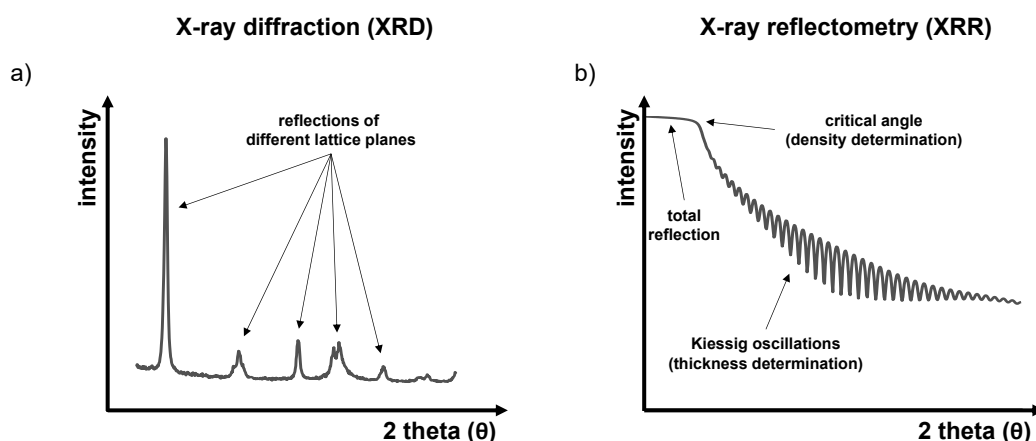


Figure 6: Illustration of a) an X-ray diffractogram of a crystalline sample and b) an X-ray reflectometry measurement of a film sample with indicating total reflection, the critical angle and Kiessig oscillations.

Using X-rays in a range of grazing incidence angles (typically $0.1 - 6^\circ$) to the sample surface, the specular reflectance of a layered sample can be measured. In this so-called X-ray reflectometry (XRR) method, X-rays are reflected from interfaces at different depths and interfere constructively or destructively depending on the relative optical path. This leads to minima and maxima in the specular reflectivity (Kiessig oscillation). At very small angles ($2\theta < 0.5^\circ$), the X-rays interact only with the surface atomic layers of the material and total reflection occurs. Above the total reflection, i.e., at higher angles of incidence, the critical angle results in a range of $0.2 - 0.6^\circ$ (depending on the material), which can be used to determine the material density. An XRR measurement of a thin layer is displayed in Figure 6b. For simple samples, the thickness can be calculated directly from the frequency of the reflectivity oscillations, but for the determination of the density and for more complex samples, the measured reflectivity curve has to be adapted to a physical model.⁸³ The literature successfully demonstrates the determination of film thickness and density by XRR of mesoporous oxide films, which are in good agreement with comparative methods.^{84, 85}

Photoelectron spectroscopy (XPS) is used to study the chemical composition of materials. It detects the kinetic energy distribution of emitted photoelectrons resulting from the interaction of monochromatic, low-energy X-rays with electrons from the inner atomic orbitals on the sample surface. With known X-ray energy, the measured kinetic energy of a photoelectron peak of the inner shell can be directly related to its characteristic binding energy, which is specific for the respective atom and orbital. Thus, differences in the oxidation state due to the resulting chemical shifts can be detected. A typical XPS survey spectrum is shown in Figure 7a, with indicated characteristic binding energies for the carbon 1s and oxygen 1s orbital. XPS studies on iridium-based catalysts showed nicely the identification of different oxidation states, allowing trends in OER activity to be deduced.⁸⁶

A drawback of this method, however, is the low penetration depth, which is approximately few nanometers (< 3 nm), and depth information is only obtained by depth profiling techniques such as sputtering, which in turn involves destruction of the sample. On the other hand, the sensitivity of this surface analysis allows the structural trends found to be transferred to other systems with larger surface areas.⁸⁶

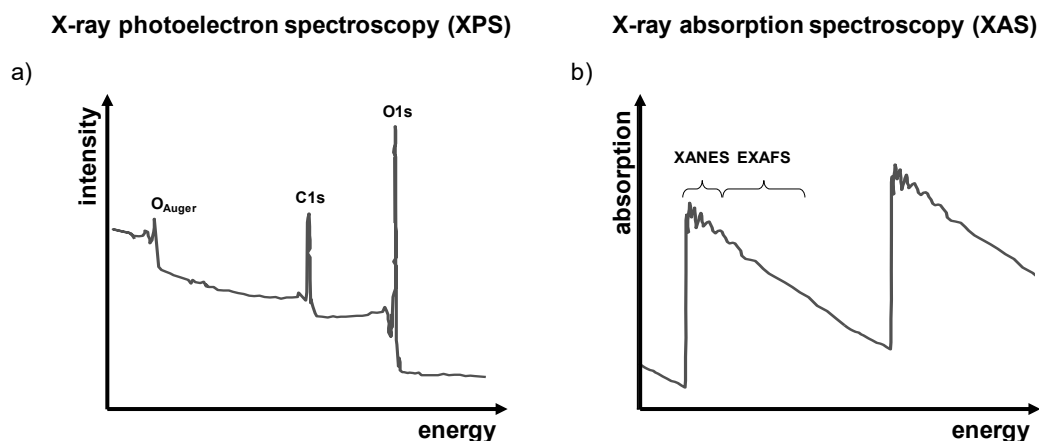


Figure 7: Illustration of a) X-ray photoelectron spectroscopic and b) X-ray absorption spectroscopic spectra.

When using high-energy X-rays, e.g., from a synchrotron, atoms are ionized and electron transitions from deep inner shell atomic levels occur. In this so-called X-ray absorption spectroscopy (XAS), X-ray ionization edges occur at energies that are characteristic for the element under investigation. Two types can be distinguished: (i) the X-ray absorption near-edge structure (XANES), where there is a direct correlation with different binding conditions of the atoms in the sample and (ii) the extended X-ray absorption near-edge structure (EXAFS), where binding lengths and coordination states can be determined (Figure 7b). XAS studies on an IrO₂ films reveal, for instance, that the average Ir oxidation state increases with increasing applied potential, which decreases again with the onset of the OER.⁸⁷ Furthermore, XAS observations show that the Ir-O bond length in amorphous materials is significantly reduced by a more flexible structure compared to crystalline materials.²⁷

The described X-ray methods, except for XRD and XRR, require a high vacuum on the one hand and partly high-energy X-rays, e.g., from a synchrotron, on the other hand, which makes investigations much more complex, especially in-situ and/or operando techniques. Besides the mentioned X-ray based characterization methods, there are further methods for the investigation of materials, especially of porous thin films, such as small angle X-ray scattering (SAXS), e.g. to investigate the pore geometry. However, these are not part of the characterization methods used in this thesis and are therefore not described further.

Optical characterization methods

In terms of optical characterization, the two simplest methods are those of measuring reflectivity and transmission or absorption as a function of wavelength. In the latter, absorption spectroscopy, for instance, the reduction of the intensity of a monochromatic light beam travelling through a sample is measured. This absorption is given for a certain wavelength by Lambert-Beer's law as follows:

$$I = I_0 e^{-\alpha d} \quad (6)$$

with

$$\alpha = \frac{4 \pi k}{\lambda} \quad (7)$$

where I is the intensity of the transmitted light, I_0 is the intensity of the incident light, α the absorption coefficient, d the film thickness, k the extinction coefficient and λ the wavelength.

The absorption coefficient can additionally be used in the Tauc relation to obtain information about the optical bandgap or intraband transitions of the materials. This relation is given by the following equation:

$$\alpha = \frac{\alpha_e (h\nu - E_g)^{1/m}}{h\nu} \quad (8)$$

with α_e as a constant proportional to the probability of an electron transition between occupied and empty states, $h\nu$ the photon energy and E_g the bandgap or transition energy.⁸⁸⁻⁹¹ The nature of the transition can be expressed with the constant m , with $m = 1/2$ or $3/2$ for direct allowed or direct forbidden transitions and $m = 2$ or 3 for indirect allowed or indirect forbidden transitions.⁸⁸⁻⁹¹ Absorption spectroscopic studies on iridium oxide films could thus determine the transitions within the Ir 5d band between the partially filled t_{2g} and empty e_g sub-level.^{92, 93} However, this analysis requires that the samples can be deposited on a transparent substrate, when using thin films as sample and must themselves be partially transparent to avoid complete absorption of the light beam. This can be adjusted by the layer thickness, as can be seen from Lambert-Beer's law.

Optical methods can also be used to study the response of the electrons in the material to the electric and magnetic field of the incident beam. This response is described by the dielectric function of the material and can be derived by determining the refractive index n and extinction coefficient k by means of reflection or transmission measurements. Thus, resonant plasmon oscillations and interband transitions can be identified. If linearly polarized light is used, reflection at the sample surface generally results in a change of the polarization state and elliptically polarized light is obtained. This measuring method is the so-called ellipsometry, which is described in more detail in the next Chapter.

2.3 Spectroscopic ellipsometry and modeling approaches

Ellipsometry is an optical technique that measures the change in polarization state of light as an electromagnetic wave reflected from or transmitted through a surface. For a better understanding, the interaction of electromagnetic waves with matter and the fundamentals of polarized light are first considered, followed by the principles of ellipsometry. Then, the relationship between the dielectric function and light is described. Furthermore, the analysis of multilayer systems, mathematical modeling, and ellipsometric characterization of absorbing layers are described. Finally, general applications of ellipsometry are shown.

Interaction of light with matter and polarization

Light can be considered as a three-dimensional transverse electromagnetic wave, where the electric field vector \vec{E} and the magnetic field vector \vec{H} oscillate perpendicular to the direction of propagation.⁹⁴⁻⁹⁷ The mathematical description of electromagnetic fields is given by Maxwell's equations. The interaction of electromagnetic radiation with matter between the electric and magnetic field strengths and the properties of matter (ϵ_r , μ_r , σ) is described by the relations (9), (10), and (11).

$$\vec{D} = \epsilon_0 \epsilon_r \vec{E} \quad (9)$$

$$\vec{B} = \mu_0 \mu_r \vec{H} \quad (10)$$

$$\vec{j} = \sigma \vec{E} \quad (11)$$

where \vec{E} and \vec{D} are the electric field strength and dielectric displacement vectors. \vec{H} and \vec{B} are the corresponding magnetic vectors and \vec{j} is the density of the electric current. ϵ_0 is the dielectric constant in vacuum, ϵ_r the relative dielectric constant, μ_0 the magnetic permeability in vacuum, μ_r the relative magnetic permeability and σ the electrical conductivity.⁹⁵⁻⁹⁹

The time response of a monochromatic plane wave propagating within an isotropic medium in z-direction can be described by the electric field \vec{E} and/or the magnetic field \vec{B} . For all other materials than ferromagnetic materials, i.e., elements that generate a permanent magnetic field themselves or are strongly attracted by one pole of an external magnetic field (such as iron, nickel, and cobalt), the relative magnetic permeability is $\mu_r = 1$. Therefore, at interfaces, the consideration of the electric field \vec{E} is sufficient to describe an electromagnetic plane wave.

From this context, \vec{E} can be defined for the two spatial directions x and y in the complex notation and the wave equation is obtained as the solution of Maxwell's equations of a plane, monochromatic light wave propagating in the z -direction:

$$\vec{E}_j(z, t) = \vec{E}_{0j} e^{\omega t - \vec{k} z} e^{i \delta_j} \quad \text{with } j = x, y \quad (12)$$

with $\omega = 2 \pi \nu$ as angular frequency with ν as frequency, t as time, $\vec{k} = \frac{2 \pi}{\lambda}$ as wave vector with λ as wavelength and δ as phase shift.^{95, 96}

Ellipsometry, as mentioned before, is a technique that measures the change in the polarization state of an electromagnetic plane wave. Therefore, in ellipsometric measurements, only the amplitude ratio ($\vec{E}_{0x}, \vec{E}_{0y}$) and the phase shift (δ_x, δ_y) are relevant and the polarization state of light can be defined via the Jones vector:^{95, 96}

$$\vec{E} = \begin{pmatrix} \vec{E}_{0x} e^{i \delta_x} \\ \vec{E}_{0y} e^{i \delta_y} \end{pmatrix} \quad (13)$$

Based on the polarization of the electromagnetic plane wave in the two spatial directions, three cases can be distinguished:^{95, 96}

- **Linear polarized light:** In the case of linearly polarized light, the oscillation of the \vec{E} field propagates in exactly one single plane, i.e., \vec{E} has the same direction x at every location in z -direction (Figure 8a).
- **Circular polarized light:** In circularly polarized light, the \vec{E} vector rotates around the wave vector with constant angular velocity and with constant magnitude, i.e. interference of two perpendicularly linearly polarized waves with the same frequency and amplitude ($\vec{E}_{0x} = \vec{E}_{0y}$) having a phase shift of $\pm \pi/2$ (Figure 8b).
- **Elliptical polarized light:** For elliptically polarized light, the amplitudes of the two interfering linearly polarized waves are either different ($\vec{E}_{0x} \neq \vec{E}_{0y}$) or equal ($\vec{E}_{0x} = \vec{E}_{0y}$) at the same frequency and have a phase shift unequal to 0 or $\pm \pi/2$. (Figure 8c).

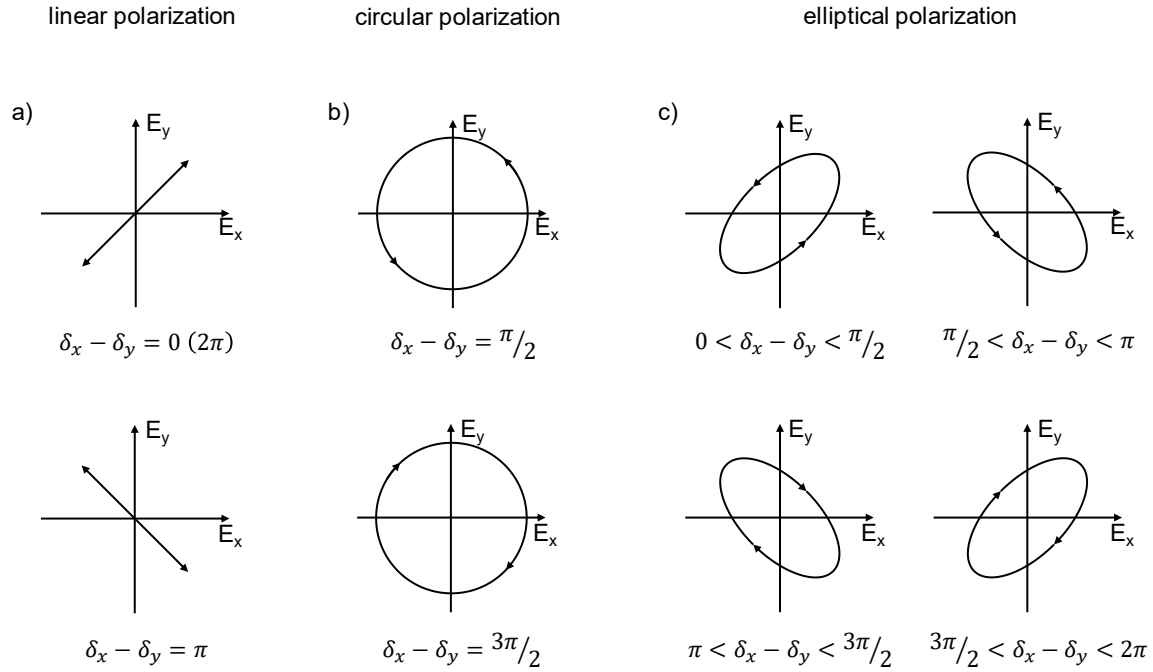


Figure 8: Representation of the three cases of the temporal change of the electric field vector of the monochromatic wave in the spatial directions x and y. a) linearly polarized light: the electric field has the same direction x at any location z. b) circularly polarized light: interference of two perpendicularly linearly polarized waves with the same frequency, amplitude ($\vec{E}_{0x} = \vec{E}_{0y}$) and a phase shift of $\pm \pi/2$. c) elliptically polarized light: interference of two perpendicularly to each other, linearly polarized waves with the same frequency and either different amplitude ($\vec{E}_{0x} \neq \vec{E}_{0y}$) or equal amplitudes ($\vec{E}_{0x} = \vec{E}_{0y}$) and a phase shift ($\delta_x - \delta_y$) unequal to 0 or $\pm \pi/2$. Top left: $\delta_x - \delta_y = \pi/4$, top right: $\delta_x - \delta_y = 3\pi/4$, bottom left: $\delta_x - \delta_y = 5\pi/4$, bottom right: $\delta_x - \delta_y = 7\pi/4$.

Principles of ellipsometry

In order to analyze the interaction of polarized light with a sample, the change of the polarization state, i.e., the difference between the polarization of the incident light and that of the outgoing light, is considered. Due to the time independence, the Jones vectors (equation (13)) for the incident (\vec{E}^i) and reflected (\vec{E}^r) electromagnetic wave can be used for the calculation. When describing the polarization in the Cartesian coordinate system, the x-axis is perpendicular, and the y-axis is parallel to the sample surface. These relationships are illustrated in Figure 9. The interaction of the light with the sample surface is represented by the complex Fresnel reflection coefficients r_p (amplitude of reflection coefficient for parallel polarization, p from the German word parallel) and r_s (amplitude of reflection coefficient for perpendicular polarization, s from the German word senkrecht), which are defined as follows:⁹⁴⁻⁹⁶

$$r_j = \frac{|E_{0j}^r|}{|E_{0j}^i|} e^{i(\delta_j^r - \delta_j^i)} \quad \text{mit } j = p, s \quad (14)$$

For simplification of equation (14), the ellipsometric angles Ψ and Δ can be introduced, which are defined as:⁹⁴⁻⁹⁶

$$\tan \Psi = \frac{|E_{0p}^r|}{|E_{0p}^i|} \bigg/ \frac{|E_{0s}^r|}{|E_{0s}^i|} \quad (15)$$

$$\Delta = (\delta_p^r - \delta_p^i) - (\delta_s^r - \delta_s^i) \quad (16)$$

By the description of the amplitude ratio $\tan \Psi$ and the phase difference Δ the ellipsometric basic equation can be obtained as result, which is expressed as:

$$\rho = \frac{r_p}{r_s} = \tan(\Psi) \cdot e^{i\Delta} \quad (17)$$

with ρ as a complex reflection ratio.⁹⁴⁻⁹⁶

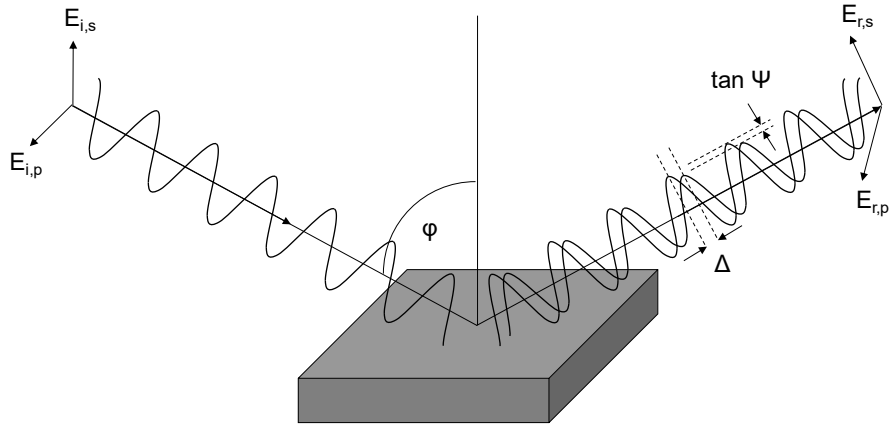


Figure 9: Schematic illustration of the reflection and change of the polarization state of a p- and s-linear polarized electromagnetic wave on a sample surface under the angle of incidence φ .

In order to derive material properties from the change of the polarization state, i.e., the change of the amplitude ratio and the phase difference of an electromagnetic wave, it is necessary to consider the optical properties of the material. These can be described with the dielectric function.

Dielectric function

The change in optical properties can be described by the derived material equation (9), which links the electric displacement field \vec{D} using the dielectric function in vacuum ϵ_0 with the electric field \vec{E} . The interaction of the electromagnetic wave with the material adds the contribution of the polarizability \vec{P} and the relationship between the electric displacement field and the electric field changes by the dielectric function of the material ϵ . This relationship can be expressed as follows:⁹⁵⁻⁹⁷

$$\vec{D} = \epsilon_0 \vec{E} + \vec{P} = \epsilon_0 \epsilon \vec{E} \quad (18)$$

The dielectric function depends on the material as well as on the frequency (angular frequency) and can be defined as a complex function in a real part (ϵ_1) and imaginary part (ϵ_2), which is described as:^{95, 96}

$$\epsilon = \epsilon_1 - i \epsilon_2 \quad (19)$$

In order to provide information about the refractive and absorption properties of the material, the complex refractive index \tilde{N} is used, which is related to the dielectric function as follows:

$$\epsilon = \tilde{N}^2 = (n - i k)^2 \quad (20)$$

with n as refractive index and k as extinction coefficient.^{95, 96}

Based on this relation, n and k can be calculated from the real and imaginary part of the dielectric function by using the following equations: ^{95, 96}

$$\varepsilon_1 = n^2 - k^2 \quad (21)$$

$$\varepsilon_2 = 2 n k \quad (22)$$

For the combination of the dielectric function or the refractive index and extinction coefficient with the ellipsometric measurement quantities Ψ and Δ the Snell's law (law of refraction) can be used, which describes the change of the direction of propagation (change of the phase velocity) of a plane wave at the transition from one medium to another medium. In this case the following relationship applies to the complex refractive index \tilde{N} :

$$\tilde{N}_0 \sin \varphi_0 = \tilde{N}_1 \sin \varphi_1 \quad (23)$$

with Φ_0 and Φ_1 as angles of incidence and refraction.⁹⁶

With the use of equation (18) and (23), the Fresnel reflection coefficients r_p and r_s can be related to the complex refractive index \tilde{N} as follows, and thus to the ellipsometric quantities Ψ and Δ according to the relation in equation (17).⁹⁵

$$r_p = \frac{\tilde{N}_1 \cos \varphi_0 - \tilde{N}_0 \cos \varphi_1}{\tilde{N}_1 \cos \varphi_0 + \tilde{N}_0 \cos \varphi_1} \quad (24)$$

$$r_s = \frac{\tilde{N}_0 \cos \varphi_0 - \tilde{N}_1 \cos \varphi_1}{\tilde{N}_0 \cos \varphi_0 + \tilde{N}_1 \cos \varphi_1} \quad (25)$$

However, this relationship is only valid for the case of a smooth surface without additional layers. Since thin mesoporous films on different substrates were analyzed, it is necessary to consider the Fresnel equations for multiple layers.

Analysis of multilayer systems

For samples consisting of multiple layers of thickness d , reflections (r_{jk}) occur mainly at the interfaces of the individual layers. In addition, there are also back reflections which have to be considered when determining the Fresnel reflection coefficients, i.e. reflections between ambient and first layer (r_{01}), between first and second layer (r_{12}) and between second and third layer or substrate (r_{23}), etc. (Figure 10).

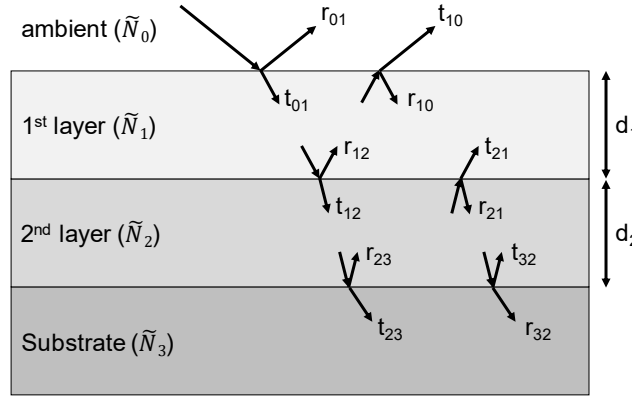


Figure 10: Schematic illustration of optical interference (reflections and transmissions) of a multilayer system.

For each individual interface, the Fresnel reflection coefficients can be calculated according to equations (24) and (25) with the respective complex refractive indices of the corresponding layer. By coherent interference of the reflected partial light waves, the reflection coefficients of the multilayer system can be calculated as follows:

$$r_p = \frac{(r_{01p} + r_{12p} e^{-i 2 \beta_1}) + (r_{01p} r_{12p} + e^{-i 2 \beta_1}) r_{23p} e^{-i 2 \beta_2}}{1 + (r_{01p} r_{12p} + e^{-i 2 \beta_1}) + (r_{12p} + r_{01p} e^{-i 2 \beta_1}) r_{23p} e^{-i 2 \beta_2}} \quad (26)$$

$$r_s = \frac{(r_{01s} + r_{12s} e^{-i 2 \beta_1}) + (r_{01s} r_{12s} + e^{-i 2 \beta_1}) r_{23s} e^{-i 2 \beta_2}}{1 + (r_{01s} r_{12s} + e^{-i 2 \beta_1}) + (r_{12s} + r_{01s} e^{-i 2 \beta_1}) r_{23s} e^{-i 2 \beta_2}} \quad (27)$$

where r_{01p} and r_{01s} are respectively the reflection coefficients between the ambient and the first layer, r_{12p} or r_{12s} and r_{23p} or r_{23s} are the reflection coefficients of the multilayer of p- and s-polarized light.⁹⁶ The variable β introduced in the equations is defined as phase factor and can be described as follows:

$$\beta_i = \frac{2 \pi d_i \tilde{N}_i}{\lambda} \cos \varphi_i \quad (28)$$

Based on the phase factor the dependence on the layer thickness can be recognized. In addition, it can be seen that the angle of incidence plays a role in determining the optical constants (n and k) and the film thickness.⁹⁴⁻⁹⁶

Effective Medium Approximation (EMA)

The multilayer system described above assumes film structures of homogeneous materials. However, the most investigated systems are not pure phases and consist of mixtures of different components, such as alloys or impurities. These include porous materials where voids are specifically introduced into the material and thus influence the optical properties. For the description of such systems the effective medium approximation (EMA) can be used. This is a combined or effective dielectric function of the medium for the entire film, based on the dielectric functions of two or more other materials. A general relationship of the interaction between such host-guest materials of an isotropic two-component system can be expressed as follows:

$$\frac{\varepsilon_{EMA} - \varepsilon_h}{\varepsilon_{EMA} + \gamma \varepsilon_h} = \sum_i f_i \frac{\varepsilon_i - \varepsilon_h}{\varepsilon_i + \gamma \varepsilon_h} \quad (29)$$

with ε_{EMA} as dielectric constant of the mixed phase, ε_h as host dielectric function, ε_i as dielectric functions and f_i as volume fraction of the i^{th} component (i.e. the guest fraction, $i = a, b, c$).^{95, 99} γ represents the factor that describes the shape of the guest volume and can be expressed as follows:

$$\gamma = \frac{1}{L} - 1 \quad (30)$$

where L defined the depolarization factor. In the isotropic case, i.e. for 3-dimensional spheres, $L = 1/3$ and $\gamma = 2$.⁹⁵

The general theory for effective medium approximation depends on the choice of host material, and three distinctions can be distinguished based on equation (29).

- **Lorentz-Lorenz:** In this EMA model the host is considered as air or vacuum ($\varepsilon_h = 1$). This theory is based on the Clausius-Mossotti equation and assumes that the components are mixed on an atomic scale.^{95, 99}

$$\frac{\varepsilon_{EMA} - 1}{\varepsilon_{EMA} + \gamma} = \sum_i f_i \frac{\varepsilon_i - 1}{\varepsilon_i + \gamma} \quad (31)$$

- **Maxwell-Garnett:** In the Maxwell-Garnett model, the host material is the component that represents the largest fraction in the mixture ($\varepsilon_h = \varepsilon_a$). This theory is applied when the fraction of inclusions is significantly smaller than the fraction of the host material and is suitable for the analysis of nano-crystallites if they do not form larger connected areas (clusters).^{95, 99}

$$\frac{\varepsilon_{EMA} - \varepsilon_a}{\varepsilon_{EMA} + \gamma \varepsilon_a} = \sum_i f_i \frac{\varepsilon_i - \varepsilon_a}{\varepsilon_i + \gamma \varepsilon_a} \quad (32)$$

- **Bruggeman:** In the Bruggeman EMA (BEMA), the mixture consists of a host medium and disordered inclusions, with the host material containing only the dielectric function of the EMA ($\varepsilon_h = \varepsilon_{EMA}$). Thus, the theory does not assume a material with the highest percentage and is therefore self-consistent. BEMA can be applied if no component forms a clear majority of the material.^{95, 99, 100}

$$0 = \sum_i f_i \frac{\varepsilon_i - \varepsilon_{EMA}}{\varepsilon_i + \gamma \varepsilon_{EMA}} \quad (33)$$

Of these theories, the BEMA model is most suitable for ellipsometric investigations of porous materials and is commonly used. As already mentioned above, spherical inclusions are considered in the first approximation in this theory, which also primarily provides good results. Mesoporous layers produced by soft-templating and subsequent thermal treatment usually show ellipsoidal pore geometries in z-direction, i.e., perpendicular to the substrate. For modeling of such layers with the BEMA theory the anisotropy of the pores has to be considered by the depolarization factor. This results in the following relationship for the anisotropic Bruggeman Effective Medium Approximation (a-BEMA):

$$\sum_i f_i \frac{\varepsilon_i - \varepsilon_{eff,j}}{\varepsilon_{eff,j} + L_j(\varepsilon_i - \varepsilon_{eff,j})} = 0 \quad (34)$$

with depolarization factors:

$$L_j = \frac{U_x U_y U_z}{2} \int_0^\infty \frac{(s + U_j^2)^{-1} ds}{\sqrt{(s + U_x^2)(s + U_y^2)(s + U_z^2)}} \quad (35)$$

$\varepsilon_{eff,j}$ describes the effective major dielectric function ($j = x, y, z$).¹⁰¹ The real depolarization factors L_j only depend on the real shape parameters U_j of the ellipsoid and the two relationships (U_x/U_z) and (U_y/U_z) serve to precisely define the shape.¹⁰¹

Modeling the dielectric function of materials

A solution of equations (26) and (27) for the general case of a system with many layers is not analytically solvable. This means that material properties (e.g., layer thickness, optical constants) of a layered system cannot be calculated directly from the measured ellipsometric parameters, due to the fact that an analytical solution of equation (17) is impossible. However, the calculation of the theoretical or simulated measured data from the material properties is possible using the Jones and Mueller formalisms, and a fit algorithm can be used for the ellipsometric data analysis. Therefore, it is necessary to develop a model that describes the experimentally measured data, where the model function should be able to reproduce the dielectric properties of the analyzed material. In this context, the laws of electromagnetic field theory offer the possibility to reduce the degrees of freedom of this fit algorithm. Herein, the Kramers-Kronig relation plays an important role, which enables the mathematical transformation of the real ε_1 and imaginary ε_2 parts of the dielectric function to each other.¹⁰²⁻¹⁰⁴

$$\varepsilon_1(\omega) = 1 + \frac{2}{\pi} P_{int} \int_0^{\infty} \frac{\omega' \varepsilon_2(\omega')}{\omega'^2 - \omega^2} d\omega' \quad (36)$$

$$\varepsilon_2(\omega) = -\frac{2\omega}{\pi} P_{int} \int_0^{\infty} \frac{\varepsilon_1(\omega') - 1}{\omega'^2 - \omega^2} d\omega' \quad (37)$$

where P_{int} denotes the principal value of the integral.

From equations (36) and (37) it can be seen that ε_1 and ε_2 are interdependent, i.e. if ε_1 is varied, ε_2 will change accordingly and vice versa.⁹⁶ This relationship is also known as the Kramers-Kronig consistency.

For the description of the dielectric function either single physical functions or their combination can be used. In the latter case the dielectric function of the model is the sum of the single function. Due to the Kramers-Kronig consistency, it is sufficient to consider the imaginary part ε_2 of the dielectric function. The functions relevant for this thesis are described in the following with their parameters.

- **Drude function:** The Drude function is applicable to free electron effects and was proposed by Paul Drude to describe transport properties of electrons in materials, especially metals.^{105, 106} In case of a semiconducting material, the absorption can be explained by electron transitions from the valence in the conduction band.¹⁰⁷ The Drude model can be described with the resistivity ρ_R and the mean scattering time τ and is expressed by the following equation:

$$\varepsilon_{Drude}(E) = \frac{-\hbar^2}{\varepsilon_0 \rho_R (\tau E^2 + i \hbar E)} \quad (38)$$

with

$$\rho_R = \frac{m^*}{N q^2 \tau} = \frac{1}{q \mu N} \quad (39)$$

where E is the photon energy ($E = h\nu = \hbar\omega$), \hbar the reduced Planck constant, ε_0 the vacuum dielectric constant, ρ_R the resistivity (Ohm cm), τ the mean scattering time (fs), m^* the electron effective mass ($9.11 \cdot 10^{-31}$ kg), N the electron concentration (cm^{-3}), q the electron charge ($1.60 \cdot 10^{-19}$ C) and μ the electron mobility ($\text{cm}^2 \text{V}^{-1} \text{s}^{-1}$).¹⁰⁸ Fit parameters for the Drude model are the resistivity ρ_R and the mean scattering time τ .

- **Lorentz function:** The Lorentz function is based on the interaction between light and matter and is applicable to atomic transitions with homogeneous line broadening. This line broadening can be described in the classical approach by a harmonic oscillator in which an excited electron is damped by energy radiation.^{95, 96} The model can be used for frequency-dependent polarizations due to bound charge and can describe a direct interband transition. The Lorentz function is expressed as follows:

$$\varepsilon_{Lorentzn}(E) = \frac{Amp_n \Gamma_n E n_n}{E n_n^2 - E^2 - i E \Gamma_n} \quad (40)$$

with Amp_n as the amplitude of the n^{th} oscillator (unitless), Γ_n width (full width at half-maximum) of the n^{th} oscillator (eV) and $E n_n$ the center energy of n^{th} oscillator (eV).¹⁰⁹ The fit parameters of the Lorentz parametrization are the amplitude Amp_n , the width Γ_n and the center energy $E n_n$.

- Tauc-Lorentz function:** The Tauc-Lorentz function is used to describe the optical properties of amorphous semiconductors near the band edge.¹¹⁰ For this purpose, the Lorentz oscillator is modified to consider the absorption near the band edge separately and is described in detail by G. E. Jellison Jr. and F. A. Modine.^{89, 111} The Tauc-Lorentz function can express as follows:

$$\varepsilon_{T-L_n}(E) = \frac{Amp_n En_n \Gamma_n (E - E_g)^2}{(E^2 - En_n^2) + \Gamma_n^2 E^2} \cdot \frac{1}{E}; \quad E \geq E_g \quad (41)$$

$$\varepsilon_{T-L_n}(E) = 0; \quad E \leq E_g \quad (42)$$

where Amp_n is the amplitude of the n^{th} oscillator (eV), En_n the center energy of n^{th} oscillator (eV), Γ_n the width (full width at half-maximum) of the n^{th} oscillator (eV) and E_g the band-gap energy (eV). Fit parameters of the Tauc-Lorentz parametrization are the amplitude Amp_n , the width Γ_n , the center energy En_n and the band-gap energy E_g .

Using such functions, a measured sample can finally be parameterized. The general procedure for the modeling is shown in Figure 10. First, the sample is measured with an ellipsometer. In the second step a suitable model is developed, e.g., using the functions described above. In the next step the ellipsometric quantities for the model are calculated and the obtained Ψ and Δ spectra are compared with the experimentally measured spectra. The model parameters are adapted in an iterative fitting process, e.g., using the Levenberg-Marquardt algorithm of non-linear regression. The aim of this process is to minimize the deviation between theoretical and experimental measurement quantities. This is done by defining a figure of merit, the root mean squared deviation (RMSD), which is expressed as follows:

$$RMSD = \sqrt{\frac{1}{3Y - Z} \sum_{i=1}^Y \left[\left(\frac{N_i^{fit} - N_i^{exp}}{0.001} \right)^2 + \left(\frac{C_i^{fit} - C_i^{exp}}{0.001} \right)^2 + \left(\frac{S_i^{fit} - S_i^{exp}}{0.001} \right)^2 \right]} \quad (43)$$

with

$$N = \cos(2\Psi) \quad (44)$$

$$C = \sin(2\Psi) \cos(\Delta) \quad (45)$$

$$S = \sin(2\Psi) \sin(\Delta) \quad (46)$$

where Y is the number of wavelengths and Z the number of fit parameters.

After each fit, it is controlled if the model parameters are converged with the measured spectra. The model parameters are changed minimally until a self-set RMSD value is reached and the model fit is converged. Finally, the material properties of the respective layer or layer system can be derived from the calculated model.

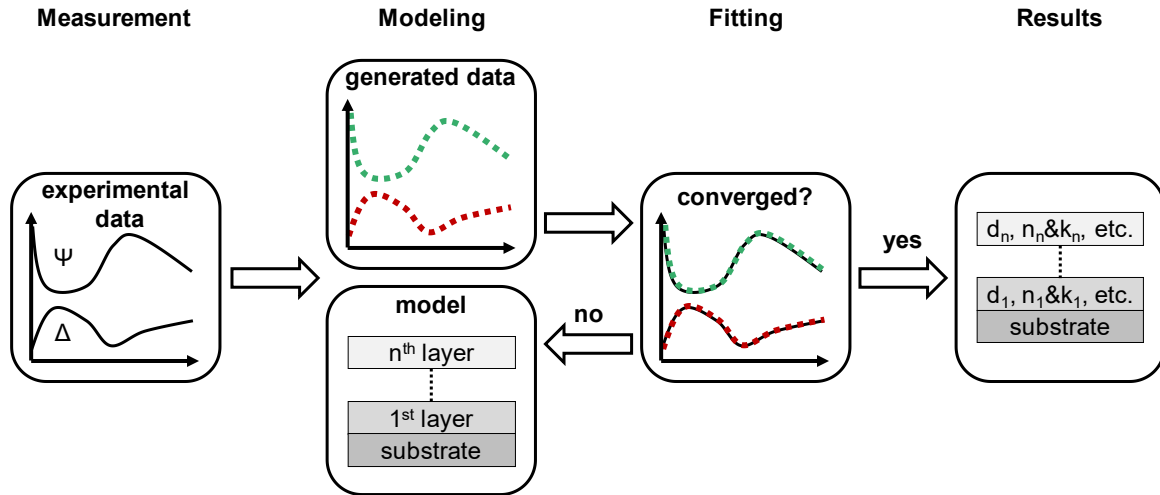


Figure 11: Schematic illustration of the general procedure for modeling of ellipsometric measured samples. The procedure includes the ellipsometric measurement of a suitable sample (e.g., thin film on a substrate), the model development of the sample, the fitting of the generated spectra from the model with the ellipsometric measured spectra and finally the derived results.

However, during this adjustment it can also occur that, e.g., by coupling of material parameters, there are different solutions for the description of the measured Ψ and Δ spectra. This coupling is especially important for thin absorbing films, as it is in the case of iridium oxide. For such absorbing materials, there is a strong correlation between film thickness and optical constants. One way to reduce this correlation is to measure the unknown parameters by suitable independent methods. However, this is not always possible because many methods require the destruction of the sample and/or are performed under high vacuum, e.g., cross-sectional SEM imaging. Another possibility is to increase the information content during the ellipsometric measurement.

Ellipsometric characterization of absorbing thin films

Ellipsometric measurements are generally used to determine optical constants and film thicknesses of transparent and semitransparent films. Since the set of parameters to be calculated is often underdetermined in the measured data, correlations between the parameters usually occur. In the presence of absorbing layers, an increased correlation may occur due to a higher number of parameters, especially in the presence of non-ideal effects such as porosity, roughness or inhomogeneities. To reduce the correlation of unknown parameters of absorbing layers, different methods can be used in ellipsometric measurements. In the following, a brief overview of the possibilities to increase the information content of absorbing films is given. All these techniques aim to reduce the high measurement uncertainty, by increasing the information content of the measurement data. A detailed overview is given by J. N. Hilfiker *et al.* in ref 112.

- **Measurements with different angles of incidence:** This allows to minimize unknown parameters by the dependence of the angle of incidence with the phase factor, as shown in equation (28). However, the information content is dependent on the significant change of the light interaction with the sample at different angles of incidence.
- **Interference enhancement:** By adding a transparent layer under the absorbing film, interference oscillations can be generated. This leads to a variation of the path length of the angle of incidence. However, it must be noted that the correlation between the optical constants and the material properties is only reduced by the simultaneous measurement of multiple angles of incidence.
- **Multi-Sample-Analysis:** Measuring multiple samples of the same material with different layer thicknesses, for example, can provide additional information about the dielectric function and reduce the correlation. In addition, this method can be combined with the two previously described, but it is strongly dependent on the consistency of the samples and thus strongly dependent on the microstructure of the films.
- **Multi-Ambient-Analysis:** The change in the refractive index of the environment changes the light interaction with the sample, providing additional information about the sample. This also increases the sensitivity to surface oxides or roughness. A big disadvantage of this method is the complexity of the measurement, due to possible window birefringence and the modeling of the correct environmental index. In addition, the film must be optically stable in different environmental conditions. However, this is not always the case and samples such as porous films change their index when a liquid penetrates the film.

Applications of ellipsometric investigations

A classical application of ellipsometry is the investigation of interfaces between Si and a dielectric layer above.¹¹³ The further development of spectroscopic ellipsometric measurements allows in-situ investigation of interfaces during layer growth, adsorption/desorption of solvents, electrochemical processes or biomolecular modifications.¹¹⁴⁻¹¹⁷ In this context, in-situ ellipsometry is mostly used to study layer growth during physical and chemical vapor deposition.¹¹⁴ This allows the thickness of the layer to be controlled during deposition and allows the nucleation behavior and layer growth rate to be studied, e.g. in atomic layer deposition (ALD), in-situ spectroscopic ellipsometry even allows the growth of ultra-thin films to be controlled with sub-monolayer resolution.

Another technique increasingly used is environmental ellipsometric porosimetry (EEP), in which an adsorption-desorption isotherm is recorded from the variations in the refractive index of the film by the change in the partial pressure of a solvent over a film.¹¹⁷ EEP thus allows the determination of the porous volume, pore size distribution (PSD), pore accessibility and the orthogonal Young's modulus (elasticity) of thin porous films.¹¹⁸

By coupling spectroscopic ellipsometry with electrochemistry, significant insights into the understanding of solid-liquid interfaces have been gained in recent years.^{115, 119} In-situ electrochemical ellipsometry was used to study the oxide growth during electrochemistry on metal surfaces such as copper or zinc.^{120, 121} In the investigation of the electrochemical oxidation of Zn, for instance, a model-free analysis scheme based on the Lekner interference parameter could be established, assuming that the thin oxide layer is not light-absorbing.^{121, 122} An extension of the analysis scheme enabled also the investigation of thin absorbing layers.¹²⁰

Ellipsometric investigations in electrochemistry have also been applied under reaction conditions such as in the oxygen evolution.¹¹⁹ However, the ellipsometric investigations were mostly used to analyze the oxide layer thickness and its potential dependent growth or reduction.¹²³ According to the current state of knowledge, no in-situ or operando ellipsometric studies during, for instance, oxygen evolution have been reported so far, which describe the investigation and correlation of material structures with activity. For this reason, the ex-situ and operando ellipsometric studies of mesoporous iridium oxide films will be described, and the derived parameters correlated with the activity in the acidic OER.

3 Experimental

3.1 Chemicals

Mesoporous iridium oxide films were synthesized using iridium acetate ($\text{Ir}(\text{CH}_3\text{COO})_n$, 99.95% metal base, approx. 48% Ir) from chemPUR and a triblock copolymer (PEO_{213} -*b*- PB_{184} -*b*- PEO_{213} , containing 20 400 g mol⁻¹ polyethylene oxide (PEO) and 10 000 g mol⁻¹ polybutadiene (PB)) purchased from Polymer Service Merseburg GmbH.⁷⁷ Ethanol (EtOH, >99%) from Sigma-Aldrich served as solvent. All chemicals were used without further purification.

For general investigations of mesoporous iridium oxide layers three different classes of Si wafers were used as substrates. The Si substrates were characterized by single-sided polished Si wafers with (100)-orientation (Siegert Wafers) and Si wafers (111) with a thermal SiO_2 layer with nominal SiO_2 thicknesses of 150 nm or approx. 1000 nm (Silicon Materials). Prior to deposition, Si wafers were cleaned with ethanol.

Electrical conductivity measurements, UV-VIS-NIR absorption spectroscopy and transmission measurement within the ellipsometer of mesoporous iridium oxide films were performed on ethanol cleaned quartz substrates.

For EPMA-EDS analyses, an iridium foil (0.25 mm thick, 99.8% (metal-based), 22.65 g cm⁻³) was employed as Ir reference material from abcr chemicals GmbH. Prior to the EPMA-EDS analyses, the Ir foil was polished with a 3 μm diamond suspension (Struers, DiaDuo-2) and cleaned with ethanol. A purified Si wafer was used as the Si reference and a TiO_2 reference material with a known oxygen stoichiometry was used as the O reference.

Electrochemical measurements of the layers were performed on polished conductive titanium substrates. Substrates for RDE measurements were polished with a 0.02 μm non-crystallizing amorphous colloidal silica suspension (Buehler, MasterMet 2) and then cleaned in ethanol. After film deposition, 5 mm diameter discs were pressed out of the titanium substrates.

For the flow cell experiments 25 x 40 mm titanium substrates were polished using a suspension consisting of non-crystallizing colloidal silica suspension (200 ml; 0.25 μm ; Struers, OP-S), hydrogen peroxide (40 ml) and nitric acid (1 ml), followed by a cleaning procedure with EtOH. The platinum foil for operando ECSE studies was polished using a 3 μm diamond suspension (Struers, DiaDuo-2) and cleaned with ethanol.

structure directing template + metal precursors $\xrightarrow[\Delta T]{\text{EtOH}}$ dip-coating solution \rightarrow dip-coating under controlled conditions (T, r.H.) $\xrightarrow[\text{in air}]{\text{calcination}}$ porous metal oxide film

36

3.3 Ellipsometry and developed operando flow cell setup

Spectroscopic ellipsometry (SE)

SE measurements were performed with a variable angle spectroscopic ellipsometer M2000 DI (J.A. Woollam) in a spectral range between 0.7 eV and 6.5 eV (192 nm and 1697 nm). Mesoporous iridium oxide films on Si wafers and Ti substrates were measured at angles of incidence of 65°, 70° and 75° and acquisition times between 5 s and 10 s. Ψ and Δ spectra were analyzed with the software CompleteEASE (v. 6.42) using a model consisting of a silicon substrate with a native oxide layer (3 nm for substrates without thermal SiO₂ layer) or a Si/SiO₂ interface (1 nm for substrates with a thermal SiO₂ layer), a SiO₂ layer for the Si substrates with thermal SiO₂, and an anisotropic Bruggeman Effective Medium Approximation (see Chapter 4.2 for detailed description). Transmission spectroscopic measurements were carried out at mesoporous iridium oxide films on quartz substrates using an angle of incidence of 90°. An uncoated quartz substrate served as reference.

Ellipsometric porosimetry (EP)

EP measurements were performed by fitting an environmental cell on the ellipsometer with a fixed angle of incidence of 60° (for Si samples) or 70° (for Ti samples). The relative humidity was adjusted by mixing dry nitrogen gas with water-saturated nitrogen gas. The latter was obtained by introducing dry nitrogen gas through two successive gas washing bottles filled with water. The total N₂ flow was 2.5 L min⁻¹, controlled by two mass flow controllers, and a constant temperature of 23 °C. The relative humidity was adjusted by mixing dry nitrogen gas with water-saturated nitrogen gas in a mixing chamber before the total flow was introduced into the environmental cell. The relative humidity was measured for the outgoing gas behind the cell with a humidity meter (Greisinger GMH 3351 with a TFS 0100 E humidity probe; GHM Messtechnik GmbH) and recorded with the software GSOF 3050 (GHM Messtechnik GmbH). The evaluation of the refractive index as a function of the relative humidity was done with the software CompleteEASE (v. 6.42) and the model described above (see Chapter 4.2 for further details).

Operando electrochemical spectroscopic ellipsometry (ECSE) setup

For operando ECSE investigations a respective flow cell was developed. ECSE measurements were performed by mounting the flow cell on the mesoporous iridium oxide films on titanium substrates and fitted the setup into the spectroscopic ellipsometer (M2000 DI). The flow cell consists of polyether ether ketone (PEEK) and is attached to the catalyst film by means of a sealing ring (Viton® FKM, 22 x 1 mm; IR Dichtungstechnik). In addition, two uncoated quartz windows (12.5 x 2.0 mm, refractive index $n_d = 1.458$, surface flatness: 1λ ; Edmund Optics Inc) were each attached to the cell with two (in front and behind the window) sealing rings (Viton® FKM, 9.25 x 1.78 mm; IR Dichtungstechnik). For electrical conduction, a single side copper printed circuit board (conductive plate) was mounted under the titanium substrate. An Ag/AgCl reference electrode and a Pt wire as counter electrode were connected to the flow cell, while the mesoporous iridium oxide films on titanium substrates served as working electrode (1.473 cm^2). N_2 purged 0.1M HClO_4 (Merck, 60%, 1.53 g cm^{-3}) was used as electrolyte, which circulated through the cell with a flow rate of 85 ml min^{-1} by using a peristaltic pump (Ismatec MCP Standard). Spectroscopic ellipsometry measurements were carried out in a spectral range between 1.1 eV and 6.4 eV (193 nm and 1127 nm) at an angle of incidence of 70° using the software CompleteEASE (v. 6.42). The acquisition time for each spectrum amounts to 0.978 s. The electrochemical measurements were performed with a Gamry interface 1000 (IFC1000) and the Gamry Framework Data Acquisition software (v. 7.07). Figure 12 illustrate the complete ECSE setup in detail.

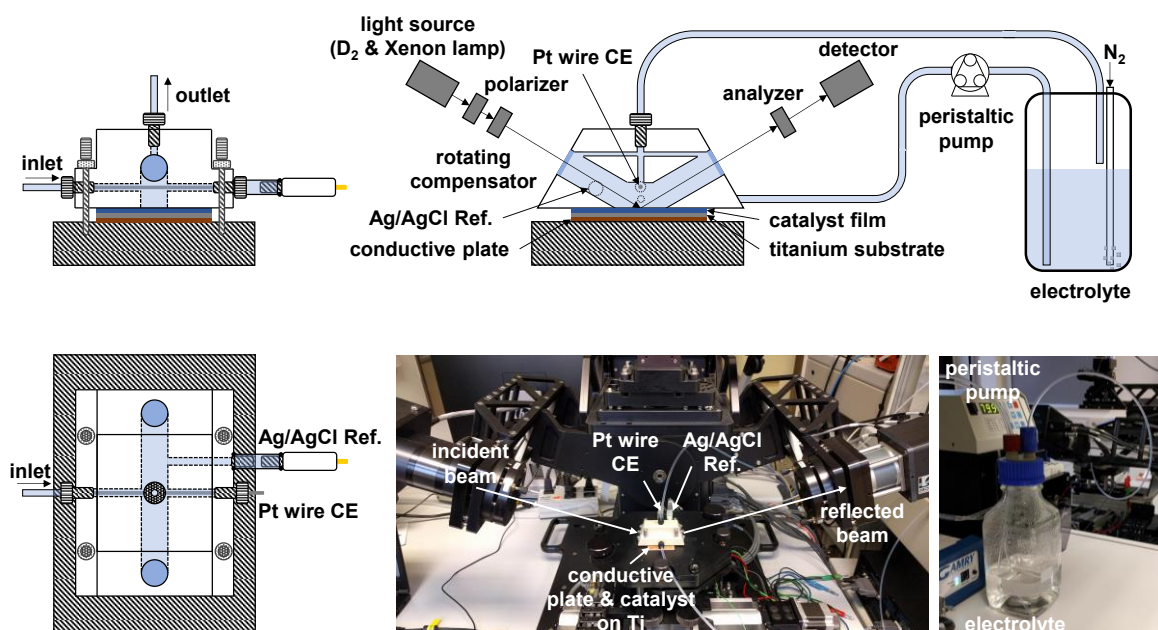


Figure 12: Illustration of the developed electrochemical spectroscopic ellipsometry setup used for operando investigations. Mesoporous IrO_x films on Ti substrates served as working electrode and a Pt wire as counter electrode. All potentials were measured against an Ag/AgCl electrode, which was referred to an RHE (+0.256 V vs. RHE at pH 1) and corrected for ohmic losses. 0.1M HClO_4 served as electrolyte with a flow rate of 85 ml min^{-1} via a peristaltic pump. Spectroscopic ellipsometry was performed in a spectra range between 1.1 eV and 6.4 eV (193 nm and 1127 nm) at an angle of incidence of 70° .

Prior to ECSE studies on mesoporous catalyst films, a silicon wafer with a known oxide thickness was analyzed for the quartz window correction. Afterwards, the N₂ purged electrolyte was analyzed using a model consists on a silicon wafer with known oxide thickness as substrate and a Sellmeier dispersion layer for the electrolyte, which is expressed as follows:

$$n = \left(\varepsilon(\infty) + \frac{Amp \lambda^2}{\lambda^2 - En^2 - E_{pole} \lambda^2} \right)^{1/2} \quad (47)$$

where $\varepsilon(\infty)$ is an index offset, Amp the amplitude, En the center energy, λ the wavelength, and E_{pole} the position of a pole in the infrared.¹²⁴ Results and a comparison of the electrolyte analysis is described in Appendix A1.

3.4 Electrochemical testing (ECSE and RDE)

Rotating disc electrode (RDE) setup

Electrocatalytic measurements using a three-electrode disc setup (Pine MSR-Rotator, BioLogic SP-200-Potentiostat) were performed with a reversible hydrogen electrode (RHE, Gaskatel, HydroFlex) as reference, Pt gauze (Chempur, 1024 mesh cm^2 , 0.06 mm wire diameter, 99.9%) as counter electrode and coated titanium discs (5 mm diameter, 0.196 cm^2) as working electrode (Figure 13). RDE measurements were recorded at room temperature in N_2 purged 0.5M H_2SO_4 (Fixanal, Fluka Analytical) or 0.1M HClO_4 (Merck, 60%, 1.53 g cm^{-3}) and the potentials were referred to the RHE. Mesoporous IrO_x coated titanium discs were mounted in a rotating disc shaft and rotated at a speed of 1600 revolutions per minute (rpm) during the EC testing. Data acquisition was performed with the BioLogic EC-Lab® Software (v. 11.10)



Figure 13: Illustration of the three-electrode disc setup used for electrocatalytic studies. Mesoporous IrO_x coated Ti substrate (5 mm) served as working electrode, a Pt gauze as counter electrode and a reversible hydrogen electrode (RHE) as reference electrode. All potentials were corrected for iR drop. Electrochemical measurements were either performed in N_2 purged (30 min) 0.5M H_2SO_4 or 0.1M HClO_4 and a rotating disc speed of 1600 rpm.

Electrochemical procedure for ECSE and RDE

OER activities were investigated by fifty cyclic voltammograms in a potential window between 1.2 V_{RHE} and 1.65 V_{RHE} at a scan rate of 6 mV s^{-1} in case of RDE measurements and three cyclic voltammograms in a potential window between 0.94 $V_{\text{Ag/AgCl}}$ and 1.22 $V_{\text{Ag/AgCl}}$ at a scan rate of 1 mV s^{-1} in case of ECSE. Prior to CV measurements, impedance spectroscopy was measured at the initial potential in order to correct recorded cyclic voltammograms for ohmic losses (iR correction). Additionally, potentials measured with the Ag/AgCl reference electrode were referred to the RHE (+0.256 V vs. RHE at pH 1). Low-potential cyclovoltammetry were performed in the range between 0.4 V_{RHE} and 1.4 V_{RHE} with scan rate of 50 mV s^{-1} (RDE) or 1 mV s^{-1} (ECSE), in order to determine the anodic and cathodic charge ($q_{(\text{a+c})/2}$). Ardizzone *et al.*¹²⁵ and Fierro *et al.*¹²⁶ described a reversible proton-inclusion-mechanism, which can take place in this potential range as follows:



The more iridium is accessible and/or available, the higher the faradaic current obtained from this reaction. An expression for the accessible iridium centers is obtained by determining the mean value of the integrated anodic and cathodic scan of the resulting CV ($q_{(\text{a+c})/2}$).

3.5 Complementary and additional analytical methods

Scanning electron microscopy (SEM)

SEM images were recorded on a JEOL 7401F at accelerating voltage of 10 kV. Images were evaluated with the ImageJ program v. 1.52e^{127, 128} with respect to film thickness, pore diameter and ordering. For the determination of the layer thickness, mesoporous iridium oxide films on Si substrates were break into two pieces followed by SEM imaging of the breaking edge. Film thicknesses of iridium oxide layers on Ti substrates were analyzed by scratching the films with a triangular tungsten carbide knife and imaging the scratch edge on tilted (45°) substrates.

Electron probe microanalysis (EPMA)

Energy dispersive X-ray spectra were recorded on a Carl Zeiss Supra 40 equipped with a Schottky field emitter and an energy dispersive X-ray spectrometer with a 10 mm² LN₂-free silicon drift detector (SDD) and an energy resolution of 123 eV (Bruker XFlash 5010). For EPMA, the X-ray intensities of interest were divided by the electron probe current and the live time to calculate k_{EPMA} values representing the ratio of the X-ray intensity of the element to be examined in the unknown sample to the X-ray intensity of the same element in a sample with known element concentration. Ir L _{α} , O K _{α} and Si K _{α} were recorded to calculate k_{EPMA} values at acceleration voltages of 15 kV, 20 kV, 25 kV and 30 kV. k_{EPMA} values were evaluated with the quantification model of Pouchou and Pichoir using the thin film analysis software StrataGem (v. 6.7 SAMx, Guyancourt, France).¹²⁹ The software iteratively adjusts calculated k_{EPMA} values to the measured ones to determine the mass-deposition and atomic ratios. Usually, the StrataGem software converts the mass-deposition into layer thickness according to the layer density specification. However, the reverse approach can also be used to determine the layer density by mass-deposition and known layer thicknesses.⁷⁸

Transmission electron microscopy (TEM) and selected area electron diffraction (SAED)

TEM images were recorded on a FEI Tecnai G2 20 S-TWIN electron microscope at 200 kV acceleration voltage. Fragments of scraped off film pieces were deposited on carbon-coated copper grids (lacey carbon, 300 mesh). Electron diffraction (SAED) was performed using an aperture resulting in a sample area with a diameter of about 180 nm.

X-ray diffraction (XRD) and X-ray reflectometry (XRR)

XRD and XRR were performed at a Bragg-Soller X-ray diffractometer system with a flat secondary monochromator and fixed Cu K α tube (Seifert XRD 3000TT). Diffractograms recorded between 25° and 75° with a resolution of 0.1° and 8 s acquisition time. XRR measurements were performed between 0.1° and 2.0° with a resolution of 0.05° and acquisition time of 2 s

X-ray absorption spectroscopy (XAS) and X-ray photoelectron spectroscopy (XPS)

XAS and XPS spectra were recorded in the ISS beamline at BESSY II (Berlin), which is equipped with a SPECS PHOIBOS 150 NAP hemispheric analyzer. The synchrotron X-rays were obtained from a bending magnet (D41) and a plane monochromator (PGM) with an excitation energy in the range of 80 eV to 2000 eV (soft X-rays) and a flux of $6 \cdot 10^{10}$ photons s⁻¹ with a ring current of 0.1 A, an output slit of 111 μ m and a beam spot size of 80 μ m x 200 μ m. Spectra were evaluated with the software package SpecsLab Prodigy v. 4.67.1-r91102 (<https://www.specs-group.com>). XPS spectra were fitted with symmetric sum Gaussian–Lorentzian functions after a Shirley background correction.

UV-VIS-NIR absorption spectroscopy

UV-VIS-NIR absorption measurements were carried out with a Varian Cary 5000 in a spectral range of 350 nm – 1000 nm with 1 nm steps on mesoporous iridium oxide films deposited on quartz substrates. An uncoated quartz substrate was used as reference sample.

Electrical conductivity

Sheet conductivity measurements were carried out on mesoporous iridium oxide films deposited on quartz substrates using a MR-1 surface resistance device (Schuetz Messtechnik) equipped with a four-point pin probe head.

Instrumented indentation testing (IIT)

Instrumented indentation testing (IIT) for determination of Young's modulus were performed using a Keysight Nano Indenter G200 with a DCM II Berkovich indenter using Nano Suite 6.50.0 software. The IrO_x films on silicon substrates were mounted on a carrier with Crystalbond™ 509 and measured using the constant penetration depth method (100 nm depth at a frequency of 75 Hz). Five points were measured on each sample with a point-to-point distance of 20 μ m in diagonal direction. For the measurement of the substrate-independent module of a thin film, a finite element analysis model was used, which is described in detail by J. Hay and B. Crawford in reference 130.

4. Ex-situ characterization of mesoporous templated iridium oxide (IrO_x) films

The methodology for the analysis of structure-activity relationships in the acidic OER via ex-situ and operando spectroscopic ellipsometry, which is given in Scheme 1, involves the synthesis of the model type catalysts in the first step. Mesoporous IrO_x films are suitable as such model catalysts due to their high activity and stability under acidic conditions as well as their high inner surface and the resulting increased intensity of the interface reactions. Established synthesis routes for mesoporous IrO_x films have been reported in literature and are based on a soft-templating procedure.^{26, 64} Thus, reproducible and active catalysts for the acidic OER can be synthesized. The approach used to prepare the materials is based on a dip-coating process of a solution containing a tri-block copolymer (PEO-PB-PEO), iridium acetate (Ir(CH₃COO)_n) and ethanol (EtOH), followed by a calcination procedure under air. A detailed description of the reproduced synthesis is given in Chapter 3.2.

This Chapter (4) discusses in general the ex-situ analysis of the morphological, chemical, electrical, electronic, and optical properties as well as the activity in electrochemical catalysis of the synthesized mesoporous IrO_x films calcined between 300 °C and 600 °C.

Chapter 4.1 describes the morphological and physicochemical properties of the materials using electron and X-ray based methods of synthesized films on silicon and titanium substrates. Furthermore, electrical and electronic properties are described using conductivity measurements and absorption spectroscopic analysis of films on quartz substrates.

Chapter 4.2 presents the development of a model for the analyses by spectroscopic ellipsometry. The first part describes the development of the model using the interference enhancement method and the second part describes the analysis of the calcination series (300 °C – 600 °C) deposited on silicon and titanium substrates using the developed model.

Chapter 4.3 then addresses the ex-situ electrochemical analyses in the acidic OER of the calcination series using rotating disk electrodes (RDE) and using the developed flow cell setup for the operando measurements, which are discussed later in Chapter 5 and 6 in detail.

Finally, in Chapter 4.4 relevant parameters, i.e. layer thickness, porosity, resistivity and intraband transitions, are validated from the derived results of the ex-situ spectroscopic ellipsometric investigations with the results from the electron and X-ray based methods, as well as conductivity measurements and absorption spectroscopic analyses. Furthermore, results from ellipsometric investigations are correlated with OER activities of the model catalysts.

4.1 Material analysis and physicochemical properties

This Chapter gives an overview of material properties of the reproduced mesoporous IrO_x films via the established synthesis route described in literature.^{26, 64} This includes first the analysis with electron-based methods, followed by the analysis with X-ray based methods. Finally, electrical and electronic parameters are deduced from conductivity measurements and from the analysis using UV-VIS-NIR absorption spectroscopy.

Electron-based characterization

To get an insight into the morphological structure and chemical composition of the reproduced and synthesized IrO_x films, the layers were first analyzed using electron-based analytical methods, i.e. SEM, TEM, SAED and EPMA-EDS. Figure 14 presents first a) top-view SEM, b) top-view high resolution (HR) SEM, c) cross-section SEM, d) TEM, and e) HR-TEM images as well as f) SAED of a mesoporous IrO_x film calcined at a temperature of 375 °C deposited on a silicon substrate.

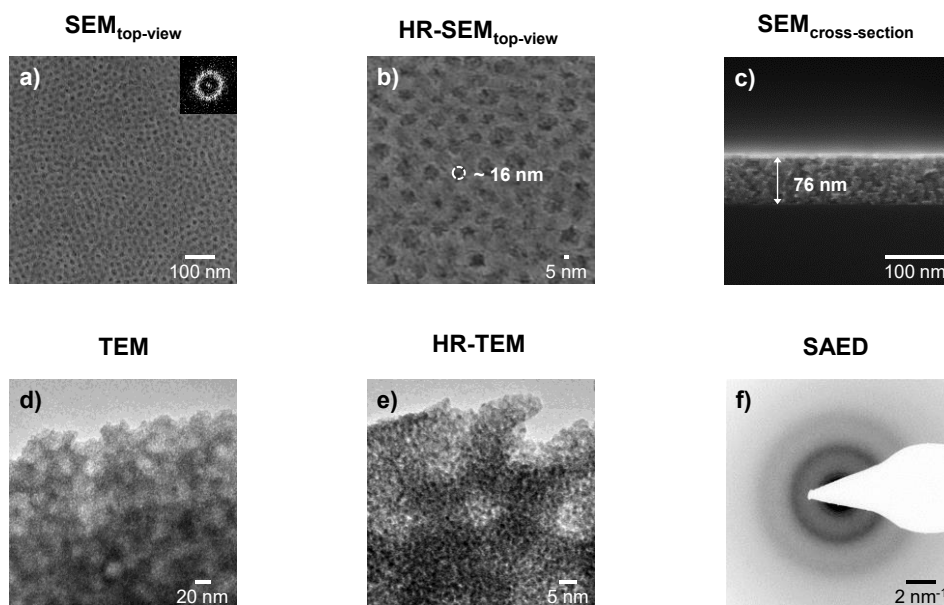


Figure 14: Electron-based characterization of a mesoporous iridium oxide film calcined at a temperature of 375 °C for 5 minutes in air. a) SEM top-view image with FFT inset, b) high resolution top-view SEM image with indicated pore diameter of about 16 nm and c) cross-section SEM image of the film with an indicated thickness of about 76 nm. d) TEM image and e) high resolution TEM image of a film fragment. f) presents selected area electron diffraction of a film fragment.

SEM images in top-view mode indicate a complete removal of the polymer template and uniform pore openings on the outer surface (Figure 14a). The corresponding Fast Fourier Transformation (FFT) of the top-view image (inset Figure 14a) shows an isotropic ring. This feature indicates an ordered pore arrangement at the outer surface plane area with periodic pore distance of 24 nm. The diameter of the pore openings amounts to 16 ± 3 nm (Figure 14b). Cross-section SEM images were provided by breaking the coated silicon substrate into two pieces. Figure 14c shows a uniform

layer thickness of about 76 ± 3 nm. The deviation was determined by measuring the film thickness at different points over a range of several millimeters.

TEM images were taken from film fragments scraped off from the Si substrate and deposited on carbon coated (lacey) copper grid. The TEM images (Figure 14d, e) show mesopores of about 10 nm to 15 nm and indicate that pores are present throughout the film volume. Furthermore, the HR-TEM image (Figure 14e) reveals small crystallites in the pore walls. However, due to the reductive nature of the electron beam, IrO₂ tends to decompose, which can lead to metallic Ir particles (see Appendix A2).¹³¹ Electron diffraction (SAED, Figure 14f) shows broad diffraction rings revealing randomly orientated crystallites. The observed rings can be attribute to lattice parameters of rutile iridium oxide (PDF: 00-015-0870).

SEM and TEM images verify the presence of mesopores, a well-defined pore structure and the formation of amorphous iridium oxide, which are very comparable to the films described in the literature and thus also confirm the high reproducibility of the synthesis.

The calcination temperature has a strong influence on the film morphology, crystallinity and catalytical activity in the oxygen evolution reaction.^{26, 64} To study the influence of the calcination temperature, IrO_x films were calcined between 300 °C – 600 °C. Figure 15 demonstrates the SEM micrographs of the calcination series on silicon substrates (Figure 15a-r) and titanium substrates (Figure 15s-x).

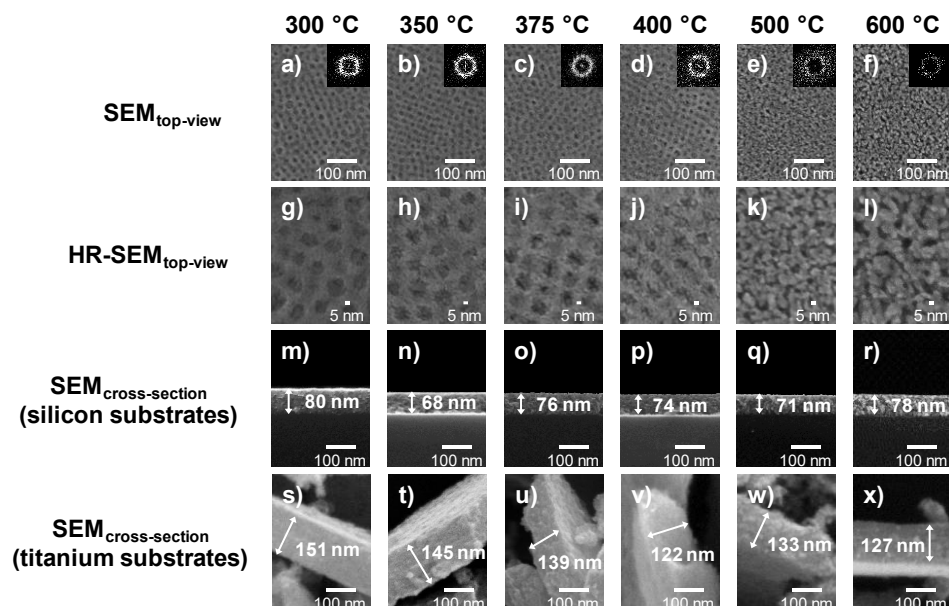


Figure 15: SEM images in top-view and cross-section mode of mesoporous IrO_x films on respective Si substrates and Ti substrates calcined at temperatures between 300 °C and 600 °C. Images indicate mesoporous IrO_x films in a) – f) top-view, g) – l) high resolution, m) – r) cross-sections of films on Si substrates, and s) – x) cross-sections of films on Ti substrates.

IrO_x films calcined between 300 °C and 400 °C show a fully developed mesopore system with periodic pore arrangement of about 24 nm at the outer surface (Figure 15a-d). The films, which were calcined at 500 °C and 600 °C, show a deformed pore system, which is due to the beginning of material sintering and crystallite growth (Figure 15e, f). However, both films still show an isotropic ring in the FFT, indicating an existing pore order with distances between two pore centers of about 23 nm. The pore openings range from 14 nm – 16 nm for the films calcined between 300 °C and 400 °C (Figure 15g-j), whereas no pore size can be determined for the higher calcined films (Figure 15k, l). The film thicknesses on silicon substrates range from 80 nm to 68 nm (Figure 15m-r), while the layers on titanium substrates have thicknesses from 151 nm to 122 nm and are thus approximately twice as thick (Figure 15s-x). In general, the films show a decrease in film thickness with increasing calcination temperature, which agrees well with other micelle templated porous oxide systems^{64, 77, 132-134}. A summary of the SEM investigations, i.e. film thickness, pore size and pore ordering can be found in Table 1 at the end of this Chapter 4.1.

Electron probe microanalysis (EPMA) employed by means of energy dispersive X-ray spectrometry (EDS) was used to study the elemental compositions, mass-depositions, and densities of the IrO_x calcination series. X-ray intensities of interest (Ir L_α, O K_α and Si K_α) were measured at a SEM and divided by the electron probe current and by live time to calculate k_{EPMA} -values. These values are the ratio of the X-ray intensity of the element to be examined in the unknown sample to the X-ray intensity of the same element in a sample of known elemental concentration. For the evaluation of elemental compositions, mass-depositions and densities, the thin film software StrataGem (EPMA-EDS / StrataGem) was used, which iteratively fits the determined k_{EPMA} -values.^{78, 129} Figure 16 presents a) exemplarily the fitting results of the EPMA analysis and b) the determined mass-deposition of the IrO_x film calcined at 375 °C as well as c) elemental compositions, d) mass-depositions, e) average densities and f) the calculated film porosities of the calcination series.

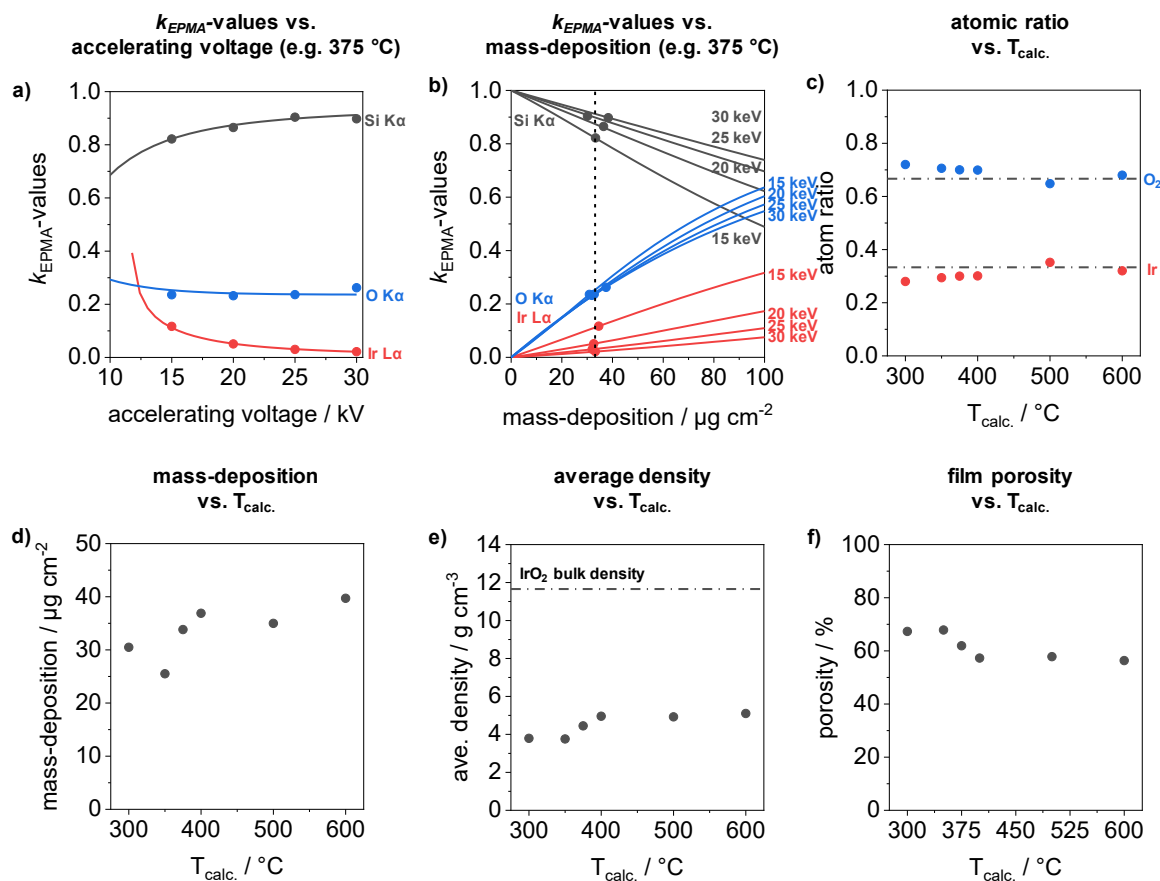


Figure 16: Electron probe microanalysis using energy dispersive X-ray spectrometry and evaluation with the thin film software StrataGem (EPMA-EDS / StrataGem) of mesoporous IrO_x films. a) fitting results of the EPMA analysis with the StrataGem software of a sample calcined at 375 °C on a silicon substrate, b) mass-deposition of the IrO_x film calcined at 375 °C, c) element compositions, d) mass-depositions, e) calculated average densities, and f) calculated film porosities of the calcination series.

Figure 16a shows as an example the k_{EPMA} -values of Ir L α , O K α and Si K α in dependence on the applied accelerating voltage and Figure 16b the k_{EPMA} -values as a function of the mass-deposition for the IrO_x film calcined at 375 °C. The experimentally determined k_{EPMA} -values (circles) decreases for Ir L α and O K α of the IrO_x film, while the values for the Si K α of the substrate increases with increasing accelerating voltage (Figure 16a). These k_{EPMA} -values were iteratively fitted by the StrataGem software (lines), using element composition and mass-deposition as free parameters. The fit curves show a good agreement with the experimental determined k_{EPMA} -values and is similar to other layer-substrate systems, which used the same model and method.¹³⁵⁻¹³⁷

As a result of the analysis, the elemental composition of each film can be derived from the fitted k_{EPMA} -values (Figure 16c). The Ir/O ratios decrease from 2.6 to 1.8 with increasing calcination temperature. Low-temperature calcined IrO_x films (≤ 400 °C) show higher Ir/O ratios, while the films at higher calcination temperatures show ratios similar to stoichiometric IrO₂. Due to the complete conversion of the metal oxide precursor (Ir(CH₃COO)_n) at a calcination temperature of 250 °C, the higher Ir/O ratios can be attributed to a significant amount of terminal hydrated oxygen species.¹³⁸⁻¹⁴⁰

Mass-deposition was used as another free parameter to adjust the k_{EPMA} -values. The mass-loadings range from $25.5 \mu\text{g cm}^{-2}$ to $39.7 \mu\text{g cm}^{-2}$ and show a wide distribution about an average value of ca. $33.6 \mu\text{g cm}^{-2}$ (Figure 16d). Due to the same parameters (withdrawal rate, temperature, humidity, etc.) during the dip-coating process, similar mass-depositions should be expected for all films and only the film thickness is supposed to change with increasing calcination temperature due to sintering effects and collapse of the pore structure. Ortel *et al.* demonstrated very well on similarly prepared mesoporous IrO_x films the influence of calcination temperature on film thickness, pore spacing perpendicular to the substrate, crystallite growth, and the accessible surface area.⁶⁴ These films exhibit a decrease in film thickness, pore spacing, and surface area, while the crystallite size increases with increasing calcination temperature.

To calculate the average density of each film, values of the mass-deposition were divided by the film thickness from cross-sectional SEM images of the films deposited on Si substrates (Figure 15m-r). Mesoporous IrO_x films show an increase in density up to a calcination temperature of 400°C (from 3.8 g cm^{-3} to 5.0 g cm^{-3}) and indicate a constant density of about 5.0 g cm^{-3} at temperatures above 400°C . These results show good agreement with the expected trend, where the film thickness decreases with increasing calcination temperature and thus the density of the film increases due to sintering effects and collapse of the pore structure.

Based on the calculated densities, the porosity of the individual film can be calculated using the following equation:

$$P = \frac{V_{pore}}{V_{total}} = \left(1 - \frac{\rho_{film}}{\rho_{bulk}}\right) \cdot 100\% \quad (48)$$

with P as porosity, V_{pore} as pore volume, V_{total} as volume of the entire layer, ρ_{film} as density of the analyzed film and ρ_{bulk} as non-porous reference material. The bulk density of IrO_2 (11.66 g cm^{-3}) was used as non-porous reference material.

The calculated porosity values range from 67.8% to 56.3%. The porosity reveals a constant behavior up to a calcination temperature of 350°C and decreases until 400°C . Above 400°C , the porosity again shows relatively constant values for the films calcined at 500°C and 600°C . In contrast to similar templated oxide materials, the values determined are about 20% higher.⁷⁸ Furthermore, comparable oxide materials show a decreasing trend in the surface area determined by Kr-BET with increasing calcination temperature. However, unlike sorption experiments, the EPMA method does not distinguish between open and closed pores, since the X-ray spectra are emitted by the atoms in the entire film regardless of their position.⁷⁸ A summary of the derived parameters, i.e. atom ratios, mass-deposition, densities and porosity values, of the calcination series by EPMA-EDS is given in Table 1 at the end of this Chapter.

X-ray based characterization

Analysis with X-ray based characterization methods such as XRD, XRR and XPS provides access to detailed information on crystallinity, analysis of layer thickness and density as a complementary method and detailed information on the chemical composition of the calcination series. The SEM micrographs reveal the dependence of the crystallinity of the IrO_x films on the calcination temperature. To study the change of the crystallinity in more detail, X-ray diffractograms of IrO_x films on Si-wafers (Figure 17a) and titanium substrates (Figure 17b) were recorded in a range of $20^\circ - 75^\circ$.

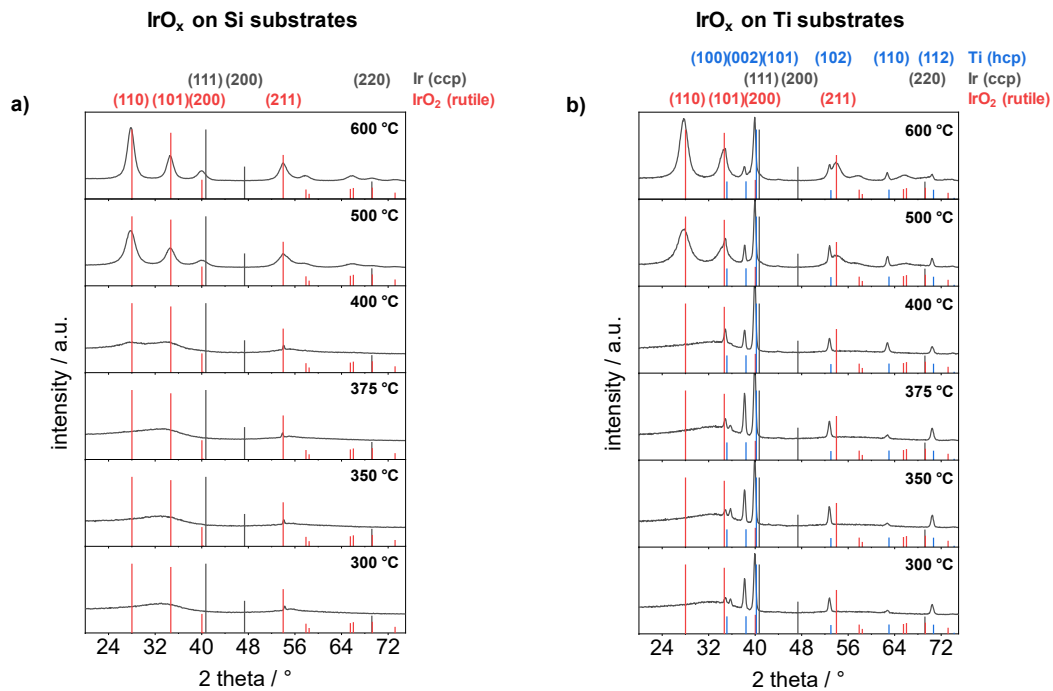


Figure 17: XRD analysis of mesoporous IrO_x films on Si and Ti substrates calcined between 300 °C and 600 °C. a) films deposited on Si substrates with diffraction patterns of cubic close packing (ccp) iridium (PDF: 00-006-0598) and rutile iridium oxide (PDF: 00-015-0870), b) films deposited on Ti substrates with diffraction patterns of ccp iridium, rutile iridium oxide and hexagonal close packing (hcp) titanium (PDF: 00-044-1294).

Diffractograms for the IrO_x films calcined between 300 °C and 375 °C on Si substrates show a broad diffraction at about 33° , which is close to the (101) lattice of an IrO_2 crystal (PDF: 00-015-0870) with rutile structure (Figure 17a). At 400 °C a second reflection at 27° become visible, which can be attributed to the (110) lattices of the IrO_2 crystal. At higher calcination temperatures ($> 400^\circ\text{C}$) several reflections are visible that can be attributed to the IrO_2 crystal, and no identification of cubic Ir (ccp, PDF: 00-006-0598) was detected. The same behavior can be observed for IrO_x films on Ti substrates, with additional reflections of hexagonal Ti (hcp, PDF: 00-044-1294). However, there is a minor difference at the IrO_x sample calcined at 400 °C. While two reflections can be detected for the film on the Si-wafer [(110) and (101)], the diffractogram on the Ti substrate shows only one broad reflection near the (101) lattice, indicating a less crystalline film. This can probably be attributed to the different substrates (Si and Ti), leading to a slight shift in the calcination temperature-dependent crystallinity.

According to the Scherrer equation (5), the size of the crystallites can be derived from the diffractograms. Crystallite sizes were estimated by the intense signal for the (101) reflection at $2\theta = 34.6^\circ$. Sizes of the crystallite increases with higher temperatures and ranges from about 1.2 nm to 7.1 nm, where the crystallite size is approximately constant (1.2 nm) for films calcined until 400 °C and increase at higher temperatures. The values of each film are summarized in Table 1 at the end of this Chapter.

XRR was used as an independent complementary method for the analysis of the film thickness and density. To determine the layer thickness and density from the XRR measurements, the reflectivity $R(\theta)$ of the sample was modeled using the matrix method.¹⁴¹ The XRR model is based on a Si substrate, a native oxide layer (SiO_2), the mesoporous IrO_2 layer and a carbonaceous contamination layer and can be expressed as follows:

$$I_{s,XRR}(\theta) = R_{XRR}(d_{\text{SiO}_2}, d_{\text{IrO}_2}, d_C, \rho_{\text{IrO}_2}, \rho_C, \sigma_{dw,1}, \sigma_{dw,2}, \sigma_{dw,3}, \sigma_{dw,4}, \theta_{XRR,i} + \theta_0) \cdot g(\sigma_\theta; \theta) \cdot I_{X-ray} \cdot \text{erf}(\sin(\theta_i + \theta_0) l_{XRR}/\sqrt{2}) + I_{\text{dark}} \quad (49)$$

where $I_{s,XRR}(\theta)$ is the simulated intensity, R_{XRR} the XRR reflectivity, d_n the thickness of the specified layer, ρ_n the density, $\sigma_{dw,n}$ a Debye-Waller-like factor for roughness and interdiffusion, $\theta_{XRR,i}$ the angle of incidence and θ_0 is an offset of the incidence angle. The expression $g(\sigma_\theta; \theta)$ describes a Gaussian beam profile where σ_θ is the width of the Gaussian beam. I_{X-ray} is the incident X-ray intensity and erf the error function. At very small angles of incidence, the X-ray beam may be longer than the sample, resulting in a smaller effective incident intensity, expressed as l_{XRR} , which describes the length of the sample relative to the length of the X-ray beam. I_{dark} serve as a correction for the dark current of the photo diode at lower photon energies. All parameters in equation (49) served as variable parameters. Tabulated values are used for the densities of the Si and SiO_2 layer.¹⁴²

In order to obtain uncertainties for the modeled parameters, the affine invariant Markov Chain Monte Carlo (MCMC) algorithm as implemented in the emcee software package is used and can be expressed as follows:^{143, 144}

$$\mathcal{L} = \prod_{\theta} \frac{1}{\sqrt{2\pi} u(\theta)} \exp\left(-\frac{(I_{s,XRR}(\theta) - I_{m,XRR}(\theta))^2}{2 u(\theta)^2}\right) \quad (50)$$

with the measured intensity $I_{m,XRR}(\theta)$ and the uncertainty $u(\theta)$. The uncertainty is estimated using the following equation:

$$u(\theta) = a I_{s,XRR}(\theta) + b \quad (51)$$

with the uncertainty factors a and b , which are treated as variable parameters.

The XRR measurements and evaluations were performed in cooperation with BAM (measurements by Mario Sahre) and PTB (evaluation by Mika Pflüger) within the HyMET project.

Figure 18 presents the results of the modeled XRR measurements of the IrO_x films calcined between 300 °C and 500 °C.

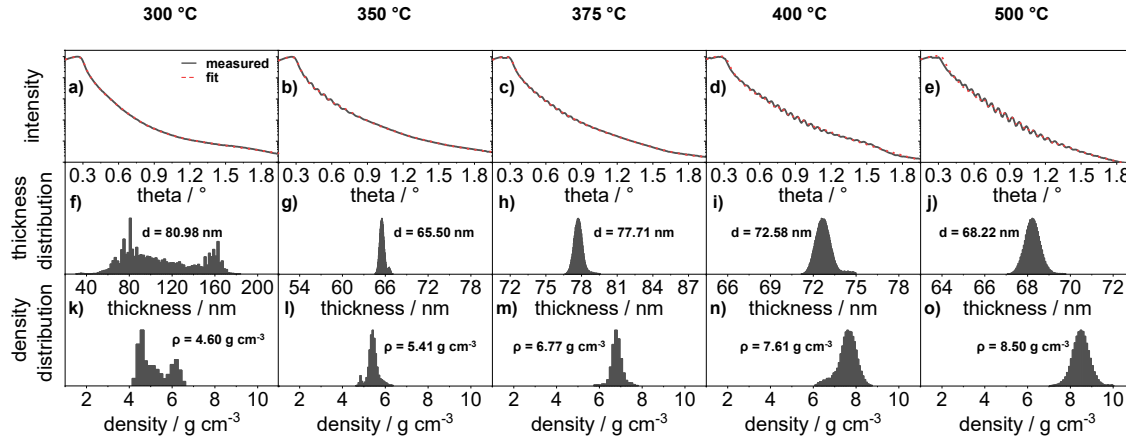


Figure 18: X-ray reflectometry measurements and fits of the IrO_x calcination series. a) – e) present the measured XRR curves with their fits, f) – j) the deduced layer thickness, and k) – o) the derived density of each film.

The XRR fits (dashed red line) show a good agreement to the measured XRR (solid black line) curves (Figure 18a-e). As a result of the adjustments, thickness (Figure 18f-j) and density distributions (Figure 18k-o) of the IrO_x films were obtained. The derived layer thicknesses range from about 81 nm to 66 nm and reveal similar values to those determined from SEM cross-section images (Figure 15m-r). The film thickness of the sample calcined at 300 °C shows a very broad distribution (Figure 18f). Due to the absence of Kiessig oscillations (interferences), an exact determination of the film thickness and density cannot be provided by the model, which is reflected in the large deviations.

The derived densities increase towards higher calcination temperatures but differ from the density values determined with the EPMA-EDS / StrataGem method. While the 300 °C sample indicates similar densities ($\rho_{EPMA-EDS} = 3.79 \text{ g cm}^{-3}$; $\rho_{XRR} = 4.6 \text{ g cm}^{-3}$), the values of the 500 °C sample differ by a factor of about 2 ($\rho_{EPMA-EDS} = 4.92 \text{ g cm}^{-3}$; $\rho_{XRR} = 8.5 \text{ g cm}^{-3}$). In XRR a density profile is determined at the interface perpendicular to the surface, whereas the EPMA-EDS / StrataGem method determines the atoms in the entire layer.^{78, 145} This would possibly indicate a density gradient between the film surface and the film volume. However, the investigated mesoporous layers are complex samples in which various factors (e.g., textural porosity and/or nano crystallites) play a role and make the density determination difficult. A summary of the layer thickness and density values as well as the comparison to the electron-based methods is given in Table 1 in the end of this Chapter.

Besides crystallinity, film thickness and density, the chemical composition of the mesoporous IrO_x films plays an important role with respect to their catalytic activity. As indicated by the EPMA-EDS analysis (Figure 16c), the Ir/O ratios depend on the calcination temperature. To study the chemical composition of the mesoporous IrO_x calcination series in detail, XPS measurements were carried out in the O1s (Figure 19a), Ir4f (Figure 19b) and the valence band region (Figure 19c) which were gratefully performed by Juan J. Velasco-Vélez and co-workers at the BESSY II (Berlin) ISISS beamline.

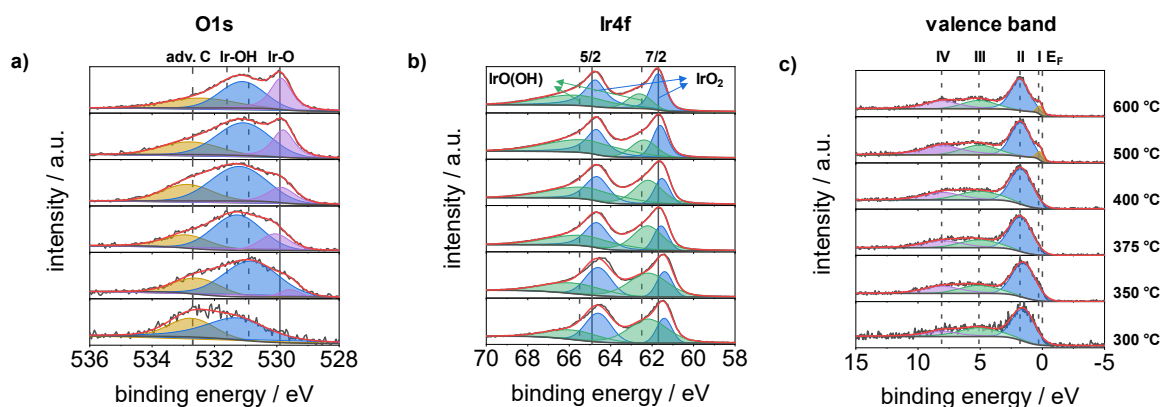


Figure 19: X-ray photoelectron spectra of the IrO_x calcination series. a) presents the spectra of each film in the O1s region, b) the spectra in the Ir4f region, and c) the spectra in the valence band region. Deconvoluted spectra were fitted with sum Gaussian–Lorentzian functions after a Shirley background subtraction.

Photoelectron spectra normalized to their maximum intensity were fitted after a Shirley background subtraction using sum Gaussian–Lorentzian functions. The deconvoluted O1s spectra of the mesoporous IrO_x film calcined at 300 °C indicate two peaks at about 532.7 eV and 531.1 eV, which can be attributed to adventitious carbon (adv. C, yellow peak) and Ir-OH species (blue peak), respectively (Figure 19a).¹⁴⁶ Adventitious carbon is usually a thin layer of carbonaceous material normally found on the surface in air-exposed samples and consists of a variety of hydrocarbon species with single and double bonded oxygen functionalities.¹⁴⁷ A third peak at about 529.8 eV becomes visible from a calcination temperature of 350 °C and higher. This peak can be attributed to Ir-O species (violet peak).¹⁴⁶ The ratio of the relative areas of Ir-OH to Ir-O decreases at higher calcination temperatures from 13.4 (350 °C) to 1.3 (600 °C).

Deconvolution of the Ir4f spectra shows two peaks in the Ir4f_{7/2} region and two peaks in the Ir4f_{5/2} region for all spectra of the calcination series (Figure 19b). The peaks can be attributed to anhydrous iridium oxide species (IrO_2 , blue peaks) and hydrated iridium oxide species (IrO(OH) , green peaks).¹⁴⁸ The peaks show a slight shift to lower binding energies for the low-temperature calcined films (≤ 400 °C). The ratios of IrO(OH) to IrO_2 species of the Ir4f_{7/2} peaks decrease from 2.8 (300 °C) to 0.5 (600 °C), while the ratios of IrO(OH) to IrO_2 species of the Ir4f_{5/2} peaks remain relatively constant for all calcination temperatures. In general, a constant trend in the ratios of IrO(OH) to IrO_2 species (relative areas of both Ir4f_{7/2} and Ir4f_{5/2} peaks) can be observed for the low-temperature calcined films (≤ 400 °C), and a decreasing trend in the IrO(OH) to IrO_2 ratios with further increase of the calcination temperature.

The valence band area reveals three peaks at binding energies of about 8.1 eV, 5.1 eV and 1.7 eV, for catalyst films calcined between 300 °C and 400 °C. These peaks can each be assigned to metal-oxygen σ bands (IV, violet peak), metal-oxygen π bands (III, green peak) and the t_{2g} sub-level of the Ir 5d orbital (II, blue peak).^{149, 150} At 500 °C and 600 °C, a shoulder of the t_{2g} sub-level becomes visible at about 0.2 eV (I, yellow peak). This shoulder can be attributed to a spin-orbital couple (SOC) splitting effect, where the five electrons in the t_{2g} splits into four electrons occupied as $J_{eff} = 3/2$ sub-band and to one electron occupied as $J_{eff} = 1/2$ sub-band.^{30, 151, 152} The detailed fit results and the analysis of the C1s spectra can be found in the Appendix Chapter A3.

Investigation of electronic and electrical properties

For a better understanding of the activities of mesoporous IrO_x films in electrochemical catalysis it is also necessary to gain insights into the electronic and electrical structure of the catalysts. Therefore, the electronic and electrical properties are investigated using UV-VIS-NIR absorption spectroscopy and electrical conductivity measurements.

From UV-VIS-NIR absorption spectroscopic measurements it is possible to calculate the optical bandgap and transition energies using the Tauc relation (equation (8)). Energy values can be obtained by extrapolation of straight-line portions to zero absorption coefficient. Figure 20 depicts a) exemplarily the UV-VIS-NIR absorption spectra for IrO_x calcined at 375 °C on a quartz substrate, b) the extrapolation of direct allowed transitions of the 375 °C calcined film and c) the obtained transition energy values of the calcination series.

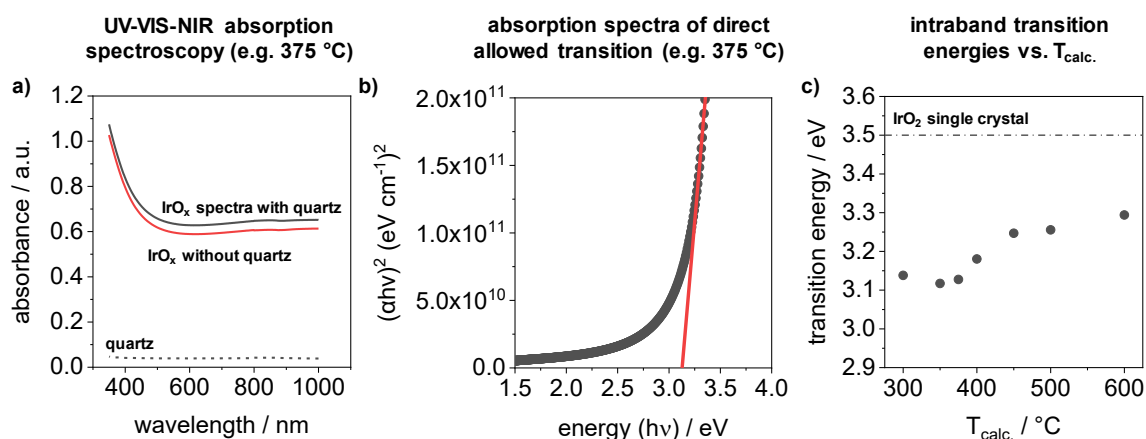


Figure 20: UV-VIS-NIR absorption spectroscopy and calculation of transition energies using the Tauc relation. a) exemplary measurements in the range of 350 nm and 1000 nm of an IrO_x film calcined at 375 °C in air on a quartz substrate, b) Tauc relation and extrapolation of direct allowed transitions for the IrO_x film, and c) transition energies of the calcination series as a function of the calcination temperature.

UV-VIS-NIR absorption spectra show a decrease of the absorbance from 400 nm to 500 nm and a slight increase at higher wavelengths (Figure 20a). To evaluate the transition energy, the absorption spectra were corrected by the quartz substrate and the absorption coefficient was calculated according to the Lambert–Beer law (equation (6)). When calculating the absorption coefficient, it was assumed that the layer thickness is twice as thick due to the coating on both sides during the dip-coating process. For the film thickness, the values of the cross-sectional SEM images were used. Figure 20b shows the absorption spectra for direct allowed transitions ($m = 1/2$) of the film calcined at 375 °C and the extrapolation of absorption coefficient. The energy value amounts to 3.13 eV. The transition energy values of the calcination series range from 3.12 eV to 3.29 eV (Figure 20c). The values indicate a slight decrease from 300 °C to 350 °C and an increase at higher temperatures. This behavior can be related to the respective increase in crystallinity and a change of oxygen species.

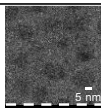
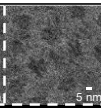
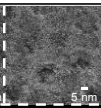
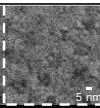
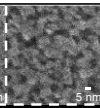
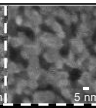
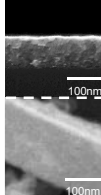
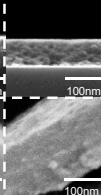
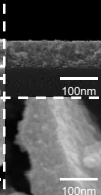
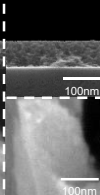
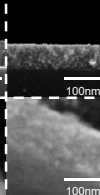
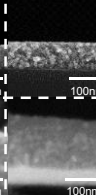
The metallic Ir 5d levels contribute to the IrO_x conduction band. Due to the octahedral crystal field, the Ir 5d levels split into e_g and t_{2g} sub-levels.^{153, 154} The values obtained from the extrapolation of the absorption coefficient can therefore be interpreted as intraband transition energies between the Ir 5d t_{2g} and e_g bands, which are comparable to values reported in literature.^{153, 155} Silva *et al.* reported a value of 3.2 eV for the separation between the t_{2g} and e_g bands for a low crystalline, anodically formed iridium oxide film and attributed the low value compared to a single crystal (3.5 eV) to the amorphous nature of the film.¹⁵⁵ The non-well-defined band edges present disorder-induced tails, which extend into the bandgap and could be responsible for the lower values.¹⁵⁶

Finally, conductivity measurements with a 4-point pin probe head of the films deposited on quartz reveal highly conductive iridium oxide films. The determined values of the layers ranges from $0.3 \cdot 10^{-3}$ Ohm cm to $1.9 \cdot 10^{-3}$ Ohm cm and are summarized in Table 1.

In summary, the analysis of the mesoporous IrO_x films calcined between 300 °C and 600 °C with different electron-based and X-ray based methods as well as conductivity measurements and absorption spectroscopy provide very well reproducible and comparable results as described in the literature.^{26, 64} Low-temperature calcined films (≤ 400 °C) exhibit a well-ordered mesopore structure with a low crystallinity and a more pronounced hydrated oxygen surface. In contrast, high-temperature calcined films (> 400 °C) show a less ordered mesopore structure with larger crystallites due to sintering effects as well as a more pronounced anhydrous oxygen surface.

4. Ex-situ characterization of mesoporous templated iridium oxide (IrO_x) films

Table 1: Summary of the deduced material properties of the mesoporous IrO_x films calcined between 300 °C and 600 °C from electron microscopy, EPMA-EDS / StrataGem, XRD, XRR, UV-VIS-NIR absorption spectroscopy and conductivity measurements.

Method	Property	T _{calc.}						
		300 °C	350 °C	375 °C	400 °C	500 °C	600 °C	
material properties								
SEM	top-view	Si-substrate						
	cross-section	Ti-substrate						
	mesopore size / nm		15.1 ± 3.1	14.7 ± 2.6	16.0 ± 2.8	14.0 ± 3.0	-	-
	mesopore distance / nm		24.0	24.0	24.0	24.0	23.0	23.0
	thickness / nm	Si-substrate	80.4 ± 1.4	67.9 ± 1.2	76.0 ± 2.3	74.4 ± 1.8	71.1 ± 2.2	77.8 ± 1.5
		Ti-substrate	150.9 ± 11.1	144.7 ± 9.9	139.1 ± 10.2	121.8 ± 8.6	132.6 ± 13.3	127.3 ± 15.8
	atom ratio / -		IrO _{2.6}	IrO _{2.4}	IrO _{2.3}	IrO _{2.3}	IrO _{1.9}	IrO _{2.1}
	mass-deposition / μg cm ⁻²		30.5	25.5	33.8	36.9	35.0	39.7
	density / g cm ⁻³		3.8	3.8	4.4	5.0	4.9	5.1
	porosity ^a / %		67.5	67.8	61.8	57.5	57.8	56.3
XRD	crystallite size / nm	1.2	1.2	1.0	1.5	5.5	7.1	
XRR	thickness / nm	80.9	65.5	77.7	72.5	68.2	-	
	density / g cm ⁻³	4.6	5.4	6.8	7.6	8.5	-	
	porosity ^a / %	60.6	53.6	41.9	34.8	27.1	-	
UV-VIS-NIR absorption spectroscopy	intraband transition energy / eV	3.14	3.12	3.13	3.18	3.26	3.29	
conductivity measurement	resistivity ^b · 10 ⁻³ / Ohm cm	1.87	1.18	1.35	0.94	0.64	0.33	

a reference density 11.66 g cm⁻³ (IrO₂)

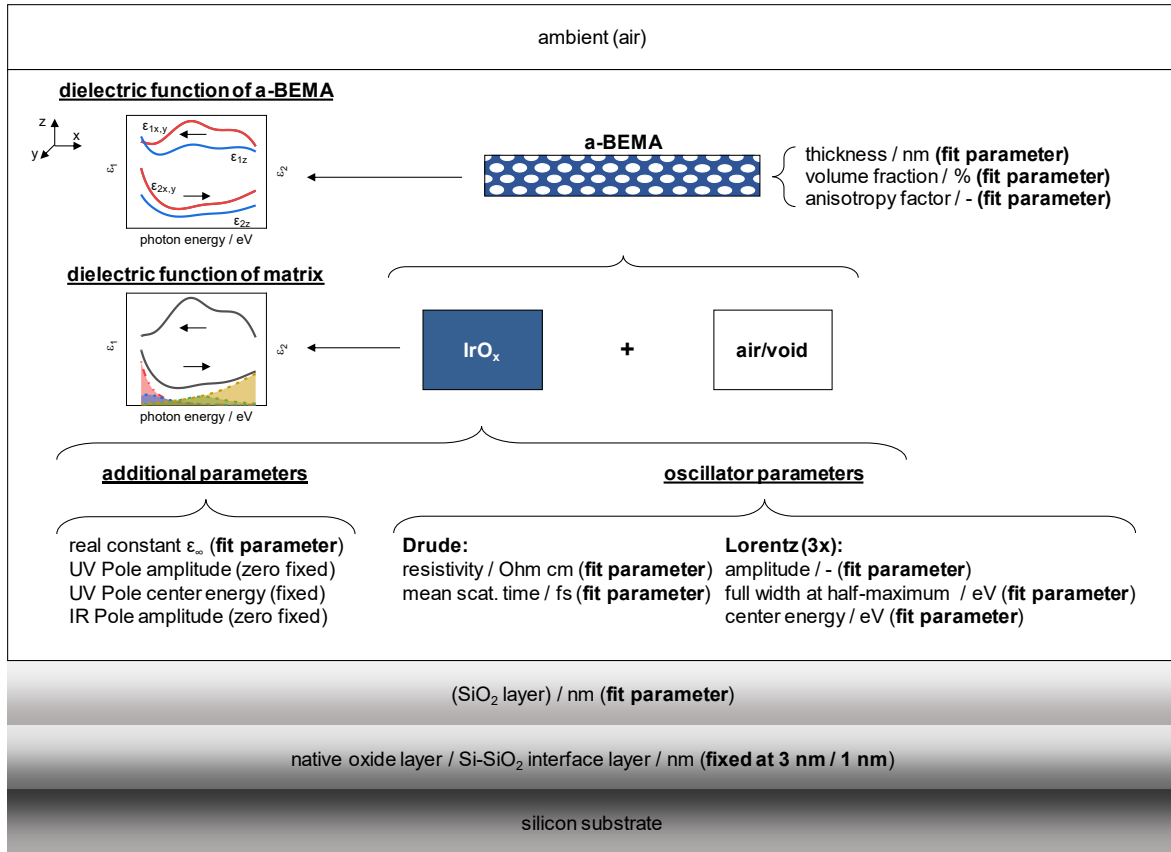
b Sheet conductivity measurements with a 4-point pin probe head

4.2 Ellipsometric investigations and modeling

In this Chapter, the analyses of mesoporous IrO_x films using spectroscopic ellipsometry are presented. In the first part the model evaluation by using the interference enhancement technique, which is described in Chapter 2.3 in detail, coupled with a multi-sample-analysis (MSA) is discussed. This approach includes the validation of the model by cross-sectional SEM imaging and ellipsometric porosimetry (EP) measurements. The following part addresses the analysis of the mesoporous IrO_x calcination series by using the previously optimized model to deduce relevant parameters such as film thickness, porosity, resistivity, electron concentration and mobility as well as intraband transition energies. Furthermore, valence electron energy loss spectra, calculated from the dielectric functions are presented.

Model evaluation via interference enhancement in a multi-sample-analysis

For the analysis with interference enhancement of mesoporous iridium oxide films in an MSA, Si substrates with and without thermal SiO_2 layers were used (see Chapter 3.1 for Si substrate specifications). To reduce the correlation between the optical constants and the material properties with interference enhancement, the films were measured at angles of incidence (AOI) of 65° , 70° , and 75° . The spectra of Ψ and Δ were then modeled using an anisotropic Bruggeman effective medium approximation (a-BEMA; equation (34)), which is described in detail in Chapter 2.3. For modeling of the dielectric function of the IrO_x material (matrix), a combination of a Drude type (equation (38)) and three Lorentz type (equation (40)) absorption bands are used. Scheme 3 illustrates the model evaluation of the a-BEMA, the used oscillators, and substrates with all fit parameters for the interference enhancement measurements.



Scheme 3: Illustration of the developed model for spectroscopic ellipsometry analysis using Si as substrate with a native oxide layer or a thermal SiO₂ layer and the mesoporous IrO_x layer. The mesoporous IrO_x layer consists of an anisotropic Bruggeman effective medium approximation (a-BEMA), which include the IrO_x material (matrix) and the air/void within the pores. The IrO_x matrix consists on a combination of a Drude type and three Lorentz type oscillators.

For the fit process, Si substrates with a native oxide layer and Si substrates with a thermal SiO₂ layer as well as the interface layer between the Si and SiO₂ were modeled with literature data.¹⁵⁷⁻¹⁵⁹ For Si substrates without a thermal SiO₂ layer, a uniform native oxide layer was assumed since the Si substrates used were treated in a muffle furnace at 600 °C in flowing air for 2h before dip-coating. An SE-mapping measurement of such a treated Si substrate resulted a native oxide layer between 2.8 nm and 3.0 nm, therefore a uniform native oxide layer of 3.0 nm was assumed for all analyses with this type of Si substrate to reduce the number of degrees of freedom (see Appendix A4).

In the course of fitting parameterized models for the material component (IrO_x matrix) of the a-BEMA layer to the measured Ψ and Δ spectra, the complex dielectric function is obtained as a result. Due to the Kramers-Kronig relationship, the number of degrees of freedom in this process are reduced as described in Chapter 2.3. Therefore, the shape of the dielectric function is determined by modeling the imaginary part of the dielectric function using the summation of the Drude and Lorentz type oscillators with the free parameters shown in Scheme 3. The real part of the dielectric function is then calculated using only the additional parameters shown in Scheme 3. For the modeling of the IrO_x layers, only the real constant (ϵ_∞), which is added as an offset to the real part of the dielectric function, was used as a free parameter. Furthermore, the thickness of the a-BEMA layer was adjusted, as well as the volume fraction (porosity) using the dielectric function of

air/void ($\varepsilon_1/n = 1$; $\varepsilon_2/k = 0$) and the anisotropy factor of the voids in the z-direction (perpendicular to the substrate). The anisotropy factor can take values between 0 and 1, where 0 corresponds to a cylindrical geometry, 0.333 to a spherical geometry, and 1 to a slit geometry.

Figure 21 presents the fit results of the Ψ (Figure 21a-c) and Δ (Figure 21d-f) spectra of the IrO_x films on the different Si substrates calcined at 375 °C in air. The spectra were measured at angles of incidence (AOI) of 65°, 70° and 75° and evaluated in an MSA.

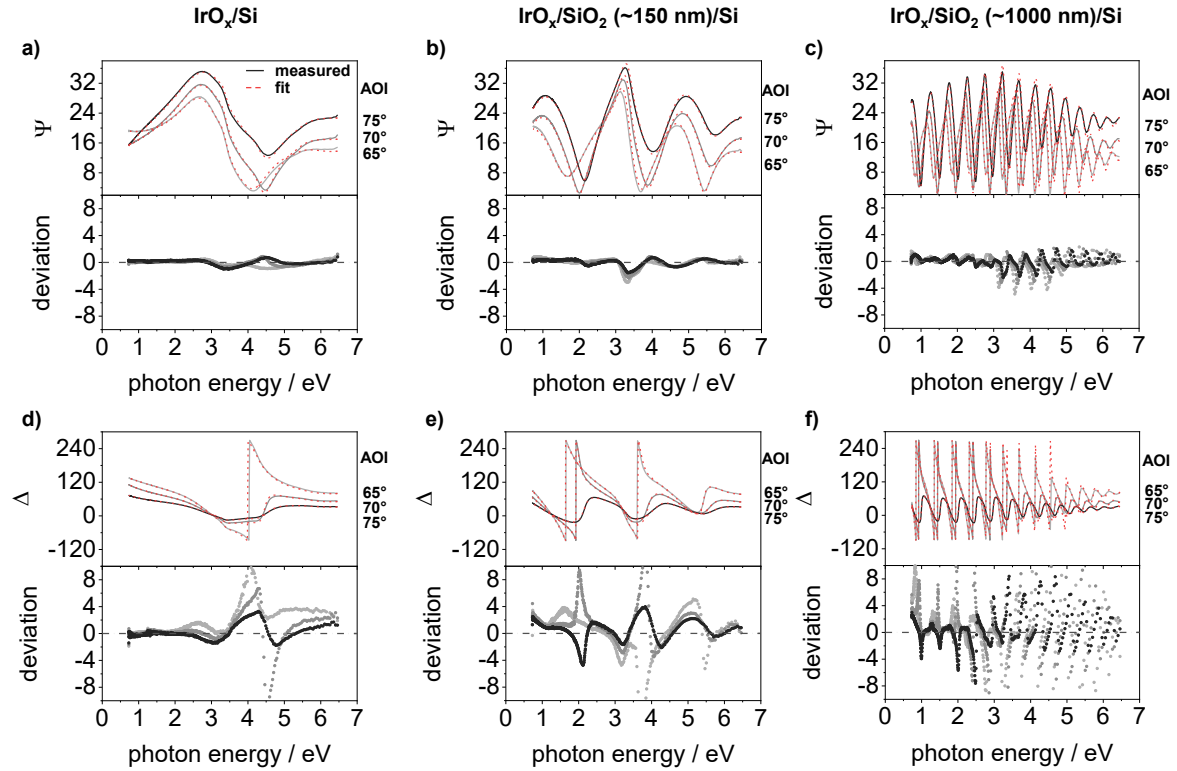


Figure 21: Spectroscopic ellipsometry analysis of the mesoporous IrO_x films calcined at 375 °C in air on Si substrates with and without a thermal SiO_2 layer. a) Ψ and d) Δ spectra of IrO_x on a Si substrate, b) Ψ and e) Δ spectra IrO_x on a Si substrate with a thermal SiO_2 layer (~150 nm) and c) Ψ and e) Δ spectra IrO_x on a Si substrate with a thermal SiO_2 layer of about 1000 nm. The RMSD of the multi-sample fit analysis amounts to 15.342.

The fit curves (dashed red lines) show good agreement with the measured spectra (grey to black lines) for the Ψ (Figure 21a-c) and Δ spectra (Figure 21d-f). In all three cases, the Ψ spectra show small deviations between the fits and measured data and the Δ spectra show slightly larger deviations between fit and measured data for the incident angles used. The RMSD value of the MSA amounts to 15.342. As a result of the interference enhancement studies, RMSD values for single sample analysis of < 10 and in the case of multi-sample analysis of < 20 have been found to be sufficiently accurate for the analyses of IrO_x coatings on various substrates and are not reported further. In the case of modeling that exhibits higher RMSD values, these are reported separately in the respective Chapters.

The thicknesses derived from the fit results for the IrO_x layer amount to 74.2 nm ± 2.1 nm, 74.4 nm ± 2.6 nm and 74.4 nm ± 2.6 nm for the IrO_x/Si, IrO_x/SiO₂ (150 nm)/Si and IrO_x/SiO₂ (1000 nm)/Si samples, respectively. The SiO₂ layer thicknesses are 150.8 nm ± 2.6 nm and 1007.1 nm ± 5.8 nm. The derived porosity values amount to 46.4% ± 1.2%, 43.1% ± 1.2% and 42.9% ± 1.2% for the IrO_x/Si, IrO_x/SiO₂ (150 nm)/Si and IrO_x/SiO₂ (1000 nm)/Si samples, respectively. The anisotropy factor ranges from 0.385 to 0.489, indicating a pore geometry between spherical and slit-shaped. This elliptical pore shape corresponds with SEM cross-section images, where an elliptical shape is also visible. However, since the anisotropy factor does not provide any further information about the pores, such as pore size, this factor will not be discussed further.

In addition, the real and imaginary part of the dielectric function as well as the refractive index and extinction coefficient are obtained from modeling the Ψ and Δ spectra. Figure 22 displays a) the dielectric function and b) the optical constants of the IrO_x material (matrix) calcined at 375 °C (see Appendix A5 for the dielectric function/optical constants of the a-BEMA layer).

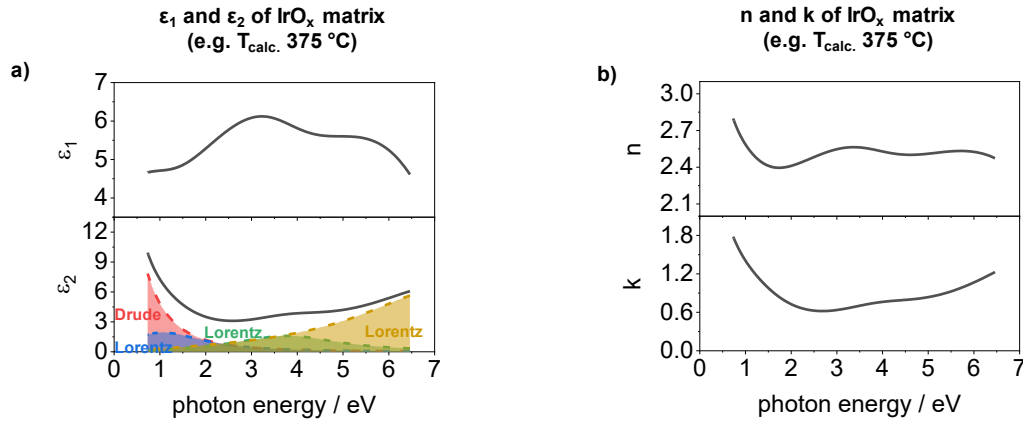


Figure 22: Dielectric function and optical constants of the IrO_x material calcined at 375 °C in air. a) real (ϵ_1) and imaginary part (ϵ_2) of the dielectric function, which modeled with a combination of a Drude type and three Lorentz type oscillators. b) refractive index (n) and extinction coefficient (k) of the IrO_x matrix.

The dielectric function obtained from the model shows for the imaginary part (ϵ_2) in the region below 2.0 eV a typical edge of conductive materials towards lower photon energies, which can be modeled by a Drude function (Figure 22a). Additionally, a weak and broad absorption band appears near 1.0 eV, which can be modeled by a Lorentz function. Above 2.0 eV, two absorptions features are visible at about 4.0 eV and 7.7 eV, which can also be modeled by two Lorentz oscillators. The real part (ϵ_1) of the dielectric function indicates three features at about 1 eV, 3.1 eV and 5.7 eV.

The optical constants n and k are calculated from ϵ_1 and ϵ_2 according to equations (21) and (22), respectively. In the spectrum of n , an inflection point near 1.8 eV and a steep increase to lower photon energies are visible. In addition, two features are present in the spectrum at about 3.4 eV and 5.7 eV. The spectrum of k has a similar shape as ϵ_2 and also shows an increase below 2.0 eV toward lower photon energies and two features at higher photon energies (Figure 22b).

The iridium oxide valence band consists of oxygen p-levels, while metallic Ir 5d levels contribute to the conduction band. These Ir 5d levels further split into e_g and t_{2g} sub-levels due to the octahedral crystal field. Goel *et al.* studied an IrO₂ single crystal by reflectivity measurements in a range of 0.5 eV to 9.5 eV and assigned the features in ε_2 below 2.0 eV to conduction band and intraband electronic transitions within the t_{2g} d-band complex.¹⁵³ Above 3.0 eV, Goel *et al.* assigned three features in ε_2 at 3.7 eV, 5.5 eV and 7.7 eV to p-d interband transitions.

The observed dielectric function shows a good agreement with the work of Goel *et al.* The features below 2.0 eV can be interpreted with excitations of the conduction band and intraband transitions from filled to empty states of the t_{2g} sub-level. The two absorption features at around 4.0 eV and 7.7 eV correlate with transitions from the p-orbitals of oxygen to empty states of the d-bands of iridium.¹⁵³ The absence of the third feature at 5.5 eV compared to a single crystal is probably related to the much lower crystallinity. This is in good agreement with reflectometry studies on sputtered low crystalline IrO₂ films deposited on Al₂O₃ substrates, where also only two features at about 4.0 eV to 7.0 eV are observed.¹⁶⁰

For the spectra of the optical constants, n differs from that of an IrO₂ single crystal in the range below 2 eV.^{153, 161} This means that for the 375 °C calcined IrO_x film, n increases toward lower photon energies from the inflection point at about 1.8 eV. In contrast, for the single crystal, there is no inflection point in this region and n continues to decrease toward lower photon energies. The spectrum of k of the 375 °C calcined IrO_x film, however, is in good agreement with that of the single crystal. The difference in n can be related to the low crystallinity and the imperfect rutile structure of the studied film compared to the single crystal.

To verify the deduced results (thickness and porosity) of the model evaluation with interference enhancement, the obtained layer thicknesses can be compared e.g., with those from the SEM images (see A6 for cross-section SEM images). However, porosity is not as easily accessible, and typical physisorption measurements such as gas adsorption (e.g., BET physisorption) or mercury intrusion porosimetry are designed for powder materials and/or require a relatively large amount of material. Ellipsometric porosimetry (EP) offers the possibility to determine the porosity of thin films by measuring an adsorption/desorption isotherm from the variations in the refractive index induced by the change in the partial pressure of a solvent over a film.^{117, 118}

The dependence of the partial pressure (p/p_0) at which condensation in pores occurs on the meniscus is given by the Kelvin equation:

$$\ln\left(\frac{p}{p_0}\right) = -\frac{f_s \gamma_s V_m \cos \theta_c}{r_K R T} \quad (52)$$

where f_s is a shape factor (equal to 1 for slit-shaped pores and equal to 2 for cylindrical pores), γ_s and V_m are respectively the surface tension and molar volume of the liquid, θ_c is the contact angle of the liquid on a non-porous surface of the matrix material, R the molar gas constant and T the temperature in K. r_K is the Kelvin radius, which is related to the pore radius (r_{pore}) by:

$$r_{pore} = r_K + d_a \quad (53)$$

with d_a as thickness of the layer absorbed on the pore walls.

In order to determine the porosity of the layers on the different substrates, the films were examined by EP using water as solvent and the change of the relative humidity. The same model as described before was used for EP measurements, where a volume fraction for air and water was added to the anisotropic Bruggeman effective medium approximation (a-BEMA), which describe the adsorption/desorption of water within the pores. Except for the volume fraction of the mesopores (porosity), the volume fractions of air and water within the pores (filling factor) and the anisotropy factor (shape of the mesopores), all parameters were assumed to be constant. A detailed analysis of the independence of the thickness due to swelling and capillary contraction is given in the Appendix Chapter A7. Figure 23 displays the change of the filling factor of the pores with water in dependence on the relative humidity.

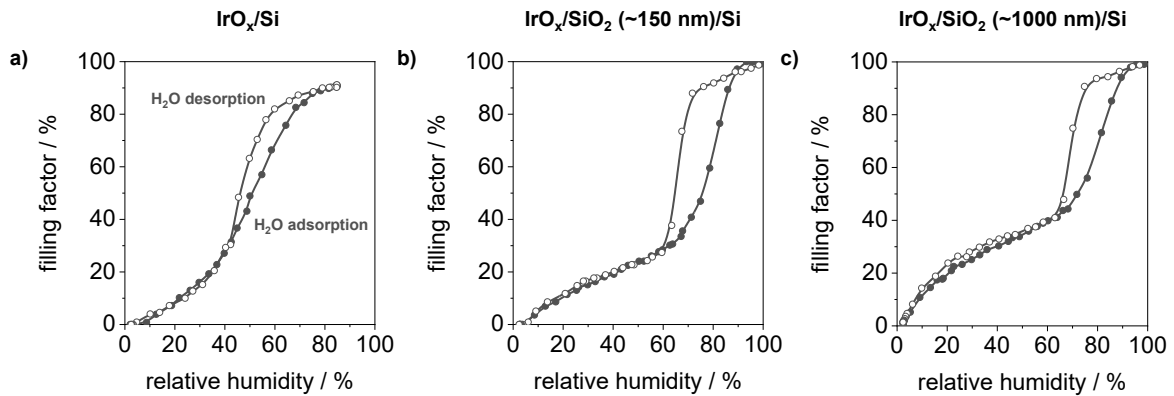


Figure 23: Sorption isotherms of mesoporous IrO_x films (375 °C) on Si substrates with and without thermal SiO₂ layer deduced from ellipsometric porosimetry analysis. Filling factor as a function of the applied relative humidity of a) IrO_x on a Si substrate, b) IrO_x on a Si substrate with a thermal SiO₂ layer (~150 nm), and c) IrO_x on a Si substrate with a thermal SiO₂ layer of about 1000 nm.

The adsorption cycle (black circles with line) for the IrO_x film on Si (Figure 23a) indicates a strong increase of the filling factor for the first relative humidity (r.H.) values (0% – 20%). This steep initial region is due to the monolayer coverage of water and the inflection point indicates a complete monolayer coverage.^{62, 162} This steep initial range also indicates the presence of micropores. The filling factor increases slightly with further increase of the relative humidity (mostly linear), which is due to a multilayer adsorption of water within the pores.^{62, 162} From a relative humidity of about 40%, a second steep increase of the filling factor can be observed, which is characteristic for the mesoporous filling of water by capillary condensation.^{62, 118, 162} The adsorption cycle reaches a plateau at about 80%, indicating completely filled pores.

The desorption cycle (white circles with line) shows a hysteresis loop of the filling factor (Figure 23a), indicating the presence of mesopores within the film. The shape of the hysteresis loop can provide information about the shape of the mesopores, which in this case are either cylindrical or bottle neck shaped.^{62, 162-164}

The IrO_x films on the Si substrates with thermal SiO_2 layers (Figure 23b, c) show the same adsorption/desorption behavior with a more pronounced steep initial region and hysteresis loop. The difference between the observed hysteresis may be due to the accessibility of the pores, which decreases with less accessible pores.^{62, 162} However, porosity analysis using EP does not differentiate between open and closed pores. Since the incident light penetrates the entire layer (depending on the extinction coefficient k and layer thickness), the difference between the refractive indices (water/air) can be analyzed to determine the porosity.

In order to compare the results obtained from the evaluated SE model, the thicknesses and porosities from the SEM and EP measurements serve as reference values and plotted as a function of the values obtained from SE modeling (Figure 24).

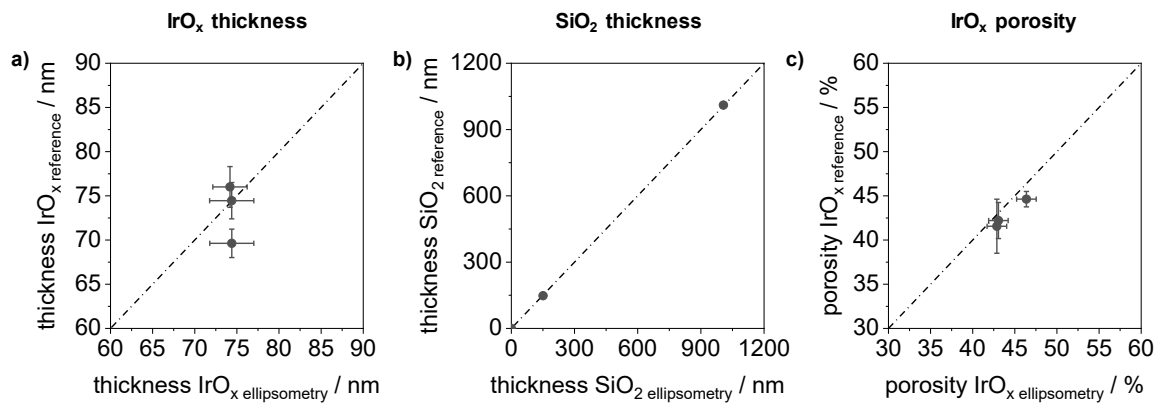


Figure 24: Validation of derived ellipsometric results with complementary methods. Parity plots show the comparison of a) film thickness, b) SiO_2 layer thickness, and c) IrO_x porosity. Thickness references were obtained from cross-sectional SEM images and porosity references from EP measurements.

SE modeling with interference enhancement in an MSA using different AOIs shows a very good agreement of the derived thickness and porosity values. The IrO_x thicknesses agrees within the deviation of the method used (Figure 24a). SiO₂ layer thicknesses are in perfect agreement with cross-sectional SEM imaging (Figure 24b) and the porosity values agree well between the SE and the EP method (Figure 24c).

Analysis of the calcination series of the mesoporous IrO_x films

For the investigation of the variation of the calcination temperature, the previously optimized fit parameters were restricted, i.e., for the dielectric function of the matrix, the center energy of each Lorentz oscillator was fixed. The resistivity ρ_R and the mean scattering time τ of the Drude function as well as the amplitudes (amp) and full widths at half maximum (Γ) of the three Lorentz oscillators were used as free parameters for the dielectric function of the matrix. In addition, ϵ_∞ was also included as an adjustable parameter in the fits. The thickness of the a-BEMA as well as the fraction of pores and the anisotropic geometry factor were kept adjustable as layer properties not directly related to the dielectric function of the matrix. The influence of the calcination temperature on the dielectric functions (a) and optical constants (b) is displayed in Figure 25.

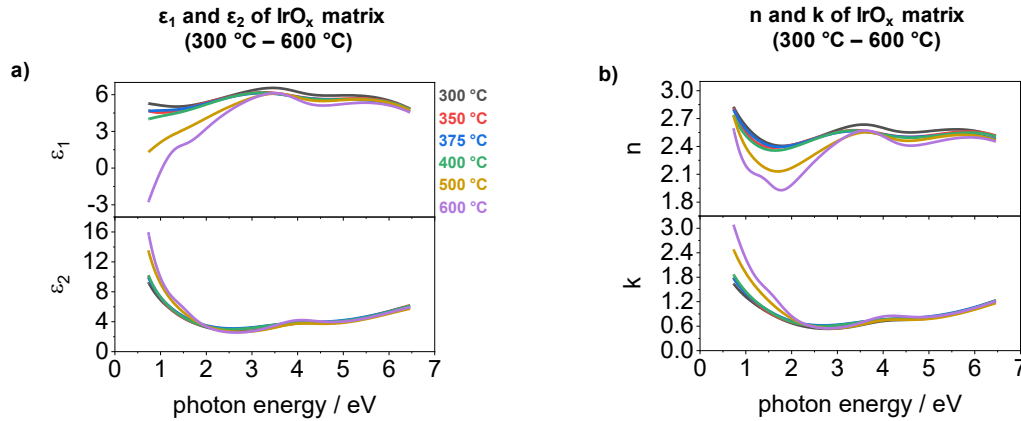


Figure 25: Dielectric function and optical constants of the IrO_x matrix material of the calcination series. a) change of the real (ϵ_1) and imaginary (ϵ_2) part of the dielectric function and b) change of the refractive index (n) and extinction coefficient (k) with varying of the calcination temperature.

As the calcination temperature changes, a systematic change in the dielectric function is observed, and thus a corresponding change in the properties of the IrO_x material (Figure 25a). This means that as the calcination temperature increases, the excitations of the conduction band increase, as can be seen in the lower photon energy region. The intensity of intraband transitions from filled to empty states of the t_{2g} sub-level near 1.0 eV, represented by the Lorentz oscillator, also increases with increasing calcination temperature. In addition, a change in the transitions from the oxygen p-orbitals to the empty d-bands of iridium is evident at about 4.0 eV. In the spectrum of ϵ_1 , a strong decrease at lower photon energies can be observed at higher calcination temperatures (≥ 500 °C). For the 600 °C calcined IrO_x film, for instance, ϵ_1 crosses zero near 1.0 eV, which agrees with data from an IrO₂ single crystal where ϵ_1 becomes zero at about 2.0 eV.¹⁵³

A similar behavior to the dielectric functions is observed for the spectra of n and k (Figure 25b). With increasing calcination temperatures, a decrease in n is observed in the range between 1.0 eV and 3.0 eV and changes in the features at 3.4 eV and 5.7 eV. The spectra of k are comparable to the spectra of ε_2 and show almost the same behavior, i.e., k changes mainly in the lower photon energy range and increases with increasing calcination temperature.

In general, the modeled spectra of the mesoporous iridium oxide films and the obtained dielectric functions and optical constants are consistent with reported data on an IrO₂ single crystal as well as crystalline sputtered iridium oxide.^{153, 160, 161} In this regard, the higher the calcination temperature, the more the dielectric function and optical constants of the IrO_x matrix material resemble those of crystalline IrO₂.

Modeling of SE spectra recorded for differently calcined mesoporous IrO_x films provides access to numerous material properties. Mesoporous IrO_x films were analyzed on Si and Ti substrates, where the Si substrates and the native oxide layer (3 nm) were modeled with literature data.¹⁵⁷⁻¹⁵⁹ The Ti substrates were parameterized by a Ti substrate layer and an overlying oxide layer (TiO_x). The Ti layer was modeled using a combination of one Drude-type and three Lorentz-type absorption bands, and the overlying TiO_x layer was modeled using a single Tauc-Lorentz oscillator. Each Ti substrate was analyzed in terms of the TiO_x thickness prior to dip-coating. For modeling of the calcined mesoporous IrO_x films on the Ti substrates, the TiO_x layer thickness served as another free parameter (see A8 for the influence of the calcination temperature on the oxide layer).

Figure 26 displays a) film thickness, b) porosity, c) resistivity, d) electron concentration e) electron mobility as well as f) transition energies for the Ir 5d t_{2g} and e_g sub-level separation as a function of the applied calcination temperature for films deposited on Si and Ti substrates.

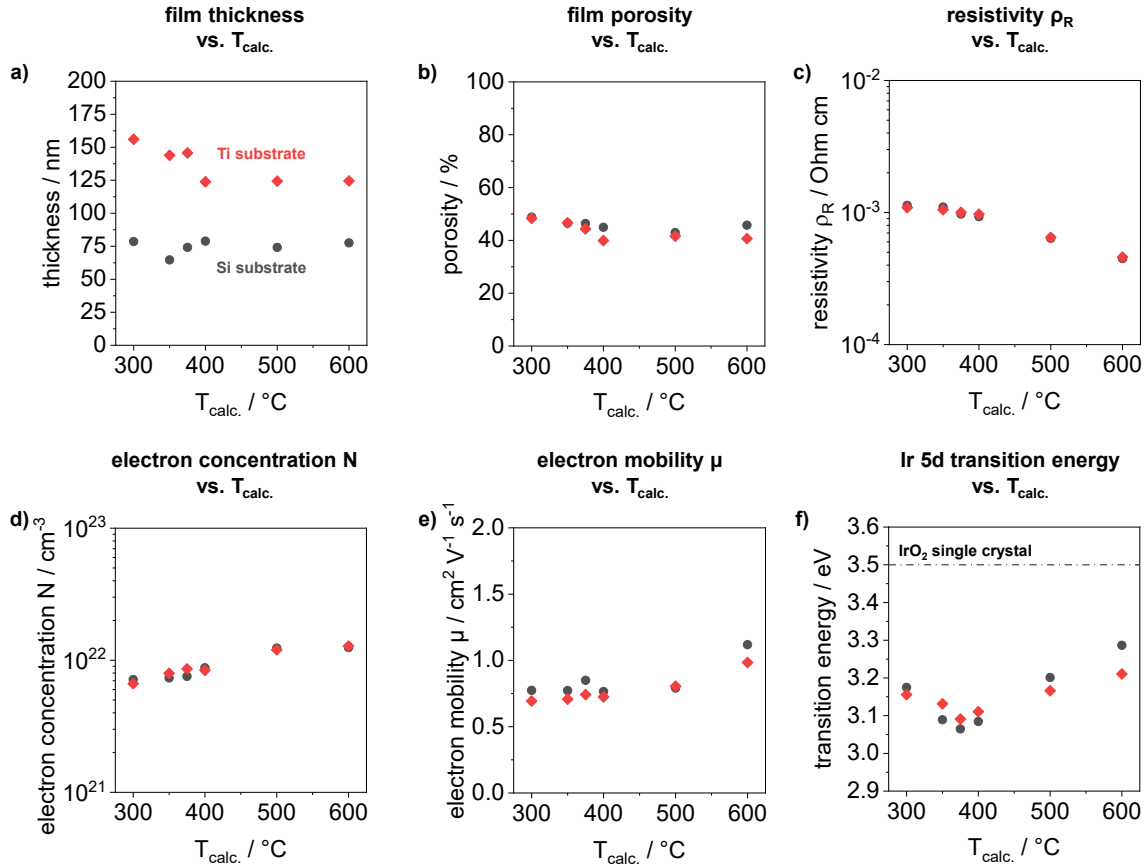


Figure 26: Deduced properties of the iridium oxide material from spectroscopic ellipsometry as a function of the calcination temperature. a) film thickness, b) porosity, c) resistivity, d) electron concentration, e) the electron mobility and f) transition energies depending on the applied calcination temperature.

The film thicknesses obtained from SE modeling (Figure 26a) range from 78.9 nm to 64.7 nm for films deposited on Si substrates and from 156.0 nm to 124.3 nm for films deposited on Ti substrates. The films on the Si substrates show a decrease in film thickness from 300 °C to 350 °C, an increase up to 400 °C and a slight decrease towards higher temperatures, while layers on Ti substrates indicate an overall decrease with increasing temperatures. In general, however, the films on both substrates show a decreasing trend in layer thickness with increasing calcination temperature. Differences in film thickness can be attributed to the surface properties of the substrates and to the different interactions of the dip-coating solution with the substrates. Studies of similarly prepared porous oxide layers show a comparable behavior of the layer thickness during the calcination process.^{26, 64, 133, 134}

A decreasing trend can also be observed for porosity values of the films on both substrates with increasing temperatures (Figure 26b). Porosities range from 48.8% to 43.0% and from 48.3% to 39.9% for the films on Si and Ti respectively. This trend corresponds with previous studies on similarly prepared porous oxide films.^{26, 64, 133, 134}

Due to free electrons iridium oxide shows a similar behavior as a metal and is therefore a highly conductive material. Derived values from the Drude model indicate decreasing resistivities (Figure 26c), which range between $1.10 \cdot 10^{-3} \Omega \text{ cm}$ and $0.46 \cdot 10^{-3} \Omega \text{ cm}$ and are very similar on both substrates (Si and Ti). In contrast the derived values are about 10 to 20 times higher than indicated for IrO_2 in literature ($\rho_R = 0.05 \cdot 10^{-3} \Omega \text{ cm}$).¹⁶⁵

The electron concentration N (Figure 26d) and the electron mobility μ (Figure 26e) can be calculated from the fit parameters resistivity ρ_R and the mean scattering time τ according to equation (38) and (39). The values for the mean scattering time τ are presented in the Appendix Chapter A9. For the calculations, it was assumed that the effective mass m^* of the electrons is equal to $9.11 \cdot 10^{-31} \text{ kg}$. Electron concentration remains roughly constant up to 375°C , i.e., in the low crystallinity range, and increases slightly above 400°C as the IrO_x crystallinity progressively increases for films on Si substrates. A similar behavior is also observed for the films on the Ti substrates (Figure 26d). These observations agree with Density Functional Theory (DFT) calculations in iridium oxide unit cells.¹⁶⁶ These DFT calculations indicate that decreasing lattice parameters lead to a higher electron concentration.¹⁶⁶ The electron mobility (Figure 26e) shows in contrast a roughly constant behavior for both substrates until 400°C and an increase at calcination temperatures of 500°C or 600°C , i.e. when pronounced crystallite growth by sintering has already occurred.

Figure 26f displays transition energy values for the Ir 5d t_{2g} and e_g sub-level separation for direct allowed transitions. For the energy estimation by the Tauc relation (equation (8)), the absorption coefficient α can be calculated from the extinction coefficient k according to equation (7). Values for the transition energy between the t_{2g} and e_g sub-levels of the Ir 5d band range from approximately 3.06 eV to 3.29 eV and show a minimum of the transition energy at a calcination temperature of 375°C for both substrates. The increase of the transition energy at higher calcination temperatures could be related to the respective increase in crystallinity and a change of oxygen species. These results show a very similar behavior to those values obtained from UV-VIS-NIR absorption spectroscopy (Figure 20c).

The dielectric function can be converted into electron energy loss spectra (VEEL) according to equations (2) and (3). This calculation provides further information about the electronic structure of the materials. Figure 27 displays calculated bulk (a) and surface (b) VEEL spectra in the low-loss region of the calcination series on Si substrates. The center energies of the identified peaks as a function of calcination temperature derived from the spectra are shown in Figure 27c. VEEL spectra and center energies of the peaks as a function of calcination temperature for IrO_x films on Ti substrates are given in Appendix A10.

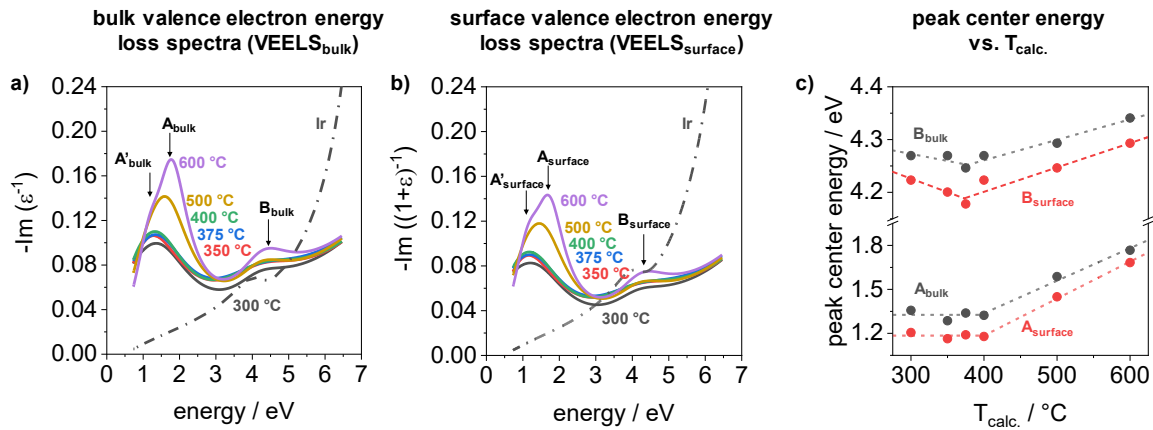


Figure 27: Valence electron energy loss spectra (VEELS) analysis and shifts of peak positions of mesoporous iridium oxide films calcined between 300 °C and 600 °C and of a polished iridium sheet for comparison. a) calculated bulk VEELS and b) surface VEELS from the dielectric functions. c) peak maximum center energy of the indicated peaks from the bulk and surface VEELS as a function of calcination temperature ($T_{\text{calc.}}$). Linear lines in the graph of the peak center energy as a function of $T_{\text{calc.}}$ have been added for orientation of the trends.

VEEL spectra of the bulk and surface energy loss function (ELF) indicate two peaks, labeled respectively as A_{bulk} and B_{bulk} or A_{surface} and B_{surface} (Figure 27a, b). The A_{bulk} peak maximum is located at an energy of about 1.3 eV for samples calcined between 300 °C and 400 °C and shifts to higher energies (up to 1.8 eV) for samples calcined at 500 °C and 600 °C (Figure 27a). Additionally, the peak intensity increases with increasing temperature above 400 °C. Moreover, at higher temperatures (above 400 °C) a shoulder of the A_{bulk} peak, labeled as A'_{bulk} , becomes visible at lower energies. The B_{bulk} peak maximum is located at about 4.3 eV and shifts slightly in energy as well as increase a little in intensity. A similar behavior can be observed for the surface VEEL spectra of the IrO_x calcination series, whereas the identified peaks are shifted in the peak maximum energy of about 0.1 eV to lower energies (Figure 27b).

For comparison, a polished iridium sheet was measured under the same conditions and parametrized with a model containing one Drude function and two Lorentz type oscillators. The calculated bulk VEEL as well as the surface VEEL spectra indicate an increase in intensity up to 4.0 eV and a steep increase at higher energies. Furthermore, only one peak can be identified at about 3.8 eV in both spectra, which can attribute to transitions between occupied and empty 5d bands.¹⁶⁰

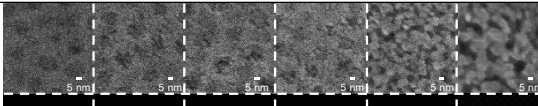
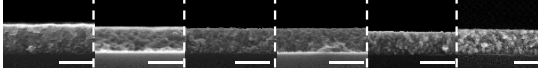
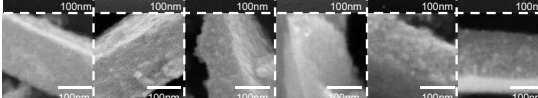
According to literature, the peaks in the IrO_x material spectra can be associated with interband transitions, while surface and volume plasmon excitations of metal oxides occur in a different energy range of about 10-20 eV.¹⁶⁷⁻¹⁷¹ The A labeled peaks of IrO_x can be interpreted as p-d interband transitions between the partially filled t_{2g} sub-band of the d-band of iridium and the p-band of the oxygen. The density of states (DOS) spectra of a single crystal indicate an interband transition between the oxygen p-bands and the iridium d-bands of about 1.5 eV to 2.0 eV,^{153, 154} which is consistent with the observed A peak center energies. Furthermore, the absence of a peak in the Ir spectra in this energy region is also consistent, due to the absence of oxygen atoms and the associated interband transitions. According to the results of the XPS valence band spectra

(Figure 19c), the indicated A'_{bulk} peak, which is visible at higher calcination temperatures, can be interpreted as SOC effect of the Ir 5d t_{2g} band.^{30, 151, 152} The B peaks at about 4.3 eV are assigned to transition energies between the oxygen p-bands and unoccupied Ir 5d t_{2g} bands, whereas transitions from O 2p bands to Ir 5d e_g bands occurs at energies of about 6.3 eV and 7.2 eV.¹⁶⁰

Figure 27c displays the influence of the calcination temperature on the shift of the observed peaks in detail. The A peaks indicate constant energy values up to 400 °C and an increase of the center energy at higher calcination temperatures for both bulk and surface spectra. In contrast, the B labeled peaks show a slight decrease in the center energy from 300 °C to 375 °C and an increase at higher temperatures. A similar behavior can also be observed for the energy values for direct allowed transitions between the Ir 5d t_{2g} and e_g band. However, the energies are about 1.0 eV to 1.2 eV higher. Probably, the transition energies between the Ir 5d t_{2g} and the e_g band are influenced by the interactions of the O 2p and the unoccupied Ir 5d t_{2g} bands.

The analysis and modeling of mesoporous IrO_x films by means of SE, calcined between 300 °C and 600 °C, provides information about material properties such as layer thickness, porosity as well as electrical properties (resistivity, electron mobility, etc.). SE also provides the access to the electronic structure of the materials which indicate a systematic change. The results of SE modeling are summarized in Table 2 and discussed in more detail in Chapter 4.4.

Table 2: Summary of the derived material properties from SEM, spectroscopic ellipsometry, ellipsometric porosimetry and VEELS analysis.

Method	Property		T _{calc.}					
			300 °C	350 °C	375 °C	400 °C	500 °C	600 °C
material properties								
SEM	top-view	Si-substrate						
	cross-section							
		Ti-substrate						
spectroscopic ellipsometric measurements and modeling								
spectroscopic ellipsometry	thickness / nm	Si-substrate	78.6 ± 1.2	64.7 ± 1.2	74.2 ± 2.3	78.9 ± 2.9	74.1 ± 2.0	77.6 ± 1.2
	porosity / %		48.8 ± 0.9	46.5 ± 1.0	46.4 ± 1.0	45.0 ± 1.9	43.0 ± 1.0	45.6 ± 0.9
	resistivity · 10 ⁻³ / Ohm cm		1.13	1.10	0.97	0.93	0.64	0.48
	electron concentration · 10 ²¹ / cm ⁻³		7.14	7.35	7.54	8.76	12.36	12.46
	electron mobility / cm ² V ⁻¹ s ⁻¹	Ti-substrate	0.77	0.77	0.85	0.77	0.79	1.12
	mean scattering time / fs		0.44	0.44	0.48	0.44	0.45	0.64
	Ir 5d transition energy / eV		3.17	3.09	3.06	3.08	3.20	3.29
	thickness / nm		156.0 ± 4.4	143.9 ± 3.3	145.6 ± 3.9	123.8 ± 2.6	124.3 ± 2.3	126.4 ± 5.2
	porosity / %	48.3 ± 1.7	46.6 ± 1.6	44.3 ± 2.0	39.9 ± 1.7	40.3 ± 1.6	40.1 ± 5.2	
	resistivity · 10 ⁻³ / Ohm cm	1.01	1.05	1.00	0.97	0.65	0.46	
	electron concentration · 10 ²¹ / cm ⁻³	6.65	7.96	8.60	8.39	11.98	12.80	
	electron mobility / cm ² V ⁻¹ s ⁻¹	0.69	0.71	0.74	0.72	0.81	0.98	
	mean scattering time / fs	0.39	0.40	0.42	0.41	0.46	0.56	
	Ir 5d transition energy / eV	3.16	3.13	3.09	3.11	3.17	3.21	
bulk valence electron energy loss spectroscopy	A _{bulk} / eV	Si-substrate	1.36	1.29	1.34	1.32	1.59	1.77
	B _{bulk} / eV		4.27	4.27	4.25	4.27	4.29	4.34
	A _{bulk} / eV	Ti-substrate	1.03	1.09	1.14	1.05	1.50	1.73
	B _{bulk} / eV		4.25	4.27	4.25	4.20	4.27	4.34
surface valence electron energy loss spectroscopy	A _{surface} / eV	Si-substrate	1.21	1.16	1.19	1.18	1.45	1.68
	B _{surface} / eV		4.22	4.20	4.18	4.22	4.25	4.29
	A _{surface} / eV	Ti-substrate	0.80	0.92	0.94	0.88	1.35	1.64
	B _{surface} / eV		4.22	4.22	4.20	4.16	4.22	4.29
ellipsometric porosimetry	porosity / %	Si-substrate	52.3 ± 1.5	45.1 ± 1.7	44.6 ± 0.9	41.8 ± 0.6	39.6 ± 1.2	-
			49.0 ± 1.3	46.1 ± 4.7	44.8 ± 1.7	41.4 ± 0.9	41.6 ± 1.8	40.7 ± 5.8
		Ti-substrate						

4.3 Electrochemical studies in the OER and lower potential regime

Mesoporous IrO_x films were used as a model system for the oxygen evolution reaction (OER) to investigate relevant structure-activity relationships. Catalyst films were tested in a three-electrode disc setup (RDE) using a nitrogen purged electrolyte (0.5M H_2SO_4), a platinum counter electrode and a reversible hydrogen electrode (RHE) as reference electrode. Coated titanium discs (5 mm) were used as working electrode and a rotating speed of 1600 rpm was applied. OER activities were measured via cyclic voltammetry ($1.20 V_{\text{RHE}}$ to $1.65 V_{\text{RHE}}$, 50 cycles, 6 mV s^{-1}) and low-potential cyclic voltammetry ($0.40 V_{\text{RHE}}$ to $1.40 V_{\text{RHE}}$; 50 mV s^{-1}) was used to evaluate the anodic and cathodic charge ($q_{(\text{a}+\text{c})/2}$). Figure 28 displays a) the OER activities of the 2nd cycle during cyclic voltammetry (CV) of the IrO_x calcination series, b) the 50th CV curves in the OER regime, c) low-potential cyclic voltammetry measurements, d) the observed current density at a potential of $1.55 V_{\text{RHE}}$ of the 2nd and 50th cycle, e) the mean value of the integrated anodic and cathodic scan, and f) the intrinsic OER activity of the catalyst films for the 2nd and 50th cycle.

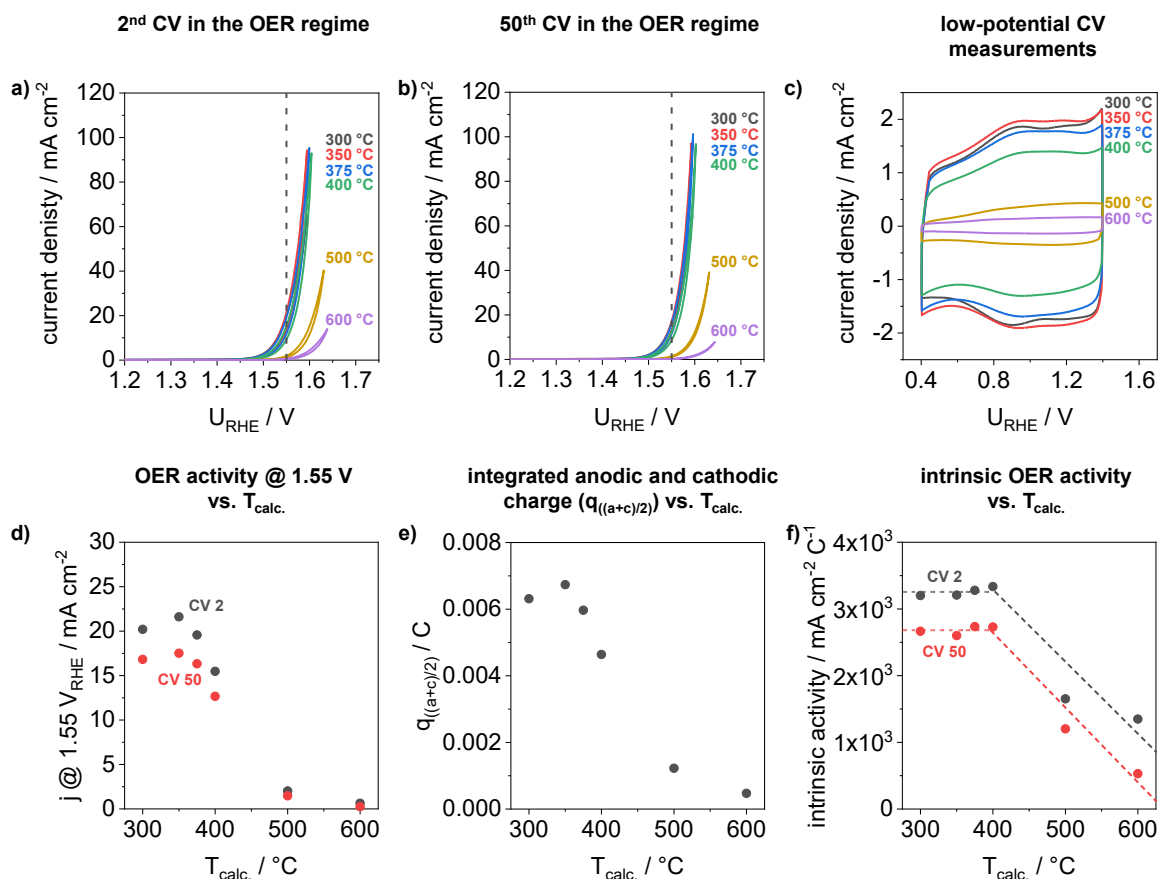


Figure 28: Electrochemical rotating disc electrode (RDE) analysis of OER activities, anodic and cathodic charge and intrinsic activities of mesoporous IrO_x films calcined between 300 °C and 600 °C. Catalyst films were deposited on conductive titanium substrates and calcined for 5 min in air. Electrochemical studies in the OER regime and in the lower potential range were recorded in N_2 purged 0.5M H_2SO_4 and corrected for ohmic losses (iR correction). a) 2nd cycle and b) 50th cycle in the OER regime with a cycle speed of 6 mV s^{-1} . c) cyclic voltammetry in a lower potential window with a cycle speed of 50 mV s^{-1} . d) OER activity at a potential of $1.55 V_{\text{RHE}}$ of the 2nd and 50th cycle. e) mean value of the integrated anodic and cathodic currents ($q_{(\text{a}+\text{c})/2}$). f) current density (at $1.55 V_{\text{RHE}}$) normalized to the charge (intrinsic activity). Linear lines in the graphs of the intrinsic activity have been added for orientation of the trend.

All mesoporous IrO_x films show a significant OER activity during CV measurements in the 2nd and 50th cycle (Figure 28a, b). The calcination temperature indicates an influence on the current response, which is normalized to the coated titanium disc surface area (0.196 cm²). Catalyst films reveal high OER activities at calcination temperatures between 300 °C and 400 °C in both the 2nd (Figure 28a) and the 50th (Figure 28b) cycle. The current density decreases with further increasing calcination temperatures. Low-potential CV measurements (Figure 28c) in the range between 0.40 V_{RHE} and 1.40 V_{RHE} offer information about the accessible and/or available iridium involved in the reaction. The current response, normalized to the geometric surface of the substrate, shows high surface charges, which decreases with increasing calcination temperature.

Figure 28d shows the geometric current density at a potential of 1.55 V_{RHE} ($j @ 1.55 V_{RHE}$) as a function of the applied calcination temperature for the 2nd and 50th cycle. The determined values indicate a slight increase up to 350 °C and a decrease with higher temperatures. Current densities up to 22 mA cm⁻² (2nd CV) and 18 mA cm⁻² (50th CV) can be observed. A similar trend can be observed for the mean value of the integrated anodic and cathodic charge (Figure 28e). In order to derive the intrinsic OER activity, the geometric current density measured at 1.55 V_{RHE} was divided by the mean value of the surface charge ($q_{((a+c)/2)}$). Intrinsic OER activities remains constant up to a calcination temperature of 400 °C and declines with further increasing calcination temperatures (Figure 28f). These findings are consistent with results of comparable electrocatalytic materials.²⁶

Before the developed flow cell setup can be used for operando investigations of mesoporous IrO_x films, the electrochemical behavior has to be validated. For the study of the electrochemical behavior of the flow cell setup, catalyst films on titanium substrates (25 x 40 mm) were used as working electrode, a platinum wire as counter electrode and an Ag/AgCl (3M NaCl) as reference electrode. Perchloric acid (0.1M HClO₄) was used as electrolyte to use anions similar to the reference electrode at a flow rate of 85 ml min⁻¹. The measured potential of the Ag/AgCl electrode was referred to RHE (+0.256 V vs. RHE at pH 1). Figure 29 illustrates a) the comparison between the RDE and flow cell setup, b) the 2nd cycle of CV measurements in the OER regime, c) low-potential cyclic voltammetry, d) observed current density at a potential of 1.45 V_{RHE} of the 2nd cycle, e) the mean value of the integrated anodic and cathodic scan, and f) intrinsic OER activities.

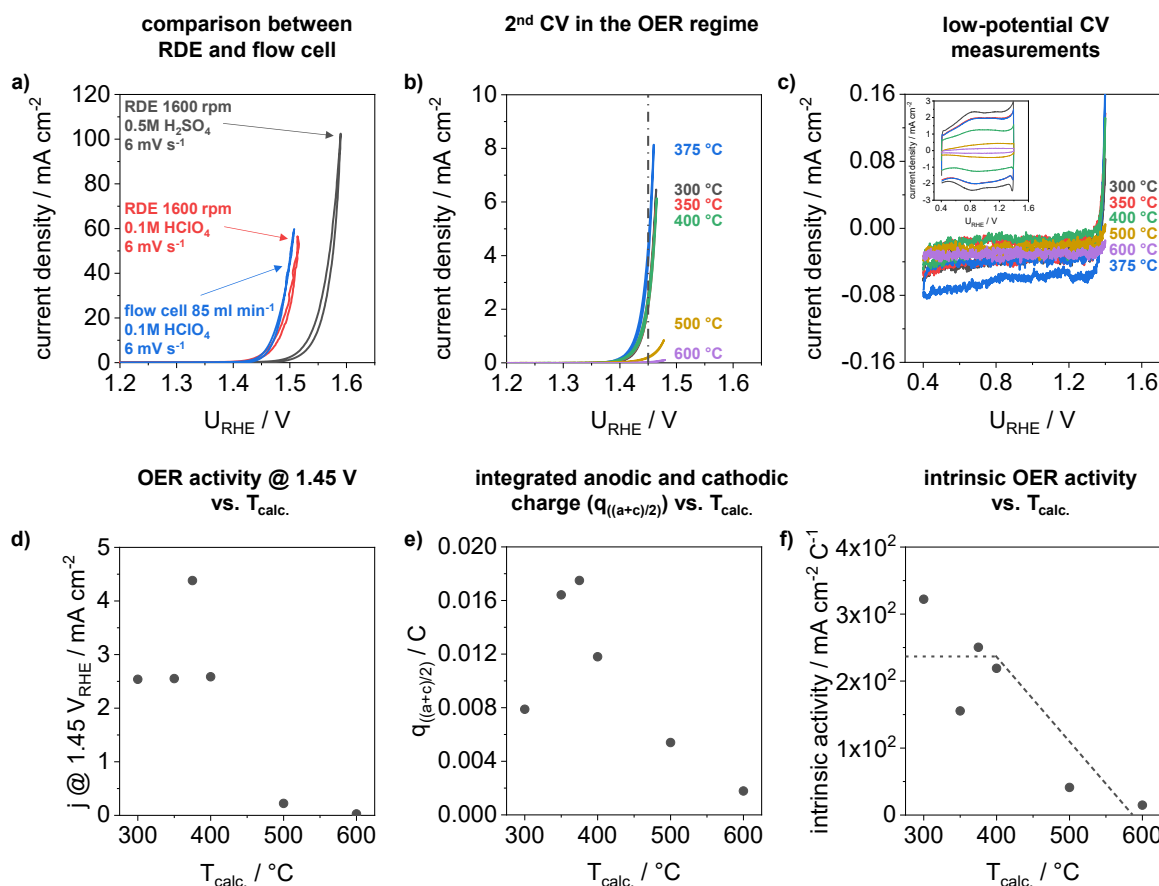


Figure 29: Electrochemical testing with the ECSE flow cell setup of OER activities, anodic and cathodic charge, and intrinsic activities of the IrO_x calcination series. Catalyst films were deposited on conductive titanium substrates and calcined for 5 min in air. Electrochemical studies in the OER regime and in the lower potential range were recorded in N₂ purged 0.1M HClO₄ and corrected for ohmic losses (iR correction). a) comparison between RDE and flow cell testing. b) 2nd cycle in the OER regime with a cycle speed of 1 mV s⁻¹. c) low-potential cyclic voltammetry in a lower potential window with a cycle speed of 1 mV s⁻¹ and 50 mV s⁻¹ (inset). d) OER activity at a potential of 1.45 V_{RHE} of the 2nd cycle. e) mean value of the integrated anodic and cathodic currents (q_{((a+c)/2)}) of cyclic voltammetry with a cycle speed of 1 mV s⁻¹. f) intrinsic OER activities calculated from current density at 1.45 V_{RHE} and the charge derived from curves at a scan rate of 1 mV s⁻¹, with linear lines for orientation of the trend.

For the comparison of the two setups, a mesoporous iridium oxide film calcined at 350 °C was used for investigations in the OER regime. Figure 29a presents the current response of the catalyst film under different testing conditions. The current density was normalized to the coated titanium disc surface area (0.196 cm²) in case of RDE and to the surface area of the cell opening (1.473 cm²) in the case of the flow cell setup (see Chapter 3.3 for detailed flow cell setup). To investigate the change of the electrolyte, RDE studies were performed with a working electrode rotation speed of 1600 rpm and a scan rate of 6 mV s⁻¹. The current response of the tested film indicates for the HClO₄ electrolyte an earlier onset of the oxygen evolution reaction compared to the H₂SO₄ electrolyte. This observation is due to the sulfate anions and their stronger affinity to the surface, which inhibit the oxidation at the interface and thus shift the reaction to more positive potentials.^{172, 173} The influence of the sulfate anions was also confirmed by measurements with electrochemical quartz crystal microbalance (EQCM).¹⁷⁴ In addition, the comparison of the current responses between the RDE and the flow cell setup using a scan rate of 6 mV s⁻¹ correspond well

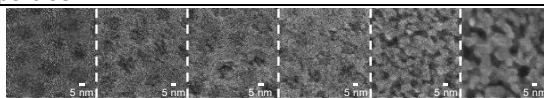
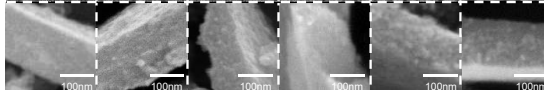
and show a similar electrochemical behavior, even at a flow rate of 85 ml min⁻¹ compared to the 1600 rpm for the RDE setup (Figure 29a).

For operando measurements it was necessary to reduce the scan rate (e.g., to 1 mV s⁻¹) in order to allow the time-consuming ellipsometry measurement to be performed alongside the electrochemical measurement. At higher scanning rates, the potential range for each SE spectrum would be too wide and the investigations could not provide potential dependent surface features. Therefore, scan rates of 1 mV s⁻¹ or 2 mV s⁻¹ were used for the operando measurements described in this thesis. Figure 29b presents CV measurements in the OER regime of the calcination series tested in the flow cell setup in a potential window of 1.20 V_{RHE} to 1.48 V_{RHE} and a scan rate of 1 mV s⁻¹. The observed current density curves show a similar behavior as RDE measurements in 0.5M H₂SO₄ (Figure 28a). Low-potential CV measurements in the range between 0.40 V_{RHE} and 1.40 V_{RHE} and a scan rate of 1 mV s⁻¹ indicate some nosing curves and very low surface charges (Figure 29c). It is known from literature that the current response depends on the scan rate and can be described e.g. for a reversible reaction by the Randles-Sevcik equation.¹⁷⁵ However, CVs measured with a scan rate of 50 mV s⁻¹ (inset Figure 29c) reveal a comparable behavior to the measurements with RDE (Figure 28c).

The geometric current density at a potential of 1.45 V_{RHE} ($j @ 1.45 V_{RHE}$) as a function of the applied calcination temperature for the 2nd cycle are shown in Figure 29d. Catalyst films show a constant current density of about 2.55 mA cm⁻² for films calcined between 300 °C and 400 °C, except for the film calcined at 375 °C, which indicate a current density of about 4.38 mA cm⁻². IrO_x films calcined at higher temperatures show very low current density values below 0.5 mA cm⁻². Mean values of the integrated anodic and cathodic charge derived from the curves at a scan rate of 1 mV s⁻¹ (inset Figure 29c) reveal an increase up to 375 °C and declines with further calcination temperatures (Figure 29e). The intrinsic OER activities (Figure 29f), calculated using the current density values at 1.45 V_{RHE} and the integrated anodic and cathodic charge values at scan rates of 1 mV s⁻¹, show a relatively constant behavior up to 400 °C and a decrease at higher calcination temperatures, which is comparable to the RDE investigation (Figure 28f).

In summary, the investigated mesoporous catalyst films show high activities in the OER, which agrees well with comparable iridium-based catalysts.^{26, 64} Moreover, all values derived in the flow cell, i.e., OER activity, integrated charge as well as intrinsic activity show very similar temperature dependencies as previously reported in RDE experiments on mesoporous IrO_x films.^{26, 64} These validations open the path for the operando measurements with spectroscopic ellipsometry. Table 3 summarizes the results of the electrochemical studies.

Table 3: Summary of electrochemical testing's in the RDE and ECSE flow cell setup.

Method	Property	$T_{calc.}$					
		300 °C	350 °C	375 °C	400 °C	500 °C	600 °C
material properties							
SEM	top-view						
	cross-section						
electrochemical testing							
RDE ^a	activity 2 nd cycle (@ 1.55 V _{RHE}) / mA cm ⁻²	20.20	21.61	19.57	15.48	2.02	0.64
	activity 50 th cycle (@ 1.55 V _{RHE}) / mA cm ⁻²	16.82	17.51	16.32	12.66	1.47	0.25
	charge $q_{((a+c)/2)} \cdot 10^{-3} / C$	6.36	6.73	5.97	4.64	1.22	0.47
	intrinsic OER activity 2 nd cycle · 10 ³ / mA cm ⁻² C ⁻¹	3.20	3.21	3.28	3.34	1.65	1.35
	intrinsic OER activity 50 th cycle · 10 ³ / mA cm ⁻² C ⁻¹	2.67	2.60	2.74	2.73	1.20	0.53
flow cell ^b	activity 2 nd cycle (@ 1.45 V _{RHE}) / mA cm ⁻²	2.54	2.55	4.38	2.59	0.22	0.03
	charge $q_{((a+c)/2)} \cdot 10^{-3} / C$	7.88	16.42	17.49	11.80	5.40	1.78
	intrinsic OER activity 2 nd cycle · 10 ³ / mA cm ⁻² C ⁻¹	0.32	0.16	0.25	0.22	0.04	0.01

a in 0.5M H₂SO₄b in 0.1M HClO₄

4.4 Validation of ellipsometric derived properties and correlation to electrochemical activity

In this Chapter, the comparison and validation of the derived parameters resulting from the SE modeling as well as the correlation with electrochemical activities in the acidic OER will be presented. In the first part the derived SE properties from Chapter 4.2, i.e., film thickness, porosity, resistivity and intraband transitions are compared with the results of the independent physicochemical methods from Chapter 4.1. Subsequently, deduced electronic parameters, i.e., p-d interband transitions, from the VEELS analysis described in Chapter 4.2 are correlated with activity trends described in Chapter 4.3.

Comparison and validation of ellipsometric properties with complementary methods

Material properties derived from SE depend strongly on the structure and quality of the optical model. Therefore, it is necessary to validate the model results independently with complementary analytical methods. Figure 30 presents a comparison between SE derived results with independently measured values for the film thickness on a) Si substrates (using SEM and XRR) and b) Ti substrates (using SEM), for the film porosity on c) Si substrates (using EP, EPMA-EDS / StrataGem and XRR) and d) Ti substrates (using EP), e) for electrical resistivity (using a 4 point conductivity measurements), and f) for transition energies of the t_{2g} and e_g separation of the Ir 5d band (using UV-VIS-NIR absorption spectroscopy and transmission measurements within the ellipsometer).

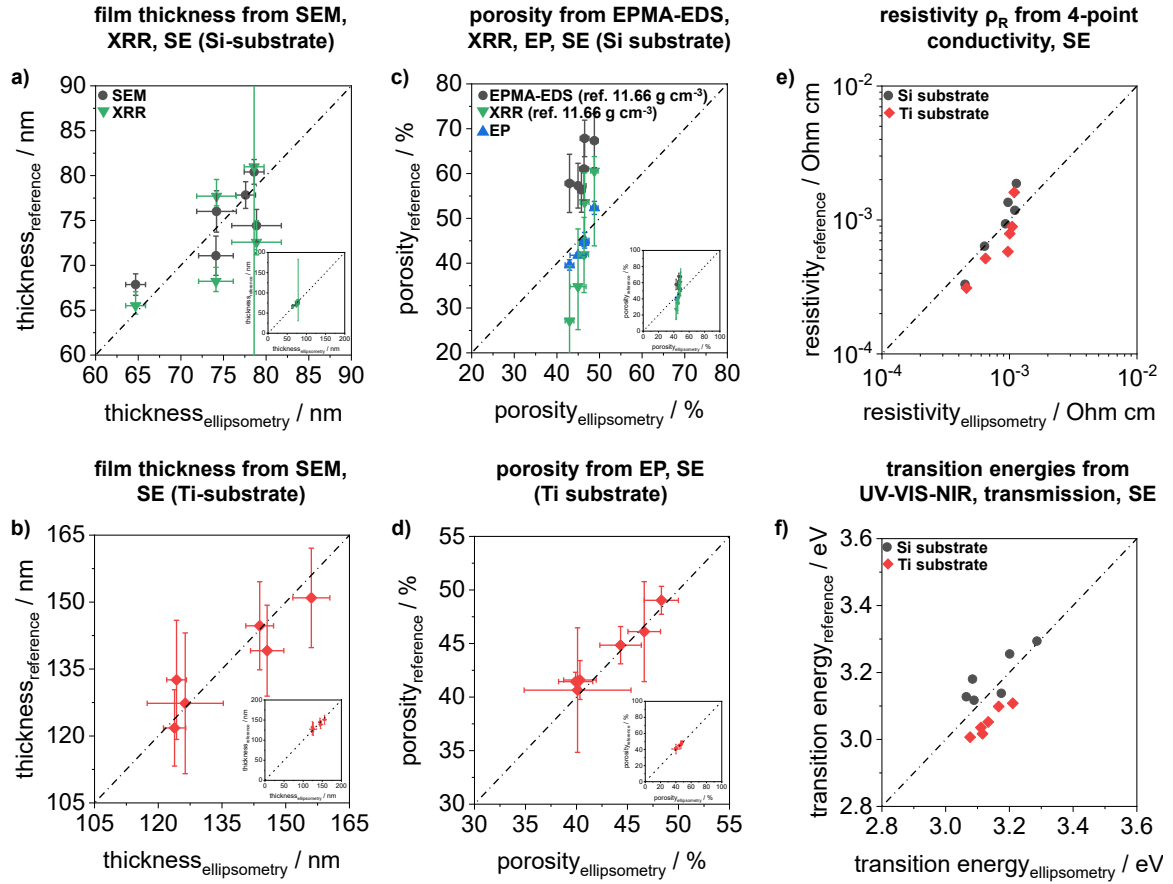


Figure 30: Validation and comparison of layer properties by independent methods: a) film thickness on Si substrates by SE, XRR and SEM cross-section images, b) film thickness on Ti substrates by SE and SEM cross-section images, c) porosity of films on Si substrates by the EPMA-EDS / StrataGem approach, SE and EP isotherms, d) porosity of films on Ti substrates by SE and EP isotherms, e) resistivity by ellipsometric modeling and sheet conductivity measurements for films on Si and Ti substrates, and f) transition energy values by SE, UV-VIS-NIR absorption spectroscopy and transmission measurements within the ellipsometer.

Film thicknesses of the IrO_x calcination series on Si substrates, measured with SE, SEM and XRR, range from about 65 to 80 nm (Figure 30a, Table 1 and Table 2). The observed values of the three independent methods provide similar values within a 10 nm range and similar trends of a decreasing layer thickness with increasing calcination temperature. The deviations in the film thickness by the three techniques are comparable with the measurement uncertainty of the individual method, but it should be noted that they were not measured at exactly the same location. The large XRR deviation of the film calcined at 300 °C is due to the fact that the measured layer shows no interference (Kiessig oscillations), which leads to the very high deviation in the film thickness (inset Figure 30a and Figure 18f). Similar trends can also be observed for the films on Ti substrates between SE and SEM, where the SEM layer thicknesses were measured by scratching the samples with a triangular tungsten carbide knife and the associated break-up of the layer, which leads to the higher deviations.

Porosities of the IrO_x samples were evaluated using SE, EP sorption isotherms (see Appendix A11 for additional data), XRR densities, and a combination of SEM, EDS and the evaluation with the StrataGem software.^{78, 129} Porosity values of XRR and EPMA-EDS / StrataGem were calculated from densities according to equation (48), using the density of crystalline IrO₂ (11.66 g cm⁻³) as reference. Figure 30c displays the porosity values of the IrO_x calcination series on Si substrates. Porosities derived from SE and EP range from 39.6% to 52.3% and agree on less than 10%. Both methods indicate a decreasing trend of porosities with increasing calcination temperatures. EPMA-EDS / StrataGem results values of about 67.5% to 56.3%, which are approximately 1.5 times higher than values derived from SE. However, a decreasing trend is also captured. It is likely that the deviations are due to the fact that the EPMA-EDS / StrataGem method requires a reference bulk density. The assumption of the bulk density in the porosity calculation could be associated with large uncertainties and possibly a systematic offset, since the studied IrO_x samples change their crystallinity with calcination temperature. Hackwood *et al.* estimated a density of about ~10.0 g cm⁻³ for sputtered iridium oxide, suggesting that synthesized iridium oxide probably cannot reach the theoretical density of crystalline IrO₂.¹⁶⁵ Furthermore, the EPMA quantification of oxygen must be considered as critical, i.e. associated with large uncertainties. Moreover, quantification with X-ray lines of the L series is generally less reliable than with K_α. The porosities derived from XRR show a reasonable trend and values between 27.1% and 60.6% are obtained. As the EPMA-EDS / StrataGem method, the calculation of the porosities values were based on the assumption of crystalline IrO₂ as bulk density, which might lead to the larger uncertainties compared to SE and EP. Porosities on Ti substrates were determined with SE and EP, which ranges from 49% to 40.1%. The values agree well within the uncertainty and show comparable trends (Figure 30d).

Resistivity values for films on Si and Ti substrates derived from the Drude function from the SE modeling compare very well to those from the 4-point sheet conductivity measurements on quartz substrates (Figure 30e).

Finally, Figure 30f compares energy values of the direct allowed transitions ($m = 1/2$) between the t_{2g} and e_g sub-level of the Ir 5d band from SE modeling with UV-VIS-NIR absorption spectroscopy for layers on Si substrates. Transition energy values for films on Ti substrates were compared by SE modeling with transmission measurements in an ellipsometer (see Appendix A12 for additionally data). UV-VIS-NIR absorption spectroscopy and transmission measurements within the ellipsometer were performed for films on quartz substrates.

The SE derived properties of film thickness, porosity, resistivity, and band transition energy prove to be in very good agreement with the results of the independent methods used, and thus a very good accuracy of the developed SE model.

VEELS properties and correlation with intrinsic OER activities

From the VEEL spectra of the calcination series, two peaks labeled as A and B were identified and correlated with p-d interband transitions, which are influenced by the calcination temperature (Figure 27). Additionally, the intrinsic OER activity also indicates an influence of the calcination temperature (Figure 28f and Figure 29f). A direct comparison between the intrinsic OER activities of the IrO_x calcination series and the maximum center energy position of the A and B peaks is exemplary for the RDE investigations shown in Figure 31.

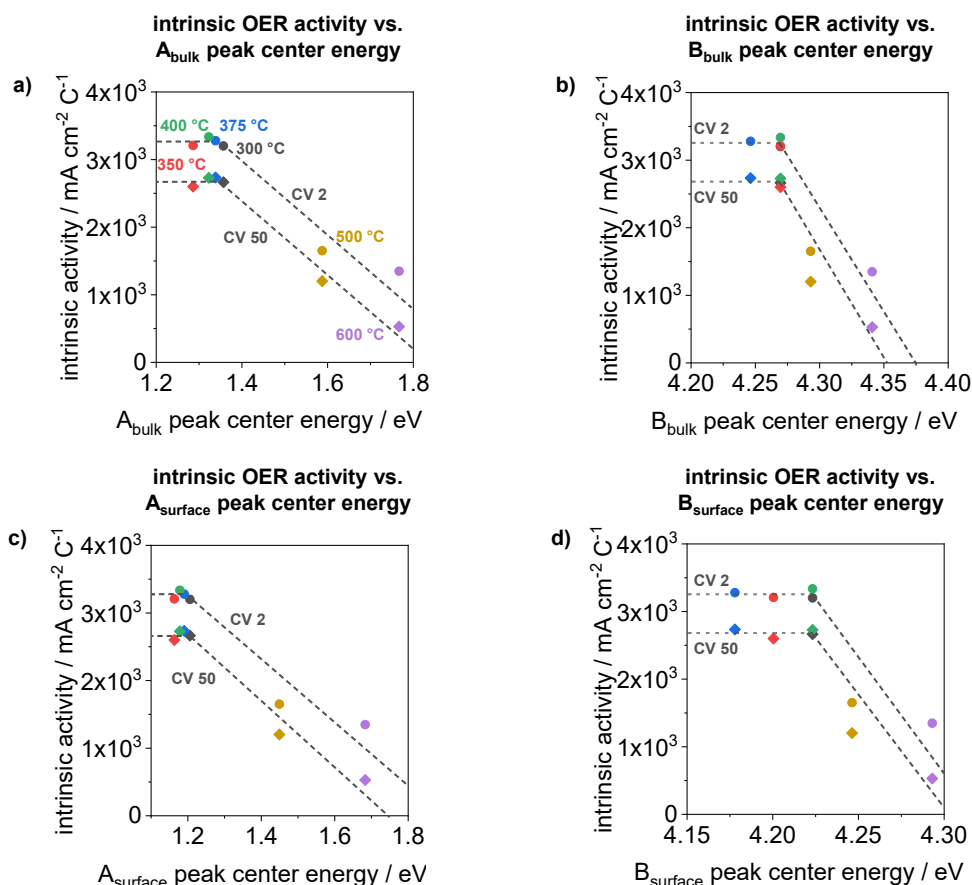


Figure 31: Correlation between identified peak energy positions from VEELS analysis and intrinsic OER activities. Comparison between the center energy of a) A_{bulk} , b) B_{bulk} , c) A_{surface} , and d) B_{surface} with the intrinsic OER activities of the mesoporous IrO_x calcination series. Linear trend lines in the graphs have been added for orientation of the course.

The comparison between the intrinsic OER activity and the center energy of the A_{bulk} (Figure 31a) and A_{surface} (Figure 31c) peaks indicates a constant behavior until an energy value of 1.4 eV and 1.2 eV, respectively. Higher energies lead to a decrease in the OER current per accessible Ir, for both the 2nd and 50th cycle. This behavior is also observed for the B_{bulk} and B_{surface} peaks, where the intrinsic OER activity is approximately constant up to an energy of about 4.25 eV and decreases at higher calcination temperatures (Figure 31b, d).

The interaction of the O 2p orbitals with the Ir 5d t_{2g} orbital directly affects the activity in the OER. Terminal electrophilic oxygen ligands (e.g. -O(H)) and the associated higher degree of covalency influence the Ir-O bonds, resulting in shorter Ir-O distances.^{15, 33} It is described by Strasser and

co-workers that nickel leaching of IrNiO_x nanoparticles leads to the formation of iridium lattice vacancies and thus represents hole doping of the lattice.³³ As a consequence, iridium ions adjacent to vacancies increase their hole character and assume more positive oxidation states. This means that terminal electrophilic oxygen ligands are formed in response to the iridium d-band holes. As a result, due to the hole character of the oxygen ligands and the associated high degree of covalency, the Ir-O bonds are contracted to short distances.^{15, 33} The shift of the energy values of the identified peaks in the VEEL spectra (Figure 27) and the change of the chemical composition from hydrated to more anhydrous IrO_x species in the XPS measurements (Figure 19), with increasing calcination temperature, are consistent with findings reported in literature on electrophilic oxygen ligands and associated shorter Ir-O distances.

VEELS studies calculated from SE data provide a direct correlation between the band structure and the activities in the OER, which can be associated with a change in electrophilic oxygen ligands and shorter Ir-O distances. A detailed discussion of the electronic band structure of the IrO_x model systems and the influence of calcination temperature is described in Chapter 7.

5. Studies combining electrochemistry and spectroscopic ellipsometry using bulk Pt as an example

Platinum is known for its reproducible characteristic cyclic voltammogram and is most likely the best known of all electrode materials.¹⁷⁶ Platinum surfaces have been intensively studied and the processes that contribute to the characteristic shape result from the formation and reduction of hydrogen and oxygen top layers. For the understanding of ellipsometric analysis in electrochemical investigations, cyclic voltammetry on a platinum surface is used as a sensitive method to study the change in the measured Ψ and Δ spectra. Typical platinum cyclic voltammograms recorded in a standard three-electrode setup (a) as well as in the flow cell setup (b) with a platinum wire as counter electrode and an Ag/AgCl reference electrode (3M NaCl, referred to RHE) are shown in Figure 32. In both setups, 0.1M HClO₄ served as electrolyte and a scan rate of 100 mV s⁻¹ was applied.

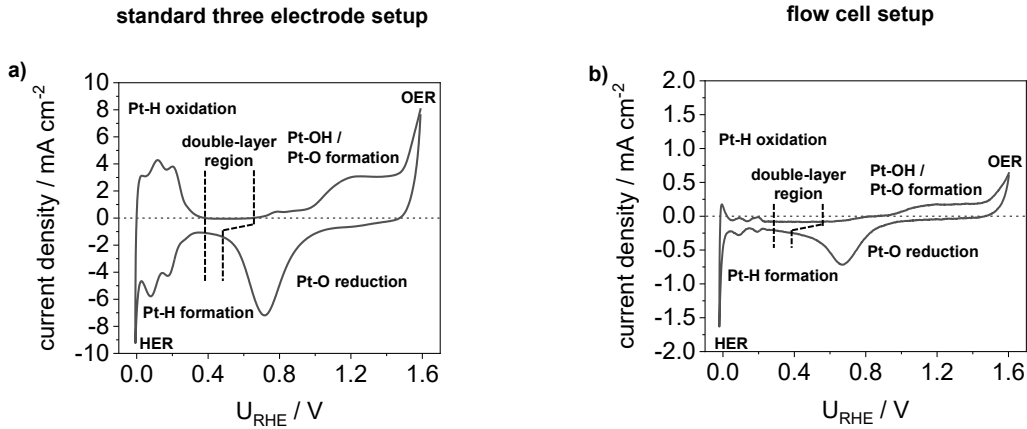


Figure 32: Cyclic voltammograms of platinum recorded in a standard three electrode setup (a) as well as in the developed flow cell setup (b) in a potential range between -0.28 V and 1.35 V against an Ag/AgCl reference electrode (+0.256 V vs. RHE at pH 1) in N₂-purged 0.1M HClO₄ and a scan rate of 100 mV s⁻¹. A platinum wire served as counter electrode and both CVs are corrected for ohmic losses (iR correction).

In the potential window of about 0.4 V_{RHE} to 0.6 V_{RHE}, a low current density (close to zero) is observed, which indicates the charging of the electrocatalytic double-layer (Figure 32a and b). In the forward scan to higher potentials, oxygen chemisorption occurs according to the following equations:



The oxygen evolution reaction (OER) starts at about 1.6 V_{RHE}. In the reverse scan, the oxygen layer is reduced and after a small double layer region the adsorption of hydrogen occurs as described as follows:



In case of strong negative potentials, the hydrogen evolution reaction (HER) takes place and hydrogen is formed.

The measured Pt CV in the standard three-electrode configuration (Figure 32a) illustrates the described processes of the Pt-H formation and oxidation, the double-layer region as well as the Pt-O formation and reduction contributing to the characteristic shape. The measurement in the flow cell setup (Figure 32b) exhibits the same characteristic processes and shape, with slightly lower signal intensity (current density response).

For examination under operando conditions, the first part of this section offers the ex-situ analysis and modeling using SE, followed by the ECSE investigation of the described platinum cyclic voltammogram.

5.1 Ex-situ ellipsometric analysis and modeling

In order to examine materials, e.g., platinum, in the context of operando ECSE, it is necessary to study the materials in advance in an ex-situ analysis and to develop dielectric functional models accordingly. Polished bulk polycrystalline Pt was analyzed using a SE model consisting of two layers, metallic platinum (Pt) as substrate and an overlying oxide layer (PtO_x) as an assumption of a partially oxidized surface. Here, the Pt substrate layer was parametrized with a model containing one Drude type (equation (38) and (39)) and two Lorentz type oscillators (equation (40)). The PtO_x layer was modeled by a single Tauc-Lorentz oscillator (equation (41) and (42)) due to the semiconducting nature of this material. Figure 33 presents a) the fit results b) the real ϵ_1 and imaginary ϵ_2 part of the Pt substrate layer, and c) ϵ_1 and ϵ_2 of the PtO_x layer.

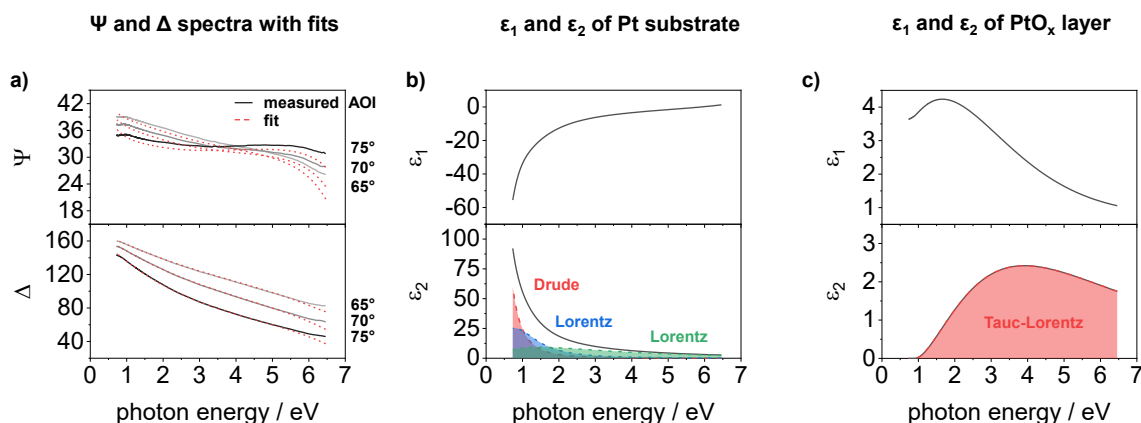


Figure 33: Ex-situ SE characterization of bulk platinum using a two-layer model consisting of a Pt substrate and a PtO_x top layer. a) Ψ and Δ spectra with their fit results of SE measurement. b) real ϵ_1 and imaginary ϵ_2 part of the Pt substrate layer, modeled using a summation of a Drude type and two Lorentz type oscillators. c) ϵ_1 and ϵ_2 of the PtO_x layer, modeled with a single Tauc-Lorentz oscillator. The RMSD value amounts to 19.604.

Figure 33a shows the fit results of the ex-situ SE analysis using AOIs of 65°, 70° and 75°. The modeled spectra (dashed red lines) agree well with the measured data (grey to black lines) and only in the high photon energy region around 6 eV some large deviations are obtained. The RMSD value amounts to 19.604.

The imaginary ε_2 part of the dielectric function of the Pt layer is dominated by the typical edge of conductive materials in the low photon energy range, which can be modeled by a Drude function (Figure 33b). In addition, two absorption peaks at about 1.0 eV and 3.3 eV can be observed, which can each be modeled with a Lorentz function. In the real ε_1 part of the dielectric function a slight decrease and from about 1.5 eV a strong decrease towards lower photon energies can be observed. Similar results were obtained in the literature for Pt from spectroscopic ellipsometric and reflectometric measurements using comparable parametrization models.¹⁷⁷⁻¹⁸⁰

For the parameterization of the PtO_x layer using a single Tauc-Lorentz oscillator (Figure 33c), a bandgap energy of 0.9 eV and a peak energy of 4.8 eV were assumed, according to the parametrization model of PtO₂ described by Knoop *et al.*¹⁸⁰ For the fitting, only the width and height of the Tauc-Lorentz oscillator were adjusted. The ε_2 spectrum shows a broad absorption peak, where ε_2 becomes zero at 0.9 eV. The ε_1 spectrum shows a peak at about 1.8 eV. The PtO_x spectra are also in good agreement with magnetron-sputtered platinum oxide films and PtO_x layers using remote plasma ALD reported in literature.^{180, 181}

As a result of the modeling of the bulk Pt material, the resistivity at the surface (Pt/PtO_x/air interface) and the layer thickness of PtO_x were obtained. The derived resistivity of the Pt surface amounts to $1.20 \cdot 10^{-5}$ Ohm cm, which is close to the bulk Pt value of $1.08 \cdot 10^{-5}$ Ohm cm reported in literature.¹⁸⁰ The slightly higher resistivity may be due to a partially oxidized platinum surface.

A PtO_x layer thickness of about 0.33 ± 0.26 nm was derived from the model. The PtO_x layer thickness indicates a high deviation, however ellipsometry is a highly surface sensitive technique even for (sub)monolayers and the thickness precision corresponds to $\delta d = 0.1$ Å.^{96, 182-185} For comparison of the accuracy of SE-derived film thicknesses, Erbe and co-workers reported on in-situ SE studies on the growth of a native oxide layer on zinc in different atmospheres and revealed a change of the layer thickness from about 0 nm to 1.1 nm with a growth rate of about 0.01 nm h^{-1} .¹⁸⁶

In summary, ex-situ characterization using SE leads to similar and comparable results of Pt and PtO_x as described in the literature. These results serve as a starting point for the operando ECSE investigation in the next section.

5.2 Operando investigations during cyclic voltammetry

For the operando investigations of Pt using the developed ECSE flow cell setup described in Chapter 3.4, the ellipsometric measurement and modeling has to be calibrated considering the influence of the quartz windows as well as the electrolyte. For this purpose, a Si wafer with a known oxide layer was used, first to calibrate the influence of the quartz windows and second to analyze the electrolyte used (N_2 purged 0.1M $HClO_4$), which is the ambient medium instead of air. Studies were performed in a potential range between -0.28 V and 1.35 V against an Ag/AgCl reference electrode (+0.256 V vs. RHE at pH 1), a Pt wire as counter electrode and a cycle speed of 2 mV s^{-1} . For the modeling, the same model as described above was used with the dielectric function of the electrolyte as ambient instead of air. Figure 34 presents a) recorded cyclic Pt voltammograms in the ECSE flow cell setup with a scan rate of 100 mV s^{-1} and 2 mV s^{-1} , respectively, b) the current density for a scan from -0.28 V_{Ag/AgCl} to 1.35 V_{Ag/AgCl} and then back to -0.28 V_{Ag/AgCl} with a scan rate of 2 mV s^{-1} as a function of time, c) the Ψ spectra, and e) the Δ spectra at different potentials as well as the corresponding Ψ (d) and Δ spectra (f) at photon energies of 2.0 eV, 3.0 eV and 5.0 eV as a function of the scan cycle acquisition time.

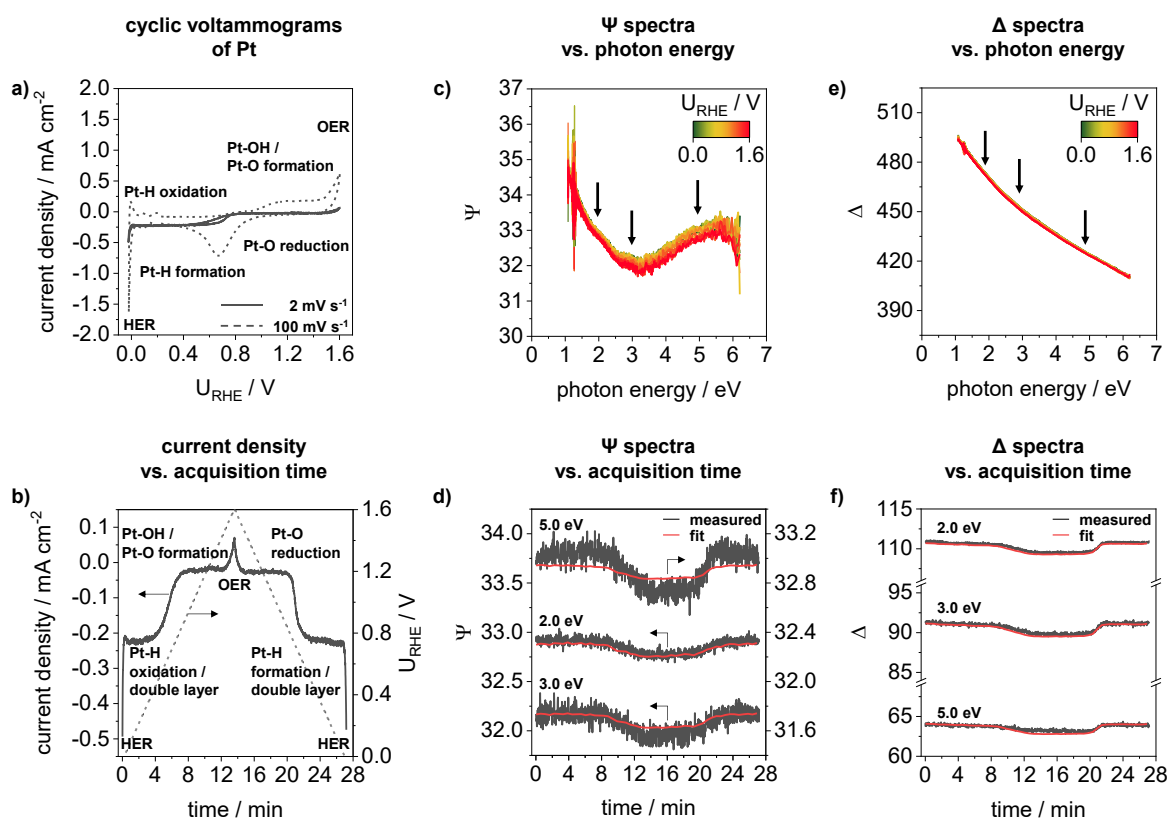


Figure 34: Operando ellipsometric investigations during cyclic voltammetry of bulk platinum. a) cyclovoltammetry in a potential range of -0.28 V and 1.35 V against an Ag/AgCl reference electrode (+0.256 V vs. RHE at pH 1) in N_2 -purged 0.1M $HClO_4$, a flow rate of 85 ml min^{-1} and a cycle speed of 100 mV s^{-1} and 2 mV s^{-1} , respectively. b) current density as a function of acquisition time under operando conditions with a scan rate of 2 mV s^{-1} . Ψ (c) and Δ (e) spectra of the measured platinum at different potentials. Ψ (d) and Δ (f) spectra at photon energies of 2.0 eV, 3.0 eV and 5.0 eV as a function of acquisition time and fitting results of the model used.

The shape of the cyclic Pt voltammogram at a reduced scan rate of 2 mV s^{-1} (solid line) differs from the CV at a scan rate of 100 mV s^{-1} (dashed line), which is due to the dependence of the current response on the scan rate (Figure 34a).¹⁷⁵ However, the characteristic HER and OER regimes as well as a change of the current density in the range of $0.6 \text{ V}_{\text{RHE}}$ are clearly visible, which probably indicates the Pt-O formation and/or reduction (oxygen chemisorption) as described in equation (V).

Figure 34b displays the recorded current density under operando conditions against the acquisition time and Figure 34c and Figure 34e the corresponding Ψ and Δ spectra. During the cyclic voltammetry measurement, changes in the Ψ and Δ spectra are observed. For a better visualization of the changes, the spectra (black lines) at selected energies (indicated by the arrows) are plotted with their fit results (red lines) against the acquisition time (Figure 34d and f). Both spectra show noticeable changes during cyclic voltammetry, and the fit results are in good agreement with the measured spectra. In the HER regime and in the Pt-H oxidation range, small changes in the Ψ spectra are observed at higher photon energies (0 min – 4 min). After an acquisition time of about 8 min, Ψ and Δ slowly decrease until 12 min. This change corresponds to the plateau between the chemisorption (4 min – 8 min) and the beginning of the OER (at about 12 min) in the current density curve (Figure 34b). In this region, Pt-O formation occurs according to equation (VI). In the OER regime (between 12 and 16 min) no further characteristic changes are observed. At about 18 min a rapid increase occurs, which is due to Pt-O reduction. The Pt-H formation and HER regime again show small changes only at higher photon energies in the Ψ spectra (24 min – 28 min).

From the results of the fitting (Figure 34d, f), changes in the dielectric functions can be deduced, which provide information about band transitions. Figure 35 displays the spectra ε_1 (a) and ε_2 (b) of Pt and PtO_x at different potentials as a function of the photon energy, the ε_1 (c) and ε_2 (d) spectra of Pt, as well as the ε_1 (e) and ε_2 (f) spectra of PtO_x at a photon energy of 2.0 eV against the applied potential.

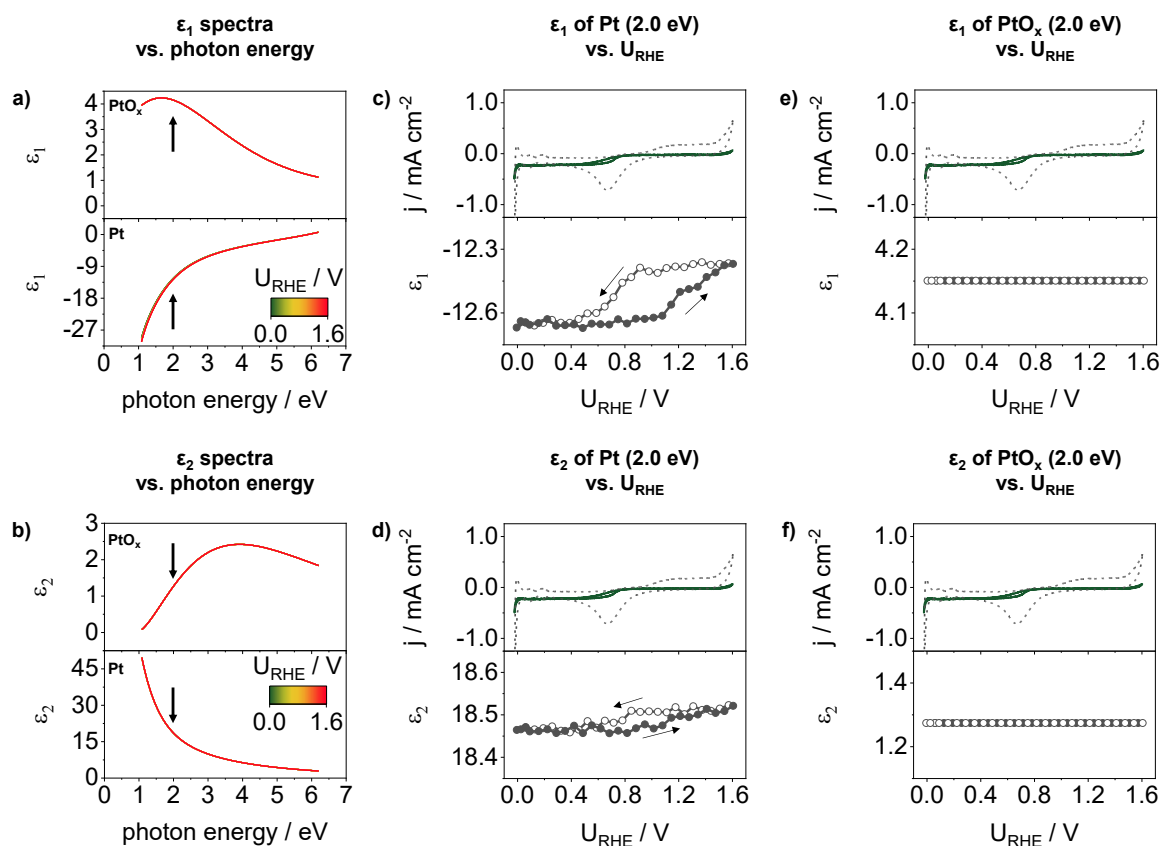


Figure 35: Dielectric functions of the Pt and PtO_x layer from the fitting results. Real ϵ_1 (a) and imaginary ϵ_2 (b) part of the dielectric function of Pt and PtO_x at different potentials as a function of photon energy. ϵ_1 (c) and ϵ_2 (d) of the Pt substrate and ϵ_1 (e) and ϵ_2 (f) of the PtO_x layer depending on the applied potential.

The ϵ_1 and ϵ_2 spectra of the Pt and PtO_x layer (Figure 35a, b) show slight changes in the low photon energy range for Pt and no visible changes for the PtO_x layer. For a better visualization, the ϵ_1 and ϵ_2 spectra of Pt (Figure 35c, d) and PtO_x (Figure 35e, f) were plotted against the potential exemplary at a photon energy of 2.0 eV. For the correlation of the spectra, the current density curves with scan rates of 100 mV s⁻¹ and 2 mV s⁻¹ are plotted. ϵ_1 of the Pt layer (Figure 35c) shows a roughly constant value between 0.0 V_{RHE} and 0.8 V_{RHE} for the scan to higher potentials (black circles). At about 0.8 V_{RHE}, ϵ_1 increases slightly to a potential of about 1.1 V_{RHE} and then increases more strongly to 1.6 V_{RHE}. In the back scan (white circles) an approximately constant behavior from 1.6 V_{RHE} to 0.9 V_{RHE} and a rapid decrease to a potential of about 0.4 V_{RHE} are observed, followed by a second constant behavior. A similar result can be also observed for the ϵ_2 spectra of the Pt layer (Figure 35d). In contrast, the dielectric functions (ϵ_1 and ϵ_2) of the PtO_x layer indicate no significant changes during the cyclic voltammetry measurement (Figure 35e, f).

The most significant changes in the dielectric functions during CV measurement occur for the Pt layer in the low photon energy region, indicating changes in the conductivity of the material at the Pt/PtO_x/electrolyte interface. The shape of these changes also suggests a relationship with the Pt oxidation/reduction mechanism described previously.

Further parameters such as the PtO_x layer thickness and electrical properties of the Pt layer can be derived from the modeling. Figure 36 displays the PtO_x film thickness (a), resistivity at the platinum interface/surface (b), as well as the electron mobility (c) and electron concentration (d) of the Pt layer as a function of applied potential.

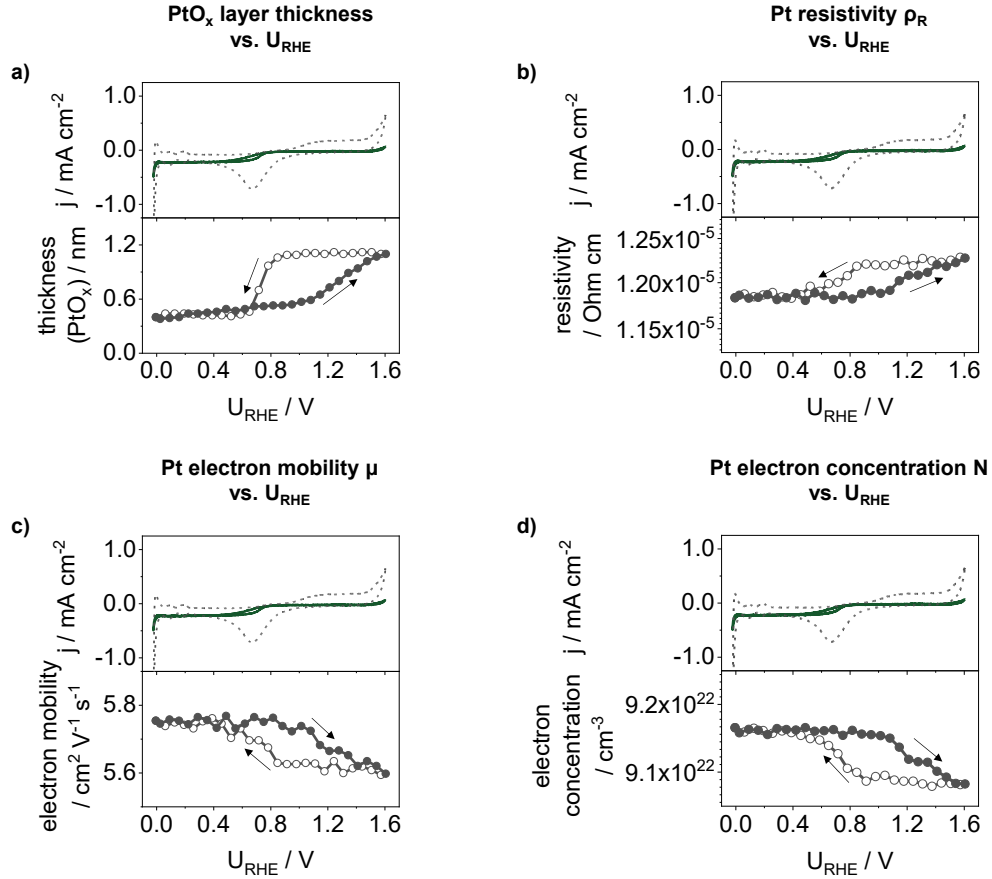


Figure 36: Changes in material properties of the Pt and PtO_x layer derived from the fitting results during cyclovoltammetry. a) dependence of the PtO_x layer thickness on the applied potential. b) Pt resistivity as a function of the potential. Changes of electron mobility (c) and concentration (d) during cyclic voltammetry.

Figure 36a displays the deduced PtO_x layer thickness as a function of the potential, starting with the thickness of about 0.33 nm as obtained from the ex-situ characterization. Scanning from 0.0 V_{RHE} towards higher potentials (black circles), a roughly constant thickness is observed until a potential of 0.6 V_{RHE} , followed by a slight increase up to 1.1 V_{RHE} . Above this potential (1.1 V_{RHE}), the PtO_x layer thickness increases more strongly to a thickness of about 1.1 nm until reaching the OER regime (1.6 V_{RHE}). In the back-scan towards lower potentials (white circles), the thickness initially remains constant at 1.1 nm until a potential of 0.8 V_{RHE} is reached. Subsequently, a decrease occurs until a potential of about 0.6 V_{RHE} and a thickness of about 0.33 nm. Below this potential (0.6 V_{RHE}) the PtO_x thickness remains relatively constant at 0.33 nm until the HER regime is reached. These findings agree well with the previously described oxidation/reduction mechanism of Pt during cyclovoltammetry.

Oxide layers on platinum of up to 1.0 nm were also previously deduced ellipsometrically in the literature.¹⁸⁷ Investigations of the formation and growth of oxide films on platinum electrodes by Percival *et al.* showed that the growth rate can be up to 1.2 nm min^{-1} at a holding potential of $1.2 \text{ V}_{\text{Ag/AgCl}}$ ($\sim 1.46 \text{ V}_{\text{RHE}}$).¹⁸⁸ In addition, Erbe and co-workers demonstrated the reduction and growth of a thin oxide layer of approximately 0.1 nm – 2.1 nm during dynamic potential scanning in an in-situ ellipsometric study on the potentiostatic treatment of zinc, showing similar results as the deduced PtO_x layer growth on Pt.¹²¹

The Pt resistivity at the surface/interface presents a similar behavior to the PtO_x layer thickness and seems to depend on the growth of the oxide layer (Figure 36b). This means that the resistivity remains constant up to a potential of $1.1 \text{ V}_{\text{RHE}}$ and then increases as the PtO_x layer grows. In the back scan up to a potential of about $0.8 \text{ V}_{\text{RHE}}$ a constant behavior of the resistivity can be observed, which returns to the initial value at lower potentials. However, it should be noted that the change of the resistivity takes place in a very small range of about $4.5 \cdot 10^{-7} \text{ Ohm cm}$.

Electron mobility and concentration values can be calculated according to equation (39). The electron mobility is displayed in Figure 36c and shows a decreasing value with increasing of the PtO_x layer, which is reversible with the reduction of the oxide layer. This behavior can also be observed for the electron concentration (Figure 36d). Due to the electrophilic nature of the oxygen ligands and the formation of Pt-O bonds, there is probably an interaction from the Pt electrons with the oxygen species. This leads to a decrease in electron concentration and mobility and the increase in resistivity. However, also in this case the changes of the electron concentration and mobility are very low.

In summary, even small changes on the platinum surface are detectable in cyclic voltammetry studies, such as oxidation and reduction of the time- and potential-dependent PtO_x layer growth and the associated changes in electrical properties. This fundamental study of operando ECSE measurement on a platinum surface demonstrates the accuracy of potential-dependent surface analysis and opens a wide field for electrochemical and electrocatalytic studies under operando conditions.

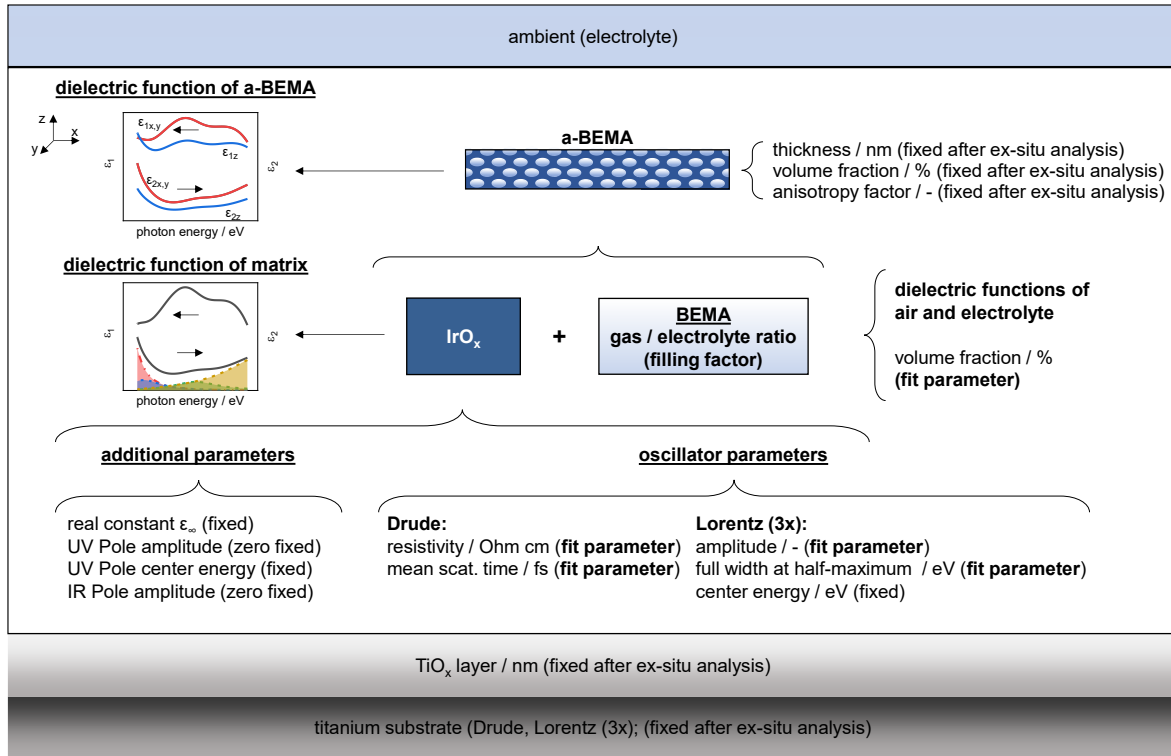
6. Operando ECSE analysis of mesoporous IrO_x films under OER conditions

With the findings from the precise ex-situ SE analyses of the mesoporous IrO_x films in Chapter 4 and the successful ECSE studies on bulk Pt and the detectable changes in surface properties in Chapter 5, the mesoporous IrO_x films can be investigated ellipsometrically under electrochemical conditions. In the first part of this section, a mesoporous IrO_x film calcined at 375 °C was exemplarily studied by linear sweep voltammetry (LSV) during OER (Chapter 6.1), followed by investigations with cyclic voltammetry in the OER regime (Chapter 6.2). Subsequently, the influence of the calcination temperature on derived material properties was studied in the OER regime (Chapter 6.3). Investigations in the potential window of 0.40 V_{RHE} – 1.40 V_{RHE} are exemplarily described for a mesoporous IrO_x film calcined at 375 °C and for the calcination series in detail in the Appendix Chapter A14 and A15, respectively.

As in the platinum ECSE investigations, the first step was to determine the offset of the quartz windows by mounting the dry flow cell on a Si wafer with a known SiO₂ layer thickness. In the next step the cell was filled with the electrolyte (N₂ purged 0.1M HClO₄) and analyzed using the Si wafer as substrate and a Sellmeier parametrization (equation (47)) for the electrolyte (see Chapter 3.4 and Appendix A1 for further details).

For modeling of mesoporous iridium oxide films during electrochemical investigations, a slightly modified model as described in Chapter 4.2 was used (see Scheme 4). The model of the Ti substrates consists of a Ti substrate layer (combination of one Drude and three Lorentz oscillators) and an overlaying TiO_x layer (single Tauc-Lorentz oscillator), same as described in the ex-situ analysis of the mesoporous IrO_x films on Ti substrates. The thickness of the TiO_x layer was determined for each Ti substrate before dip-coating and served as a starting point for the analyses after dip-coating and calcination. The derived TiO_x layer thicknesses after the calcination procedure were fixed for the ECSE analysis (see A8 for more details). The parameters of the titanium substrate layer were also fixed after the initial modeling of these values.

The mesoporous IrO_x layer was modeled by the a-BEMA parameterization with an additional isotropic BEMA for the volume fractions of gas (air/void) and electrolyte within the pores instead of the air/void in the ex-situ characterization. In addition, the electrolyte with the parameters obtained from the calibration procedure was used as the ambient layer above the mesoporous IrO_x layer. Assuming that during electrochemistry the material properties as well as the interactions between iridium and oxygen change with the applied potential, the resistivity (ρ_R) and mean scattering time (τ) of the Drude, the amplitude (Amp) and full width at half-maximum (Γ) of each Lorentz oscillator as well as the volume fraction of the produced gas within the pores were used as free parameters. It was also assumed that the film thickness and pore anisotropy (geometry) are not affected during electrochemical investigation. To prove the independence of the layer thickness, XRR measurements were performed to determine the film thickness at different ambient humidity conditions (between 16% and nearly 100%). Furthermore, instrumented indentation testing was carried out to determine the Young's modulus of the films. A detailed description of both measurements is given in Appendix A7.



Scheme 4: Illustration of the developed model for spectroscopic ellipsometric analysis during electrochemical investigations for mesoporous iridium oxide films on titanium substrates. The model includes the IrO_x material (matrix), modeled by a combined Drude-Lorentz parametrization, the volume fraction of electrolyte and produced gas within the pores (filling factor) and the electrolyte as ambient. A titanium layer (Drude-Lorentz) served as substrate with an overlaying TiO_x layer (Tauc-Lorentz).

6.1 Study of the ellipsometric behavior using linear sweep voltammetry

Mesoporous IrO_x films are more complex than bulk polycrystalline Pt due to their low crystallinity and the additional consideration of film thickness and porosity (volume fraction and geometry). To investigate the behavior of ellipsometric studies during oxygen evolution of mesoporous IrO_x catalysts, a film on a titanium substrate calcined at 375 °C (see Chapter 4 for ex-situ characterization) was exemplary measured by linear sweep voltammetry (LSV), starting at 1.20 V_{RHE} and ending at a potential of 1.40 V_{RHE}. Subsequently, a 30-minute chronoamperometric (CA) step was performed at 1.20 V_{RHE}. For following LSV measurements, the final potential was increased by 0.02 V at each step until a final potential of 1.50 V_{RHE} was reached, followed by a 30-minute CA step at 1.20 V_{RHE} in each case. Figure 37 displays first a) the potential steps, b) the current density, c) the amplitude of the reflection coefficient for parallel polarization (r_p), and d) the amplitude of the reflection coefficient for perpendicular polarization (r_s), at an exemplary photon energy of 2.2 eV during LSV and CA measurements.

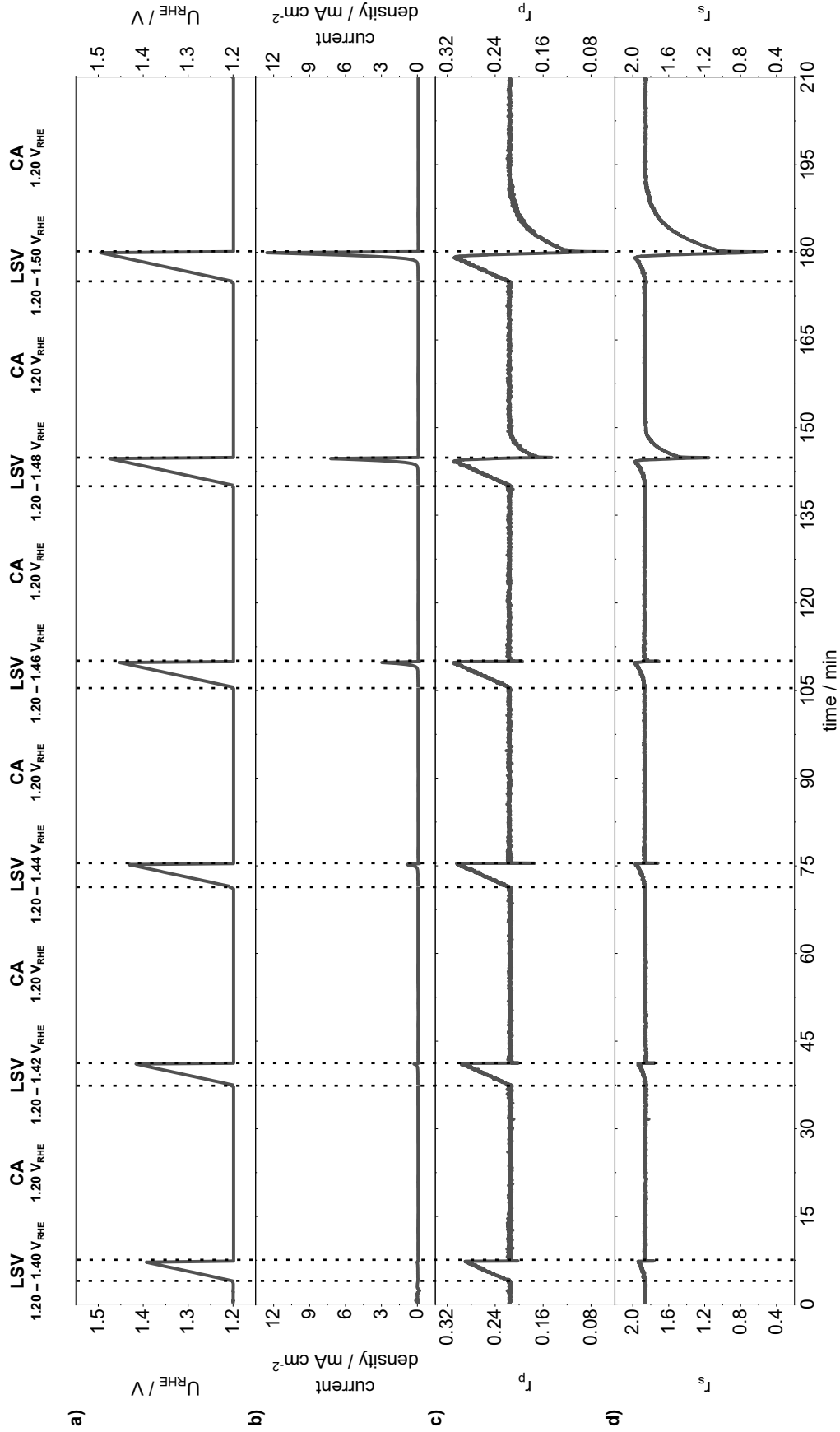


Figure 37: Electrochemical and optical results during ECSE studies of a mesoporous IrO_x film calcined at 375°C . a) linear sweep voltammetry (LSV) at potentials between $1.20\text{ V}_{\text{RHE}}$ and $1.50\text{ V}_{\text{RHE}}$ in 0.02 V steps and scan rates of 1 mV s^{-1} as well as chronoamperometry (CA) at $1.20\text{ V}_{\text{RHE}}$. EC measurements were performed in N_2 -purged 0.1M HClO_4 with a flow rate of 85 ml min^{-1} . b) current response during LSV and CA. c) amplitude of the reflection coefficient for parallel polarization (r_p) and d) amplitude of the reflection coefficient for perpendicular polarization (r_s) at a photon energy of 2.2 eV .

LSV measurement from 1.20 V_{RHE} to 1.40 V_{RHE} shows the linear increase of the potential (Figure 37a) and a constant behavior of the current response (Figure 37b) close to 0 mA cm⁻². Subsequently, a constant potential of 1.20 V_{RHE} is applied during CA and the current response also reveals a constant behavior at 0 mA cm⁻². The second LSV (until 1.42 V_{RHE}) provides a similar result. At the third LSV (from 1.20 V_{RHE} to 1.44 V_{RHE}), a low current response of about 1 mA cm⁻² is observed. The current density increases with reaching higher potentials up to a value of about 12 mA cm⁻² (at 1.50 V_{RHE}). For each CA measurement, a constant behavior is obtained for the potential and current density.

The amplitude of the reflection coefficient for parallel polarization (r_p) in Figure 37c indicates a similar behavior as the potential (Figure 37a) and increases linearly during the LSV and returns abruptly to the initial state in the CA. However, in the LSV step until 1.48 V_{RHE} a significantly lower value than the initial value can be observed at the end of the LSV and at the beginning of the CA, which returns to the initial value within about 3 min during the CA measurement. This effect is even more pronounced at 1.50 V_{RHE} and the return to the initial value takes approximately 9 min. In addition, the curve decreases strongly at higher potentials (> 1.46 V_{RHE}), when higher current densities are reached and before the CA measurement takes place. A similar behavior is also observed for the amplitude of the reflection coefficient for perpendicular polarization (r_s), with a smaller increase during LSV (Figure 37d).

The linear increase in both amplitudes of r_p and r_s during LSV measurements can likely be associated with changes in the electrical and/or electronic state of the IrO_x material due to the change of the potential. Thus, the abrupt decreases at higher potentials can probably be related to an exponential increase in the current density response and the associated gas production. The different refractive indices of the electrolyte and the produced oxygen gas lead to the rapid change in the amplitudes of r_p and r_s . Thus, the slow return of the two amplitudes to the initial values probably indicates a slow removal of the produced oxygen gas from the pores.

For a better understanding of these behaviors, the Ψ and Δ spectra were evaluated using the model described above. Figure 38 shows a) the applied potential and b) the obtained current response for comparison and additionally the measured Ψ and Δ spectra with their fit results at an exemplary photon energy of 2.2 eV (c), the resistivity (d) and the ratio of gas and electrolyte (e), both derived from the model.

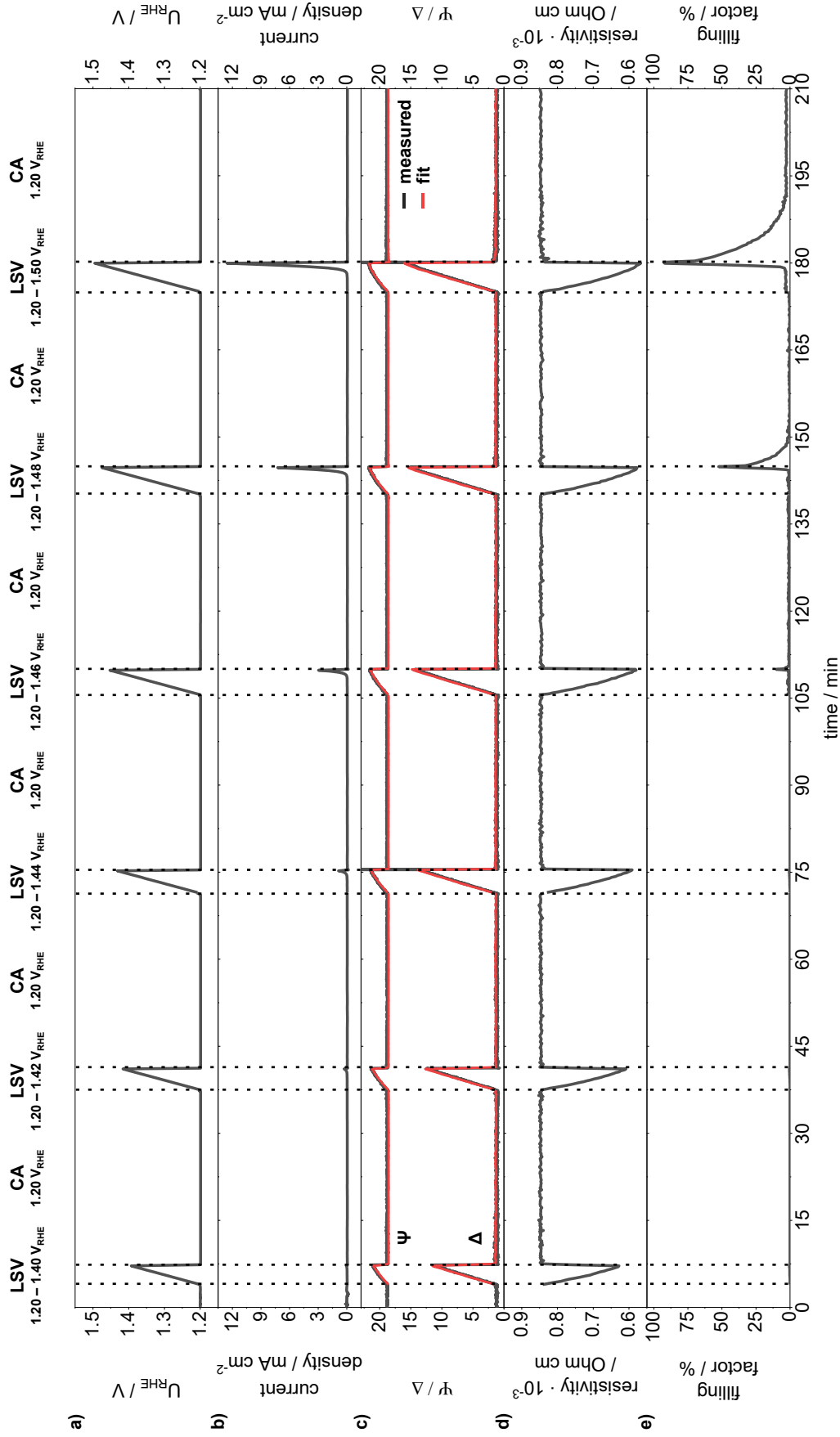


Figure 38: Electrochemical and spectroscopic ellipsometry results of the ECSE investigation of the mesoporous IrO_x film calcined at 375 °C. a) potential of LSV and CA measurement and b) current densities obtained from EC measurements in 0.1M $HClO_4$ with a flow rate of 85 $ml\ min^{-1}$ and scan rates of 1 $mV\ s^{-1}$. c) ψ and Δ spectra with their fit results at a photon energy of 2.2 eV. Derived resistivity (d) and ratio of gas and electrolyte (e) from model analysis during LSV and CA measurements.

The Ψ and Δ curves (black curves), exemplarily shown at a photon energy of 2.2 eV (Figure 38c), increase linearly for all LSVs and decrease abruptly to the initial value with the beginning of the CA procedure. Figure 38c additionally displays the results of the model fit for the same photon energy (red curves). This fit was calculated for the entire measured spectral range between 1.1 eV and 6.4 eV, yielding the result parameter values such as resistivity and the volume fraction of produced gas (filling factor), which shown in Figure 38d and e, respectively.

The deduced resistivity (Figure 38d) shows an almost linear decrease during LSV and returns to the initial value during CA measurements. In addition, lower resistivity values are obtained with increasing potential. This could indicate a linear dependence of the resistivity on the applied potential. In order to verify if this is an effect of the applied potential on the modeled Ψ and Δ spectra, operando measurements are performed on a non-conductive mesoporous titanium oxide (TiO_x) film in the OER regime and in the potential range between 0.40 V_{RHE} and 1.40 V_{RHE}. In both potential regions, no changes in the Ψ and Δ spectra with changes in potential were observed (see A13 for the complete operando ECSE investigation of a mesoporous TiO_x film).

In addition to the resistivity, the volume fraction of the produced gas (filling factor) can be derived from the model (Figure 38e). For LSV measurements until a potential of 1.44 V_{RHE}, no volume fraction of gas is deduced from the model, although a current density of 1 mA cm⁻² is reached at a potential of 1.44 V_{RHE}. At a current density of 3 mA cm⁻² (1.46 V_{RHE}) the filling factor increases to a volume fraction of about 10% and decreases rapidly during subsequent CA at 1.20 V_{RHE}. When a potential of 1.48 V_{RHE} and a current density of 7 mA cm⁻² are reached, the filling factor increases to a value of about 52% and at 1.50 V_{RHE} (12 mA cm⁻²) to a volume fraction of almost 100%. In both cases, the filling factor slowly decreases and takes about 4 minutes (1.48 V_{RHE}) or 10 minutes (1.50 V_{RHE}) to reach the initial value. These results are similar to the progress of the amplitudes of r_p and r_s .

From the derived filling factor at a potential of 1.50 V_{RHE}, a volume fraction of almost 100% oxygen gas is present within the pores. In order to avoid scattering of light at gas bubbles that might adhere to the surface, following ECSE measurements in the OER regime of mesoporous IrO_x films were performed until a potential of 1.48 V_{RHE}.

6.2 Ellipsometric analysis and modeling during cyclic voltammetry

With the knowledge gained in Chapter 6.1 on the behavior of the ellipsometric quantities at different potentials, a complete operando analysis of the material properties of the IrO_x film calcined at 375°C using cyclic voltammetry under OER conditions is now possible. In the following of this Chapter, the measured data and modeling as well as the derived material properties will be described first and discussed at the end of the Chapter. Figure 39 shows a cyclic voltammetry measurement in the OER region (a), the Ψ and Δ spectra during cyclovoltammetry (b) and Ψ (c) and Δ (d) spectra at selected photon energies as a function of the measurement time of the mesoporous IrO_x film calcined at 375°C .

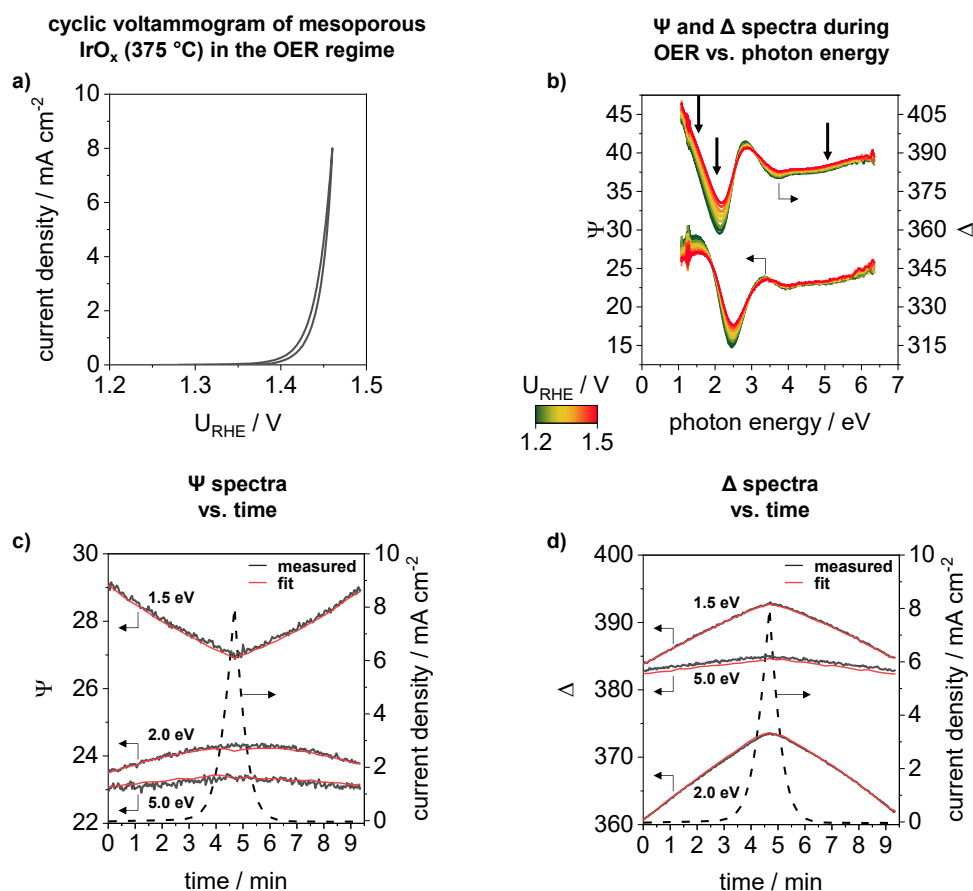


Figure 39: Operando ECSE investigations in the OER regime of the mesoporous IrO_x film calcined at 375°C . a) cyclic voltammetry measurement in a potential range of $1.20 U_{\text{RHE}}$ and $1.48 U_{\text{RHE}}$ in N_2 purged 0.1M HClO_4 with a scan rate of 1 mV s^{-1} and an electrolyte flow rate of 85 ml min^{-1} . Potentials were measured against an Ag/AgCl electrode, which referred to RHE ($+0.256 \text{ V}$ at $\text{pH } 1$). b) Ψ and Δ spectra measured during cyclic voltammetry. c) Ψ and d) Δ spectra with fit results at photon energies of 1.5 eV , 2.0 eV and 5.0 eV together with the current density curve as a function of acquisition time.

The cyclic voltammetry measurement of the catalyst film (Figure 39a) shows a typical progress of the current response, which is discussed in detail in Chapter 4.3. The Ψ and Δ spectra display noticeable changes over the entire spectral range during the cyclovoltammetry measurement (Figure 39b). For a better comparison, the Ψ and Δ spectra at photon energies of 1.5 eV , 2.0 eV and 5.0 eV (black curves) are plotted together with the current response (dashed line) against the acquisition time (Figure 39c, d). The largest changes in both spectra are observed in the low

photon energy range, where electronic effects occur. This is in good agreement with the preliminary analysis in Chapter 6.1, where the resistivity indicates a dependence on the applied potential. The spectra show an increase or decrease with increasing current density and a reversible curve for the back scan. However, especially in the low photon energy range, the spectra are not completely reversible and indicate a slight offset, with the initial value not being reached again at the end of the cycle (see e.g., Ψ at 1.5 eV or Δ at 2.0 eV). Nevertheless, the modeled spectra (red curves) are in good agreement with the measured Ψ and Δ spectra.

In order to get further insights into the observed behaviors, changes in the dielectric functions were deduced from the fitting results, which provide information about band transitions as discussed in detail in Chapter 4.2. Figure 40 displays the ε_1 (a) and ε_2 (b) spectra during cyclic voltammetry as a function of the photon energy and ε_1 (c) and ε_2 (d) spectra together with the current response against the potential.

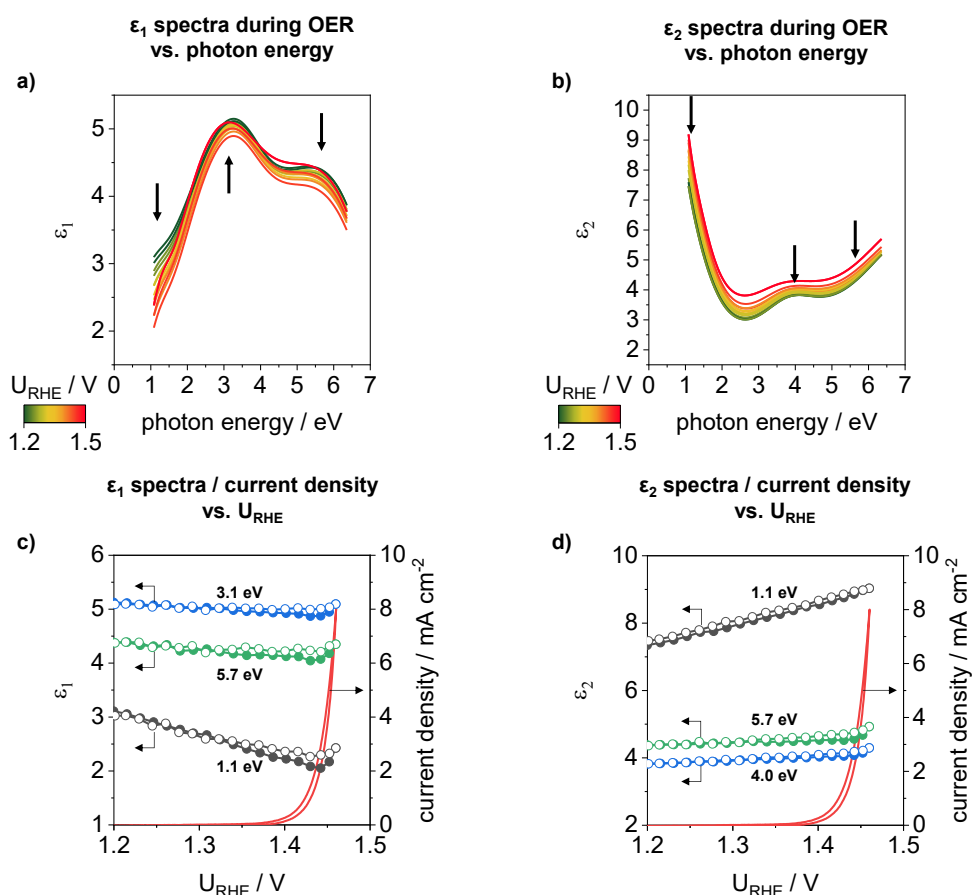


Figure 40: ε_1 and ε_2 spectra of the IrO_x material (matrix) derived from modeling during ECSE investigation. a) ε_1 and b) ε_2 spectra during cyclic voltammetry measurements. c) ε_1 at photon energies of 1.1 eV, 3.1 eV and 5.7 eV as well as d) ε_2 at photon energies of 1.1 eV, 4.0 eV and 5.7 eV.

The ε_1 and ε_2 spectra of the IrO_x material show changes over the entire spectral range in both cases (Figure 40a, b). This is based on the assumption that both the electrical properties and the interactions between Ir and O change during cyclic voltammetry. As described in Chapter 4.2, features in the ε_2 spectra below 2.0 eV can be mostly attributed to excitations of the conduction band and intraband transitions from filled to empty states of the t_{2g} sub-level. Absorption features

above 2.0 eV can be correlated with transitions from the p-orbitals of oxygen to the d-bands of iridium. During cyclovoltammetry, changes in conduction band excitations (below 2.0 eV) and intraband transitions (near 1.0 eV) as well as in interband transitions (above 3.0 eV) can be observed in the ε_2 spectra (Figure 40b). The features in the ε_1 spectra at photon energies of 1.0 eV, 3.1 eV and 5.7 eV (see Figure 22 for ex-situ SE characterization) also indicate noticeable changes (Figure 40a).

By plotting the characteristic features against the potential, the variations can be correlated with the current density curve. The selected features in the ε_1 spectra show a linear decrease with increase of the potential, while at about 1.44 V_{RHE} a slight increase is visible (Figure 40c). Except for the curve at 1.1 eV, which indicates a small hysteresis loop, the spectra appear to be almost completely reversible. A similar behavior is also observed for the characteristics in the ε_2 spectra, whereas the features indicate an increase with increasing potential (Figure 40d).

For a more detailed analysis of the electronic structure of the IrO_x material, the bulk ($-\text{Im}(\varepsilon^{-1})$) and surface ($-\text{Im}((1 + \varepsilon)^{-1})$) VEEL spectra can be calculated from the dielectric function using equation (2) and (3). Additionally, d-d intraband transition energies can be deduced from the Tauc relation as described in Chapter 4.1 and 4.2. Figure 41 shows a) the bulk and surface VEELS, the center energy values of the identified peaks for b) bulk and c) surface VEELS as well as d) the intraband transition energies as a function of the potential.

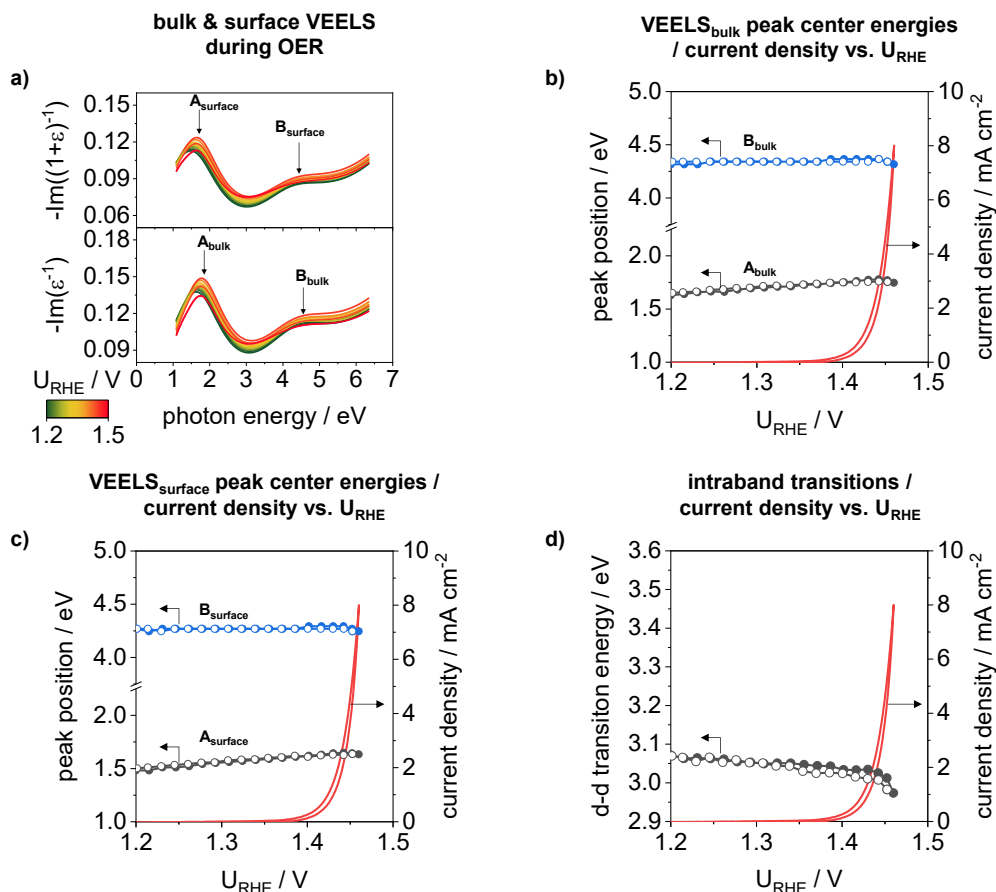


Figure 41: Valence electron energy loss spectra analysis and intraband transition energies during ECSE measurements in the OER regime. a) calculated bulk and surface VEEL spectra at different potentials during OER. A and B peaks of b) bulk VEELS and c) surface VEELS as a function of the applied potential. d) derived intraband transition energies between the Ir 5d t_{2g} and e_g band in dependence on the potential.

Both VEEL spectra clearly show the presence of the two previously identified A and B peaks. A shift of the center energy is observed especially for the A peaks as well as a change in intensity for both A and B peaks. Compared to the center energy from the ex-situ characterization of the mesoporous IrO_x film calcined at 375 °C on a titanium substrate, the peaks in both spectra are shifted to higher energies by about 0.5 eV for the A peaks and by 0.1 eV for the B peaks (see Appendix A10 for detailed ex-situ VEELS analysis of mesoporous IrO_x films on Ti substrates).

Figure 41b displays the center energy of the A and B peak derived from the bulk VEELS together with the current density curve as a function of the potential. The A_{bulk} peak indicates a linear shift of the center energy with an increase in potential. The maximum energy value is reached at a potential of about 1.44 V_{RHE} and then remains approximately constant. In contrast, the B_{bulk} peak demonstrates an almost constant energy value. The center energies of the two peaks in the surface VEELS show a similar behavior, shifted by about 0.1 eV to lower energies (Figure 41c).

The transition energies from the Tauc relationship show a linear decreasing trend of the energy values with increasing potential (black circles). A stronger decrease of the transition energy in the range of 1.44 V_{RHE} is observed. In the back scan (white circles) slightly lower energy values until a potential of about 1.30 V_{RHE} are observed.

In addition to the electronic structures of the material, modeling can also be used to derive electrical parameters and the volume fraction of the produced gas (filling factor), as shown in the preliminary analysis. Figure 42 displays a) the filling factor, b) the resistivity, c) the electron mobility, and d) the electron concentration.

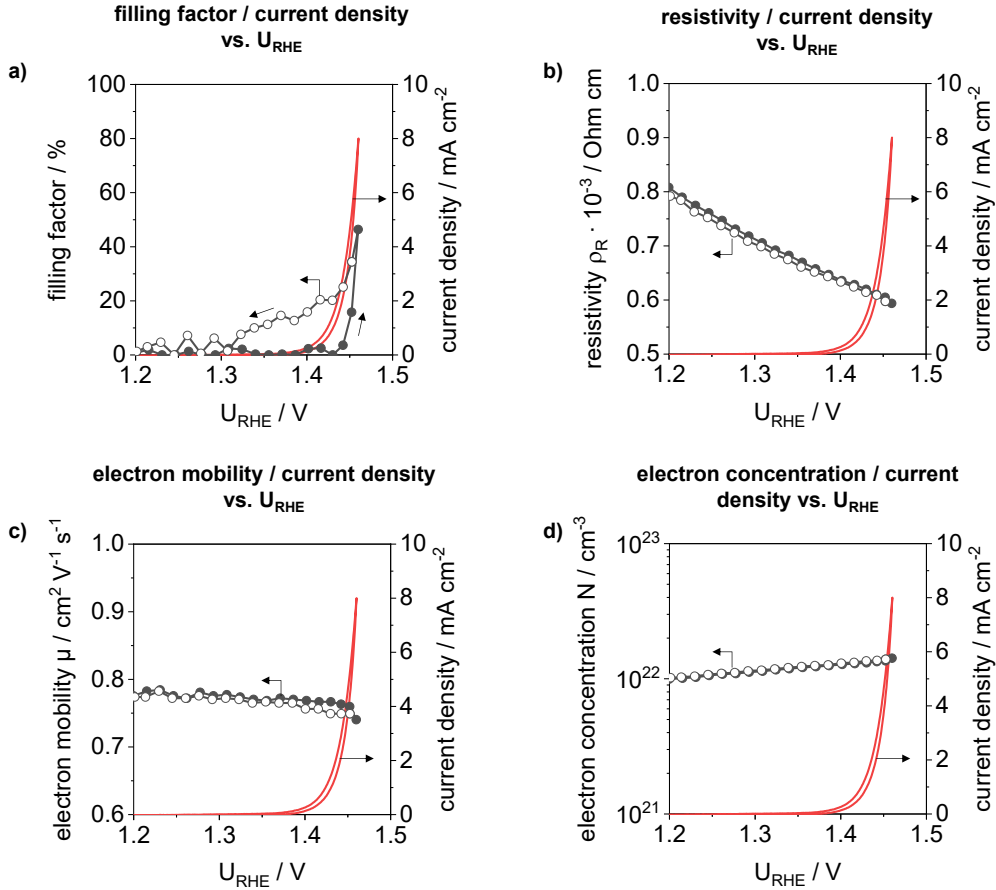


Figure 42: Derived properties from the model analysis during ECSE measurements in the OER regime. a) volume fraction of the produced gas (filling factor), b) resistivity, c) electron mobility, and d) electron concentration as a function of the applied potential.

The deduced filling factor (Figure 42a) indicates a constant value close to zero for the forward-scanning cycle (black circles) until a potential of about 1.45 V_{RHE} and a current density of 2 mA cm^{-2} are reached. As the potential continues to increase, the filling factor increases rapidly to a value of about 46%. In the back-scanning cycle (white circles), the filling factor decreases more slowly than in the forwards cycle and reaches a value close to zero at a potential of about 1.30 V_{RHE} . The model analysis thus indicates that the gas adheres in the pores and is only slowly replaced by the electrolyte. A similar behavior was observed in the preliminary analysis through the model evaluation in Chapter 6.1, where the filling factor indicates a slow decrease when reaching a potential of 1.48 V_{RHE} and higher during the CA measurement at a constant potential of 1.20 V_{RHE} (Figure 38e).

In contrast, the resistivity (Figure 42b) shows a completely reversible behavior and decreases with increasing potential. Haverkamp and co-workers studied the electronic structure of electrochemically formed iridium oxide films.¹⁸⁹ Conductivity measurements (inverse of resistivity) with two epoxy-embedded gold electrodes on these iridium oxide films suggest a constant to slightly increasing conductivity at low-potentials and a stronger increase at a potential of about 1.20 V_{RHE}, which remains almost constant at higher potentials. The resistivity derived from the model analysis indicates a similar behavior to this conductivity measurements.

The calculated electron mobility (Figure 42c) is approximately constant and decreases slightly at higher potentials. A small hysteresis is observed in the back-scanning cycle until a potential of 1.40 V_{RHE} is reached. In contrast, the electron concentration increases with increasing of potential and also remains completely reversible (Figure 42d).

The changes in the electrical and electronic properties of the IrO_x film can be explained by the proposed different oxidation states of Ir. During catalysis, several proton-coupled electron transfer steps take place, which can occur at potentials between 1.20 V_{RHE} and 1.50 V_{RHE}.^{23, 190-193} A further progress of catalysis depends on the electrode potential. In case of a relatively low-potential, as in this case, decomposition of an Ir^{VO}₂OH species is assumed with the release of O₂ and a formation of an Ir^{III} intermediate.^{194, 195} Finally, the metastable Ir^{III} species can be converted back to an Ir^{IV} species. The assumption that Ir is simultaneously in oxidation states between Ir^{III} and Ir^V during the OER reaction may be an explanation for the slight increase in the ϵ_1 and ϵ_2 spectra at higher potentials in Figure 40c and d, respectively.

The oxidation or deprotonation of adsorbed OH species and the subsequent formation of Ir-OO(H) species also have a direct effect on the interband transitions between the Ir 5d t_{2g} levels and the O 2p bands. From the observations reported in the literature, higher p-d interband transition energies can be interpreted with a shift of the Ir 5d t_{2g} band to lower energies and an increased electron density as well as a more filled d-band.^{34, 35, 44} Consequently, the covalent character of the M-O bond is strengthened.³⁴⁻³⁶ The A peaks in the VEEL spectra represent interband transitions between the partially filled t_{2g} level of the d-band of iridium and the p-band of oxygen. In both cases, in the bulk and surface VEEL spectra, shifts in the interband transition energies can be observed (Figure 41b and c). A slight change of the transitions between the p-bands of oxygen and the unoccupied t_{2g} bands of Ir 5d are also evident in the B peaks at higher potentials (Figure 41b and c). These changes indicate a shift of the Ir 5d t_{2g} band. The change in electron concentration is also in good agreement with the increase in electron density with increasing covalency and overlap of the p-d bands reported in literature.^{34, 35} The slight decrease in electron mobility may also indicate a more pronounced electron density, due to the higher scattering of electrons and the associated change in energy.⁴²⁻⁴⁴ Subsequent decomposition of the Ir^V species and the release of O₂ then leads to the relatively constant or slightly decreasing transition energy values of the A and B peaks at higher potentials (Figure 41b and c), since it is assumed that oxidations states between Ir^{III} and Ir^V are present in this potential range.^{23, 194} The change in oxidation state shifts the Ir 5d t_{2g} band upward, increasing the adsorption of O species.^{45, 46}

Another parameter from the ECSE analysis of the IrO_x film is the derived intraband transition energies between the Ir 5d t_{2g} and e_g bands, which show a decreasing trend with increasing potential (Figure 41d). Shao-Horn and coworkers studied the relative occupancy of the t_{2g} and e_g states of oxide materials (e.g., in perovskites) and propose that the occupation of electrons at a d-orbital splitting larger than the energy of the electron pairing energy leads to a low-spin configuration (complete occupation of the low-energy t_{2g} states).¹⁹⁶ If the splitting is smaller than the electron pairing energy, electrons occupy the e_g states before pairing in the t_{2g} states (high spin configuration).¹⁹⁶ These spin state configurations can influence e.g. the electronic conductivity and/or the catalytic activity.^{197, 198} This would agree with the changes in interband transition energies and the shift in the Ir 5d t_{2g} band described above. This implies that the down shift of the t_{2g} band leads to a higher d-orbital splitting and the electrons fully occupy the low-energy t_{2g} states. In addition, an investigation in the lower potential range (0.40 V_{RHE} - 1.40 V_{RHE}) of this mesoporous IrO_x film shows an up shift of the intraband transition energies to lower potentials and a broad feature at about 0.95 V_{RHE}, indicating a lower d-orbital splitting and the Ir^{III}/Ir^{IV} redox couple, respectively (see Appendix A14 for more details).

Finally, the adhesion of the produced gas should be discussed. The derived volume fraction of the produced gas (filling factor) shows a hysteresis loop in the back scan (Figure 42a). This indicates an accumulation of oxygen bubbles within the catalyst layer. Results from EP measurements (see Appendix A11) of the IrO_x film on the Ti substrate show that micropores are present in addition to mesopores. The rapid decrease of the filling factor in the back-scanning cycle is probably due to the release/dissolution of the gas from the mesopores, while the slow decrease of the filling factor indicates the release/dissolution from the micropores. Due to the much smaller pore diameter of the micropores (≤ 2 nm) compared to the mesopores (~ 15 nm, see Figure 14 and Table 1), the release/dissolution of the gas is inhibited, and the observed hysteresis loop occurs. Stoerzinger *et al.* also suggest a hysteresis behavior of oxygen during OER in their studies on the contribution of lattice oxygen from RuO₂ films and nanoparticles to the produced oxygen using online electrochemical mass spectrometry (OLEMS).²¹

In summary, operando ECSE analysis in the OER regime of the mesoporous IrO_x film, calcined at 375 °C, proves the existence of changes within the dielectric function due to the change of Ir oxidation states and the change of the p-d interaction. In addition, a shift of the A peak in the VEEL spectra is visible, which was previously associated with a linear correlation of the intrinsic OER activity. Moreover, a change in the transition energies between the Ir 5d t_{2g} and e_g band is observed, which can probably be attributed to changes in the spin state configuration. The changes in the Ir 5d t_{2g} band and the p-d interband transitions are also directly reflected in the electrical properties of the material. Furthermore, according to the current state of knowledge, the model analysis provides for the first time an analysis of the volume fraction of the produced gas and gives an indication of an accumulation of gas bubbles within the pores.

6.3 Influence of calcination temperature on material properties

The calcination temperature has a strong impact on film morphology and crystallinity and thus a direct influence on material properties, band structures and catalytic activities in the oxygen evolution reaction as shown by the results of the ex-situ analyses in Chapter 4. The proposed changes in electrical properties and band structures as well as the change in Ir oxidation state successfully explain the operando ECSE analyses of a mesoporous IrO_x film (375 °C) in the OER range (Chapter 6.2) as well as in a potential range from 0.40 V_{RHE} to 1.40 V_{RHE} (Appendix A14). In addition, an indication of gas formation during OER could be provided. Now the influence of the calcination temperature on these parameters can be investigated of mesoporous IrO_x films on Ti substrates from the calcination series (300 °C – 600 °C). As described in the introduction part of this Chapter 6, each catalyst film was modeled using the same procedure. In this section the influence of the calcination temperature on derived IrO_x parameters during the OER is described. The ECSE investigations of the influence of calcination temperature on the material properties in the potential range of 0.40 V_{RHE} and 1.40 V_{RHE} are described in detail in the Appendix Chapter A15. In the following, the measured data and the modeling as well as the derived material properties are first described and discussed at the end of this section.

Figure 43 presents first a) the measured current responses in the OER regime during ECSE measurement, b) Ψ and c) Δ curves as well as ε_1 (d) and ε_2 (e) curves of mesoporous IrO_x samples calcined at 300 °C, 350 °C, 375 °C, 400 °C, 500 °C and 600 °C in dependence on the applied potential. The current densities (Figure 43a I-VI) show an increasing OER activity until a calcination temperature of 375 °C and decrease with higher temperatures and thus have a similar behavior as described for the ex-situ characterization in Chapter 4.3. The electrochemical investigations are therefore not discussed in detail and only used for comparison and correlation of the obtained model parameters.

Ψ curves of the calcination series indicate a systematic change with increasing calcination temperature (Figure 43b I-VI). The Ψ values at a photon energy of 1.5 eV (black curves) decrease from 1.20 V_{RHE} to 1.48 V_{RHE} for catalysts calcined between 300 °C and 400 °C (Figure 43b I-IV), while they are approximately constant at this photon energy for the 500 °C and 600 °C calcined films (Figure 43b V-VI). At photon energies of 2.0 eV and 5.0 eV, a general decreasing trend with increasing calcination temperature is observed in the Ψ values, except for the 400 °C and 500 °C films and a photon energy of 2.0 eV. Additionally, films calcined between 350 °C and 400 °C reveal a slight offset of the curves at a photon energy of 2.0 eV. A similar trend is observed for the Δ curves, where a systematic increase of the values occurs for photon energies of 1.5 eV and 2.0 eV with increasing calcination temperature and an almost constant behavior for photon energies of 5.0 eV (Figure 43c I-VI).

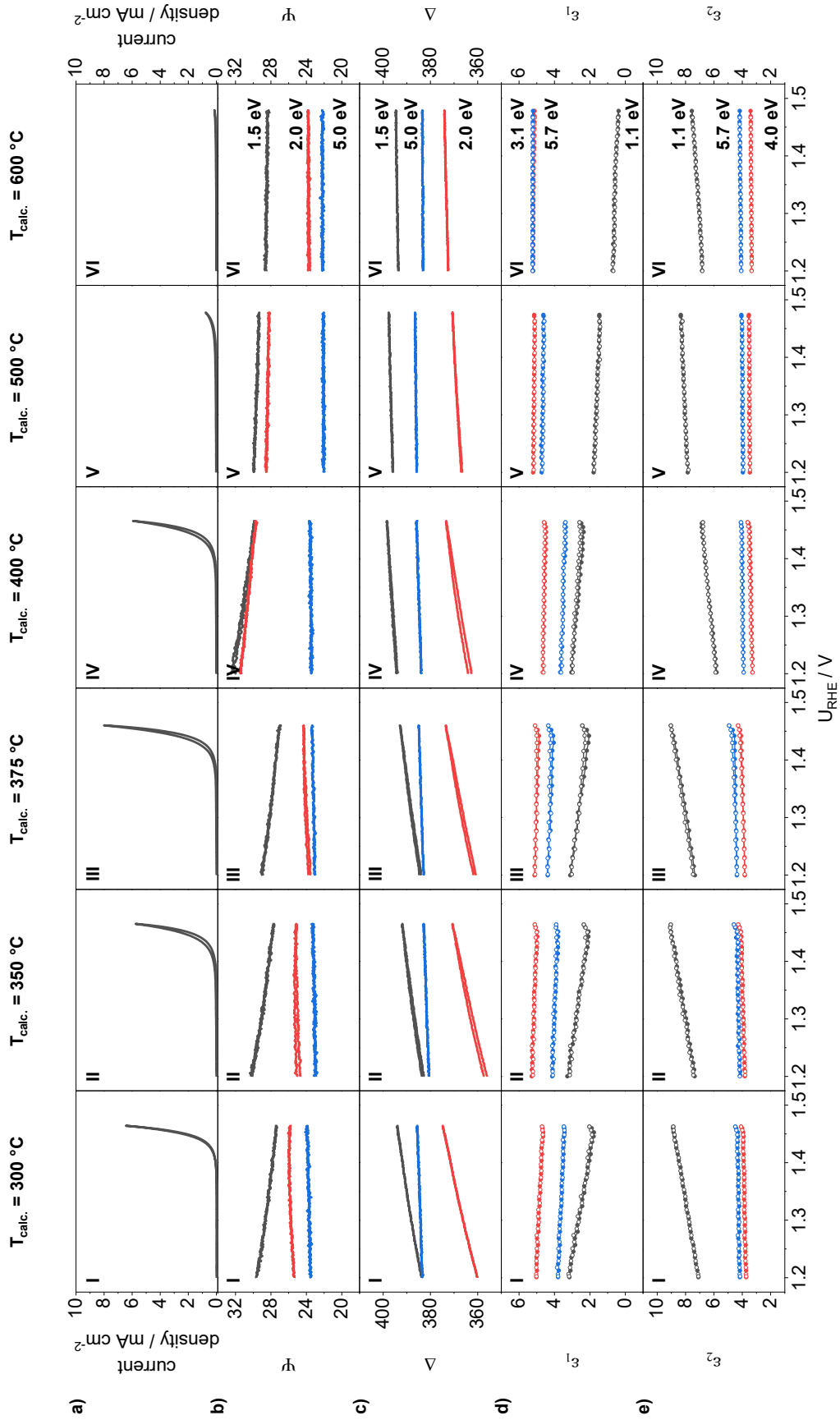


Figure 43: Operando ECSE investigations and derived ϵ_1 and ϵ_2 spectra of mesoporous IrO_x films calcined between 300 °C and 600 °C during the OER. a) obtained current density curves from EC measurements in the potential range of 1.20 V_{RHE} and 1.48 V_{RHE} with a scan rate of 1 mV s^{-1} in 0.1M HClO_4 and a flow rate of 85 ml min^{-1} . Selected photon energies of 1.5 eV, 2.0 eV and 5.0 eV from Ψ (b) and Δ (c) spectra during EC. Characteristic features of d) ϵ_1 and e) ϵ_2 spectra at photon energies of 1.1 eV, 3.1 eV or 4.0 eV and 5.7 eV.

ε_1 values decrease at a photon energy of 1.1 eV, 3.1 eV and 5.7 eV for catalysts calcined between 300 °C and 400 °C (Figure 43d I-IV), whereas the higher calcined films are roughly constant within their ε_1 values (Figure 43d V-VI). Additionally, a slight increase at potentials from 1.46 V_{RHE} is observed for the films calcined between 300 °C and 400 °C. In contrast, the derived ε_2 curves reveal an increasing trend at a photon energy of 1.1 eV for low-temperature calcined films (≤ 400 °C) and approximately constant values at higher temperatures as well as almost constant values for photon energies at 4.0 eV and 5.7 eV over the complete calcination series.

In order to obtain further insights into the influence of the calcination temperature on the electronic structure, properties are deduced from the VEELS analysis. Figure 44 depicts a) the current density curves for comparison and correlation, the center energy of the bulk and surface A (b) and B (c) peaks as well as d) intraband transitions from the Tauc relation.

The A peaks center energy values for the bulk and surface VEELS increase strongly with increasing potential for catalyst films calcined in the range of 300 °C and 400 °C (Figure 44b I-IV), while a slight increase is observed for the films calcined at 500 °C and 600 °C (Figure 44b V-VI). Furthermore, the slight decrease and/or constant values of the center energy are observed at higher potentials (> 1.44 V_{RHE}). The B peaks reveal for the complete calcination series approximately constant values during the OER and shifted in general to lower energies with increasing calcination temperature (Figure 44c I-VI).

A trend is also observed in the values for transition energies between the Ir 5d t_{2g} and e_g sub-levels during the OER. (Figure 44d I-VI). Values for the low-temperature calcined catalyst films (≤ 400 °C) decline slightly until a potential of about 1.44 V_{RHE} is reached, followed by a stronger decrease. At higher calcination temperatures (> 400 °C), approximately no further changes in the transition energies are observed during the OER.

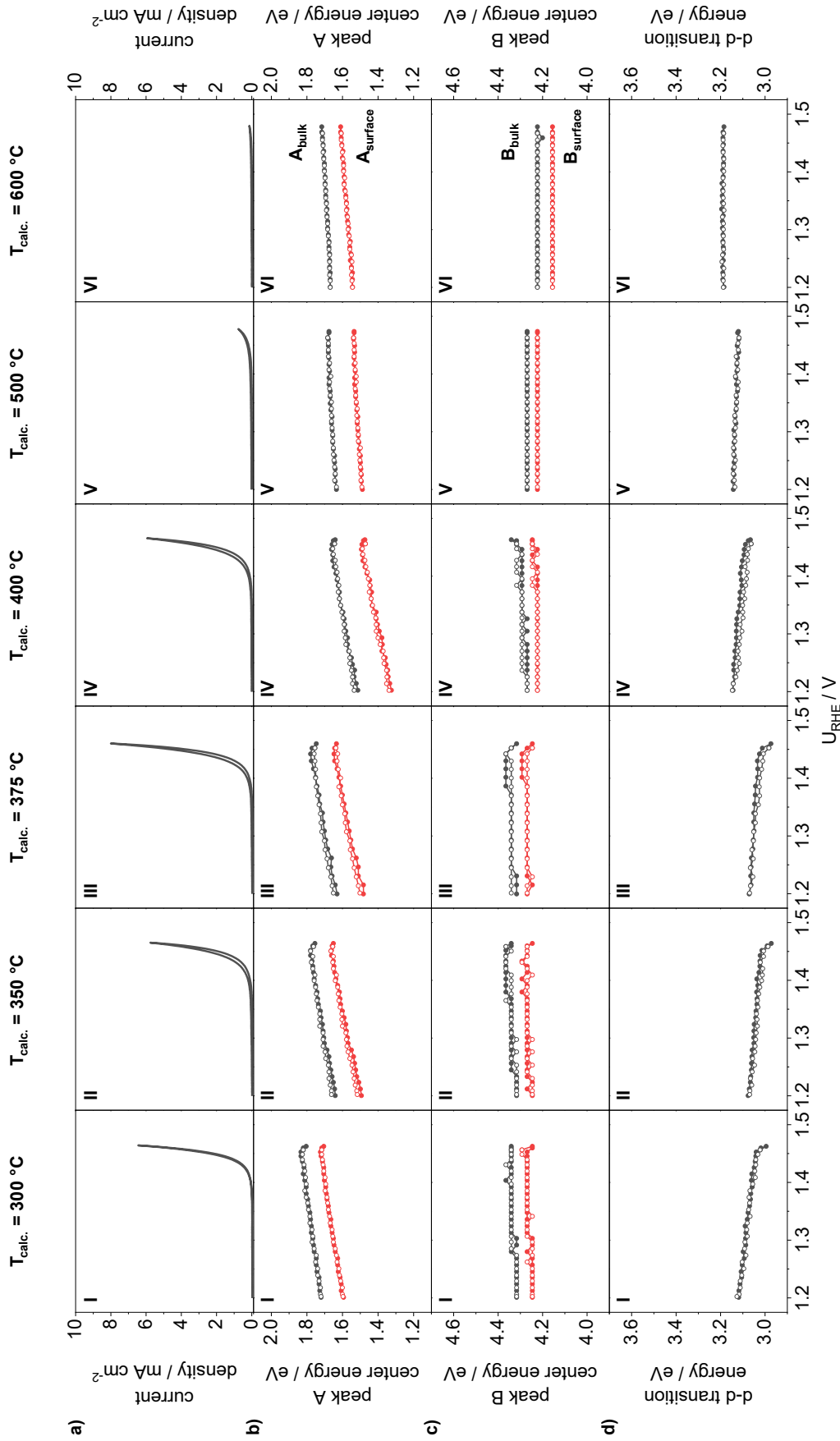


Figure 44: Electronic properties from VEELS analysis and Tauc relations of the mesoporous IrO_x calcination series in the OER regime. a) current density curves from EC measurements. Center energies of the identified A peak (b) and B peak (c) of bulk and surface VEEL spectra in dependence of the applied potential. d) d-d intraband transition energy values deduced from the Tauc relation as a function of the potential.

In addition to the electronic structures of the materials, calcination temperature-dependent electrical properties of the materials can also be derived from the model analysis during the OER reaction. Figure 45 displays again the current density curves (a), the resistivity (b), the electron mobility (c) and concentration (d). In addition, the volume fraction of the oxygen gas (filling factor) is also deduced and shown in Figure 45e for the complete calcination series.

The resistivity values decrease during cyclovoltammetry in the OER regime with increasing potential for IrO_x films calcined between 300 °C and 400 °C (Figure 45b I-IV) and slightly for 500 °C (Figure 45b V). No further changes in resistivity values are visible at a calcination temperature of 600 °C (Figure 45b VI). In addition, similar values can be observed for the catalyst films between 300 °C and 375 °C, followed by a sharp increase in total values at 400 °C, which then decrease again.

The derived electron mobility shows, except for the 350 °C film, similar values at relatively constant behavior for the low-temperature calcined (≤ 400 °C) IrO_x films (Figure 45c I-IV). For the 350 °C film, a slightly decreasing trend is observed and in addition, a slight noise or scattering of the electron mobility (Figure 45c II). The electron mobility for the 500 °C film (Figure 45c V) generally exhibits slightly higher values and also a constant trend. The catalyst film calcined at 600 °C (Figure 45c VI) shows the highest electron mobility of all catalyst films and a slightly decreasing trend towards higher potentials.

For the electron concentration for films calcined between 300 °C and 400 °C, slightly increasing trends can be derived which are generally of the same order of magnitude (Figure 45d I-IV). For the higher calcined films (> 400 °C), the electron concentration remains almost constant over the entire potential range (Figure 45c V-VI).

The deduced volume fraction of the produced gas is shown in Figure 45e for the complete calcination series. The values are close to zero at calcination temperatures of 300 °C to 500 °C for the forward scanning (black circles) until a potential of about 1.45 V_{RHE} is reached and then increases to values between 6% and 46% at higher potentials (Figure 45e I-V). In the back scanning cycle (white circles), the volume fraction of the oxygen gas is almost completely reversible for films calcined at 300 °C, 350 °C and 500 °C, except for noise at 300 °C and 350 °C, and returns to the initial value at a potential of about 1.45 V_{RHE} (Figure 45e I-II, V). In contrast, the catalyst films calcined at 375 °C and 400 °C show a hysteresis loop of the filling factor in the back scanning and reach values close to zero at potentials of 1.30 V_{RHE} and 1.20 V_{RHE}, respectively (Figure 45e III-IV). For the 600 °C calcined film no change of the derived filling factor is observed from the model analysis in the investigated potential range and a constant value of about 25% is obtained (Figure 45e VI).

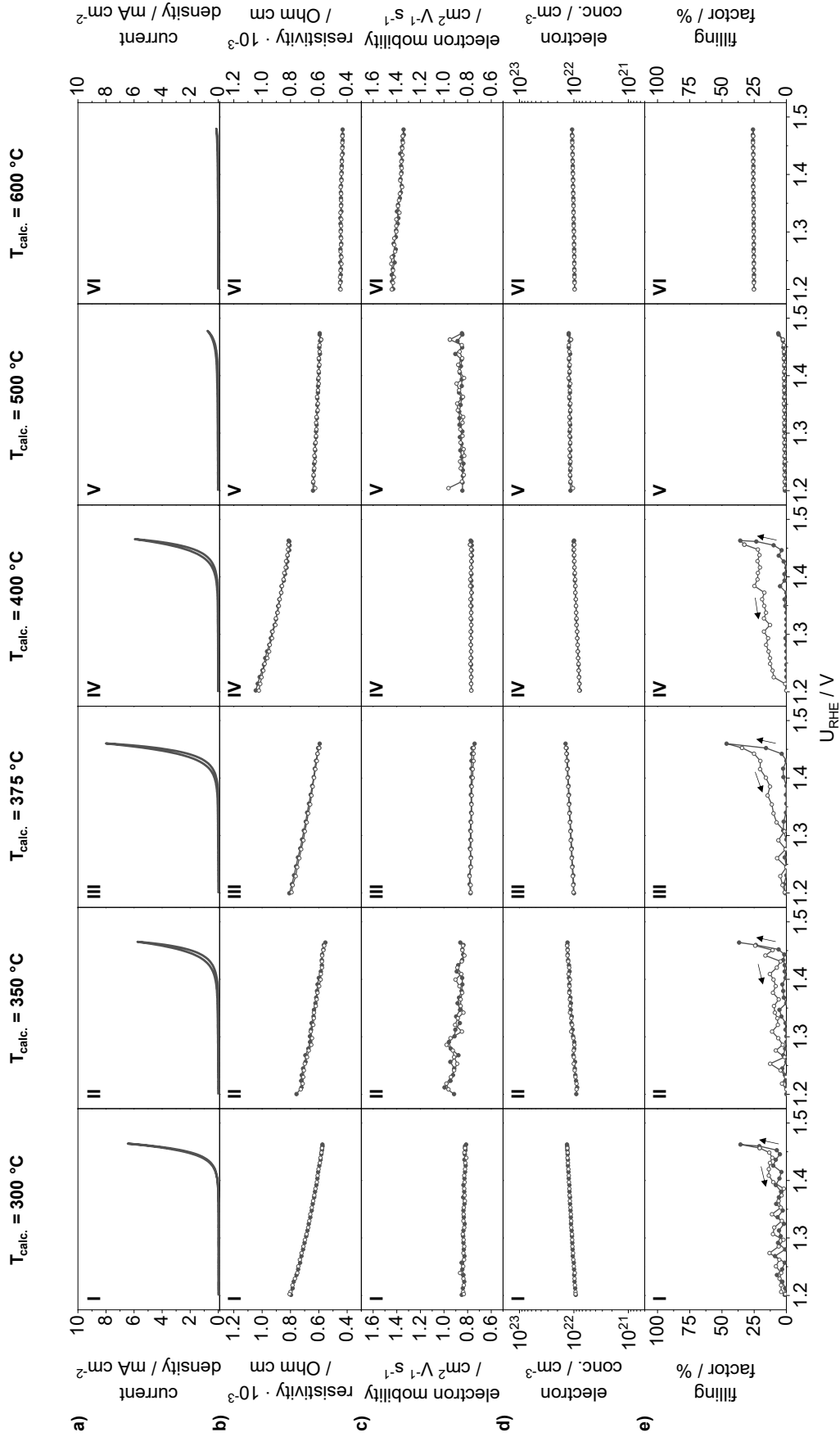


Figure 45: Derived material properties from the model analysis during ECSE investigations of the calcination series in the OER, a) current density curves from cyclic voltammetry measurements. b) resistivity values deduced from the Drude term, c) electron mobility and d) concentration of the IrO_x materials. e) volume fraction of generated gas within the pores during EC measurements in the OER regime.

From all SE data, clearly different regimes of material property behavior can be identified, i.e., samples calcined between 300 °C and 400 °C (low-temperature calcined films) vs. samples calcined at 500 °C and 600 °C (high-temperature calcined films). The observed trends in dielectric functions can be explained by the OER catalysis process with the different intermediates and proton-coupled electron transfer steps involved. As described in Section 6.2, the individual steps can occur at potentials in the range between 1.20 V_{RHE} and 1.50 V_{RHE}, resulting in a change of the Ir oxidation state.¹⁹²⁻¹⁹⁵ These oxidation state changes also directly affect the dielectric functions of the IrO_x films (Figure 43). The low-temperature calcined films show significant changes in the potential range considered, while hardly any changes are observed for the high-temperature calcined films. It is likely that a higher potential is required for the high-temperature calcined films to occur the individual proton-coupled electron transfer steps.

In terms of electronic properties, an increase in the p-d interband transition energies can generally be deduced for the low-temperature calcined films, while the higher-calcined films show only minor to non-significant changes (Figure 44b and c). The changes for the lower calcined films can be interpreted as a shift of the Ir 5d t_{2g} band toward lower energies. This shift also causes the Ir 5d t_{2g} and O 2p bands to come closer, resulting in a weakening of the M-O bond. This effect can also be reflected in the electrical parameters such as resistivity and electron concentration, where the nearing of the Ir 5d t_{2g} band (conduction band) and the O 2p band (valence band) leads to a decrease or increase in the values, respectively (Figure 45 I-IV and Figure 45d I-IV). At higher potentials (> 1.46 V_{RHE}), the p-d transition energies for the low-temperature calcined films seem to decrease, which is probably due to O-O bond formation and the release of molecular O₂ as well as a slight up shift of the Ir 5d t_{2g} band to increase the adsorption of oxygen species. The p-d interband transition energies of the high-temperature calcined films indicate no significant change in the Ir 5d t_{2g} band, probably due to the low potential range up to 1.48 V_{RHE}. There are also minor to none changes in the electrical properties of the high-temperature calcined films, indicating no change in the Ir 5d t_{2g} band (Figure 45b V-VI and Figure 45d V-VI).

In addition, the d-d intraband transition energies decrease for the low-temperature calcined films, which is likely related to the down shift of the t_{2g} band and the higher d-orbital splitting. These effects i.e., the down shift of the t_{2g} band and the high d-orbital splitting, are less to non-existent for the high-temperature calcined films, which can be attributed to the more pronounced crystallinity of the materials. In addition, studies of the high-temperature calcined mesoporous IrO_x films in the lower potential range between 0.40 V_{RHE} and 1.40 V_{RHE} show no changes and no feature at the potential of the Ir^{III}/Ir^{IV} redox couple (at about 0.95 V_{RHE}) for the intraband transition energies, suggesting that the high-temperature calcined films mainly retain their Ir oxidation state (probably Ir^{IV}). For further information about ECSE investigations in the potential range between 0.40 V_{RHE} and 1.40 V_{RHE} of the calcination series see Appendix A15.

Finally, the influence of the calcination temperature on the filling factor will be discussed. From ex-situ SEM imaging (Figure 15) and XRD (Figure 17) measurements of the calcination series, an increase in crystallinity is observed, which influences the film morphology and pore geometry and thus probably induces stronger gas accumulation. This could explain the increasing hysteresis of the filling factor for the 375 °C and 400 °C calcined films (Fig. 48e III and IV). It is possible that a strong hysteresis would also be observable in the higher calcined films when cycling to higher potentials and reaching higher values of produced oxygen gas. From the ex-situ analyses, it can be seen that by increasing the calcination temperature the pore walls begin to sinter (SEM images in Figure 15) and the porosity decreases (see e.g., SE analysis in Chapter 4.2). These sintering effects create larger and more diffuse pores, which probably also prevent the gas from being removed, e.g., when cycling to higher potentials. In addition, the 600 °C calcined film shows a high initial value of the filling factor, which could be an indication of closed pores within the film. EP measurement of the 600 °C calcined film on the Ti substrate indicates a maximum adsorption of water of about 75% at a relative humidity of almost 100% (see A11 for more EP results). Both analyses reveal similar behavior of the pores filled with water or electrolyte, which could confirm the presence of closed pores. However, this needs to be quantified by other methods, such as tomography. In addition, however, it should be noted that the determined pore fillings for the ECSE studies are only valid for the flow rate of 85 ml min⁻¹ and probably other behaviors could be observed at higher flow rates.

In summary, ECSE investigations on mesoporous IrO_x films in the OER regime show distinct changes of the derived parameters depending on the calcination temperature. The analyses reveal changes of the p-d interband transition energies which are more pronounced for low-temperature calcined films. This behavior is also evident in the electrical properties of the films, where the resistivity and electron concentration show more significant changes for films calcined between 300 °C and 400 °C. Furthermore, the volume fraction of the produced gas is deduced for each catalyst film, where the morphology and pore geometry of the films indicate a direct effect on adherent gas within the layers.

7. General discussion

This Chapter contains a general discussion of the gained knowledge from the Chapters 4 and 6, which are valid for the investigated mesoporous IrO_x films. Electronic parameters such as p-d interband transitions, electrical parameters, and film morphology, i.e., crystallinity and pore geometry, were identified as relevant parameters influencing the OER activity.

In the first part of this Chapter (7.1), the electronic structure of the synthesized mesoporous IrO_x films and their dependence on the calcination temperature is proposed based on the ellipsometric ex-situ characterization (see Chapter 4.2). The suggested structure is supported by results of complementary methods such as valence band XPS (see Chapter 4.1) and XAS measurements.

ECSE investigations showed that, in addition to the energetic position of the p-d interband transitions in the VEEL spectra, the intensity during the OER seems to play a significant role as well (Chapter 6.1). Therefore, in Chapter 7.2 is discussed the influence of the potential and calcination temperature on the normalized intensity of the VEEL spectra.

In the following Chapter 7.3, the correlation of potential and calcination temperature dependent properties with OER activity is discussed in order to derive trends that govern the OER activity.

The ECSE investigations under OER conditions demonstrated that the amount of oxygen gas produced and retained in the catalyst pores depends on the film morphology (see Chapter 6.3). Therefore, in Chapter 7.4, the influence of catalyst morphology on gas accumulation and gas removal is discussed in relation to the potential and calcination temperature.

7.1 Impact of the calcination temperature on a proposed band structure of mesoporous IrO_x films

As Chapter 4.4 shows, the identified peaks (A and B) in the bulk and surface VEEL spectra (Figure 27), which are interpreted as p-d interband transition between the O 2p orbitals and the occupied and unoccupied Ir 5d t_{2g} orbital directly affect the activity in the OER (Figure 31). It was assumed that the p-d interactions are related to electrophilic oxygen ligands such as protonated oxygen species, which influence the Ir-O bonds due to their higher degree of covalency. To further understand the change of the peak center energies from VEELS, the mesoporous IrO_x calcination series was studied with XAS at the O K-edge. The analysis was performed by Juan J. Velasco-Vélez and co-workers at the BESSY II (Berlin) ISISS beamline. Figure 46 displays the results of the XAS O K-edge measurements in total electron yield (TEY) mode (a) and the change of characteristic peaks (b). From the XAS measurements at the O K edge, different oxygen species such as μ_1 -OH and μ_3 -O can be assigned. Figure 46c illustrates the proposed species schematically.

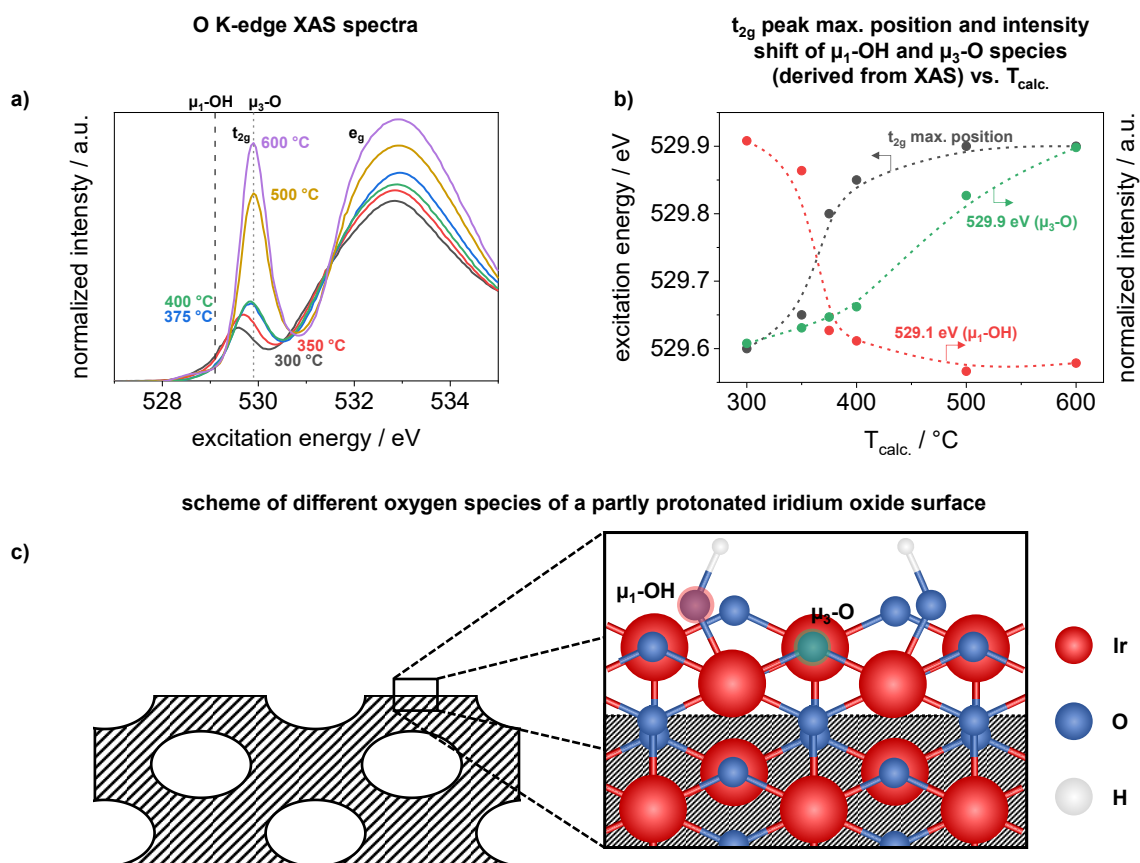


Figure 46: Analysis of the IrO_x calcination series with XAS at the O K-edge and illustration of the different oxygen species, detected from the XAS study. a) O K-edge spectra of IrO_x samples calcined between 300 °C and 600 °C, with indication of the Ir 5d t_{2g} and e_g sub-band and μ_1 -OH and μ_3 -O species. b) corresponding changes of the characteristic peaks from the O K-edge spectra. c) illustration of the different identified oxygen species of a partly protonated IrO_x film.

The O K-edge spectra of the calcination series indicate two peaks at about 530 eV and 533 eV corresponding to Ir 5d t_{2g} and e_g sub-levels (Figure 46a).^{199, 200} In addition, the t_{2g} sub-level shows a shift to higher excitation energies, depending on the calcination temperature as shown in Figure 46b. Furthermore, the mesoporous IrO_x films indicate the presence of μ_1 -OH (529 eV) and μ_3 -O (530 eV) species.²⁰¹ Figure 46c schematically illustrates the two oxide species, where the μ_1 -OH are terminal/single-coordinated and protonated oxygen species (highlighted in red), while the μ_3 -O are triple-coordinated oxygen species (highlighted in green).

The low-temperature calcined IrO_x films (≤ 400 °C) reveal more protonated μ_1 -OH and less triple-coordinated oxygen μ_3 -O species, while films calcined at higher temperatures (> 400 °C) show the formation of more μ_3 -O species (Figure 46b). This is consistent with the XPS measurements, as shown in Figure 19, where a change of the chemical composition from hydrated to more anhydrous IrO_x species is observed with increasing calcination temperature. The generation of more μ_3 -O species at higher calcination temperatures can be attributed to the formation of a rutile-like crystal structure as seen in the XRD measurements in Chapter 4.2 (Figure 17). Moreover, the trend observed in the XAS spectra for the transition from protonated μ_1 -OH to triple-coordinated oxygen μ_3 -O species in Figure 46b displays a similar behavior to the shift of the A peak from bulk and surface VEEL spectra derived from the ex-situ SE analysis (Figure 27). Hence, the transition from protonated μ_1 -OH to triple-coordinated μ_3 -O oxygen species seems to have an impact on the t_{2g} sub-level and thus a direct influence on the p-d interband transitions.

Based on these results, Figure 47 schematically illustrates a proposed impact of the calcination temperature on the electronic structure of the IrO_x material.

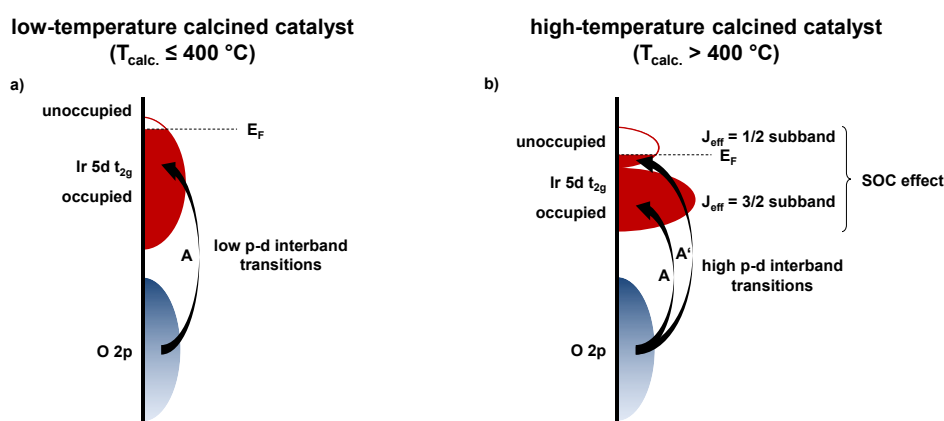


Figure 47: Illustration of a proposed impact of the calcination temperature on the electronic structure of the IrO_x material. A and A' correspond to interband transitions derived from the VEELS analyses between the partially filled Ir 5d t_{2g} sub-band and the O 2p band and between the partially occupied $J_{\text{eff}} = 1/2$ sub-band and the O 2p band, respectively.

According to the current interpretation, a higher amount of terminal/single coordinated and protonated μ_1 -OH species is observed for films calcined at 400 °C or below (Figure 46b), resulting in an almost completely filled broad t_{2g} band (Figure 47a). Due to this nearly completely filled t_{2g} band, the Fermi level is shifted to higher energies. This effect is also reflected in the electron concentration and electrical conductivity (reciprocal resistivity) values derived from the ellipsometric model, with low-temperature calcined layers showing lower values for both parameters compared to the higher calcined layers (Figure 26). The broad t_{2g} band results also in the low p-d interband transitions from the O 2p to the occupied (A) Ir 5d t_{2g} states observed in the VEELS analysis (Figure 27).

With increasing calcination temperature, i.e., from 300 °C to 400 °C, there is a partial transition from protonated μ_1 -OH to unprotonated μ_3 -O species, leading to a slight increase in electron concentration, electrical conductivity, and p-d transition energy (Figure 26).

At high calcination temperatures, i.e., above 400 °C, more unprotonated μ_3 -O species are observed (Figure 46b). The increased amount of unprotonated μ_3 -O species can be related to the crystalline structure of the material (see XRD in section 4.1). This also leads to a SOC splitting effect of the t_{2g} band. As described in the XPS valence band measurement in Chapter 4.1 (Figure 19) and the VEELS analysis in Chapter 4.2 (Figure 27), the five electrons in the t_{2g} band split into four electrons occupied as $J_{eff} = 3/2$ sub-band and to one electron occupied as $J_{eff} = 1/2$ sub-band. This effect is illustrated in Figure 47b. Furthermore, the higher amount of unprotonated μ_3 -O species and the pronounced rutile-like crystal structure as well as the higher Ir oxidation state (Ir⁴⁺; see EPMA and XPS analysis in Chapter 4.1) lead to an increase in electron concentration and density. As a result, the Fermi level shifts to a lower energy and reduces the gap between the valence and conduction band, which therefore increase the electrical conductivity.

In summary, the SE data agree well with the results of the XPS valence band and XAS investigations. Thus, also the results from SE investigations can be used to assess the band structure of materials.

7.2 Influence of potential and calcination temperature on the intensity of VEEL spectra

Operando ECSE investigation under OER conditions as well as in the low potential range ($0.40 V_{\text{RHE}} - 1.40 V_{\text{RHE}}$) indicate a dependence between the intensity of the bulk ($-\text{Im}(\varepsilon^{-1})$) and surface ($-\text{Im}((1 + \varepsilon)^{-1})$) VEEL spectra and the applied potential. This dependence is shown for the exemplary measured mesoporous IrO_x film calcined at 375°C in Chapter 6.2 (OER conditions) and Appendix A14 (lower potential range). A systematic change in the intensity of the spectra was also observed as a function of the calcination temperature in the ex-situ VEELS characterizations described in Chapter 4.2 (mesoporous IrO_x films on Si substrates) and Appendix A10 (mesoporous IrO_x films on Ti substrates). To demonstrate the impact of the applied potential and of the calcination temperature on the intensity of the spectra, Figure 48 displays the bulk and surface VEELS analysis of the IrO_x film calcined at 375°C (highest OER activity) and of the IrO_x film calcined at 600°C (lowest OER activity) obtained from both catalysts during operando analysis under OER conditions.

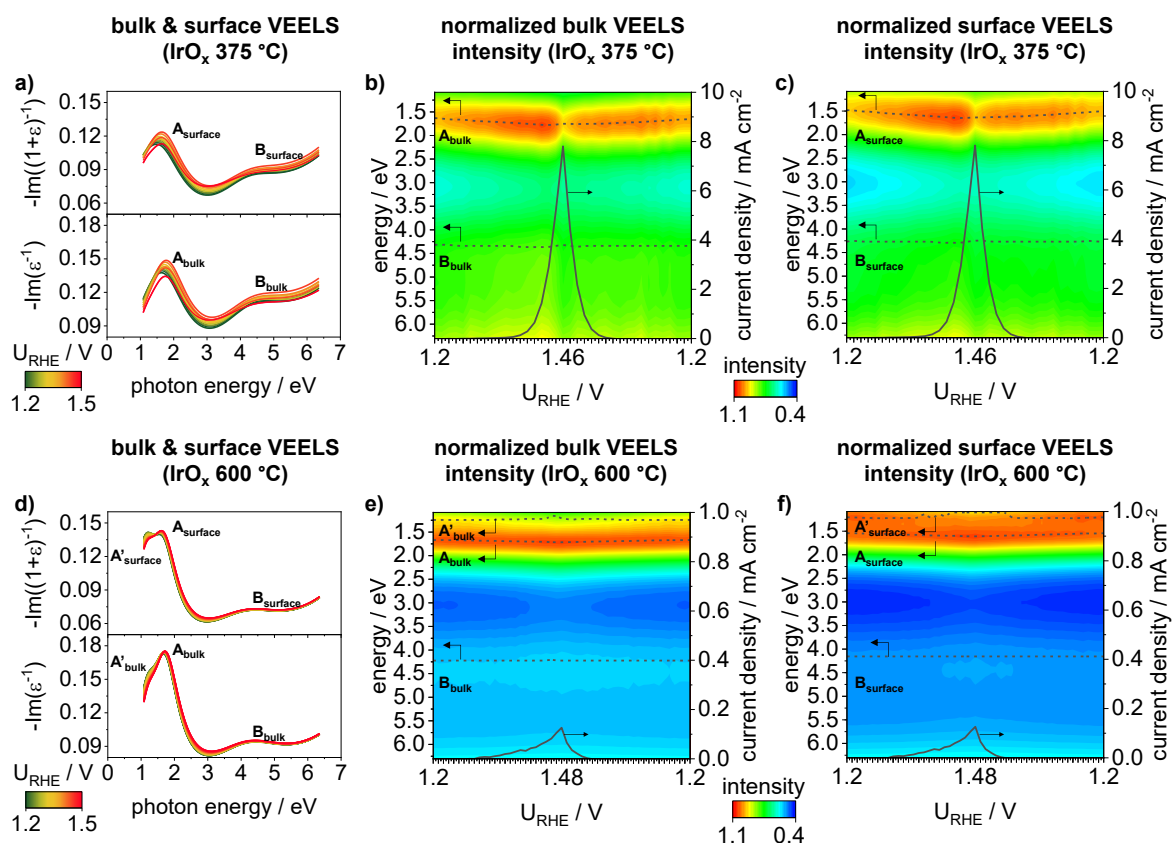


Figure 48: VEELS intensity analyses measured under operando ECSE conditions in the OER region on the mesoporous IrO_x films calcined at either 375°C (a, b, c) or 600°C (d, e, f). a,d) bulk and surface VEEL spectra of the respective IrO_x film. b,e) normalized intensity spectra of the bulk VEELS analyses with indication of the energetic position of the A, A' and B peaks as well as the measured current response, displayed as a function of the applied potential. e,f) corresponding normalized surface VEELS intensity spectra. OER analysis was performed in the potential range between $1.20 V_{\text{RHE}}$ and $1.48 V_{\text{RHE}}$ (iR corrected) by cyclic voltammetry with a scan rate of 1 mV s^{-1} in 0.1M HClO_4 using the operando flow cell setup.

Figure 48a displays the bulk and surface VEEL spectra of the mesoporous IrO_x film calcined at 375 °C. In both spectra, the shift of the peaks and an increase in intensity with increasing potential are visible, where the intensity indicates a decrease at higher center energies and higher potentials.

Figure 48b shows as a function of applied potential the normalized bulk VEEL spectra, with color-coded intensity along with the measured OER current. Figure 48b displays the corresponding surface intensity VEEL spectra. The center energy values of the A and B peaks as well as the current response are indicated. The intensity of the A peaks reveals an increase in both spectra until reaching a potential of about 1.45 V_{RHE}. Between 1.45 V_{RHE} and 1.46 V_{RHE}, where the highest current density is reached and a higher amount of oxygen gas is produced, an abrupt decrease in both the intensity and width of the A peak is observed. The intensity of the A peak returns rapidly in the down scan between 1.46 V_{RHE} and 1.45 V_{RHE}. Yet, the peak width is not exactly the same as in the up scan. In contrast, the intensity changes of the B peak are relatively small, therefore no changes are seen in the intensity spectrum.

For the mesoporous IrO_x film calcined at 600 °C, a shoulder at the A peak (A' peak) is visible in addition to the A and B peaks in the measured bulk and surface VEEL spectra (Figure 48d). The additionally peak is attributed to the described SOC effect. A slight shift in the energetic positions of the A and A' peaks is observed in both spectra. Moreover, the A' peaks reveal a more pronounced change in intensity compared to the A peaks, while no further changes are observed for the B peaks. Figure 48e and f display the two intensity spectra of the bulk and surface VEELS together with the center energies of the identified peaks and the current response as a function of potential. It should be noted that the current response is about 10 times lower compared to the IrO_x film calcined at 375 °C. It is noticeable in both spectra that the A peak shows no change in intensity or width and only changes are observed in the A' peak. In contrast, the A' Peak shows a decrease in intensity with increasing potential and a slight shift of the energetic position to low energies, which are both completely reversible. As for the 375 °C calcined IrO_x film, no significant changes are observed in the intensity spectra of the B peaks.

Significant potential-dependent changes of the p-d transitions can be recognized from the intensity analyses of the 375 °C calcined IrO_x film (Figure 48b and c) as well as of the 600 °C calcined IrO_x film (Figure 48e and f). Interesting is the strong decrease at higher potential for the low-temperature calcined film (375 °C), which is probably not related to gas formation. The intensity in this area is comparable to the initial intensity at a potential of 1.20 V_{RHE}, where the entire layer is filled with electrolyte (see deduced filling factor in Chapter 6.2; Figure 42a). In addition, the intensity of the $J_{eff} = 1/2$ sub-band of t_{2g} for the 600 °C calcined film also decreases at higher voltages, without significant oxygen evolution. It is suggested in literature that the higher degree of electrophilic O¹⁻ species formed from μ₁-OH species shortens the Ir-O bond length and in extreme cases leads to an overlap of the Ir 5d t_{2g} and the O 2p band.^{15, 33, 202}

A similar behavior has been reported for ruthenium oxide (RuO_2). Rao *et al.* studied the surface structural changes on single-crystal RuO_2 (110) as a function of potential in acidic electrolyte using in-situ surface X-ray scattering measurements combined with density functional theory (DFT).²⁰ They proposed a contraction of the Ru-O bond length with increasing potential, e.g. by increasing the potential from 1.00 V_{RHE} to 1.30 V_{RHE} . A further increase of the potential ($\geq 1.50 V_{\text{RHE}}$) resulted in an increase of the Ru-O bond length, due to the formation of oxo-oxyl species (Ru-OO), which is similar or comparable to bond length at lower potentials (e.g., 1.00 V_{RHE}). This could explain the behavior of the intensity and the p-d transition energies. Due to more pronounced electrophilic O^- species at lower calcination temperatures, the Ir-O bond length contracts in the potential range of about 1.20 V_{RHE} and 1.40 V_{RHE} , inducing an increase of the p-d interband transition energies and intensity. At higher potentials, the formation of oxo-oxyl species increases the Ir-O bond length, resulting in a rapid decrease of the p-d transition intensity and energy values in addition to the release of oxygen. In contrast, the 600 °C calcined film, where the formation of a more pronounced rutile-like structure leads to an increase of $\mu_3\text{-O}$ species, indicates a decrease in intensity and energy values for the $J_{\text{eff}} = 1/2$ sub-band as well. This behavior could be explained by deprotonation steps and the formation of M=O bonds proposed for high-valent metal oxo species.^{13, 14}

Furthermore, the formation of Ir^{V} species and the subsequent formation of $\text{Ir}^{\text{III}}/\text{Ir}^{\text{IV}}$ species have been discussed in literature in terms of different possible reaction mechanisms of the oxygen evolution.^{23, 194} The increase in intensity with increasing potential of the 375 °C calcined IrO_x film probably indicates a progressively filled t_{2g} band, which may be due to the formation of Ir^{V} species. The strong decrease during the oxygen evolution then indicates the formation of $\text{Ir}^{\text{III}}/\text{Ir}^{\text{IV}}$ species, which are also present at lower potentials (e.g., at 1.20 V_{RHE}). In contrast, the filled t_{2g} band ($J_{\text{eff}} = 3/2$ sub-band) of the 600 °C calcined film seems to be almost uninvolved, and the Ir-O interaction takes place mainly in the partially filled t_{2g} band ($J_{\text{eff}} = 1/2$ sub-band). The mostly constant p-d interactions to the $J_{\text{eff}} = 3/2$ sub-band could be interpreted with stable Ir^{IV} species and the slight changes within the $J_{\text{eff}} = 1/2$ sub-band could be attributed to deprotonation steps.

In summary, the intensity analyses of the VEEL spectra provide further insight of the electronic structure of the materials during OER. It is likely that the variations can be attributed to the proposed changes in the M-O bond length and/or to the different oxidation states during the reaction. Another interesting fact is that for the high-temperature calcined film (more crystalline film), the changes in the considered potential range (1.20 V_{RHE} – 1.48 V_{RHE}) occur mainly in the partially occupied $J_{\text{eff}} = 1/2$ sub-band.

7.3 Effect of $T_{\text{calc.}}$ on potential-dependent changes of catalyst properties under OER conditions

The electrical and electronic properties obtained from the ex-situ analyses (Chapter 4) and operando ECSE investigations (Chapter 6) show a dependence on the calcination temperature as well as potential-dependent changes during OER. In addition, different regimes of material property behavior for low-temperature calcined films (between 300 °C and 400 °C) and for high-temperature calcined films (500 °C and 600 °C) could be identified from the ECSE data in the OER range. In order to correlate these dependencies with the OER activity and to identify trends, the electrical and electronic properties from the individual Chapters are summarized from the as-prepared state to the oxygen evolution in Figure 49.

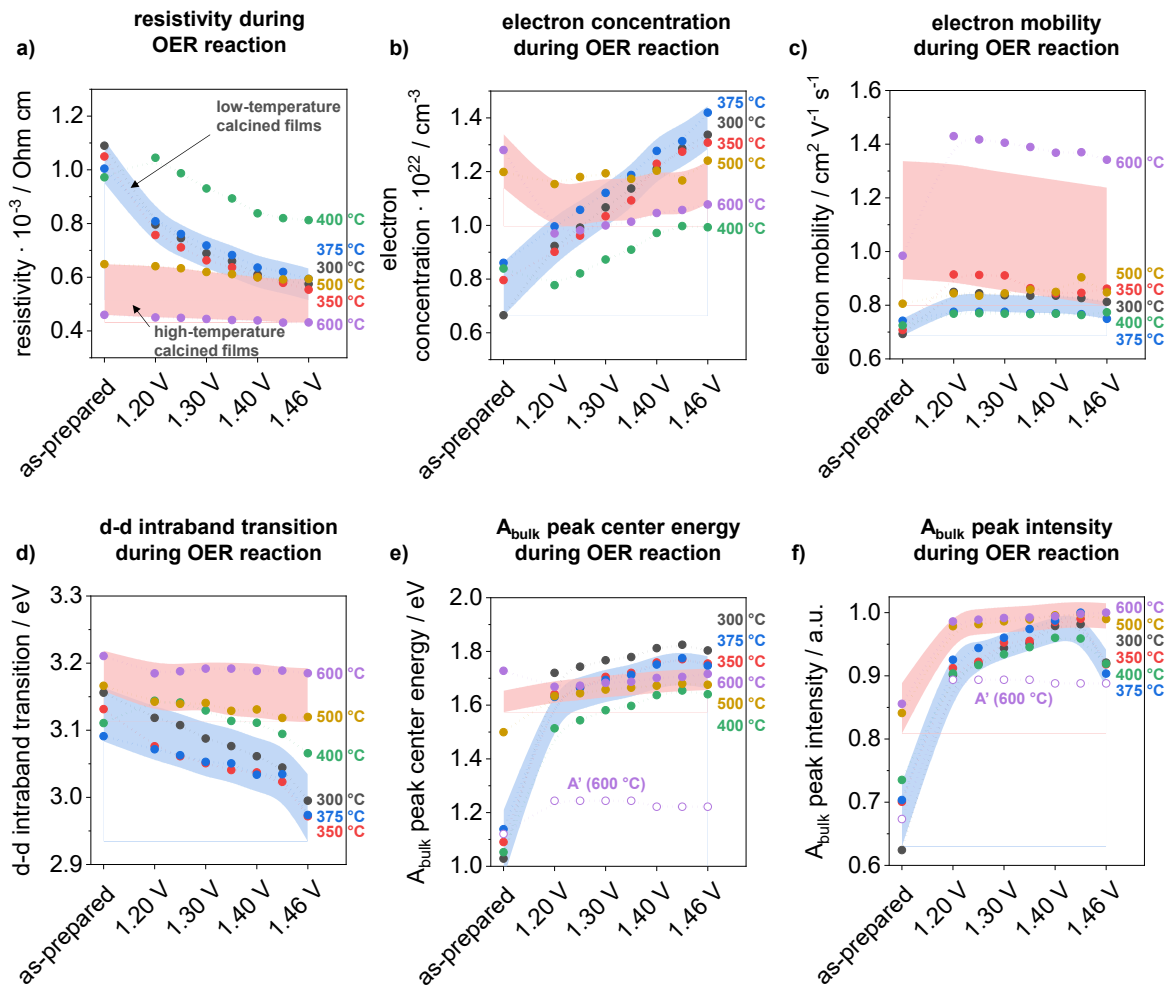


Figure 49: Overview and summary of deduced electrical and electronic parameters from an as-prepared state to the electrochemical reaction in the OER regime at different potentials of the mesoporous IrO_x calcination series. a) resistivity values, b) electron concentration, c) electron mobility, d) d-d intraband transition energies, e) center energies of the A_{bulk} peak from VEELS analysis, and f) normalized intensity of the A_{bulk} peaks. Highlighted areas were added to visualize trends of catalysts calcined at low temperature (300 °C – 400 °C; blue color) vs. IrO_x films calcined at higher temperature (500 °C and 600 °C; red color).

Figure 49a displays for all samples of the calcination series the resistivity values derived via spectroscopic ellipsometric analysis. The values include the as-prepared state (ex-situ analysis, see Figure 26) and the values at different potentials from the operando ECSE analysis under OER conditions (see Figure 45). The low-temperature calcined films (≤ 400 °C, highlighted in blue) show a strong decrease of the resistivity when a potential of 1.20 V_{RHE} is applied. Upon further increase of the potential, the resistivity decreases and finally approaches values similar to IrO_x films calcined at higher temperature (> 400 °C, highlighted in red). In contrast, the high-temperature calcined films show no significant changes from the as-prepared state to higher potentials in the OER range.

The electron concentration trends show a strong increase from the as-prepared state to higher potentials for the derived values of the low-temperature calcined films (highlighted in blue), while a slight decrease is observed for the high-temperature calcined films (highlighted in red) when a potential of 1.20 V_{RHE} is applied. With further increase of the potential, the values of the high-temperature calcined films remain rather constant (Figure 49b). The values of the electron mobility (Figure 49c) indicate a slight increase for low-temperature calcined films (highlighted in blue) and a decreasing trend of the values for the high-temperature calcined films (highlighted in red).

For the d-d intraband transitions between the Ir 5d t_{2g} and the e_g sub-level (Figure 49d), the energy values generally decrease from the as-prepared state to higher potentials for the low-temperature calcined films (highlighted in blue), where a stronger decrease is observed at 1.46 V_{RHE} . Similar to the electrical parameters, no further changes are observed for the d-d intraband transitions for the high-temperature calcined films from the as-prepared state to higher potentials (highlighted in red).

The energy values for the p-d interband transitions between the O 2p and partially filled Ir 5d t_{2g} band increase sharply from the as-prepared state for the low-temperature calcined films when a potential of 1.20 V_{RHE} is applied (Figure 49e, highlighted in blue). As the voltage is further increased, the values of the interband transition energies continue to increase, with a slight decrease in energies at a potential of about 1.46 V_{RHE} . For the high-temperature calcined films (highlighted in red), a slight increase in the interband transition energies can be seen with increasing potential. The trends of the calcined films also show an overlap of the energy values at the initial potential of 1.20 V_{RHE} . Due to the SOC effect of the film calcined at 600 °C, the interband transitions between the O 2p and the $J_{eff} = 1/2$ (A' peak) sub-band are additionally shown. The energy values show a slight increase when applying a potential, which remains relatively constant or decreases slightly at higher potentials.

Figure 49e shows the normalized intensity changes of the p-d interband transitions at the respective center energy from the as-prepared state to the applied potentials. The intensities for all catalyst films show an increase at the transition from the as-prepared state to the initial potential of 1.20 V_{RHE} , where the increase of the values is more pronounced for the low-temperature calcined films (highlighted in blue) than for the high-temperature calcined films (highlighted in red). While the intensity values for the high-temperature calcined films remain constant over the entire potential range, a decrease in intensity is visible for the low-temperature calcined films at higher potentials (> 1.40 V_{RHE}) and values similar to the initial potential of 1.20 V_{RHE} are reached. For the partially

filled $J_{\text{eff}} = 1/2$ sub-band of the 600 °C film (A'), an increase in intensity is observed by applying a potential, which remains relatively constant as the potential is further increased.

The trends in Figure 49 indicate that properties such as resistivity, electron concentration and electron mobility of the low-temperature calcined films are initially very different from the high-temperature calcined films (as-prepared), however as the potential increases, they become closer to the values of the high-temperature calcined films. This is probably related to the band structure of the low-temperature calcined films, where the conduction band consists of a broad Ir 5d t_{2g} band, as suggested in section 7.1. As a result, the t_{2g} band is more flexible in its energetic position and probably shifts to lower energies as the potential is increased, which also results in a nearing of the Fermi level to the O 2p band. This would also explain the strong increase in the p-d interband transition energies and the decrease in the d-d intraband transition energy, due to a higher d-orbital splitting. The shift and the consequent nearing of the Ir 5d t_{2g} and O 2p bands would also cause a contraction of the Ir-O bond length, leading to an increase in covalency and promote the activation of a redox active center of the O 2p orbital. At higher potentials ($> 1.46 \text{ V}_{\text{RHE}}$), the p-d transition energies for the low-temperature calcined films appear to decrease, likely due to the formation of O-O bonds and the release of molecular O_2 , as well as a slight upward shift of the Ir 5d t_{2g} band to increase the adsorption of oxygen species from the electrolyte.

The trends of the high-temperature calcined films (Figure 49) show only slight to non-significant changes in the electrical and electronic properties from the as-prepared state to higher potentials ($1.46 \text{ V}_{\text{RHE}}$). Due to the SOC effect, the t_{2g} band splits into a $J_{\text{eff}} = 3/2$ and $J_{\text{eff}} = 1/2$ sub-band as suggested in Section 7.1. The results from the intensity spectra of the VEELS analysis in Section 7.2 indicate that the potential-dependent changes occur mainly in the $J_{\text{eff}} = 1/2$ sub-band, which could explain the small changes of the parameters in Figure 49. In addition, the high-temperature calcined films exhibit fewer $\mu_1\text{-O(H)}$ species and increased $\mu_3\text{-O}$ species due to their more crystalline structure, making it more difficult to shift the t_{2g} band in its energetic position. This also causes a more difficult activation of a redox active site of the O 2p orbital, which is reflected in the lower OER activities.

The derived shift of the Ir 5d t_{2g} band from the trends of the electrical and electronic parameters of the low-temperature calcined films indicates a catalytic process consistent with a previously proposed acid-base mechanism. Accordingly, nucleophilic attack of reactive O species at lower potentials and thus oxygen evolution is possible. In contrast, the trends of electrical and electronic parameters for the high-temperature calcined films are more consistent with a direct or radical coupling mechanism. Since radical formation and/or direct coupling occurs probably at higher potentials, no parameter changes are observed in the potential range studied.

In summary, the developed operando ECSE cell can be used to investigate changes in material properties (electrical and electronic) as a function of potential in a vacuum-free and non-destructive environment. The results of the ECSE investigations agree well with findings reported for similar materials in literature. Furthermore, the potential-depending properties give an indication of the catalytic reaction mechanism.

7.4 Impact of calcination temperature, potential and time on gas transport

In the operando ECSE analyses in the OER range ($1.20 V_{\text{RHE}} - 1.48 V_{\text{RHE}}$) described in detail in Chapter 6.3, a volume fraction of the produced oxygen gas (filling factor) could be determined for the IrO_x calcination series. This filling factor was found to depend on the applied potential and exhibit a hysteresis when the potential is changed, which suggests a slow removal of the gas from the pore system of the catalyst. The film morphology and pore geometry appear to influence this behavior, which will be discussed in more detail later in this Chapter.

Figure 50a displays exemplarily for films calcined at 300°C , 375°C and 500°C the fraction of pores filled with produced gas, i.e. filling factor vs. the applied potential in the first measured CV. Figure 50b illustrates the maximum pore filling factors as a function of calcination temperature for films calcined at 300°C , 350°C , 375°C , 400°C , and 500°C for the respective first three CVs.

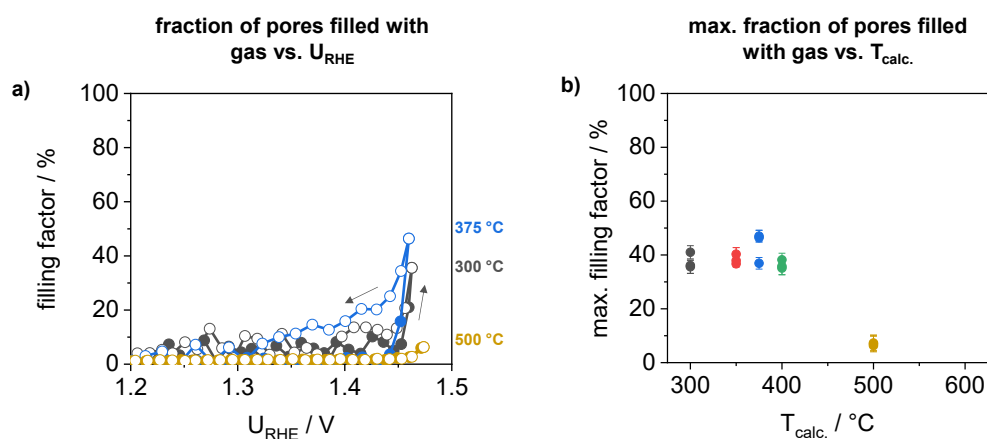


Figure 50: Potential and calcination temperature dependence of the fraction of pores filled with produced gas (filling factor) of the mesoporous IrO_x films calcined between 300°C and 500°C . a) potential dependent changes of the filling factor. b) calcination temperature dependence of the maximum pore filling factor.

In the forward scan of the first CV (Figure 50a, colored filled circles), the pores in all three catalysts appear to hold no gas bubbles until a potential of about $1.45 V_{\text{RHE}}$ is reached. Above $1.45 V_{\text{RHE}}$, the pore filling with gas increases rapidly, with higher amounts of gas accumulating in the more active films, i.e., low-temperature calcined films (300°C and 375°C). In the back scan (open circles), a hysteresis is observed. Here, the most active catalyst, calcined at 375°C , shows the largest hysteresis, the 300°C a smaller hysteresis, and the least active catalyst (500°C) hardly any hysteresis.

From the plot of the filling factor as a function of potential, the calcination temperature dependence can also be obtained, where the low-temperature calcined films show a higher value than the high-temperature calcined film (Figure 50a). For comparison, the maximum value of the accumulated gas in the pores was determined for the respective CV measurement and plotted as a function of the calcination temperature (Figure 50b). The low-temperature calcined films (≤ 400 °C) show a relatively similar value, while at higher calcination temperatures (> 400 °C) the filling factor decreases strongly, in particular due to the low produced oxygen gas in the investigated potential range.

The high oxygen gas production of the films is consistent with the current density values obtained, for instance, at a potential of $1.45 V_{\text{RHE}}$ (see Chapter 4.3, Figure 29). The determined increase of the observed hysteresis from 300 °C to 400 °C appears to result from a combination of effects, i.e. higher activity, different pore geometry and size (Figure 15) as well as the lower porosity (Figure 26), which all can affect the transport of the produced oxygen gas.

From the delayed removal of gas from the catalyst in the back scan, it appears that one possible (slow) path of gas transport is the dissolution of the produced gas into the electrolyte. Here, the gas transport from the gas phase to the liquid phase or in the liquid phase could be limiting. In order to quantify this effect the film theory can be used, which describes the relationship of mass transport between two phases.^{203, 204} In this model, the limiting transport processes can be ascribed to diffusion in a thin film at the interface between two phases. For a rough mathematical approximation, it can be assumed that:

- Diffusion controls the kinetics, i.e., no chemical reaction takes place.
- The partial pressure of the gas is negligibly small, i.e., for the mathematical evaluation the concentration of the gas is sufficient.
- The concentration of the gas within the liquid can be considered as constant or neglected, since a continuous flow of electrolyte is guaranteed.
- The phase interface is a smooth layer, i.e., curvatures due to the pore geometry are not considered.

Hence, the diffusion of the gas in the liquid can be simplified as a 1st order kinetic law, which is described as follows:

$$\dot{m}_A = -k_A \cdot c_g \cdot V \quad (54)$$

with \dot{m}_A as mass flow, k_A as kinetic constant, c_g as concentration of the gas and $V = A \cdot d$ as considered volume of the measuring area with A as area of the measuring spot of the ellipsometric light beam (21.2 mm^2) and d as film thickness (see Table 1 and/or Table 2 for the thickness on Ti substrates).

To simplify the equation (54), only the material flow or the time-related concentration change on the gas side is considered. Furthermore, the derived volume fraction is used as concentration of the gas. This results in the following formulations:

$$\frac{df}{dt} = -k_A V \cdot f \quad (55)$$

$$f(t) = f_0 + e^{-k_A V \cdot t} \quad (56)$$

with f as filling factor, $k_A V = k_A \cdot V$ as volume related constant and t as time.

The linearization of equation (56) results in:

$$\ln\left(\frac{f(t)}{f_0}\right) = -k_A V \cdot t \quad (57)$$

The results of the mathematical approximation are shown in Figure 51.

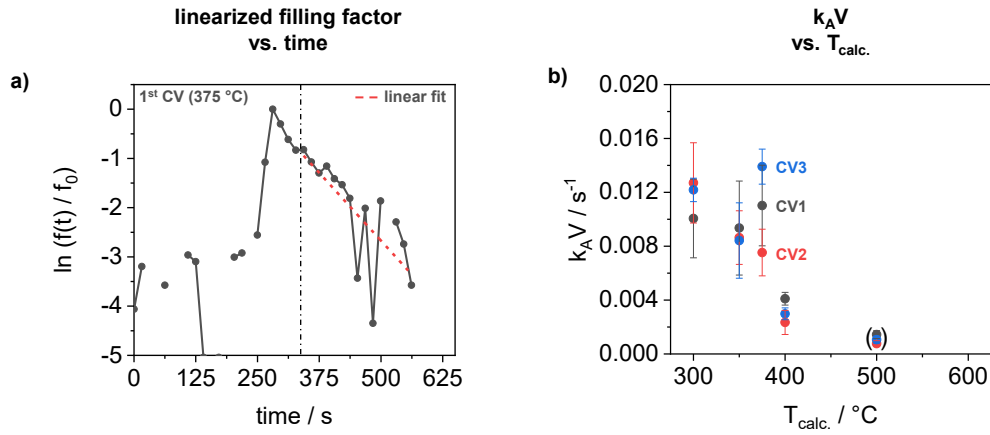


Figure 51: Results of the linearization analysis of the gas diffusion during the OER. a) time dependent changes of the derived filling factor and linearization of the filling factor for the first CV of the mesoporous IrO_x film calcined at 375 $^{\circ}\text{C}$. b) determined volume-related constants ($k_A V$) from the linearization of the three CV measurements.

In Figure 51a, exemplary the term $\ln\left(\frac{f(t)}{f_0}\right)$ is plotted as a function of time to prove the relation to the experimental data for the time-resolved change of the filling factor during a CV up and down scan in the OER regime of the mesoporous IrO_x film calcined at 375 $^{\circ}\text{C}$. For the calculation of the term $\ln\left(\frac{f(t)}{f_0}\right)$, the maximum filling factor for f_0 and the respective filling factor at time t for $f(t)$ were used. The linear adjustment was adapted from a potential of 1.40 V_{RHE} ($j < 0.2 \text{ mA cm}^{-2}$) to ensure that the gas evolution does not influence the linear fitting.

It can be seen that from a time above 340 s, i.e., during the back scan, a linear regime can be identified. Therefore, diffusion could be indeed limiting the gas dissolution and transport. Thus, the slope of the linear region, which should correspond to $k_A V$, was estimated for the first three CVs of each catalyst in the IrO_x calcination series. The derived values are plotted as a function of the calcination temperature in Figure 51b. No values could be determined for the film calcined at 600 °C because no significant gas evolution was observed in the potential range considered. In general, the determined $k_A V$ values agree well between the measured CVs on the same catalyst. Moreover, a general trend towards lower $k_A V$ values for higher calcination temperature can be observed.

A definite explanation for this trend cannot be given with the current data. It is possible that the specific surface area of the films plays a significant role, which could lead to a smaller interface between the individual phases (solid, liquid, gas) at higher calcination temperatures. The SEM analysis of the films (Figure 15) indicates that the pore geometry changes as a function of the calcination temperature. The pores become both smaller and more unshapely with increasing calcination temperature. This could be a reason for the decrease of the $k_A V$ values since probably the interface between gas and electrolyte is reduced by the change of the pore geometry. In addition, the ellipsometric analyses as well as the chemical composition analyses (EPMA, XPS, XAS) show that also the surface properties of the catalyst materials change with increasing calcination temperature. Hence, the interaction between produced gas and surface could also change.

In addition, poor gas transport can lead to blockage of active sites in the catalyst. Gasteiger and co-workers have shown that RDE-based galvanostatic stability testing does not provide a measure of the deterioration/dissolution of the OER catalyst and that this is mainly due to the accumulation of oxygen bubbles within the catalyst layer and/or near its interface with the electrolyte.²⁰⁵ Thus, by holding the catalyst during open circuit potential (OCP) for a longer period of time and simultaneously purging the electrolyte with argon gas, the catalyst activity could essentially be restored.

While no definitive conclusion can be reached with the present data, the analysis clearly shows a complex interplay between the calcination temperature, the resulting surface and pore properties, and the observed gas transport. Since poor gas transport can lead to blocking of the active sites within the catalyst, further detailed analysis and future work seems to be justified.

In summary, the developed flow cell and measurement setup allow, according to the current state of knowledge, for the first time a time-resolved and potential-dependent quantification analysis of gas transport and the gas adhesion in the pores of the catalyst systems. However, since a complex interplay of different factors is involved and many conditions were defined to simplify the approach, this behavior should be investigated in more detail, especially under the aspect of equal conditions such as uniform gas evolution.

8. Conclusion and Outlook

A major aim of this thesis was to develop a vacuum-free and non-destructive analysis by spectroscopic ellipsometry of electrocatalysts for the oxygen evolution reaction under real conditions. To achieve this aim, established and highly reproducible mesoporous iridium oxide catalyst films were synthesized.

An essential aspect includes a complementary analytical methodology and metrology to develop a suitable model for spectroscopic ellipsometry. For this purpose, reproducible model type mesoporous iridium oxide catalyst films were calcined at different temperatures (300 °C – 600 °C) and examined by independent methods for their properties such as layer thickness, porosity, crystallinity, chemical composition, interband and intraband transitions as well as electrical conductivity. Electrochemical investigations using rotating disc electrodes showed on the one hand a high activity of the catalysts and on the other hand a dependence of the activity on the calcination temperature, which are comparable to earlier investigations. Moreover, the electrochemical studies with the developed flow cell setup show accurate and comparable results for a wide range of operating conditions.

The ellipsometric model was developed using interference enhancement in a multi-sample analysis approach. By using silicon wafers with and without thermal silicon dioxide layers, a model consisting of an anisotropic Bruggeman effective medium approximation and the use of a Drude oscillator and three Lorentz oscillators was developed. Thus, layer properties such as film thickness, porosity, resistivity, electron concentration and mobility, and intraband transitions could be derived. Validation of the derived parameters with independent methods showed good agreements.

Furthermore, the optical properties, i.e., dielectric function as well as refractive index and extinction coefficient, were obtained as a function of the calcination temperature. From the valence electron energy loss spectra derived from the dielectric functions, interband transitions between the Ir 5d t_{2g} band and the O 2p orbital could be identified and correlated with the intrinsic OER activity of the catalysts. The results show that low-temperature calcined IrO_x films (≤ 400 °C) have low p-d interband transitions, indicating a broad and nearly completely filled Ir 5d t_{2g} band with a low electron density. In contrast, the higher calcined films tend to split the Ir 5d t_{2g} band into a $J_{eff} = 3/2$ sub-band and a $J_{eff} = 1/2$ sub-band, as well as indicating a high electron density and thus higher interband transition energies. Thus, the effects of calcination temperature on crystallinity and electronic structure have been revealed.

Electrochemical spectroscopic ellipsometric investigations on a platinum surface were used to validate the developed flow cell setup and to improve the understanding of the measured and modeled spectra. The results show the potential dependent oxidation and reduction of a PtO_x layer on the surface, which are in good agreement with the postulated mechanisms on a platinum surface.

Finally, the developed ECSE setup could be used for investigations of the mesoporous IrO_x calcination series using the validated model. Results of these investigations show potential dependent changes of the electrical and electronic structure. Low-temperature calcined films show an increase in electron concentration, resistivity, and p-d interband transitions with increasing potential. These changes may indicate an increase in electron density and a decrease in the energetic position of the Ir 5d t_{2g} sub-level as well as an increase of the covalent nature of the M-O bonds. Thus, the O-O bond formation could be due to an acid-base mechanism. In contrast, the higher calcined films show small changes in the electrical and electronic structure. For example, the operando measurements indicate that such changes occur mainly in the $J_{eff} = 1/2$ sub-band. This indicates an increased Ir-O binding energy, which probably indicates a direct coupling mechanism for the O-O binding formation.

With the developed method for vacuum-free and non-destructive analysis changes of relevant material properties during the OER as well as in a lower potential range (0.40 V_{RHE} – 1.40 V_{RHE}) could be investigated. Furthermore, according to the current state of knowledge, the filling of mesopores with the generated oxygen gas was detected for the first time, where a dependence on the potential, pore geometry, and the degree of crystallization was observed. A higher degree of crystallinity suggests a more pronounced adhesion or accumulation of the oxygen gas within the pore structure. However, this would have to be investigated in further measurements, e.g., with different flow rates and/or constant potential steps as well as uniform filling degrees of the pores. Also conceivable are investigations with additives such as surfactants in order to reduce the surface tension and ensure the better removal of the generated gas. In addition, the influence of such additives on the activity can be investigated simultaneously.

This method approach can also be applied to other systems, e.g., mixed metal oxides. The operando ECSE investigations could also be used for these types of catalysts for a better understanding of the OER activity.

Studies of other electrochemical processes such as the hydrogen evolution reaction or corrosion processes are also conceivable. The successful ECSE analysis on a platinum surface and also the literature demonstrate a high sensitivity of ellipsometric investigations to changes on a surface, such as oxidation.

The developed method is an additional possibility for fast, vacuum-free, and non-destructive analysis of different coating materials that require low sample preparation or can even be applied directly to industrially used materials with a variety of applicable analysis methods.

Bibliography

1. Z. W. Seh, J. Kibsgaard, C. F. Dickens, I. Chorkendorff, J. K. Nørskov and T. F. Jaramillo, *Science*, 2017, **355**, eaad4998.
2. G. A. Olah, A. Goepfert and G. S. Prakash, *Beyond oil and gas: the methanol economy*, John Wiley & Sons, 2018.
3. J. M. Campos-Martin, G. Blanco-Brieva and J. L. Fierro, *Angewandte Chemie International Edition*, 2006, **45**, 6962-6984.
4. M. Hirscher, *Angewandte Chemie International Edition*, 2011, **50**, 581-582.
5. S. Camillo, K. J. T. Hong, B. Arman, W. D. P. and S. Peter, *Angewandte Chemie International Edition*, 2017, **56**, 5994-6021.
6. S. Sá, H. Silva, L. Brandão, J. M. Sousa and A. Mendes, *Applied Catalysis B: Environmental*, 2010, **99**, 43-57.
7. J. A. Velasco, C. Fernandez, L. Lopez, S. Cabrera, M. Boutonnet and S. Järås, *Fuel*, 2015, **153**, 192-201.
8. M. Ni, M. K. Leung, D. Y. Leung and K. Sumathy, *Renewable and Sustainable Energy Reviews*, 2007, **11**, 401-425.
9. M. Carmo, D. L. Fritz, J. Mergel and D. Stolten, *International Journal of Hydrogen Energy*, 2013, **38**, 4901-4934.
10. I. Moussallem, J. Jörissen, U. Kunz, S. Pinnow and T. Turek, *Journal of Applied Electrochemistry*, 2008, **38**, 1177-1194.
11. M. G. Walter, E. L. Warren, J. R. McKone, S. W. Boettcher, Q. Mi, E. A. Santori and N. S. Lewis, *Chemical Reviews*, 2010, **110**, 6446-6473.
12. J. Rossmeisl, Z. W. Qu, H. Zhu, G. J. Kroes and J. K. Nørskov, *J. Electroanal. Chem.*, 2007, **607**, 83-89.
13. M. G. Mavros, T. Tsuchimochi, T. Kowalczyk, A. McIsaac, L.-P. Wang and T. V. Voorhis, *Inorganic Chemistry*, 2014, **53**, 6386-6397.
14. T. A. Betley, Q. Wu, T. Van Voorhis and D. G. Nocera, *Inorganic Chemistry*, 2008, **47**, 1849-1861.
15. T. Reier, H. N. Nong, D. Teschner, R. Schlögl and P. Strasser, *Advanced Energy Materials*, 2017, **7**, 1601275.
16. I. C. Man, H.-Y. Su, F. Calle-Vallejo, H. A. Hansen, J. I. Martínez, N. G. Inoglu, J. Kitchin, T. F. Jaramillo, J. K. Nørskov and J. Rossmeisl, *ChemCatChem*, 2011, **3**, 1159-1165.
17. J. Rossmeisl, A. Logadottir and J. K. Nørskov, *Chemical Physics*, 2005, **319**, 178-184.
18. M. T. M. Koper, *J. Electroanal. Chem.*, 2011, **660**, 254-260.
19. P. Sabatier, *Berichte der deutschen chemischen Gesellschaft*, 1911, **44**, 1984-2001.
20. R. R. Rao, M. J. Kolb, N. B. Halck, A. F. Pedersen, A. Mehta, H. You, K. A. Stoerzinger, Z. Feng, H. A. Hansen, H. Zhou, L. Giordano, J. Rossmeisl, T. Vegge, I. Chorkendorff, I. E. L. Stephens and Y. Shao-Horn, *Energy & Environmental Science*, 2017, **10**, 2626-2637.

21. K. A. Stoerzinger, O. Diaz-Morales, M. Kolb, R. R. Rao, R. Frydendal, L. Qiao, X. R. Wang, N. B. Halck, J. Rossmeisl, H. A. Hansen, T. Vegge, I. E. L. Stephens, M. T. M. Koper and Y. Shao-Horn, *ACS Energy Letters*, 2017, **2**, 876-881.
22. C.-J. Chang, Y.-C. Chu, H.-Y. Yan, Y.-F. Liao and H. M. Chen, *Dalton Transactions*, 2019, **48**, 7122-7129.
23. A. Minguzzi, C. Locatelli, O. Lugaresi, E. Achilli, G. Cappelletti, M. Scavini, M. Coduri, P. Masala, B. Sacchi, A. Vertova, P. Ghigna and S. Rondinini, *ACS Catalysis*, 2015, **5**, 5104-5115.
24. V. Pfeifer, T. E. Jones, J. J. Velasco Vélez, R. Arrigo, S. Piccinin, M. Hävecker, A. Knop-Gericke and R. Schlögl, *Chemical Science*, 2017, **8**, 2143-2149.
25. C. Massué, X. Huang, A. Tarasov, C. Ranjan, S. Cap and R. Schlögl, *ChemSusChem*, 2017, **10**, 1958-1968.
26. M. Bernicke, E. Ortel, T. Reier, A. Bergmann, J. F. d. Araujo, P. Strasser and R. Kraehnert, *ChemSusChem*, 2015, **8**, 1908-1915.
27. J. Gao, C.-Q. Xu, S.-F. Hung, W. Liu, W. Cai, Z. Zeng, C. Jia, H. M. Chen, H. Xiao, J. Li, Y. Huang and B. Liu, *Journal of the American Chemical Society*, 2019, **141**, 3014-3023.
28. C. Shang, C. Cao, D. Yu, Y. Yan, Y. Lin, H. Li, T. Zheng, X. Yan, W. Yu, S. Zhou and J. Zeng, *Advanced Materials*, 2019, **31**, 1805104.
29. J. Kim, P.-C. Shih, K.-C. Tsao, Y.-T. Pan, X. Yin, C.-J. Sun and H. Yang, *Journal of the American Chemical Society*, 2017, **139**, 12076-12083.
30. W. Sun, J.-Y. Liu, X.-Q. Gong, W.-Q. Zaman, L.-M. Cao and J. Yang, *Scientific Reports*, 2016, **6**, 38429.
31. J. T. Mefford, X. Rong, A. M. Abakumov, W. G. Hardin, S. Dai, A. M. Kolpak, K. P. Johnston and K. J. Stevenson, *Nature Communications*, 2016, **7**, 11053.
32. S. Yagi, I. Yamada, H. Tsukasaki, A. Seno, M. Murakami, H. Fujii, H. Chen, N. Umezawa, H. Abe, N. Nishiyama and S. Mori, *Nature Communications*, 2015, **6**, 8249.
33. H. N. Nong, T. Reier, H.-S. Oh, M. Gliech, P. Paciok, T. H. T. Vu, D. Teschner, M. Heggen, V. Petkov, R. Schlögl, T. Jones and P. Strasser, *Nature Catalysis*, 2018, **1**, 841-851.
34. F. G. Sen, A. Kinaci, B. Narayanan, S. K. Gray, M. J. Davis, S. K. R. S. Sankaranarayanan and M. K. Y. Chan, *Journal of Materials Chemistry A*, 2015, **3**, 18970-18982.
35. J. Chen, P. Cui, G. Zhao, K. Rui, M. Lao, Y. Chen, X. Zheng, Y. Jiang, H. Pan, S. X. Dou and W. Sun, *Angewandte Chemie International Edition*, 2019, **58**, 12540-12544.
36. D. A. Kuznetsov, M. A. Naeem, P. V. Kumar, P. M. Abdala, A. Fedorov and C. R. Müller, *Journal of the American Chemical Society*, 2020, **142**, 7883-7888.
37. A. Grimaud, A. Demortière, M. Saubanère, W. Dachraoui, M. Duchamp, M.-L. Doublet and J.-M. Tarascon, *Nature Energy*, 2016, **2**, 16189.
38. A. Grimaud, O. Diaz-Morales, B. Han, W. T. Hong, Y.-L. Lee, L. Giordano, K. A. Stoerzinger, M. T. M. Koper and Y. Shao-Horn, *Nature Chemistry*, 2017, **9**, 457-465.
39. J. Kim, P. C. Shih, Y. Qin, Z. Al-Bardan, C. J. Sun and H. Yang, *Angewandte Chemie*, 2018, **130**, 14073-14077.

-
40. P. Chen, Y. Tong, C. Wu and Y. Xie, *Accounts of Chemical Research*, 2018, **51**, 2857-2866.
41. T. Reier, Z. Pawolek, S. Cherevko, M. Bruns, T. Jones, D. Teschner, S. Selve, A. Bergmann, H. N. Nong, R. Schlögl, K. J. J. Mayrhofer and P. Strasser, *Journal of the American Chemical Society*, 2015, **137**, 13031-13040.
42. J. K. Nørskov, *Physica B+C*, 1984, **127**, 193-202.
43. A. Ruban, B. Hammer, P. Stoltze, H. L. Skriver and J. K. Nørskov, *Journal of Molecular Catalysis A: Chemical*, 1997, **115**, 421-429.
44. J. Hwang, R. R. Rao, L. Giordano, Y. Katayama, Y. Yu and Y. Shao-Horn, *Science*, 2017, **358**, 751-756.
45. B. Hammer and J. K. Nørskov, *Nature*, 1995, **376**, 238-240.
46. B. Hammer and J. K. Nørskov, *Surface Science*, 1995, **343**, 211-220.
47. H.-S. Oh, H. N. Nong, T. Reier, A. Bergmann, M. Gliech, J. Ferreira de Araújo, E. Willinger, R. Schlögl, D. Teschner and P. Strasser, *Journal of the American Chemical Society*, 2016, **138**, 12552-12563.
48. G. Wu, X. Zheng, P. Cui, H. Jiang, X. Wang, Y. Qu, W. Chen, Y. Lin, H. Li, X. Han, Y. Hu, P. Liu, Q. Zhang, J. Ge, Y. Yao, R. Sun, Y. Wu, L. Gu, X. Hong and Y. Li, *Nature Communications*, 2019, **10**, 4855.
49. Y. Pi, Q. Shao, P. Wang, J. Guo and X. Huang, *Advanced Functional Materials*, 2017, **27**, 1700886.
50. Y. Zhao, M. Luo, S. Chu, M. Peng, B. Liu, Q. Wu, P. Liu, F. M. F. de Groot and Y. Tan, *Nano Energy*, 2019, **59**, 146-153.
51. M. Faustini, M. Giraud, D. Jones, J. Rozière, M. Dupont, T. R. Porter, S. Nowak, M. Bahri, O. Ersen, C. Sanchez, C. Boissière, C. Tard and J. Peron, *Advanced Energy Materials*, 2019, **9**, 1802136.
52. T. Audichon, S. Morisset, T. W. Napporn, K. B. Kokoh, C. Comminges and C. Morais, *ChemElectroChem*, 2015, **2**, 1128-1137.
53. B.-J. Kim, D. F. Abbott, X. Cheng, E. Fabbri, M. Nachtegaal, F. Bozza, I. E. Castelli, D. Lebedev, R. Schaublin, C. Copéret, T. Graule, N. Marzari and T. J. Schmidt, *ACS Catalysis*, 2017, **7**, 3245-3256.
54. L. C. Seitz, C. F. Dickens, K. Nishio, Y. Hikita, J. Montoya, A. Doyle, C. Kirk, A. Vojvodic, H. Y. Hwang, J. K. Nørskov and T. F. Jaramillo, *Science*, 2016, **353**, 1011-1014.
55. M. A. Subramanian, G. Aravamudan and G. V. Subba Rao, *Progress in Solid State Chemistry*, 1983, **15**, 55-143.
56. D. Lebedev, M. Povia, K. Waltar, P. M. Abdala, I. E. Castelli, E. Fabbri, M. V. Blanco, A. Fedorov, C. Copéret, N. Marzari and T. J. Schmidt, *Chemistry of Materials*, 2017, **29**, 5182-5191.
57. S. Cherevko, S. Geiger, O. Kasian, A. Mingers and K. J. J. Mayrhofer, *J. Electroanal. Chem.*, 2016, **774**, 102-110.
58. S. Cherevko, S. Geiger, O. Kasian, A. Mingers and K. J. J. Mayrhofer, *J. Electroanal. Chem.*, 2016, **773**, 69-78.

59. S. Geiger, O. Kasian, B. R. Shrestha, A. M. Mingers, K. J. J. Mayrhofer and S. Cherevko, *Journal of The Electrochemical Society*, 2016, **163**, F3132-F3138.
60. S. Geiger, O. Kasian, M. Ledendecker, E. Pizzutilo, A. M. Mingers, W. T. Fu, O. Diaz-Morales, Z. Li, T. Oellers, L. Fruchter, A. Ludwig, K. J. J. Mayrhofer, M. T. M. Koper and S. Cherevko, *Nature Catalysis*, 2018, **1**, 508-515.
61. M. Zhao, Z. Chen, Z. Lyu, Z. D. Hood, M. Xie, M. Vara, M. Chi and Y. Xia, *Journal of the American Chemical Society*, 2019, **141**, 7028-7036.
62. K. S. W. Sing, *Pure and Applied Chemistry*, 1985, **57**, 603.
63. D. Gu and F. Schüth, *Chemical Society Reviews*, 2014, **43**, 313-344.
64. E. Ortel, T. Reier, P. Strasser and R. Kraehnert, *Chemistry of Materials*, 2011, **23**, 3201-3209.
65. M. Bernicke, D. Bernsmeier, B. Paul, R. Schmack, A. Bergmann, P. Strasser, E. Ortel and R. Kraehnert, *Journal of Catalysis*, 2019, **376**, 209-218.
66. D. Bernsmeier, M. Bernicke, R. Schmack, R. Sachse, B. Paul, A. Bergmann, P. Strasser, E. Ortel and R. Kraehnert, *ChemSusChem*, 2018, **11**, 2367-2374.
67. D. Chandra, N. Abe, D. Takama, K. Saito, T. Yui and M. Yagi, *ChemSusChem*, 2015, **8**, 795-799.
68. S. Bradbury, B. Bracegirdle, S. Bradbury and B. Bracegirdle, *Introduction to light microscopy*, Bios Scientific Oxford, UK, 1998.
69. P. J. Goodhew and J. Humphreys, *Electron microscopy and analysis*, CRC Press, 2000.
70. C. Hammond and C. Hammond, *The basics of cristallography and diffraction*, Oxford, 2001.
71. R. Keyse, *Introduction to scanning transmission electron microscopy*, Routledge, 2018.
72. J. Stöhr, *NEXAFS spectroscopy*, Springer Science & Business Media, 2013.
73. J. F. Watts and J. Wolstenholme, *An introduction to surface analysis by XPS and AES*, John Wiley & Sons, Ltd, 2003.
74. D. B. Williams and C. B. Carter, in *Transmission electron microscopy*, Springer, 1996, pp. 3-17.
75. B. D. Cullity, *Elements of X-ray Diffraction*, Addison-Wesley Publishing, 1956.
76. R. F. Egerton, *Electron energy-loss spectroscopy in the electron microscope*, Springer Science & Business Media, 2011.
77. E. Ortel, A. Fischer, L. Chuenchom, J. Polte, F. Emmerling, B. Smarsly and R. Kraehnert, *Small*, 2012, **8**, 298-309.
78. E. Ortel, A. Hertwig, D. Berger, P. Esposito, A. M. Rossi, R. Kraehnert and V.-D. Hodoroba, *Analytical Chemistry*, 2016, **88**, 7083-7090.
79. G. Brockt and H. Lakner, *Micron*, 2000, **31**, 435-440.
80. Ø. Prytz, O. M. Løvvik and J. Taftø, *Physical Review B*, 2006, **74**, 245109.
81. F. Espinosa-Magaña, A. Rosas, H. E. Esparza-Ponce, M. T. Ochoa-Lara and A. Aguilar-Elguezabal, *Micron*, 2009, **40**, 787-792.
82. J. Gong, R. Dai, Z. Wang and Z. Zhang, *Scientific Reports*, 2015, **5**, 9279.

83. J. Wernecke, A. G. Shard and M. Krumrey, *Surface and Interface Analysis*, 2014, **46**, 911-914.
84. J. Loizillon, M. Putero and D. Grosso, *The Journal of Physical Chemistry C*, 2019, **123**, 30398-30406.
85. O. M. Ishchenko, G. Lamblin, J. Guillot, I. C. Infante, M. Guennou, N. Adjero, I. Fechte, F. Garin, P. Turek and D. Lenoble, *RSC Advances*, 2020, **10**, 38233-38243.
86. C. Spöri, P. Briois, H. N. Nong, T. Reier, A. Billard, S. Kühl, D. Teschner and P. Strasser, *ACS Catalysis*, 2019, **9**, 6653-6663.
87. L. Li, J. Yang, H. Ali-Löytty, T.-C. Weng, F. M. Toma, D. Sokaras, I. D. Sharp and A. Nilsson, *ACS Applied Energy Materials*, 2019, **2**, 1371-1379.
88. J. Tauc and A. Menth, *Journal of Non-Crystalline Solids*, 1972, **8-10**, 569-585.
89. J. Tauc, R. Grigorovici and A. Vancu, *physica status solidi (b)*, 1966, **15**, 627-637.
90. J. Tauc, in *Optical Properties of Solids*, eds. S. Nudelman and S. S. Mitra, Springer US, Boston, MA, 1969, ch. 5, pp. 123-136.
91. D. L. Wood and J. Tauc, *Physical Review B*, 1972, **5**, 3144-3151.
92. R. K. Kwar, P. S. Chigare and P. S. Patil, *Applied Surface Science*, 2003, **206**, 90-101.
93. S. A. Mahmoud, A. A. Akl and S. M. Al-Shomar, *Physica B: Condensed Matter*, 2009, **404**, 2151-2158.
94. R. Azzam and N. Bashara, *Ellipsometry and polarized light*, North-Holland Pub. Co., 1977.
95. H. Tompkins and E. A. Irene, *Handbook of Ellipsometry*, William Andrew Publishing, 2005.
96. H. Fujiwara, *Spectroscopic ellipsometry: principles and applications*, John Wiley & Sons, 2007.
97. F. Wooten, in *Optical Properties of Solids*, ed. F. Wooten, Academic Press, 1972, pp. 15-41.
98. M. Lax and D. F. Nelson, *Physical Review B*, 1976, **13**, 1777-1784.
99. A. Röseler, *Infrared Spectroscopic Ellipsometry*, Berlin. Akademie-Verlag. 1990.
100. D. A. G. Bruggeman, *Annalen der Physik*, 1935, **416**, 636-664.
101. D. Schmidt and M. Schubert, *J. Appl. Phys.*, 2013, **114**, 083510.
102. H. A. Kramers and W. Heisenberg, *Zeitschrift für Physik*, 1925, **31**, 681-708.
103. R. d. L. Kronig, *Zeitschrift für Physik*, 1925, **33**, 261-272.
104. J. S. Toll, *Physical Review*, 1956, **104**, 1760-1770.
105. P. Drude, *Annalen der Physik*, 1904, **319**, 677-725.
106. A. Sommerfeld and H. Bethe, *Elektronentheorie der Metalle*, Springer-Verlag, 2013.
107. H. Fujiwara and M. Kondo, *Physical Review B*, 2005, **71**, 075109.
108. T. E. Tiwald, D. W. Thompson, J. A. Woollam, W. Paulson and R. Hance, *Thin Solid Films*, 1998, **313-314**, 661-666.
109. F. Wooten, in *Optical Properties of Solids*, ed. F. Wooten, Academic Press, 1972, pp. 42-84.
110. B. von Blanckenhagen, D. Tonova and J. Ullmann, *Appl. Opt.*, 2002, **41**, 3137-3141.
111. G. E. Jellison Jr. and F. A. Modine, *Applied Physics Letters*, 1996, **69**, 371-373.

112. J. N. Hilfiker, N. Singh, T. Tiwald, D. Convey, S. M. Smith, J. H. Baker and H. G. Tompkins, *Thin Solid Films*, 2008, **516**, 7979-7989.
113. D. E. Aspnes and J. B. Theeten, *Journal of The Electrochemical Society*, 1980, **127**, 1359-1365.
114. E. Langereis, S. B. S. Heil, H. C. M. Knoop, W. Keuning, M. C. M. van de Sanden and W. M. M. Kessels, *Journal of Physics D: Applied Physics*, 2009, **42**, 073001.
115. T. Ohtsuka and K. Fushimi, *Electrochemistry*, 2016, **84**, 826-832.
116. B. Kalas, E. Agocs, A. Romanenko and P. Petrik, *physica status solidi (a)*, 2019, **216**, 1800762.
117. M. R. Baklanov, K. P. Mogilnikov, V. G. Polovinkin and F. N. Dultsev, *J. Vac. Sci. Technol. B*, 2000, **18**, 1385-1391.
118. C. Boissiere, D. Grosso, S. Lepoutre, L. Nicole, A. B. Bruneau and C. Sanchez, *Langmuir*, 2005, **21**, 12362-12371.
119. C. Toparli, A. Sarfraz, A. D. Wieck, M. Rohwerder and A. Erbe, *Electrochimica Acta*, 2017, **236**, 104-115.
120. C. Toparli, A. Sarfraz and A. Erbe, *Physical Chemistry Chemical Physics*, 2015, **17**, 31670-31679.
121. Y. Chen and A. Erbe, *Surface Science*, 2013, **607**, 39-46.
122. J. Lekner, *Theory of reflection of electromagnetic and particle waves*, Springer Science & Business Media, 2013.
123. M. Rabe, C. Toparli, Y.-H. Chen, O. Kasian, K. J. J. Mayrhofer and A. Erbe, *Physical Chemistry Chemical Physics*, 2019, **21**, 10457-10469.
124. W. Sellmeier, *Annalen der Physik*, 1872, **223**, 386-403.
125. S. Ardizzone, A. Carugati and S. Trasatti, *Journal of Electroanalytical Chemistry and Interfacial Electrochemistry*, 1981, **126**, 287-292.
126. S. Fierro, L. Ouattara, E. H. Calderon and C. Comninellis, *Electrochemistry Communications*, 2008, **10**, 955-959.
127. C. A. Schneider, W. S. Rasband and K. W. Eliceiri, *Nature Methods*, 2012, **9**, 671-675.
128. W. Rasband, *Google Scholar There is no corresponding record for this reference*, 2014.
129. J.-L. Pouchou, *Microchimica Acta*, 2002, **138**, 133-152.
130. J. Hay and B. Crawford, *Journal of Materials Research*, 2011, **26**, 727.
131. P. Jovanovič, N. Hodnik, F. Ruiz-Zepeda, I. Arčon, B. Jozinović, M. Zorko, M. Bele, M. Šala, V. S. Šelih, S. Hočevar and M. Gaberšček, *Journal of the American Chemical Society*, 2017, **139**, 12837-12846.
132. M. Bernicke, B. Eckhardt, A. Lippitz, E. Ortel, D. Bernsmeier, R. Schmack and R. Kraehnert, *ChemistrySelect*, 2016, **1**, 482-489.
133. B. Eckhardt, E. Ortel, D. Bernsmeier, J. Polte, P. Strasser, U. Vainio, F. Emmerling and R. Kraehnert, *Chemistry of Materials*, 2013, **25**, 2749-2758.
134. B. Eckhardt, E. Ortel, J. Polte, D. Bernsmeier, O. Görke, P. Strasser and R. Kraehnert, *Advanced Materials*, 2012, **24**, 3115-3119.

-
135. V.-D. Hodoroba, K. J. Kim and W. E. S. Unger, *Surface and Interface Analysis*, 2012, **44**, 1459-1461.
136. M. Procop, M. Radtke, M. Krumrey, K. Hasche, S. Schädlich and W. Frank, *Analytical and Bioanalytical Chemistry*, 2002, **374**, 631-634.
137. M. Koshino, H. Kurata and S. Isoda, *Microscopy and Microanalysis*, 2007, **13**, 96.
138. J. Hämäläinen, T. Hatanpää, E. Puukilainen, T. Sajavaara, M. Ritala and M. Leskelä, *Journal of Materials Chemistry*, 2011, **21**, 16488-16493.
139. T. Reier, I. Weidinger, P. Hildebrandt, R. Kraehnert and P. Strasser, *ECS Transactions*, 2013, **58**, 39-51.
140. R. Sanjinés, A. Aruchamy and F. Lévy, *Journal of The Electrochemical Society*, 1989, **136**, 1740-1743.
141. A. Gibaud and G. Vignaud, in *X-ray and Neutron Reflectivity: Principles and Applications*, eds. J. Daillant and A. Gibaud, Springer Berlin Heidelberg, Berlin, Heidelberg, 2009, pp. 85-131.
142. B. L. Henke, E. M. Gullikson and J. C. Davis, *Atomic Data and Nuclear Data Tables*, 1993, **54**, 181-342.
143. J. Goodman and J. Weare, *Comm. App. Math. and Comp. Sci.*, 2010, **5**, 65-80.
144. D. Foreman-Mackey, D. W. Hogg, D. Lang and J. Goodman, *Publications of the Astronomical Society of the Pacific*, 2013, **125**, 306-312.
145. W. C. Johnson, B. Relja, L. Koppel and S. Gopinath, *AIP Conference Proceedings*, 2001, **550**, 461-467.
146. D. F. Abbott, D. Lebedev, K. Waltar, M. Povia, M. Nachtegaal, E. Fabbri, C. Copéret and T. J. Schmidt, *Chemistry of Materials*, 2016, **28**, 6591-6604.
147. G. Greczynski and L. Hultman, *ChemPhysChem*, 2017, **18**, 1507-1512.
148. S. J. Freakley, J. Ruiz-Esquius and D. J. Morgan, *Surface and Interface Analysis*, 2017, **49**, 794-799.
149. G. K. Wertheim and H. J. Guggenheim, *Physical Review B*, 1980, **22**, 4680-4683.
150. T. Li, O. Kasian, S. Cherevko, S. Zhang, S. Geiger, C. Scheu, P. Felfer, D. Raabe, B. Gault and K. J. J. Mayrhofer, *Nature Catalysis*, 2018, **1**, 300-305.
151. B. J. Kim, H. Jin, S. J. Moon, J. Y. Kim, B. G. Park, C. S. Leem, J. Yu, T. W. Noh, C. Kim, S. J. Oh, J. H. Park, V. Durairaj, G. Cao and E. Rotenberg, *Physical Review Letters*, 2008, **101**, 076402.
152. A. Subedi, *Physical Review B*, 2012, **85**, 020408.
153. A. K. Goel, G. Skorinko and F. H. Pollak, *Physical Review B*, 1981, **24**, 7342-7350.
154. L. F. Mattheiss, *Physical Review B*, 1976, **13**, 2433-2450.
155. T. M. Silva, A. M. P. Simões, M. G. S. Ferreira, M. Walls and M. Da Cunha Belo, *J. Electroanal. Chem.*, 1998, **441**, 5-12.
156. R. Zallen, *The physics of amorphous solids*, John Wiley & Sons, 2008.
157. C. M. Herzinger, B. Johs, W. A. McGahan and W. Paulson, *Thin Solid Films*, 1998, **313-314**, 281-285.

158. C. M. Herzinger, B. Johs, W. A. McGahan, J. A. Woollam and W. Paulson, *Journal of Applied Physics*, 1998, **83**, 3323-3336.
159. M. Morita, T. Ohmi, E. Hasegawa, M. Kawakami and M. Ohwada, *Journal of Applied Physics*, 1990, **68**, 1272-1281.
160. W. S. Choi, S. S. A. Seo, K. W. Kim, T. W. Noh, M. Y. Kim and S. Shin, *Physical Review B*, 2006, **74**, 205117.
161. J. S. de Almeida and R. Ahuja, *Physical Review B*, 2006, **73**, 165102.
162. M. Thommes, K. Kaneko, A. V. Neimark, J. P. Olivier, F. Rodriguez-Reinoso, J. Rouquerol and K. S. W. Sing, *Pure and Applied Chemistry*, 2015, **87**, 1051.
163. P. Löbmann, *Journal of Sol-Gel Science and Technology*, 2017, **84**, 2-15.
164. D. W. Gidley, H.-G. Peng, R. Vallery, C. L. Soles, H.-J. Lee, B. D. Vogt, E. K. Lin, W.-L. Wu and M. R. Baklanov, in *Dielectric Films for Advanced Microelectronics*, eds. M. R. Baklanov, M. L. Green and K. Maex, 2007, ch. 3, pp. 85-136.
165. S. Hackwood, A. H. Dayem and G. Beni, *Physical Review B*, 1982, **26**, 471-478.
166. S. H. Brewer, D. Wicaksana, J.-P. Maria, A. I. Kingon and S. Franzen, *Chemical Physics*, 2005, **313**, 25-31.
167. K. v. Benthem, C. Elsässer and R. H. French, *Journal of Applied Physics*, 2001, **90**, 6156-6164.
168. Z. H. Zhang, X. Y. Qi, J. K. Jian and X. F. Duan, *Micron*, 2006, **37**, 229-233.
169. R. F. Egerton, *Reports on Progress in Physics*, 2008, **72**, 016502.
170. R. Erni and N. D. Browning, *Ultramicroscopy*, 2008, **108**, 84-99.
171. D. Tahir and S. Tougaard, *Journal of physics: Condensed matter*, 2012, **24**, 175002.
172. A. Ganassin, V. Colic, J. Tymoczko, A. S. Bandarenka and W. Schuhmann, *Physical Chemistry Chemical Physics*, 2015, **17**, 8349-8355.
173. K. Hideaki, G. Yunzhi and O. Koh-ichi, *Chemistry Letters*, 1994, **23**, 73-76.
174. C. Bock and V. I. Birss, *J. Electroanal. Chem.*, 1999, **475**, 20-27.
175. C. H. Hamann, A. Hamnett and W. Vielstich, *Electrochemistry*, Wiley-VCH, Weinheim, 2., completely rev. and updated ed. edn., 2007.
176. P. Daubinger, J. Kieninger, T. Unmüssig and G. A. Urban, *Physical Chemistry Chemical Physics*, 2014, **16**, 8392-8399.
177. A. Y. C. Yu, W. E. Spicer and G. Hass, *Physical Review*, 1968, **171**, 834-835.
178. J. H. Weaver, *Physical Review B*, 1975, **11**, 1416-1425.
179. A. D. Rakić, A. B. Djurišić, J. M. Elazar and M. L. Majewski, *Appl. Opt.*, 1998, **37**, 5271-5283.
180. H. C. M. Knoops, A. J. M. Mackus, M. E. Donders, M. C. M. van de Sanden, P. H. L. Notten and W. M. M. Kessels, *Electrochemical and Solid-State Letters*, 2009, **12**, G34-G36.
181. H. Neff, S. Henkel, E. Hartmannsgruber, E. Steinbeiss, W. Michalke, K. Steenbeck and H. G. Schmidt, *Journal of Applied Physics*, 1996, **79**, 7672-7675.
182. T. Smith, *Journal of the Optical Society of America*, 1968, **58**, 1069-1079.
183. B. E. Hayden and G. P. Nicholson, *Surface Science*, 1992, **274**, 277-286.

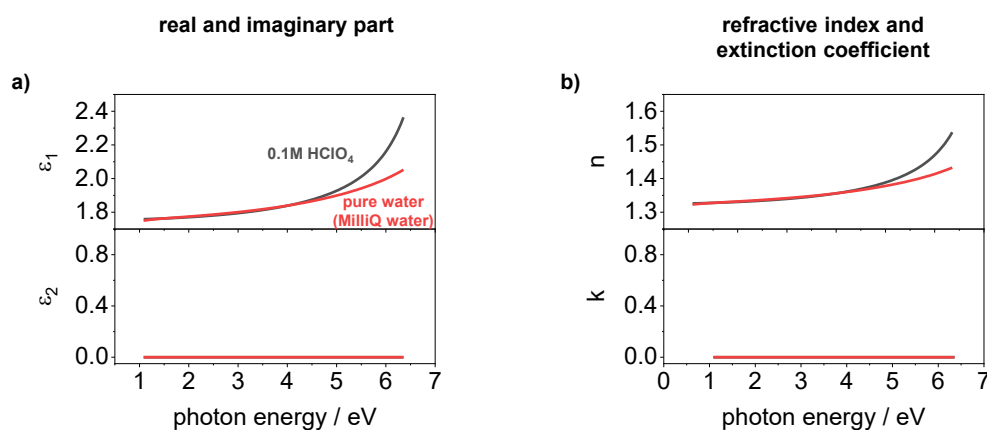
-
184. G. A. Bootsma and F. Meyer, *Surface Science*, 1969, **14**, 52-76.
185. F. H. P. M. Habraken, O. L. J. Gijzeman and G. A. Bootsma, *Surface Science*, 1980, **96**, 482-507.
186. Y. Chen, P. Schneider and A. Erbe, *physica status solidi (a)*, 2012, **209**, 846-853.
187. D. Gilroy and B. E. Conway, *Canadian Journal of Chemistry*, 1968, **46**, 875-890.
188. S. J. Percival and B. Zhang, *Langmuir*, 2014, **30**, 11235-11242.
189. L. Ilyukhina, S. Sunde and R. G. Haverkamp, *Journal of The Electrochemical Society*, 2017, **164**, F1662-F1670.
190. H. G. Sanchez Casalongue, M. L. Ng, S. Kaya, D. Friebel, H. Ogasawara and A. Nilsson, *Angewandte Chemie International Edition*, 2014, **53**, 7169-7172.
191. J. O. M. Bockris, *The Journal of Chemical Physics*, 1956, **24**, 817-827.
192. M. A. Petit and V. Plichon, *J. Electroanal. Chem.*, 1998, **444**, 247-252.
193. M. Hüppauff and B. Lengeler, *Journal of The Electrochemical Society*, 1993, **140**, 598-602.
194. A. Minguzzi, O. Lugaresi, E. Achilli, C. Locatelli, A. Vertova, P. Ghigna and S. Rondinini, *Chemical Science*, 2014, **5**, 3591-3597.
195. J. D. E. McIntyre, S. Basu, W. F. Peck, W. L. Brown and W. M. Augustyniak, *Physical Review B*, 1982, **25**, 7242-7254.
196. W. T. Hong, M. Risch, K. A. Stoerzinger, A. Grimaud, J. Suntivich and Y. Shao-Horn, *Energy & Environmental Science*, 2015, **8**, 1404-1427.
197. J. Suntivich, H. A. Gasteiger, N. Yabuuchi, H. Nakanishi, J. B. Goodenough and Y. Shao-Horn, *Nature Chemistry*, 2011, **3**, 546-550.
198. M. A. Señarís-Rodríguez and J. B. Goodenough, *Journal of Solid State Chemistry*, 1995, **118**, 323-336.
199. H. M. Tsai, P. D. Babu, C. W. Pao, J. W. Chiou, J. C. Jan, K. P. K. Kumar, F. Z. Chien, W. F. Pong, M.-H. Tsai, C.-H. Chen, L. Y. Jang, J. F. Lee, R. S. Chen, Y. S. Huang and D. S. Tsai, *Applied Physics Letters*, 2007, **90**, 042108.
200. F. Frati, M. O. J. Y. Hunault and F. M. F. de Groot, *Chemical Reviews*, 2020, **120**, 4056-4110.
201. L. J. Frevel, R. Mom, J.-J. Velasco-Vélez, M. Plodinec, A. Knop-Gericke, R. Schlögl and T. E. Jones, *The Journal of Physical Chemistry C*, 2019, **123**, 9146-9152.
202. J. J. Velasco-Vélez, T. E. Jones, V. Streibel, M. Hävecker, C. H. Chuang, L. Frevel, M. Plodinec, A. Centeno, A. Zurutuza, R. Wang, R. Arrigo, R. Mom, S. Hofmann, R. Schlögl and A. Knop-Gericke, *Surface Science*, 2019, **681**, 1-8.
203. M. Kraume, *Transportvorgänge in der Verfahrenstechnik*, Springer, 2004.
204. G. Emig and E. Klemm, *Technische Chemie: Einführung in die chemische Reaktionstechnik*, Springer-Verlag, 2006.
205. H. A. El-Sayed, A. Weiß, L. F. Olbrich, G. P. Putro and H. A. Gasteiger, *Journal of The Electrochemical Society*, 2019, **166**, F458-F464.
206. M. Boudot, H. Elettro and D. Grosso, *ACS Nano*, 2016, **10**, 10031-10040.
207. P. Steegstra, M. Busch, I. Panas and E. Ahlberg, *The Journal of Physical Chemistry C*, 2013, **117**, 20975-20981.

208. P. Lettenmeier, L. Wang, U. Golla-Schindler, P. Gazdzicki, N. A. Cañas, M. Handl, R. Hiesgen, S. S. Hosseiny, A. S. Gago and K. A. Friedrich, *Angewandte Chemie International Edition*, 2016, **55**, 742-746.

A Appendix

A1 Dielectric function and optical constants of pure water / perchloric acid

0.1M perchloric acid was analyzed using a silicon wafer with known oxide thickness after quartz window correction in the flow cell setup, in which the electrolyte flowed over the silicon wafers. The modeling was performed using a Sellmeier dispersion layer (equation (47)) and the obtained dielectric functions were used during ECSE analysis. The dielectric functions of 0.1M perchloric acid were determined before each measurement.

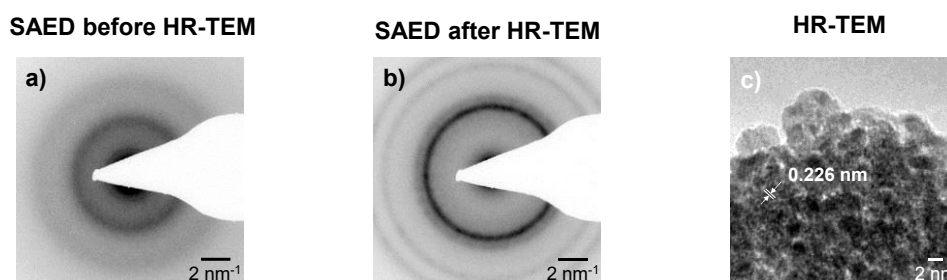


Appendix figure A1.1: Spectroscopic ellipsometric analysis of 0.1M perchloric acid. Analysis was performed in the flow cell setup by using a silicon wafer with known oxide thickness. For comparison the dielectric functions and optical constants of pure water (MilliQ water) are displayed. a) dielectric functions of the 0.1M perchloric acid and pure water. b) optical constants of 0.1M perchloric acid and pure water.

A2 TEM / SAED analysis of a mesoporous IrO_x film

Appendix figure A2.1 presents TEM and SAED analysis of an IrO_x film fragment calcined in air at 375 °C. The SAED analysis after direct transfer of the sample into the TEM (Appendix figure A2.1a) reveals broad diffuse rings that can be assigned to IrO_2 (PDF: 00-015-0870).

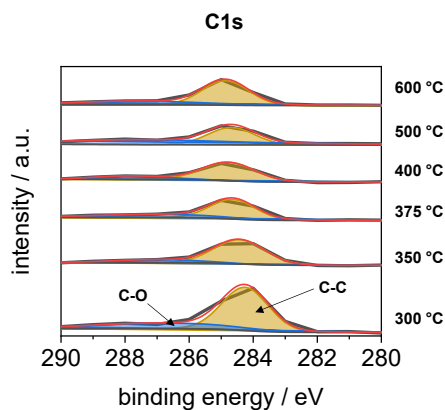
After a high-resolution analysis, the SAED (Appendix figure A2.1b) displays diffuse rings that can be assigned to metallic Ir (PDF: 00-006-0598). In addition, the HR-TEM image (Appendix figure A2.1c) shows small crystalline particles, where the lattice distances can also be assigned to metallic Ir. Therefore, the IrO_x decomposes to metallic Ir upon prolonged irradiation with the reductive beam.



Appendix figure A2.1: TEM/SAED analysis of an IrO_x film fragment, which was calcined in air at 375 °C. a) SAED analysis of the fresh sample, b) SAED analysis after HR-TEM microscopy and c) HR-TEM image with indication of lattice distances of small particles within the film fragment.

A3 XPS C1s spectra and summarization of the fitted photoelectron spectra

Photoelectron spectra normalized to their maximum intensity were fitted after a Shirley background subtraction using sum Gaussian–Lorentzian functions. The deconvoluted C1s spectra indicate two peaks at about 284.6 eV and 287.2 eV, which can be attributed to adventitious carbon species with C-C/C-H bonds and C-O bonds, respectively.¹⁴⁷



Appendix figure A3.1: X-ray photonelectron spectra of the IrO_x calcination series in the C1s region. Deconvoluted spectra were fitted with sum Gaussian–Lorentzian functions after a Shirley background subtraction.

Summarization of the fitted photoelectron spectra in the C1s, O1s, Ir4f and in the valence band (VB) region using a summation of Gaussian-Lorentzian functions after a Shirley background subtraction of the IrO_x calcination series on silicon substrates.

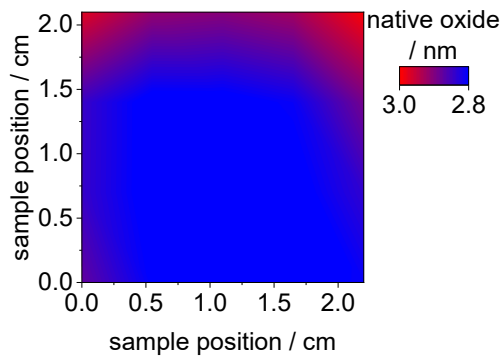
Appendix table A3.1: Summary of the adjusted photoelectron spectra using sum Gaussian-Lorentzian functions after a Shirley background subtraction.

Region		Property	T _{calc.}					
			300 °C	350 °C	375 °C	400 °C	500 °C	600 °C
C1s	C-C	E _{bin} / eV	284.3	284.4	284.6	284.8	284.7	284.9
		relative area / %	72.1	82.9	62.1	80.0	63.7	61.6
	C-O	E _{bin} / eV	286.8	287.0	287.1	287.9	287.3	287.7
		relative area / %	27.9	17.1	37.9	20.0	36.3	38.4
O1s	Ir-O	E _{bin} / eV	-	529.6	530.1	529.8	529.8	529.9
		relative area / %	-	5.1	18.3	15.3	23.8	32.5
	Ir-OH	E _{bin} / eV	531.2	530.8	531.3	531.2	531.1	531.1
		relative area / %	67.6	68.7	58.0	59.5	53.5	43.1
	adventitious carbon	E _{bin} / eV	532.8	532.5	532.9	532.9	532.8	532.5
		relative area / %	32.4	26.2	23.7	25.2	22.7	24.4
Ir4f	anhydrous IrO ₂ (7/2)	E _{bin} / eV	61.4	61.4	61.6	61.5	61.6	61.7
		relative area / %	14.1	14.0	13.6	14.5	20.9	26.1
	anhydrous IrO ₂ (5/2)	E _{bin} / eV	64.6	64.6	64.7	64.6	64.7	64.7
		relative area / %	27.4	26.0	27.1	25.1	27.2	33.3
	hydrated IrO(OH) (7/2)	E _{bin} / eV	62.2	62.2	62.2	62.2	62.4	62.6
		relative area / %	40.3	37.7	32.2	29.2	16.3	13.4
	hydrated IrO(OH) (5/2)	E _{bin} / eV	65.8	65.8	65.3	65.2	65.2	65.8
		relative area / %	18.2	22.3	27.2	31.2	35.7	27.1
VB	I	E _{bin} / eV	-	-	-	-	0.2	0.2
		relative area / %	-	-	-	-	3.2	3.3
	II	E _{bin} / eV	1.5	1.5	1.7	1.7	1.8	1.8
		relative area / %	51.0	55.6	55.7	53.2	43.9	49.9
	III	E _{bin} / eV	5.1	5.1	5.1	5.1	5.0	5.1
		relative area / %	31.0	21.3	21.0	23.4	21.0	20.3
	IV	E _{bin} / eV	8.1	8.1	8.1	8.1	8.1	8.1
		relative area / %	18.0	23.0	23.3	23.4	31.9	26.4

A4 Analysis of an uncoated Si substrate treated in a muffle furnace at 600 °C in flowing air for 2h

An uncoated Si substrate treated in a muffle furnace at 600 °C in flowing air for 2h was measured by SE to determine the thickness of the native oxide layer and the influence of the thermal treatment step before layer deposition. The SE mapping analysis shows a uniform thickness of the native oxide layer between 2.8 and 3.0 nm. The fits were modeled using literature data for the Si substrate and the native oxide layer.¹⁵⁷⁻¹⁵⁹

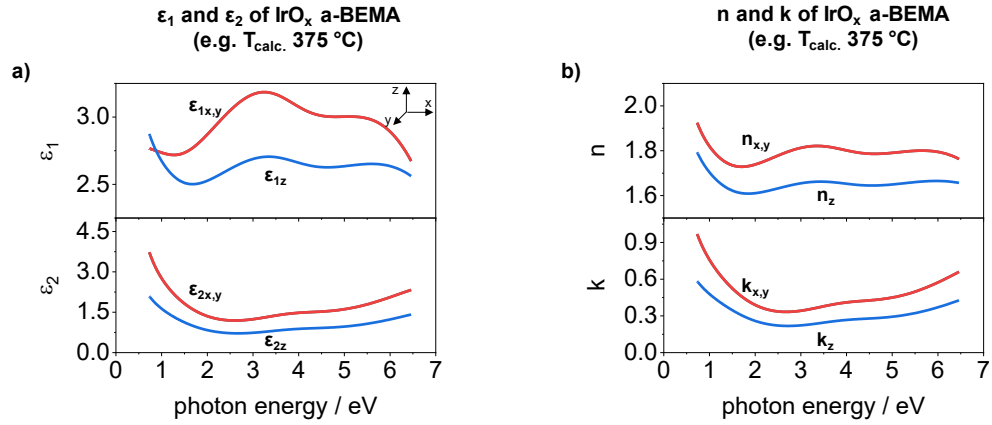
SE mapping analysis of the native oxide layer of a Si substrate



Appendix figure A4.1: SE mapping analysis of an uncoated Si substrate, which treated in a muffle furnace at 600 °C in flowing air for 2h.

A5 Dielectric functions and optical constants of the a-BEMA (IrO_x 375 °C)

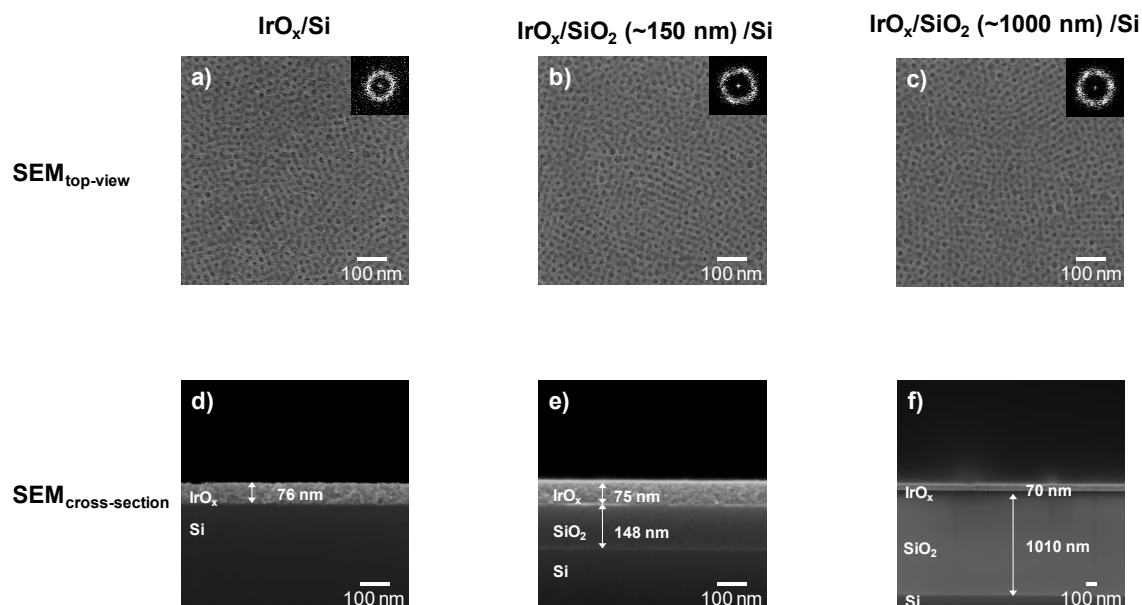
Dielectric functions and optical constants of the a-BEMA layer of the mesoporous IrO_x film calcined at 375 °C for 5 minutes in air.



Appendix figure A5.1: Dielectric functions (a) and optical constants (b) from the a-BEMA layer with anisotropy in z-direction of an IrO_x film calcined at 375 °C

A6 SEM cross-section images of mesoporous IrO_x films (375 °C) at Si and Si/SiO₂ substrates

SEM images of the IrO_x films on a silicon substrate and silicon substrates with a thermal SiO₂ layer of 150 nm and 1000 nm for ellipsometric interference enhancement measurements.



Appendix figure A6.1: SEM images of mesoporous IrO_x films calcined at 375 °C in air on different substrates. a) top-view and d) cross-section image of IrO_x on a Si substrate, b) top-view and e) cross-section image IrO_x on a Si substrate with a thermal SiO₂ layer (~150 nm), and c) top-view and f) cross-section image IrO_x on a Si substrate with a thermal SiO₂ layer of about 1000 nm.

IrO_x films produced on the different substrates and calcined at 375 °C reveal a complete developed mesopore system with periodic pore arrangements (Appendix figure A6.1a-c). Estimated IrO_x film thicknesses amount to 76 nm, 75 nm and 70 nm for the samples deposited on the Si substrate, Si/SiO₂-substrate (150 nm SiO₂) and Si/SiO₂-substrate (1000 nm SiO₂), respectively. SiO₂ thicknesses of the Si/SiO₂-substrates amount to 148 nm and 1010 nm.

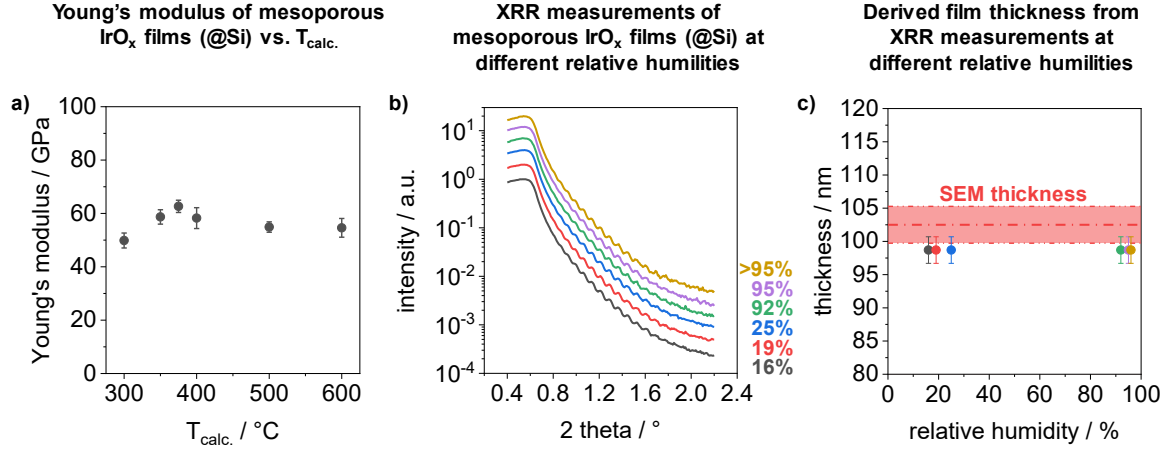
A7 Instrumented indentation testing and XRR measurements at different humidity conditions

In order to investigate the influence of pore geometry and layer thickness in liquids, i.e. deformations due to swelling or capillary contractions, instrumented indentation testing (IIT) were performed to determine the Young's modulus and layer thickness using XRR at different humidity conditions.

IIT was performed with a Berkovich indenter using a constant depth method for IrO_x layers on silicon substrates. Substrate corrections were used to obtain the substrate-independent Young's moduli of the films, which are described in detail in the following reference ¹³⁰. The determined Young's moduli (Appendix figure A7.1a) are in the range between 50 GPa and 60 GPa with a slight increase from 300 °C to 375 °C and then remain approximately constant at higher calcination temperatures.

XRR relative humidity measurements (Appendix figure A7.1b) were carried out by placing an attachment cell with X-ray windows consisting of a polyethylene film (amorphous, thickness nominally 4 µm) on the sample. Compressed air was mixed with water to set the desired humidity. After a constant humidity value, the air flow was introduced into the attachment cell with approx. 4-6 ml s⁻¹. Results of the XRR measurements of an IrO_x films calcined at 350 °C at different humidity conditions indicate defined Kiessig oscillations. The minima and maxima of these oscillations are identical for all measurements. By a simple layer modeling, consisting of a silicon substrate, a native oxide layer (2 nm) and an IrO₂ layer (literature values) the layer thickness of the individual measurements could be derived. As a result, the same layer thickness is obtained at all humidity values (Appendix figure A7.1c).

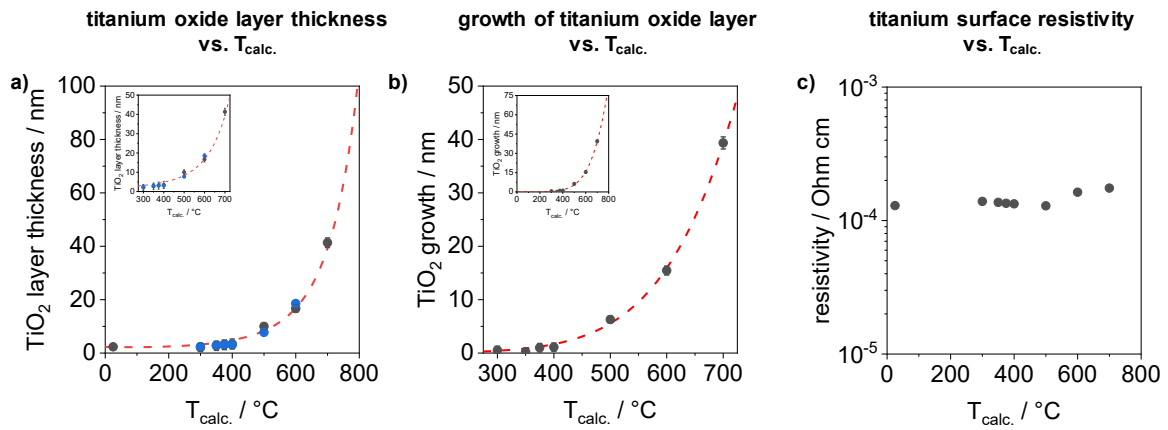
In summary, the two measurements reveal that the layer thickness of the studied IrO_x films does not change at different humidity levels or in liquids. In addition, the IIT shows that the films have a high Young's modulus and are therefore relatively rigid, which hinders deformation in liquids by swelling or capillary contractions, as is the case for instance of mesoporous silicon oxide films.²⁰⁶



Appendix figure A7.1: Instrumented indentation testing and XRR measurements of mesoporous IrO_x films. a) Young's modulus of mesoporous IrO_x films calcined between 300 °C and 600 °C. b) XRR measurements at relative humidity values between 16% and approximately 100% of an IrO_x film calcined at 350 °C. c) derived film thicknesses from XRR measurements with a simple 3 layer model, consisting of a silicon substrate, a native oxide layer and an IrO_2 layer.

A8 SE analysis of titanium substrates

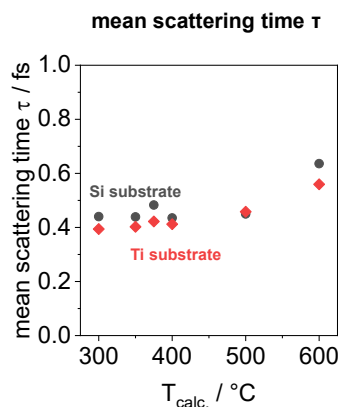
Titanium substrates were analyzed after grinding and polishing by SE and fitted with a model consisting of a titanium layer (Drude-Lorentz parameterization) and a titanium oxide layer (Tauc-Lorentz parameterization). After coating and calcination of the IrO_x films, the titanium oxide layer was also considered as a free parameter. In addition, the titanium substrate was also analyzed with SE at the uncoated area. In both cases, i.e., under the IrO_x layer and the uncoated area, the titanium dioxide layer seems to grow exponentially with increasing calcination temperature. Appendix figure A8.1a) shows the titanium oxide layer thickness derived by SE and b) the difference between the oxide layer after polishing and after calcination. Additionally, the surface conductivity could be derived from the modeling of the titanium layer. It can be seen that with increasing calcination temperature an increase of the resistivity is achieved. However, this resistivity is still low enough to ensure sufficient conductivity.



Appendix figure A8.1: SE Analysis of the titanium oxide layer on the titanium substrates used as a function of the calcination temperature. a) Derived titanium oxide layer thicknesses before the calcination procedure and after the calcination of the film. Black circles show the titanium oxide layer thickness of the uncoated area and blue circles show the layer thickness under the IrO_x layer. b) Difference in titanium oxide layer thickness before and after calcination. c) Surface conductivity of the titanium substrates as a function of the calcination temperature.

A9 Mean scattering time as a function of calcination temperature

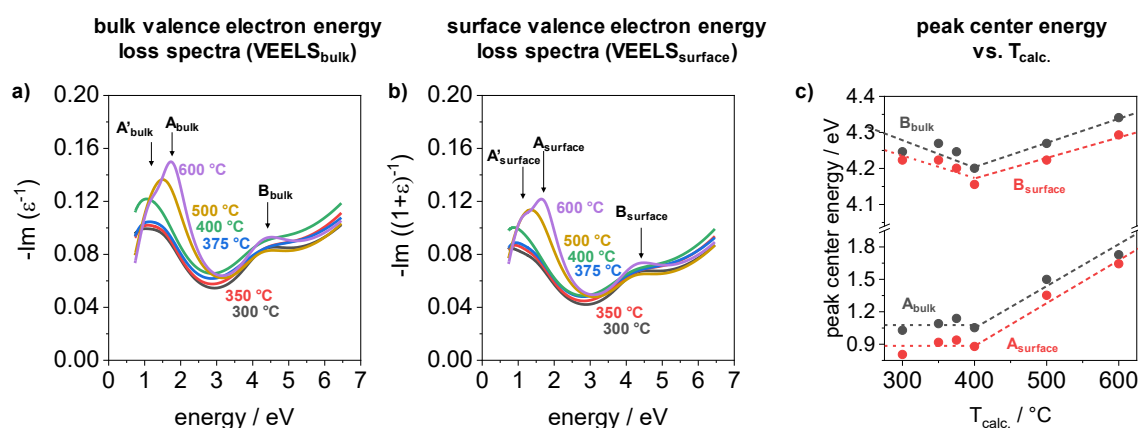
Mean scattering time τ from ex situ SE modeling. The values were derived from the fit parameter of the Drude model (equation (38)) for the IrO_x material of the mesoporous IrO_x films deposited on Si and Ti substrates. The values range from 0.44 fs to 0.64 fs for films on Si substrates and from 0.39 fs to 0.56 fs for films on Ti substrates. In both cases, a relatively constant value of the mean scattering time can be observed up to a calcination temperature of 400°C and an increase at higher calcination temperatures.



Appendix figure A9.1: Deduced mean scattering time of the iridium oxide material from ex-situ spectroscopic ellipsometry as a function of the calcination temperature.

A10 Ex-situ VEELS analysis of mesoporous IrO_x films on titanium substrates

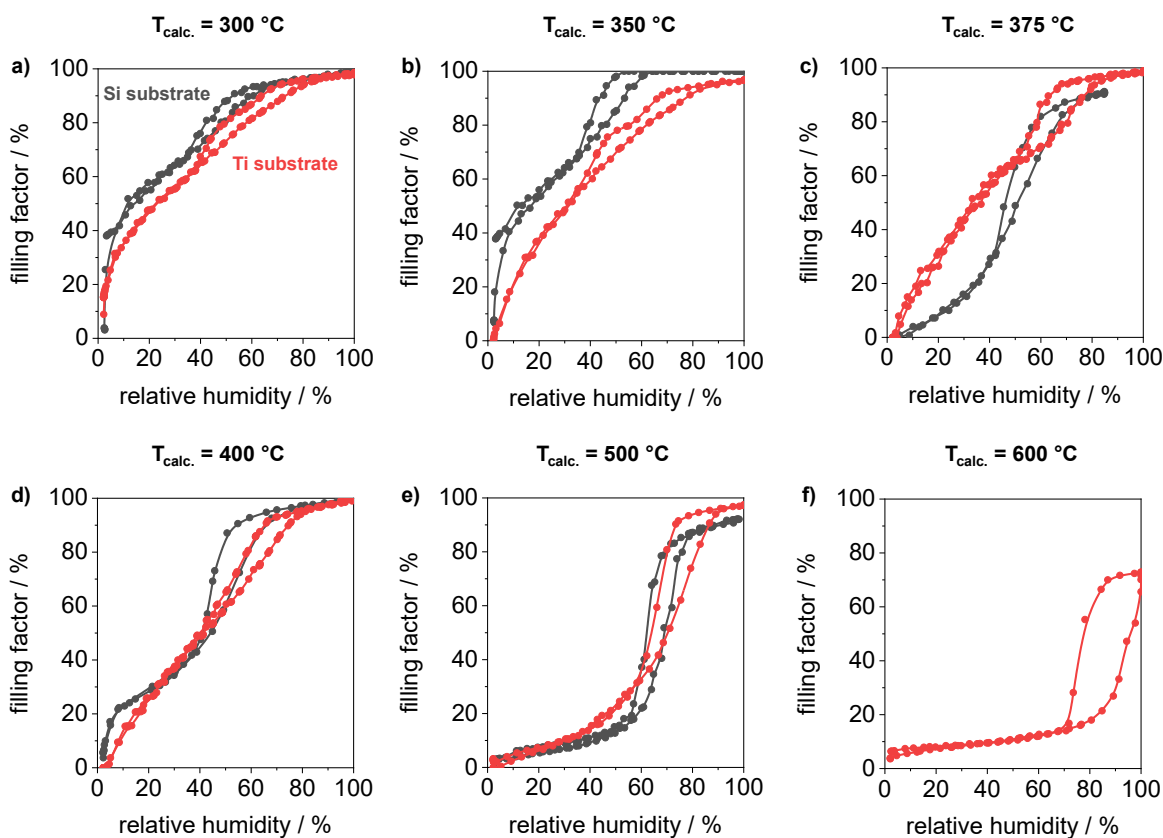
Valence electron energy loss spectra (VEELS) analysis of the mesoporous IrO_x films on titanium substrate indicate the two peaks labeled respectively as A_{bulk} and B_{bulk} or A_{surface} and B_{surface} as well as the shoulder (A'_{bulk} and A'_{surface}) at 600 °C. Energy values of the A_{bulk} peak maximum are located at about 1.1 eV for the films calcined between 300 °C and 400 °C and shifts to higher energies (up to 1.7 eV) for samples calcined at 500 °C and 600 °C. A_{surface} peak maximum energies are shifted about 0.1 eV to lower energies. The B peaks indicate a slight decrease of the energy values until 400 °C and increase at higher calcination temperatures.



Appendix figure A10.1: Valence electron energy loss spectra (VEELS) analysis and shifts of identified peak position of mesoporous iridium oxide films calcined between 300 °C and 600 °C on titanium substrates. a) calculated bulk VEELS and b) surface VEELS from the obtained real and imaginary part of the dielectric functions. c) peak maximum center energy of the indicated peaks from the bulk and surface VEELS as a function of calcination temperature (T_{calc.}).

A11 Physisorption via ellipsometric porosimetry

Ellipsometric porosimetry investigation of mesoporous IrO_x films on silicon and titanium substrates by varying the relative humidity between 0% and approx. 100%. Measurements of the IrO_x films on silicon substrates were performed in an environmental cell at a fixed angle of incidence (AOI) of 60° and IrO_x films on titanium substrates in an environmental cell at a fixed AOI of 70° . In both cases, water was used as a solvent to adjust the humidity at constant room temperature and a gas flow rate of 2.5 L min^{-1} . The model described in Chapter 4.2 was used for modeling, where the degree of pore filling with water (filling factor), the porosity and the pore geometry factor served as free parameters.



Appendix figure A11.1: Ellipsometric porosimetry measurements of the mesoporous IrO_x calcination series. Obtained isotherms of the filling factor as a function of the relative humidity for a) the 300°C , b) the 350°C , c) the 375°C , d) the 400°C , e) the 500°C , and f) the 600°C films on silicon substrates (black) and titanium substrates (red).

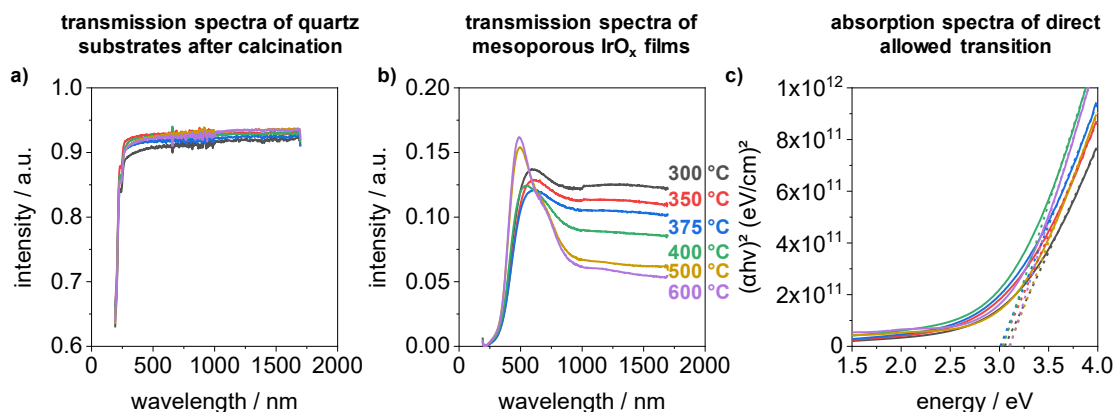
Low-temperature calcined films ($\leq 400\text{ }^{\circ}\text{C}$) show a strong increase in the filling factor in the initial range (0% - 10%), which is representative for micropores. With further increase of relative humidity, the filling factor increases slightly (mostly linear), which is due to multilayer adsorption of water within the mesopores. At higher relative humidity's, a second steep increase in the filling factor is observed, which is characteristic of mesoporous filling of water by capillary condensation. Reaching a plateau (filling factor $\approx 100\%$) at relative humidity's $> 80\%$ indicates completely filled pores.

In the case of the high-temperature calcined films ($> 400\text{ }^{\circ}\text{C}$), no steep increase can be seen in the initial range and the filling factor increases only slightly. At higher relative humidity values of respectively 60% or 70%, the filling factor increases strongly, indicating the filling of the mesopores. Reaching a plateau at a filling factor of about 90% or 75%, indicates a pore system that is not completely accessible.

In all cases, the desorption cycle shows a hysteresis loop of the fill factor, indicating the presence of mesopores within the film.

A12 Transmission spectra of mesoporous IrO_x films on quartz substrates

Mesoporous IrO_x films on quartz substrates were used for transmission spectroscopic measurements inside the ellipsometer. IrO_x films on quartz substrates were derived from the same synthesis as the coated films on the titanium substrates and were used as a comparison for intraband transition energies.



Appendix figure A12.1: Transmission spectroscopic investigations of mesoporous IrO_x films on quartz substrates to determine the Ir d-d intraband transitions. a) Transmission spectra of the quartz substrates after the calcination procedure. b) Transmission spectra of the mesoporous IrO_x layers. c) Absorption spectra of direct allowed transitions.

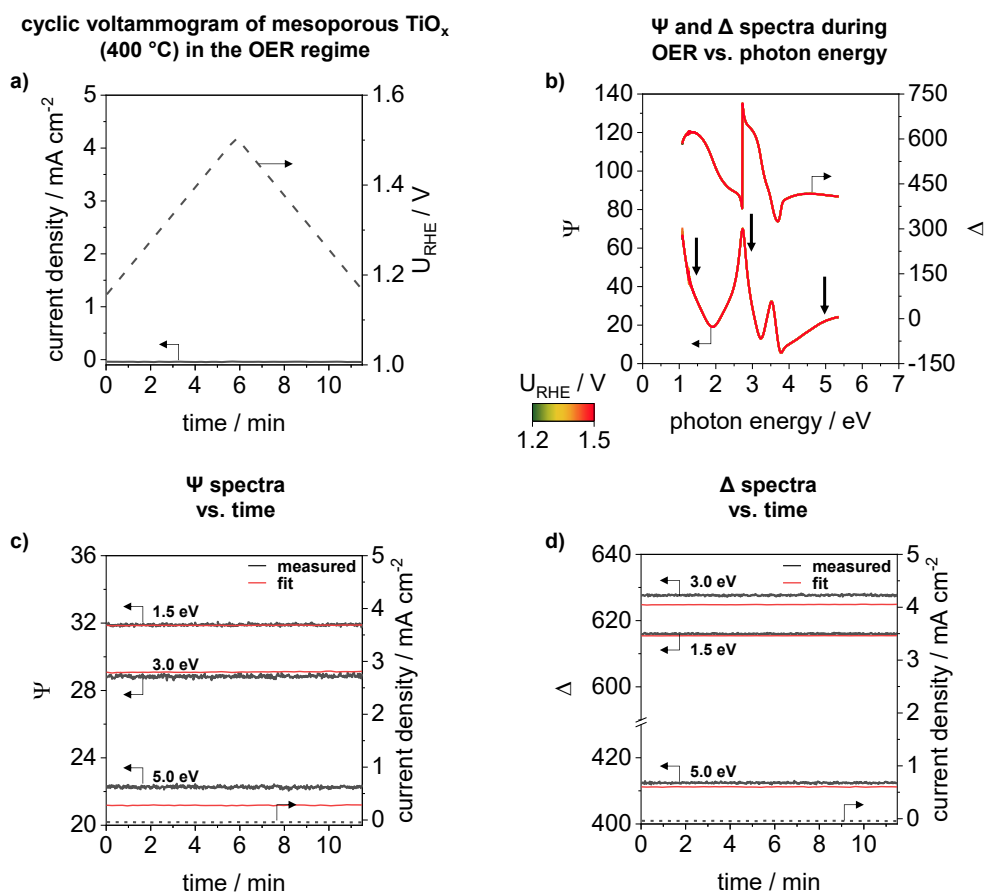
Appendix figure A12.1a) shows the intensity of the transmission spectra of the quartz substrates used, on which the mesoporous IrO_x films were deposited and calcined in air at temperatures between 300 °C and 600 °C. The transmission spectra show comparable intensity for all quartz substrates and are used for substrate correction of the respective transmission measurement of the mesoporous IrO_x layers.

Appendix figure A12.1b) shows the quartz substrate corrected intensities of the transmission spectra of the mesoporous IrO_x films calcined at temperatures between 300 °C and 600 °C in air. The intensities of the spectra show a decrease in the wavelength range between 700 nm and 1600 nm. In addition, a peak at about 700 nm is evident for the low-temperature calcined films (≤ 400 °C), which shifts to lower wavelengths at higher calcination temperatures (> 400 °C).

Appendix figure A12.1c) shows the determination of the direct allowed transition energies of the mesoporous IrO_x films using the Tauc relationship given in equation (8).

A13 Operando ECSE investigation of a non-conductive mesoporous titanium oxide film

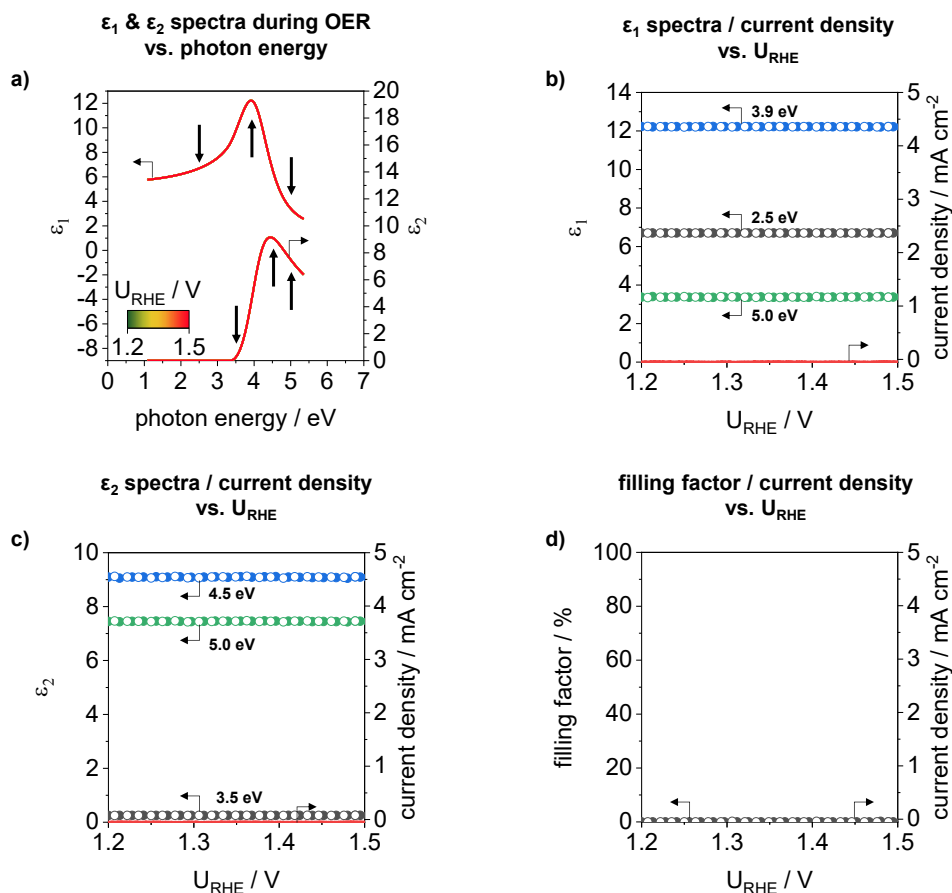
In order to verify independent potential effects on the modeled Ψ and Δ spectra, operando measurements are performed on a non-conductive mesoporous titanium oxide (TiO_x) film, calcined at 400 °C for 20 minutes in air, in the OER regime and in the potential range between 0.40 V_{RHE} and 1.40 V_{RHE} . The mesoporous TiO_x layer was model with an a-BEMA layer using a parametrization of two coupled Tauc-Lorentz (equation (41) and (42)). The electrolyte (0.1M HClO_4) was analyzed before ECSE measurements with a silicon wafer with known oxide layer. For the operando ECSE investigations, the pore anisotropic factor as well as the filling factor were used as free parameters. Appendix figure A13.1 displays a) the cyclic voltammometry measurement, b) the Ψ and Δ spectra during CV measurements, c) the Ψ spectra with fits and d) the Δ spectra with fits at photon energies of 1.5 eV, 3.0 eV and 5.0 eV



Appendix figure A13.1: Operando ECSE investigations of a mesoporous TiO_x film calcined at 400 °C for 10 min in air in the OER regime. a) applied potential and current density as a function of time. b) Ψ and Δ spectra during CV. c) Ψ and d) Δ spectra at selected photon energies with fit results.

The CV measurement indicates a linear increase and decrease of the applied potential and no changes of the current density (Appendix figure A13.1a). Also, the Ψ and Δ spectra reveal no changes in the complete spectra as well as at the selected photon energies (Appendix figure A13.1b-d). Fitting results of the model are in good agreement with the measured spectra (Appendix figure A13.1c and d).

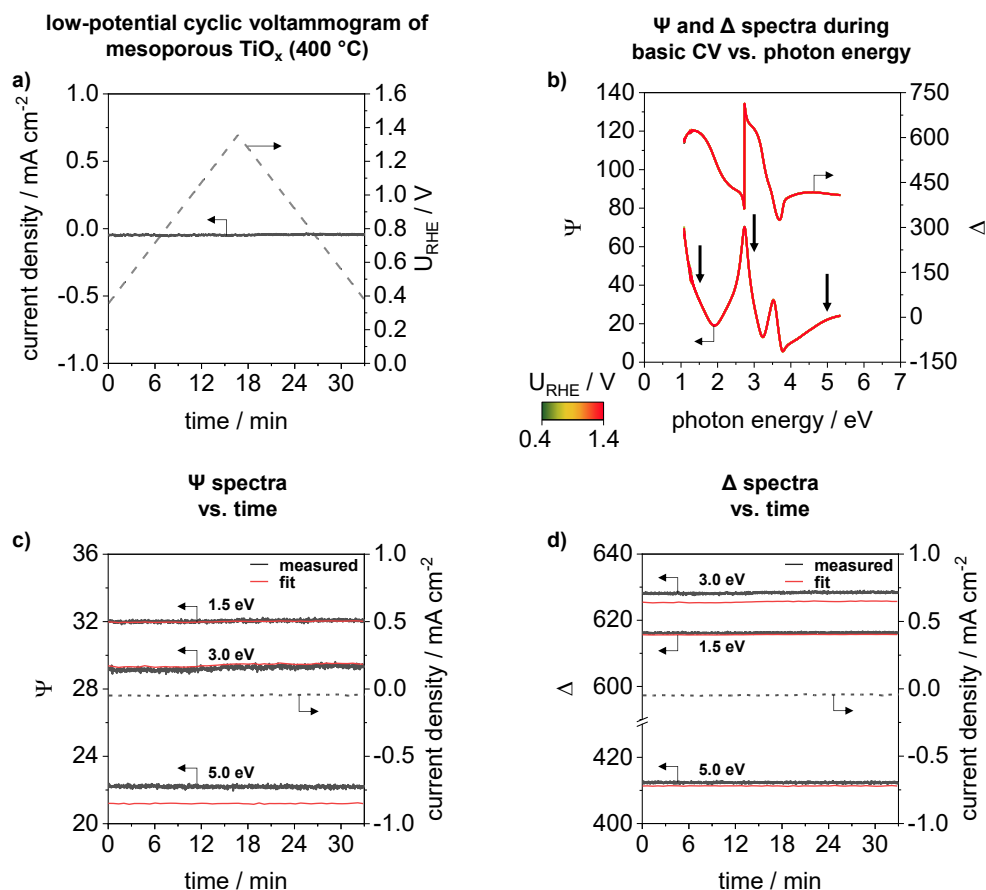
Appendix figure A13.2 shows a) the dielectric functions of the TiO_x material during EC measurements, b) ϵ_1 at photon energies of 2.5 eV, 3.9 eV and 5.0 eV as well as c) ϵ_2 at photon energies of 3.5 eV, 4.5 eV and 5.0 eV. The change of the filling factor is displayed Appendix figure A13.2d.



Appendix figure A13.2: ϵ_1 and ϵ_2 spectra of the TiO_x material (matrix) derived from modeling during ECSE investigation in the OER regime. a) ϵ_1 and ϵ_2 spectra during cyclic voltammetry measurements. b) ϵ_1 at photon energies of 2.5 eV, 3.9 eV and 5.0 eV and c) ϵ_2 at photon energies of 3.5 eV, 4.5 eV and 5.0 eV. d) filling factor as a function of the applied potential.

The derived dielectric functions indicate no changes in the entire spectra during CV measurements in the OER regime as well as no indication of pore filling due to the change in volume fraction with produced gas.

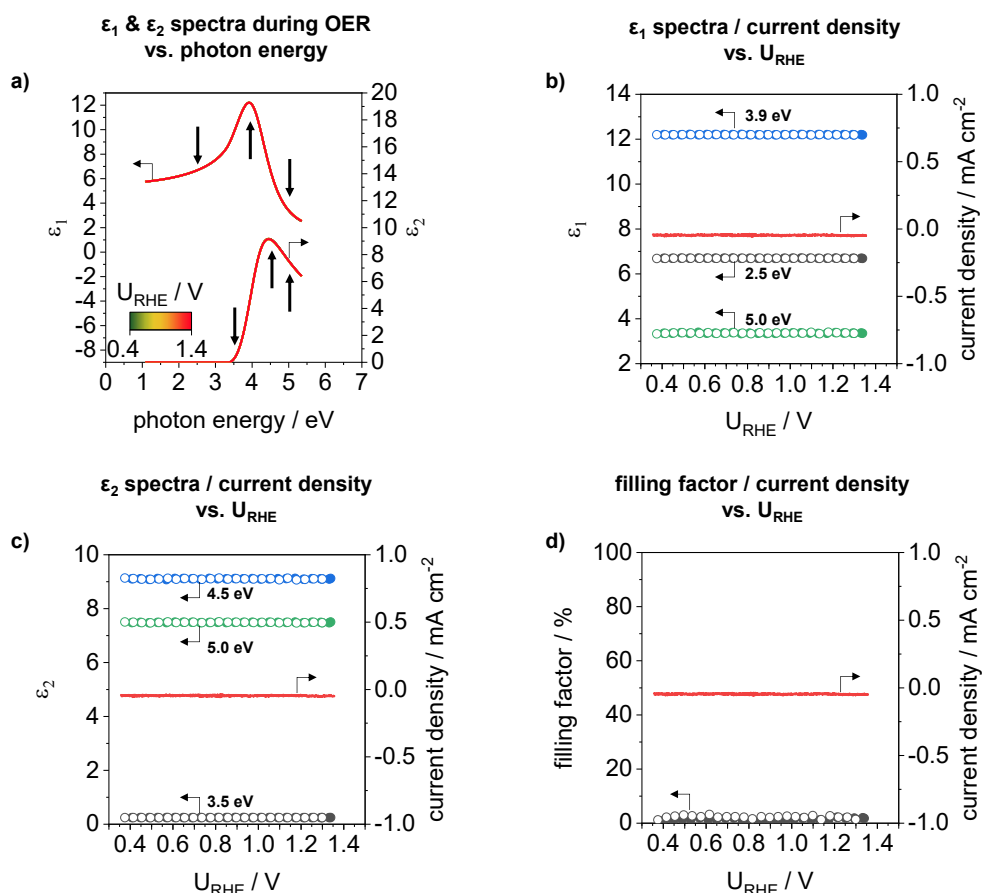
The mesoporous TiO_x film was additionally used for the operando ECSE investigation in the potential range between $0.40 \text{ V}_{\text{RHE}}$ and $1.40 \text{ V}_{\text{RHE}}$. Appendix figure A13.3 displays a) the low-potential cyclic voltammogram, b) the changes of the Ψ and Δ spectra during the measurements as well as c) the Ψ and d) the Δ spectra at selected photon energies.



Appendix figure A13.3: Operando ECSE investigations of a mesoporous TiO_x film in a potential range between $0.40 \text{ V}_{\text{RHE}}$ and $1.40 \text{ V}_{\text{RHE}}$. a) applied potential and current density as a function of time. b) Ψ and Δ spectra during CV. c) Ψ and d) Δ spectra at selected photon energies with fit results.

As in the case of EC measurements in the OER regime, low-potential cyclic voltammetry measurements in the potential range of $0.40 \text{ V}_{\text{RHE}}$ and $1.40 \text{ V}_{\text{RHE}}$ indicate a linear increase and decrease of the applied potential and no further changes of current density (Appendix figure A13.3a). The Ψ and Δ spectra thus reveal as well, no further changes in the complete spectra (Appendix figure A13.3b). The fit results are for both spectra in good agreement (Appendix figure A13.3c and d).

Appendix figure A13.4 shows the a) the changes of the dielectric function during CV measurements, b) ϵ_1 at photon energies of 2.5 eV, 3.9 eV and 5.0 eV, c) ϵ_2 at photon energies of 3.5 eV, 4.5 eV and 5.0 eV and d) the filling factor.



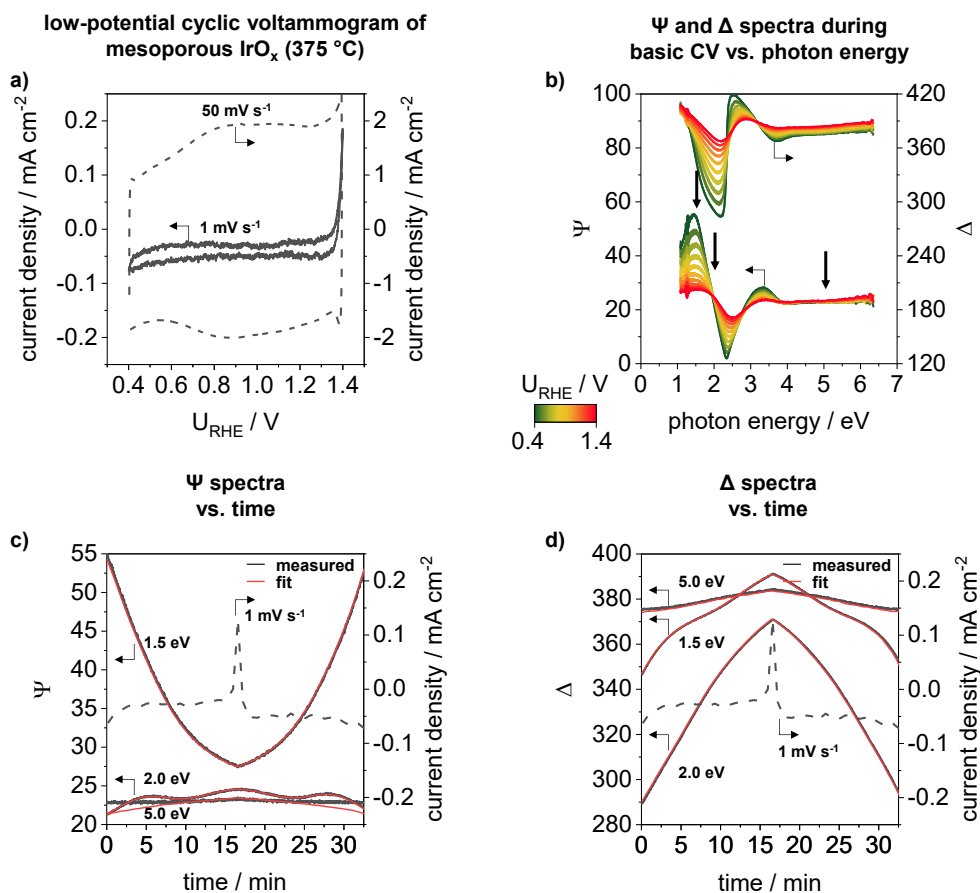
Appendix figure A13.4: ϵ_1 and ϵ_2 spectra of the TiO_x material (matrix) during ECSE investigation in the potential window of 0.40 V_{RHE} and 1.40 V_{RHE} . a) ϵ_1 and ϵ_2 spectra during cyclic voltammetry measurements. b) ϵ_1 at photon energies of 2.5 eV, 3.9 eV and 5.0 eV and c) ϵ_2 at photon energies of 3.5 eV, 4.5 eV and 5.0 eV. d) filling factor as a function of the applied potential.

Similar to the investigations in the OER regime, no changes in the entire spectra of the dielectric function during CV measurements as well as no indication of pore filling due to the change in volume fraction with produced gas are derived from the modeling.

A14 Operando ECSE investigations of mesoporous IrO_x (375 °C) in the lower potential range

The mesoporous IrO_x film calcined at 375 °C, was exemplarily investigated by cyclic voltammetry in the lower potential window between 0.4 V_{RHE} and 1.4 V_{RHE} with spectroscopic ellipsometry. Within this potential range, changes in the Ir oxidation state can be observed and gives an indication of the accessible and/or available Ir due to the obtained anodic and cathodic charge. ECSE measurements were carried out with a scan rate of 1 mV s⁻¹ in N₂ purged 0.1M HClO₄ and a flow rate of 85 ml min⁻¹. For a better overview, the measured data are described first and discussed at the end of this Chapter.

Appendix figure A14.1 displays a) the electrochemical studies in the lower potential range, b) the Ψ and Δ spectra as well as c) Ψ and d) Δ spectra and their fit results at selected photon energies in dependence on the measuring time.

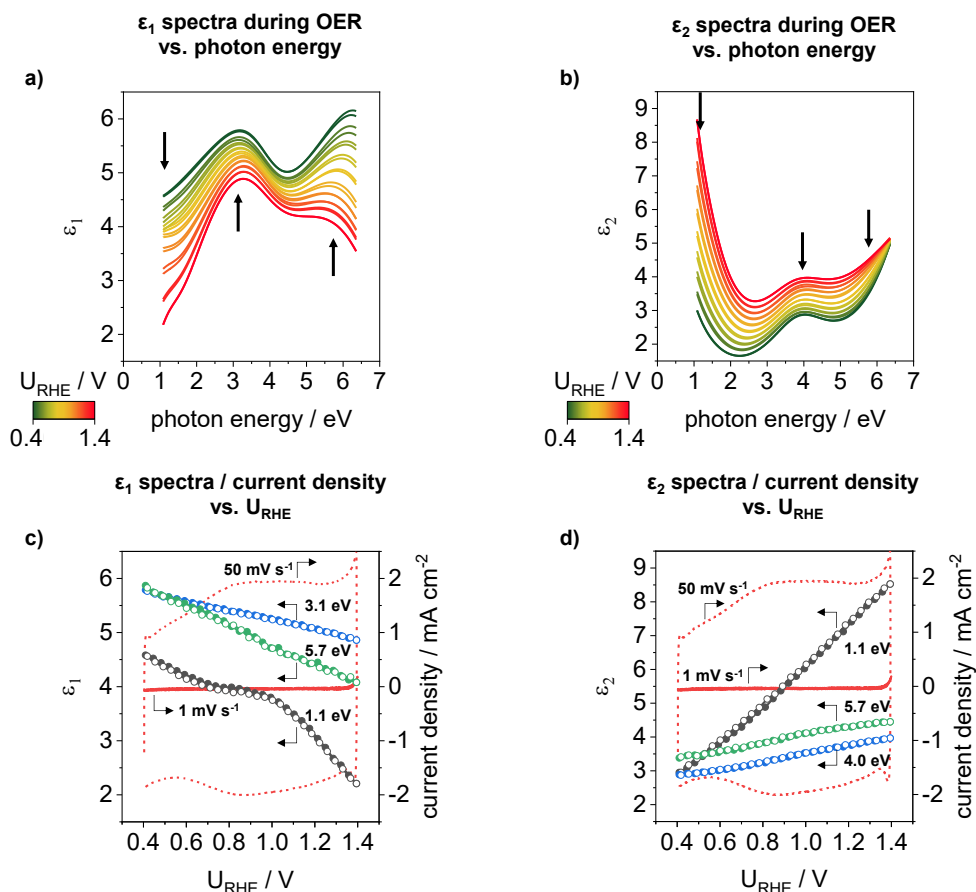


Appendix figure A14.1: Operando ECSE investigations in a lower potential window of a mesoporous IrO_x film calcined at 375 °C. a) low-potential cyclic voltammetry measurements in a potential range of 0.40 V_{RHE} and 1.40 V_{RHE} in N₂ purged 0.1M HClO₄ with a scan rate of 1 mV s⁻¹ and 50 mV s⁻¹. For both measurements an electrolyte flow rate of 85 ml min⁻¹ was applied. Potentials were measured against an Ag/AgCl electrode, which referred to RHE (+0.256 V at pH 1). b) Ψ and Δ spectra measured during cyclic voltammetry. c) Ψ and d) Δ spectra with fit results at photon energies of 1.5 eV, 2.0 eV and 5.0 eV together with the current density curve obtained from the CV measurement with a scan rate of 1 mV s⁻¹ as a function of the measuring time.

The low-potential CV measurement with a scan rate of 1 mV s⁻¹ is comparable to the measurements described in Chapter 4.3 and indicates a very low surface charge, which can be explained by the low scan rate (Appendix figure A14.1a). For comparison, the same measurement is plotted with a scan rate of 50 mV s⁻¹. In this CV, two broad peaks at about 0.95 V_{RHE} are detected in the anodic and cathodic scan. These peaks can be associated with an Ir^{III}/Ir^{IV} redox couple.^{59, 207, 208}

Appendix figure A14.1b depicts the corresponding Ψ and Δ spectra for the CV measurement with a scan rate of 1 mV s⁻¹. Noticeable changes in the photon energy range from 1.0 eV to 4.0 eV are visible in both spectra. To correlate these changes with the CV curve, the spectra were plotted at energies of 1.5 eV, 2.0 eV and 5.0 eV together with the current density curve against the measuring time (Appendix figure A14.1c, d). Ψ values at a photon energy of 1.5 eV displays a strong decrease for the anodic scan (until a measuring time of about 16 min) and a strong increase for the cathodic scan. At 2.0 eV, three features at 6 min, 16 min, and 28 min are visible during the CV. At 5.0 eV, however, only a slight change in the Ψ spectrum is observed. A similar behavior is detected for the Δ spectra, where at 1.5 eV three features are visible and at 2.0 eV a strong increase in the anodic scan and a strong decrease in the cathodic scan can be observed (Appendix figure A14.1d). The fit results from the model analysis (red lines) are in good agreement with the measured spectra, except for the Ψ fit in the range of 5.0 eV, where a slight deviation is obtained.

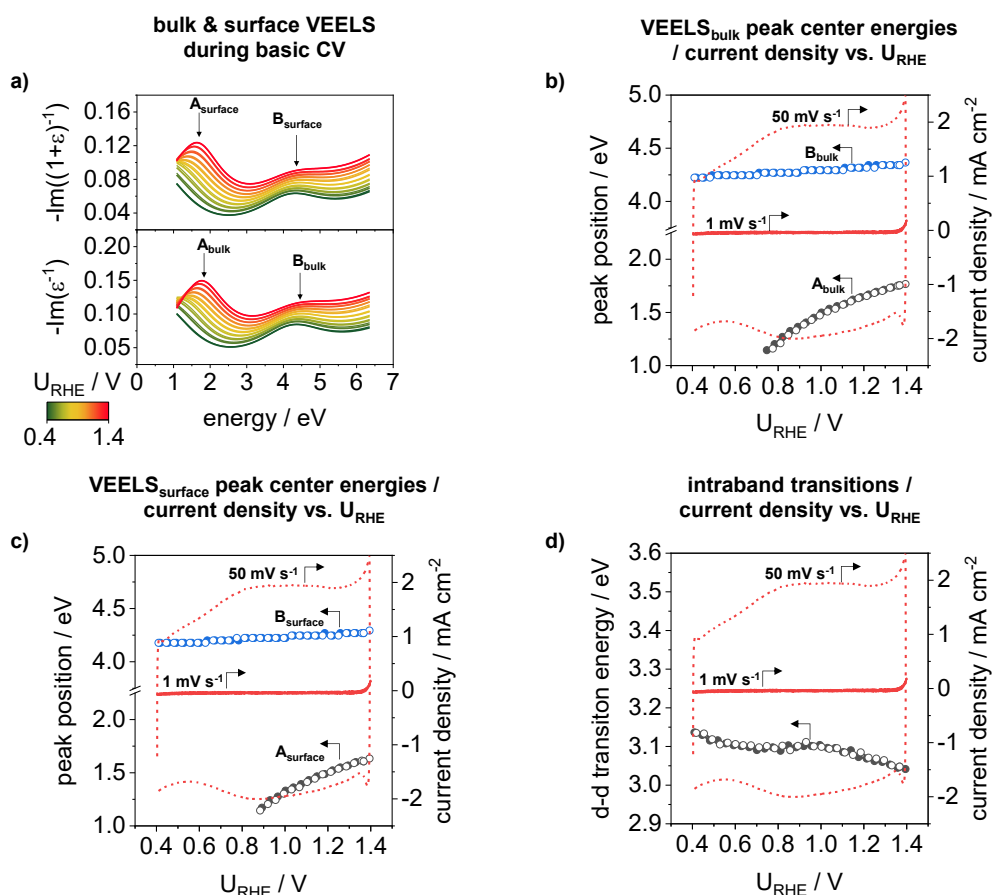
As with the ECSE measurements in the OER region in Chapter 6.2, the dielectric functions of the material can be derived from the fit results of the model analysis. Appendix figure A14.2 shows the ε_1 (a) and ε_2 (b) spectra at different potentials of the low-potential cyclovoltammetry measurement as a function of the photon energy and ε_1 (c) and ε_2 (d) at selected photon energies together with the current response of the 1 mV s⁻¹ and 50 mV s⁻¹ scan in dependence on the potential.



Appendix figure A14.2: ϵ_1 and ϵ_2 spectra of the IrO_x material (matrix) derived from modeling during ECSE investigation in the lower potential window. a) ϵ_1 and b) ϵ_2 spectra at different potentials. c) ϵ_1 at photon energies of 1.1 eV, 3.1 eV and 5.7 eV as well as d) ϵ_2 at photon energies of 1.1 eV, 4.0 eV and 5.7 eV.

Both spectra show significant changes in the complete spectral range during cyclic voltammetry (Appendix figure A14.2a, b). Similar to the spectra from the ECSE measurement in the OER region described in Chapter 6.2, changes in conduction band excitations (below 2.0 eV) and intraband transitions (near 1.0 eV) as well as in interband transitions (above 3.0 eV) are observed in the ϵ_2 spectra (Appendix figure A14.2b). The characteristics in the ϵ_1 spectra at photon energies of 1.0 eV, 3.1 eV and 5.7 eV exhibit pronounced variation as well (Appendix figure A14.2a). By plotting the characteristic features against the potential, a general decreasing trend with increase of the potential is observed in the ϵ_1 spectra (Appendix figure A14.2c). At 1.1 eV, a kind of peak at about 0.95 V_{RHE} can be additionally detected. In contrast, the features in the ϵ_2 spectra increase with increasing potential, whereas at 1.1 eV a relatively strong behavior can be recognized (Appendix figure A14.2d). Both spectra also indicate a fully reversible trend of the dielectric functions during the anodic and cathodic scan.

For a more detailed analysis of the electronic characteristic of the IrO_x material during the anodic and cathodic scan, VEEL spectra are calculated from the dielectric functions. Appendix figure A14.3 depicts the bulk and surface VEELS (a), the A and B peaks of the bulk (b) and surface (c) spectra as well as intraband transition energies (d) from the Tauc relation.



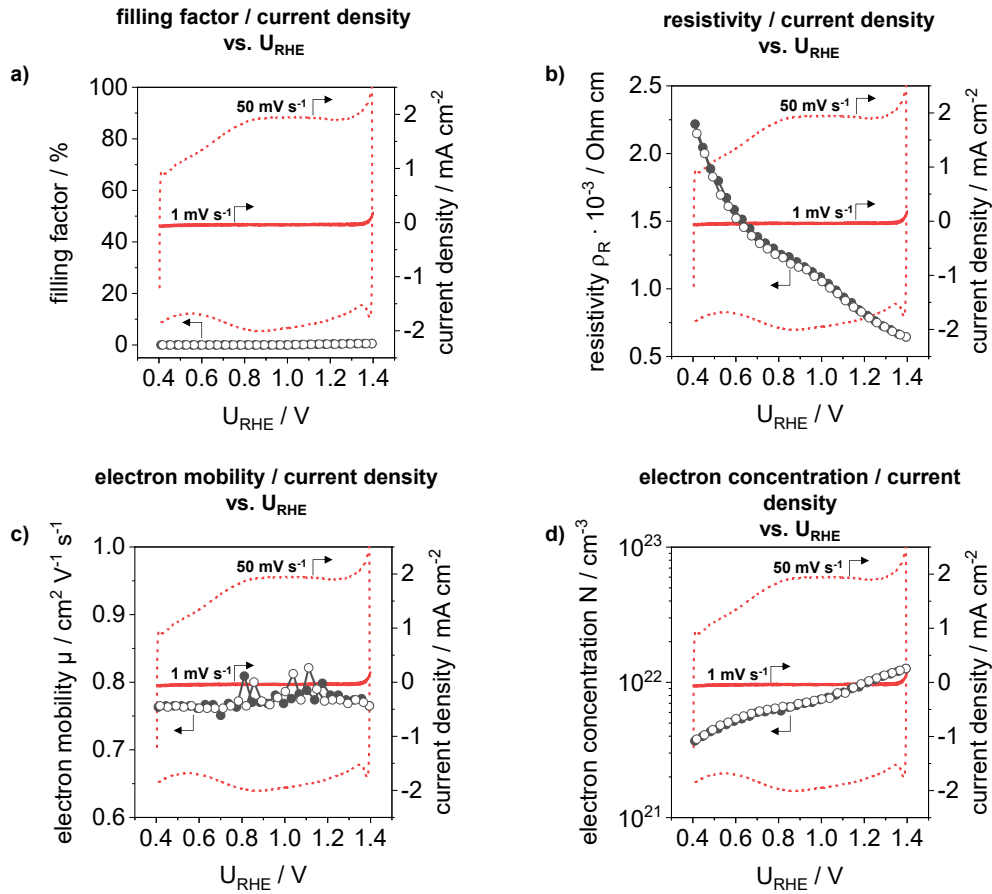
Appendix figure A14.3: Valence electron energy loss spectra study during ECSE measurements in the lower potential range of 0.40 V_{RHE} and 1.40 V_{RHE} . a) Calculated bulk and surface VEEL spectra at different potentials. A und B peaks of b) bulk VEELS and c) surface VEELS as a function of the potential as well as derived intraband transition energies (d) between the Ir 5d t_{2g} and e_g band.

Similar to the dielectric functions, the VEEL spectra (Appendix figure A14.3a) reveal significant changes during the anodic and cathodic scan, especially the A peaks, which are strongly shifted in their center energy. The center energy of the B peaks also shifts to higher values in the anodic scan and are completely reversible in the cathodic scan. Furthermore, the individual spectra differ strongly within their intensities.

The nonlinear shift of the center energy of the A peaks ranges from about 1.2 eV to 1.7 eV and from about 1.1 eV to 1.6 eV for the bulk and surface spectra, respectively (Appendix figure A14.3b and c). Due to the strong shift, the center energy can only be detected until a potential of 0.78 V_{RHE} and 0.88 V_{RHE} in the bulk and surface spectra, respectively. In the low photon energy range (IR range), the strong interaction of light with the electrolyte and the associated molecule oscillations unfortunately lead to a low signal to noise ratio. In contrast, the B peaks in both spectra indicate a stepwise increase of the center energy in the anodic scan and a completely reversible behavior in the cathodic scan.

Transition energies between the Ir 5d t_{2g} and e_g band (Appendix figure A14.3d) reveal a general decreasing trend with higher potentials. Additionally, a broad peak at around 0.95 V_{RHE} is observed, which can be attributed to the Ir^{III}/Ir^{IV} redox couple.

Electrical properties as well as the volume fraction of produced gas (filling factor) can also be derived from the modeling during the anodic and cathodic scan in the potential range between 0.40 V_{RHE} and 1.40 V_{RHE}. Appendix figure A14.4 shows the filling factor (a), the resistivity (b) as well as the electron mobility (c) and electron concentration (d) of the IrO_x material in dependence on the potential.



Appendix figure A14.4: Deduced properties from model analysis during ECSE measurements in the potential range of 0.40 V_{RHE} and 1.40 V_{RHE}. a) filling factor, b) resistivity, c) electron mobility, and d) electron concentration as a function of the potential.

As shown in Appendix figure A14.4a, the filling factor deduced from the model analysis is close to zero over the whole scan range. This is in good agreement with the expectation that no oxygen gas is produced in this potential range.

The resistivity indicates a decrease from 0.40 V_{RHE} to 1.40 V_{RHE} and a slight peak at 0.95 V_{RHE} (Appendix figure A14.4b). This behavior is completely reversible for the cathodic scan. The electron mobility (Appendix figure A14.4c) reveal a slightly reduced value in the range of 0.40 V_{RHE} to 0.80 V_{RHE} compared to higher potentials (> 1.20 V_{RHE}) and between 0.80 V_{RHE} and 1.20 V_{RHE} a slight scattering in electron mobility. In contrast, the electron concentration (Appendix figure A14.4d) decreases continuously with decreasing potential.

The results from ECSE analysis in the potential range between 0.40 V_{RHE} and 1.40 V_{RHE} can be correlated mostly with the Ir^{III}/Ir^{IV} redox couple.^{59, 207, 208} Thus, the dielectric functions show a pronounced change in the lower photon range, indicating a change in conduction band excitations and intraband transitions (Appendix figure A14.2). Due to the reduction of the material during scanning to lower potentials and the change of the Ir oxidation state from Ir^{IV} to Ir^{III} when exceeding the potential of 0.95 V_{RHE}, there is also a change in the interactions of the O p and Ir d orbitals.

These changes are also evident in the VEEL spectra, where a strong decrease in the energy values of the interactions between the partially filled t_{2g} sub-level of the d-band of iridium and the p-band of oxygen (A peak) to lower potentials is observed (Appendix figure A14.3). This behavior suggests enhanced adsorption of OH species and/or H₂O molecules, or conversion of O species to OH species.¹⁹¹ In addition, the decrease in p-d interaction can be associated with a shift of the t_{2g} band to higher energies, leading to enhanced adsorption of O species (probably OH species).^{45, 46} This shift of the t_{2g} band is also directly reflected in the electrical properties such as resistivity (Appendix figure A14.4b) and electron concentration (Appendix figure A14.4d).

A change in the p-d interactions and the shift of the Ir 5d t_{2g} band also affect the d-d intraband transitions between the Ir 5d t_{2g} and the e_g bands (Appendix figure A14.3d). The up shift of the t_{2g} band to higher energies leads to a lower d-orbital splitting and the t_{2g} and e_g bands become closer, probably resulting in a high spin configuration. In addition, the broad feature at about 0.95 V_{RHE} also indicates the change of the Ir oxidation state from Ir^{IV} to Ir^{III}.

In summary, operando ECSE investigations in the potential range between 0.40 V_{RHE} and 1.40 V_{RHE} of the exemplary tested mesoporous IrO_x film, which was calcined at 375 °C, provide noticeable changes within the material. The Ir^{III}/Ir^{IV} redox couple can be detected in the dielectric functions as well as in Ir d-d intraband transitions. The shift in the d-d intraband transition energies may also indicate a high spin configuration of the relative occupancy of the t_{2g} and e_g states. The change of the Ir oxidation state is also reflected in the electrical properties such as resistivity and electron concentration, where an increase or decrease is observed. Furthermore, the change of the oxidation state probably results in a shift of the Ir 5d t_{2g} sub-level to higher energies and an increased adsorption of O species.

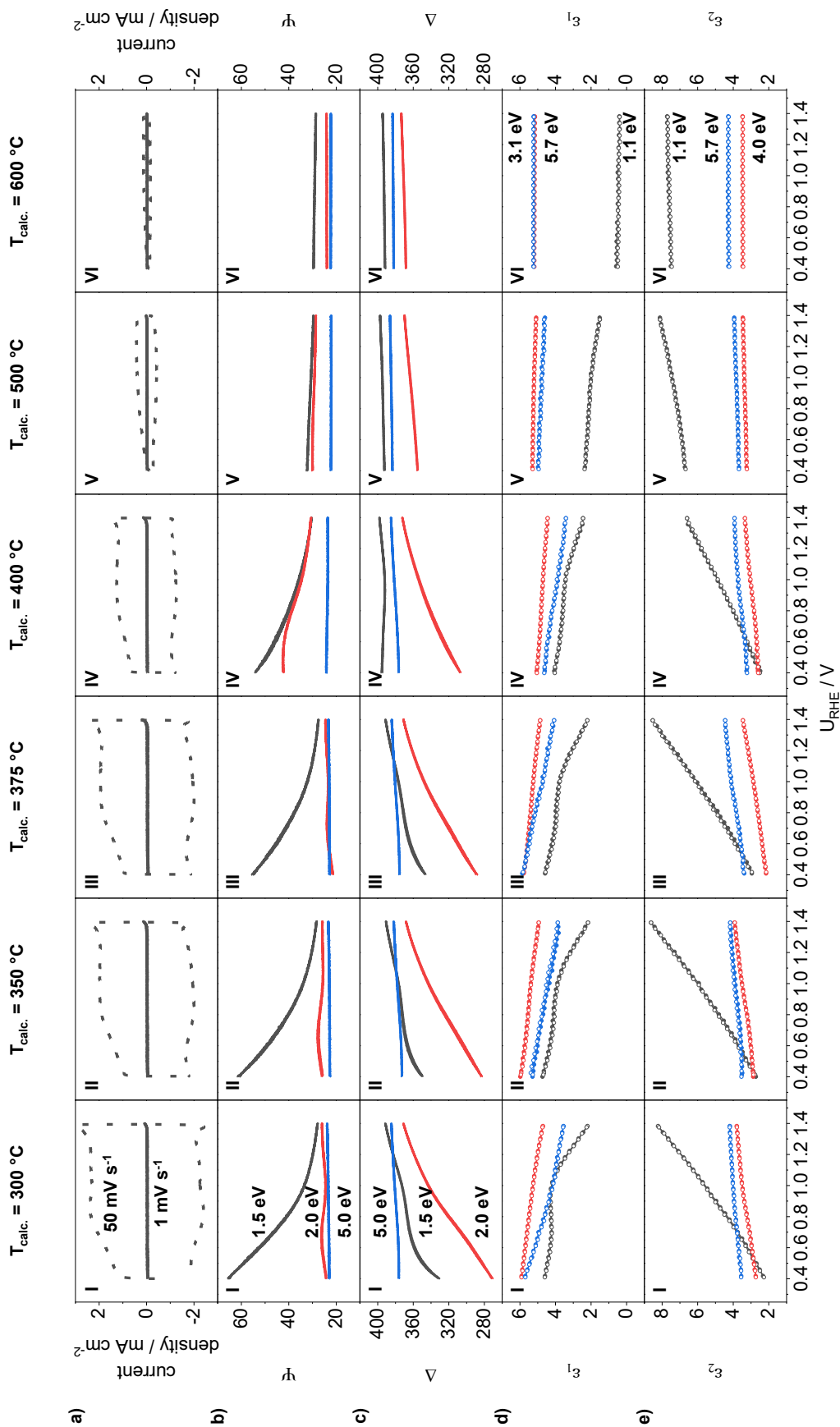
A15 Operando ECSE investigations of the calcination series in the lower potential range

Mesoporous IrO_x samples calcined at 300 °C, 350 °C, 375 °C, 400 °C, 500 °C and 600 °C are also investigated by ECSE analysis in the potential range of 0.40 V_{RHE} and 1.40 V_{RHE}. In the following, the measured data, and the model analysis as well as the derived material properties are first described and discussed at the end of this Chapter. ECSE studies of the influence of calcination temperature in the lower potential window is demonstrated in Appendix figure A15.1, where a) the current responses, b) Ψ and c) Δ curves as well as ε_1 (d) and ε_2 (e) curves of the calcination series in dependence of the applied potential are plotted.

Current responses of scan rates of 1 mV s⁻¹ and, for comparison, 50 mV s⁻¹ indicate a decrease of anodic and cathodic charge from calcination temperatures of 300 °C to 600 °C, which is clearly demonstrated in the case of a scan rate of 50 mV s⁻¹ (Appendix figure A15.1a I-VI). This trend is like the ex-situ characterization described in Chapter 4.3 in detail and used again for comparison and correlation of the derived parameters.

Ψ values of the calcination series reveal systematic changes with increasing calcination temperature, especially at a photon energy of 1.5 eV (Appendix figure A15.1b I-VI). While the Ψ values at 1.5 eV decrease strongly with increasing potential for catalysts calcined between 300 °C and 400 °C (Appendix figure A15.1b I-IV), films at higher calcination temperatures show only slight to no further changes (Appendix figure A15.1b V-VI). At 2.0 eV a kind of wave shape feature at about 0.70 V_{RHE} is measured for the low-temperature calcined films ($\leq 400^\circ\text{C}$), whereas at 5.0 eV no further changes are visible for the complete calcination series. In contrast, Δ at 1.5 eV shows a feature in the values for films calcined between 300 °C and 375 °C (Appendix figure A15.1c I-III), while at higher temperatures an almost constant behavior is observed (Appendix figure A15.1c IV-VI). At 2.0 eV a strong to slight increase of the values is visible with increasing calcination temperatures. Similar to the Ψ values, no further changes at 5.0 eV are observed.

Characteristic features in the ε_1 spectra at photon energies of 1.1 eV, 3.1 eV and 5.7 eV reveal a decreasing trend for catalyst films calcined between 300 °C and 500 °C (Appendix figure A15.1d I-V), while at 600 °C no further changes are observed (Appendix figure A15.1d VI). A broad peak at 1.1 eV is visible in the curves by scanning in the potential range at about 1.00 V_{RHE}, which becomes less obvious with increasing calcination temperature. In contrast, photon energies at 1.1 eV, 4.0 eV and 5.7 eV in the ε_2 curves generally increase when scanning to higher potentials, although this trend is less present with increasing calcination temperatures and mostly constant for the 600 °C calcined film.



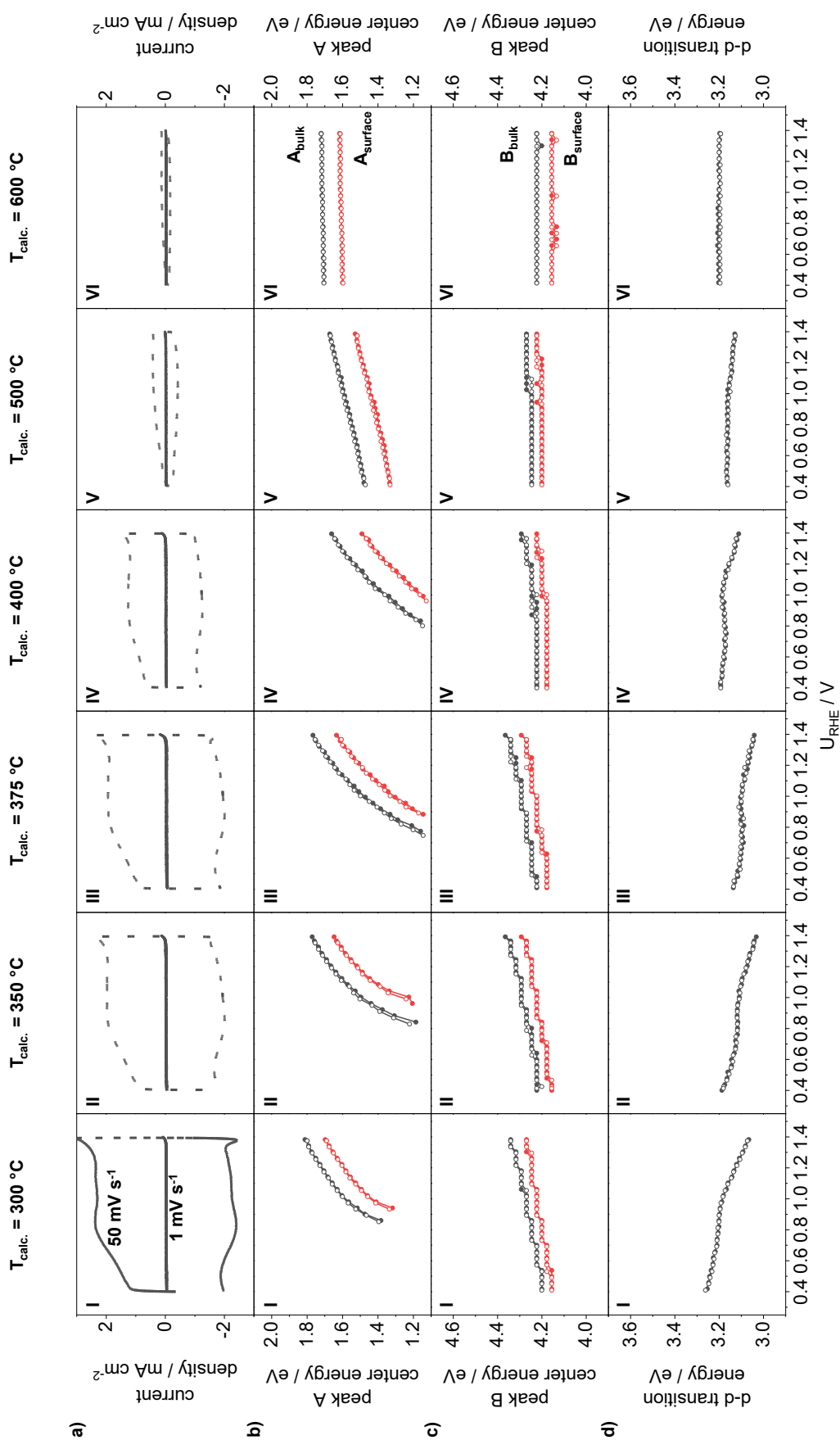
Appendix figure A15.1: Operando ECSE investigations and derived ϵ_1 and ϵ_2 spectra of mesoporous IrO_x films calcined between 300 °C and 600 °C in the potential range between 0.40 V_{RHE} and 1.40 V_{RHE} . a) obtained current density curves from EC measurements at scan rates of 1 mV s^{-1} and 50 mV s^{-1} in 0.1M HClO_4 and a flow rate of 85 ml min^{-1} . Photon energies of 1.5 eV, 2.0 eV and 5.0 eV from ψ (b) and Δ (c) spectra in dependence of the applied potential. Characteristic features of d) ϵ_1 and e) ϵ_2 spectra at photon energies of 1.1 eV, 3.1 eV or 4.0 eV and 5.7 eV as a function of the potential.

Properties derived from the VEELS analysis are used to gain further insight into the electronic structure of the materials and the influence of calcination temperature. Appendix figure A15.2 displays a) the current density curves for comparison and correlation, the center energy of the bulk and surface A (b) and B (c) peaks as well as d) intraband transitions of the calcination series during low-potential cyclovoltammetry.

The A peaks in both bulk and surface spectra indicate a change in their center energy, with a stronger shift at lower calcined films ($\leq 400\text{ }^{\circ}\text{C}$) and less pronounced changes at higher calcination temperatures (Appendix figure A15.2b I-VI). The center energy shifts to higher energies in the anodic scan and is reversible to lower energies in the cathodic scan. A non-linear behavior is observed for the $300\text{ }^{\circ}\text{C}$ to $400\text{ }^{\circ}\text{C}$ calcined films (Appendix figure A15.2b I-IV), which changes into a relatively linear curve at higher temperatures (Appendix figure A15.2b V-VI). Additionally, the shift to lower energies is very significant for low-temperature calcined films. In the region where the change of the $\text{Ir}^{\text{III}}/\text{Ir}^{\text{IV}}$ oxidation state takes place, the curves of the center energy cannot be further detected due to the interaction of light with H_2O molecules.

The B peaks, which are associated with transitions from the O 2p to unoccupied Ir 5d t_{2g} bands, exhibit a stepwise increase of the center energy in the anodic scan and a reversible stepwise decrease in the cathodic scan for films calcined between $300\text{ }^{\circ}\text{C}$ and $375\text{ }^{\circ}\text{C}$ (Appendix figure A15.2c I-III). At a calcination temperature of $400\text{ }^{\circ}\text{C}$ a slight increase at higher potentials and at $500\text{ }^{\circ}\text{C}$ und $600\text{ }^{\circ}\text{C}$ no further changes of the center energy are observed (Appendix figure A15.2c IV-VI).

The d-d intraband transition energies from the Tauc relation generally show a reversible decreasing trend of energies with increasing potential for all catalyst films (Appendix figure A15.2d I-VI). In addition, a broad feature can be observed at a potential of about $0.95\text{ V}_{\text{RHE}}$, similar to the ε_1 values at a photon energy of 1.1 eV , which is less pronounced at higher calcination temperatures ($> 400\text{ }^{\circ}\text{C}$).



Appendix figure A15.2: VEELS analysis during ECSE investigations of the mesoporous IrO_x calcination series in the lower potential window. a) current density curves from EC measurements at scan rates of 1 mV s^{-1} and 50 mV s^{-1} . Center energies of the identified A peak (b) and B peak (c) of bulk and surface VEEL spectra during cyclic voltammetry. d) d-d intraband transition energy values deduced from the Tauc relation in dependence of the potential.

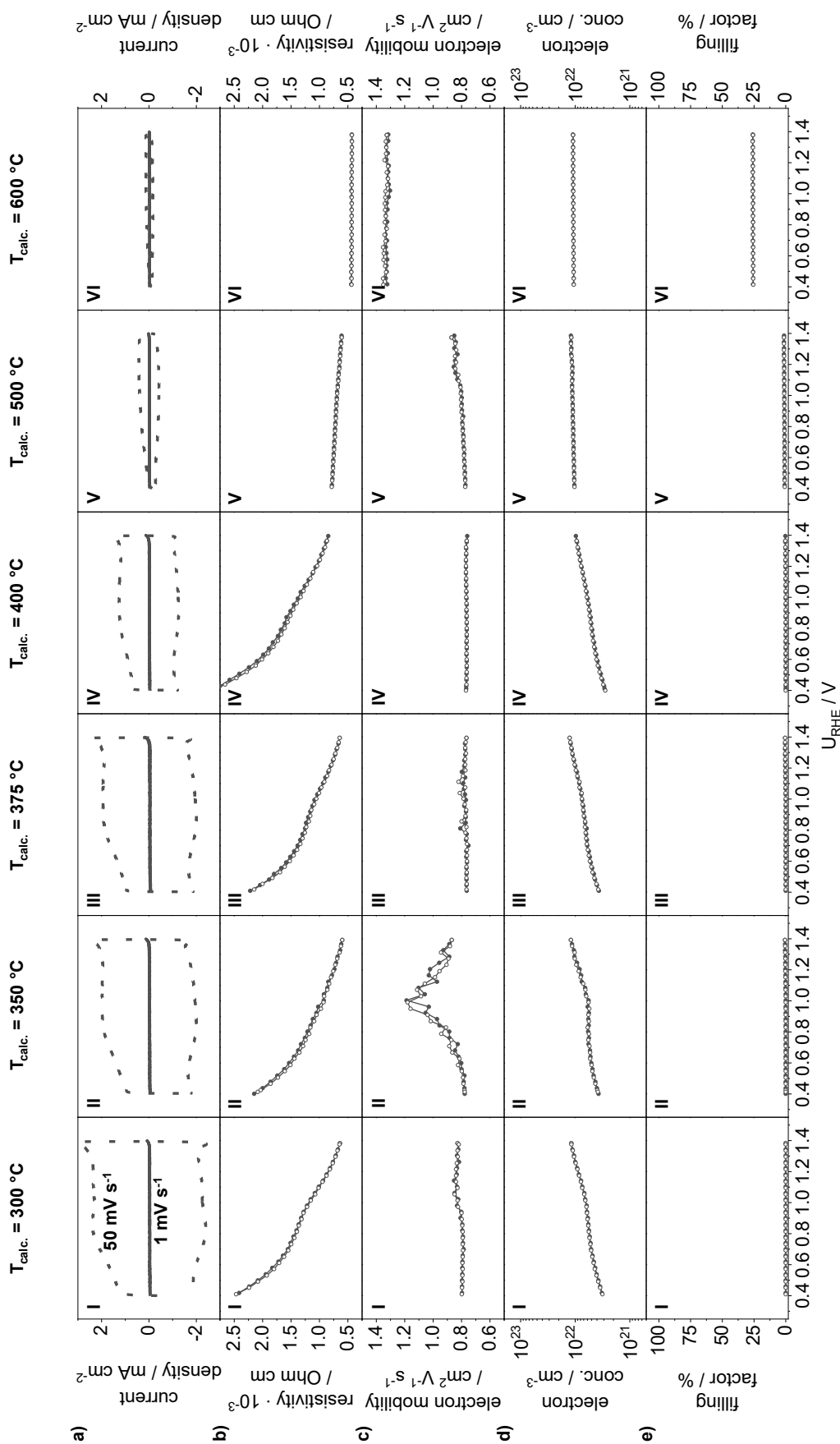
Finally, the electrical properties of the materials and the volume fraction of the generated gas during the low-potential cyclic voltammetry measurements are presented. Appendix figure A15.3 shows for correlation the current density curves (a), the resistivity (b), the electron mobility (c) and electron concentration (d) as well as the filling factor (e).

The resistivity values Appendix figure A15.3b I-VI) decrease with anodic scanning and increase reversibly with cathodic scanning, similar to the behavior described for the ε_2 curves at a photon energy of 1.1 eV (Appendix figure A15.1e I-VI). Therefore, low-temperature calcined catalyst films (≤ 400 °C) indicate a more pronounced resistivity behavior than higher calcined films, i.e. the decreasing trend, with increasing potential, declines towards higher calcination temperatures and is almost constant at 600 °C. Additionally, a slight feature at a potential of $0.95 V_{RHE}$ is observed for films calcined between 300 °C and 400 °C (Appendix figure A15.3b I-IV). The change of the oxidation state also seems to be visible and directly influences the resistivity of the catalyst films, i.e., higher values in range of the Ir^{III} ($< 0.95 V_{RHE}$) species and lower values in the Ir^{IV} species range ($> 0.95 V_{RHE}$).

Except for the film calcined at 350 °C (Appendix figure A15.3c II, V), the electron mobility during the anodic and cathodic scan exhibits almost constant values of about $0.8 \text{ cm}^2 \text{ V}^{-1} \text{ s}^{-1}$ (Appendix figure A15.3c I, III-V) or $1.4 \text{ cm}^2 \text{ V}^{-1} \text{ s}^{-1}$ (Appendix figure A15.3c VI). Additionally, the 300 °C and 500 °C calcined films (Appendix figure A15.3c I, V) indicate a slight increase of the electron mobility at higher potentials and a small feature at about $1.10 V_{RHE}$ and $1.20 V_{RHE}$, respectively. The catalyst film calcined at 350 °C (Appendix figure A15.3c II) reveals an increase from an electron mobility of $0.8 \text{ cm}^2 \text{ V}^{-1} \text{ s}^{-1}$ to $1.2 \text{ cm}^2 \text{ V}^{-1} \text{ s}^{-1}$ at $0.95 V_{RHE}$, followed by a decrease to $0.9 \text{ cm}^2 \text{ V}^{-1} \text{ s}^{-1}$. The peak at 350 °C seems to be related to the Ir^{III}/Ir^{IV} redox pair, however no peak is observed for the other films.

The fit results of the electron concentrations show an increasing behavior in anodic scans and a reversible decrease in cathodic scans for films calcined between 300 °C and 400 °C (Appendix figure A15.3d I-IV), while at higher temperatures no further changes are indicated (Appendix figure A15.3d V-VI). At lower potentials, i.e., in the range where more Ir^{III} species are present, a lower electron concentration is observed, whereas at higher potentials, i.e., in the range of predominantly Ir^{IV} species, higher values of the electron concentration are deduced for the low-temperature calcined films (≤ 400 °C).

Appendix figure A15.3e depicts the filling factor of each catalyst film of the calcination series during cyclic voltammetry in the potential window of $0.40 V_{RHE}$ and $1.40 V_{RHE}$. As expected, no volume fraction of produced gas is derived from the model analysis. Similar to the ECSE investigations in the OER regime, the 600 °C (see Chapter 6.3; Figure 45) calcined film shows a constant value of about 25%, which is due to the film morphology and pore geometry and probably gas inclusion within closed pores.



Appendix figure A15.3: Material properties derived from the model analysis during ECSE investigations of the calcination series in the lower potential window. a) obtained current density curves from cyclic voltammetry measurements and scan rates of 1 mV s^{-1} and 50 mV s^{-1} . b) resistivity values, c) electron mobility and d) concentration of the IrO_x materials. e) filling factor during EC measurements in the potential range of $0.40 \text{ V}_{\text{RHE}}$ and $1.40 \text{ V}_{\text{RHE}}$.

The results of the ECSE analysis on the dependence of the calcination temperature on the material properties in the investigated potential range between 0.40 V_{RHE} and 1.40 V_{RHE} can be predominantly attributed to the Ir^{III}/Ir^{IV} redox couple. Features in the dielectric functions appear mainly in the region of the redox couple at about 0.95 V_{RHE}. The decreasing visibility of this feature at higher calcination temperatures indicates a less pronounced change in oxidation state. This implies that more crystalline IrO_x films (high-temperature calcined films) are less able to form Ir^{III} species during cyclic voltammetry. In addition, more significant changes in the lower photon energy range are observed for the low-temperature calcined films (≤ 400 °C) compared to the high-temperature calcined films (> 400 °C). This indicates a more pronounced change in conduction band excitations, probably due to an increased amount of Ir^{III} species.

Noticeable changes are also visible in the interband transitions between the partially filled t_{2g} sub-level of the d-band of iridium and the p-band of oxygen in the Ir^{III}/Ir^{IV} redox couple region (at about 0.95 V_{RHE}). This change clearly depends on the calcination temperature, where low crystalline films (≤ 400 °C) show a pronounced change in the oxidation state. This can be explained by a better interaction of OH species and/or H₂O molecules adsorbed on the surface, leading to a shift of the Ir 5d t_{2g} band to higher energies. Due to the more crystalline structure of the material, fewer interactions and/or fewer adsorbed molecules on the surface are expected at higher calcination temperatures, which can be attributed to a less electrophilic character and/or fewer adsorption sites.

The d-d intraband transition energies between the Ir 5d t_{2g} and e_g sub-level also show a change in the oxidation state of the Ir for low-temperature calcined films, while the high-temperature calcined films show relatively constant values. The shift of the t_{2g} band to higher energies when scanning to lower potentials for the low-temperature calcined films results in a nearing of the t_{2g} and e_g sub-level and increase the intraband transition energies due to a high spin configuration. In contrast, the more ordered crystal structures of the high-temperature calcined films lead to a lower oxidation state transition, where the films predominantly retain their Ir^{IV} oxidation state and slight to non-changes of the t_{2g} band energy position during cyclic voltammetry measurements.

In summary, ECSE investigations of the calcination series in the low-potential range (0.40 V_{RHE} and 1.40 V_{RHE}), provide noticeable changes within the material and the influence of the calcination temperature. The Ir^{III}/Ir^{IV} redox couple can be detected in the interband and intraband transitions, which are less pronounced at higher calcination temperatures. The change of the Ir oxidation state directly influences the electrical properties, where an increase or decrease in the resistivity or electron concentration is observed, when more Ir^{III} species are present.

B List of publications and presentations

PUBLICATIONS

Note that parts of this thesis, in particular parts of Chapter 4, 5, 6.2 and 7.1 as well parts in the appendix section (A1, A7, A13 and A14), have already been published in:

R. Sachse, M. Pflüger, J.-J. Velasco-Vélez, M. Sahre, J. Radnik, M. Bernicke, D. Bernsmeier, V.-D. Hodoroaba, M. Krumrey, P. Strasser, R. Kraehnert and A. Hertwig, Assessing Optical and Electrical Properties of Highly Active IrO_x Catalysts for the Electrochemical Oxygen Evolution Reaction via Spectroscopic Ellipsometry. *ACS Catalysis*, **2020**, 10, 14210-14223.

As well as a preprint, which is a preliminary version of a manuscript that has not yet been peer-reviewed by a journal or is in the process of being peer-reviewed:

René Sachse, Mario Sahre, Michael Bernicke Denis Bernsmeier, Vasile-Dan Hodoroaba, Peter Strasser, Ralph Kraehnert and Andreas Hertwig, Operando electrochemical spectroscopic ellipsometry: Insights into electrochemical behavior of catalyst materials under realistic working conditions, 25 October 2021, PREPRINT (Version 1) available at Research Square <https://doi.org/10.21203/rs.3.rs-934130/v1>. This work is licensed under a CC BY 4.0 License.

In addition, the following publications were published as first and co-author during the PhD:

R. Sachse, D. Bernsmeier, R. Schmack, I. Häusler, A. Hertwig, K. Kraffert, J. Nissen and R. Kraehnert, Colloidal bimetallic platinum–ruthenium nanoparticles in ordered mesoporous carbon films as highly active electrocatalysts for the hydrogen evolution reaction. *Catalysis Science & Technology*, **2020**, *10*, 2057-2068.

R. Sachse, V. D. Hodoroaba, A. Hertwig, L. Kotil, R. Kraehnert, Analysis of elemental composition and porosity of mesoporous iridium-titanium mixed oxide thin films for energy application by SEM/EDS. *Microscopy and Microanalysis* **2019**, *25*, 1770-1771. (Conference Proceedings)

D. Bernsmeier, R. Sachse, M. Bernicke, R. Schmack, F. Kettemann, J. Polte, R. Kraehnert, Outstanding hydrogen evolution performance of supported Pt nanoparticles: Incorporation of preformed colloids into mesoporous carbon films. *Journal of Catalysis* **2019**, *369*, 181-189.

R. Sachse, A. Hertwig, R. Kraehnert, V.-D. Hodoroaba, Analysis of Mesoporous Iridium Oxide Thin Films by the Combined Methodical Approach SEM/EDS/STRATAGem. *Microscopy and Microanalysis* **2018**, *24*, 762-763. (Conference Proceedings)

D. Bernsmeier, M. Bernicke, R. Schmack, R. Sachse, B. Paul, A. Bergmann, P. Strasser, E. Ortel, R. Kraehnert, Oxygen Evolution Catalysts Based on Ir–Ti Mixed Oxides with Templated Mesopore Structure: Impact of Ir on Activity and Conductivity. *ChemSusChem* **2018**, *11*, 2367-2374.

ORAL PRESENTATIONS OF CONFERENCES

Correlative analysis of mesoporous thin $\text{IrO}_x\text{-TiO}_x$ mixed oxide films for understanding the impact of synthesis conditions, R. Sachse, L. Matjacic, G. McMahon, A. Hertwig, R. Kraehnert V.-D. Hodoroaba; 18th European Conference on Applications of Surface and Interface Analysis, Dresden, Germany, 2019.

Analysis of elemental composition and porosity of mesoporous iridium titanium mixed oxide thin films for energy application by SEM/EDS, R. Sachse, V.-D. Hodoroaba, A. Hertwig, L. Matjacic, G. McMahon, L. Kotil, D. Bernsmeier, R. Kraehnert; Microscopy & Microanalysis 2019 Meeting, Portland, Oregon, USA, 2018. (invited student speaker)

Spectroscopic ellipsometric analysis of elemental composition and porosity of mesoporous iridium titanium mixed oxide thin films for electrocatalytic splitting of water, R. Sachse, L. Kotil, V.-D. Hodoroaba, D. Bernsmeier, R. Kraehnert and A. Hertwig; 8th International Conference on Spectroscopic Ellipsometry, Barcelona, Spain, 2019.

Spectroscopic ellipsometric analysis of elemental composition and porosity of mesoporous iridium-titanium mixed oxide thin films for electrocatalytic splitting of water, R. Sachse, L. Kotil, V.-D. Hodoroaba, A. Hertwig, R. Kraehnert, 31. Deutsche Zeolith-Tagung, Dresden, Germany, 2019.

Multi-method analysis of pore-controlled mesoporous oxide materials, A. Hertwig, R. Sachse, R. Kraehnert, V.-D. Hodoroaba; European Optical Society Biennial Meeting 2018, Delft, Netherlands, 2018.

Spectroscopic ellipsometry for the determination of thickness and porosity of mesoporous metal oxide films, R. Sachse, A. Hertwig, V.-D. Hodoroaba, R. Kraehnert; 10th workshop ellipsometry, Chemnitz, Germany, 2018.

Metal nanoparticle containing ordered mesoporous carbon coatings as highly active electrocatalysts for the hydrogen evolution, R. Sachse, D. Bernsmeier, R. Kraehnert; 51. Jahrestreffen Deutscher Katalytiker, Weimar, Germany, 2018. (Kurzvortrag)

Spectroscopic ellipsometry for the determination of thickness and porosity of mesoporous metal oxide films, R. Sachse, A. Hertwig, V.-D. Hodoroaba, R. Kraehnert; 30. Deutsche Zeolith-Tagung, Kiel, Germany, 2018. (Kurzvortrag)

Preformed bimetallic nanoparticles in ordered mesoporous carbon coatings as highly active electrocatalysts for the hydrogen evolution reaction, R. Sachse, D. Bernsmeier, R. Schmack, I. Häusler, R. Kraehnert; 29. Deutsche Zeolith-Tagung, Frankfurt am Main, Germany, 2017.

In addition, 7 posters have been presented as first author at national and international conferences.

